



TECHNISCHE UNIVERSITÄT MÜNCHEN

TUM School of Natural Sciences

## **Catalytic conversion of biomass-based resources to transportation fuels**

Lara Patricia Milaković

Vollständiger Abdruck der von der TUM School of Natural Sciences der  
Technischen Universität München zur Erlangung einer

Doktorin der Naturwissenschaften (Dr. rer. nat.)

genehmigten Dissertation.

Vorsitz: Hon.-Prof. Dr. Richard W. Fischer

Prüfer der Dissertation: 1. Prof. Dr. Johannes A. Lercher

2. Prof. Dr. Klaus Köhler

Die Dissertation wurde am 15.06.2023 bei der Technischen Universität  
München eingereicht und durch die TUM School of Natural Sciences am  
19.07.2023 angenommen.

*Für meine Familie.*

*When you have exhausted all possibilities, remember this – you haven't.  
– Thomas Edison*



## Acknowledgements

First and foremost, I would like to express my sincere gratitude to *Prof. Johannes A. Lercher* for the invaluable opportunity to pursue my PhD research within his group. Thank you for sharing your knowledge, guidance, and confidence, and for granting me the freedom to explore and grow in my research. It has been a pleasure learning from and working with you throughout this journey.

Next, I would like to express my deep appreciation to my supervisors. I warmly thank *Dr. Eszter Barath* for her unwavering support, always having my back, and taking time for me. I am very thankful to *Dr. Yue Liu* for giving me great advice, sharing your fruitful ideas and theories, and all the engaging scientific discussions. I also want to extend my thanks to *Prof. Andreas Jentys* for many valuable conversations and insights.

Des Weiteren möchte ich mich bei *Xaver Hecht, Muhammed Iqbal, Andreas Marx* und *Martin Neukamm* für die großartige technische Unterstützung bedanken. Ebenso möchte ich *Bettina Federmann, Kateryna Kryvko* und *Stefanie Seibold* für ihre hervorragende administrative und organisatorische Hilfe sowie ihre herzliche Art meinen aufrichtigen Dank aussprechen.

Ein riesiger Dank gilt meinen TC II Kollegen – ohne euch wäre diese Zeit nur halb so schnell verfliegen. Tausend Dank für eure Hilfe und Unterstützung im Labor, aber auch für all die schönen Momente außerhalb des Labors, sei es bei leckeren Grillfeiern, lustigen und feuchtfröhlichen Konferenzen, Weihnachtsfeiern oder gemeinsamen Wiesn-Besuchen. Ich möchte mich bei *Dr. Andreas Ehrmaier, Teresa Schachtl, Dr. Laura Löbber, Mirjam Wenig, Christoph Denk, Dr. Verena Höpfl, Dr. Niklas Pfriem, Dr. Manuel Weber, Dr. Martin Baumgärtl, Dr. Insu Lee, Dr. Roland Weindl, Simon Krebs, Dr. Felix Kirchberger, Dr. Peter Hintermeier, Dr. Daniel Melzer, Jakub Pazdera, Dr. Lingli Ni, Alexander Wellmann, Dr. Philipp Fischer, Ferdinand Vogelgsang, Dr. Fuli Deng, Dr. Ruixue Zhao, Florian Zahn, Lennart Wahl* und vielen anderen von Herzen bedanken.

Ein besonderer Dank geht an all die Studenten, die ich während meiner Promotion bei ihren Forschungspraktika, Bachelor- oder Masterarbeiten betreuen durfte. *Baran Şahin, Christian Weindl, Enes Caliskan, Greta Zámbo, Ke Jin, Lukra Sirok, Margot Hilt, Patrick Gotthardt, Svenja Knösch, Tim Schlachta*, und vor allem meine Masteranden *Amelie Mühlbach, Andreas Brenig* und *Mirjam Wenig*, ich weiß all eure Hilfe, euren Fleiß und Engagement wirklich sehr zu schätzen.

Außerhalb der TC II Labore, aber innerhalb der Uni, möchte ich mich von ganzem Herzen bei meinen lieben Studienkollegen *Dr. Fabian Hörmann, Dr. Jens Oberkofler, Dr. Kathrin Weger, Dr. Lorenz Pardatscher, Dr. Michael Weger, Dr. Sebastian Hölzl* und *Dr. Patrick Zanon* sowie ihren wundervollen Frauen *Dr. Anna Trebo, Dr. Annika Oberkofler, Brigita Bratić* und *Dr. Christina Hölzl* bedanken. Wir haben uns bereits früh im Studium gefunden und seitdem gemeinsam jeden Meilenstein erreicht und gebührend gefeiert. Vielen Dank an jeden einzelnen von euch für all die besonderen Grüppchen innerhalb der Gruppe (Muskeltiere, Batschaka Buddies, Nightowls, usw.), für all die unvergesslichen Reisen, Ausflüge, Familienbesuche, Konzerte und

traditionelle Weihnachtsfeiern. Ich bin mir sicher, dass noch unzählige weitere Traditionen folgen werden. Ihr seid für mich viel mehr als nur ein Uni-Freundeskreis – ihr seid zu meiner zweiten Familie geworden. In diesem Sinne: „Auf die Kinder!“

Ich bin unendlich dankbar für all die tollen und inspirierenden Menschen, die ich während des Studiums kennenlernen durfte und die mich seither begleiten, insbesondere *Dr. Ireen Vogt* und *Dr. Darina Pronin*.

*Alexandra Rudnik* und *Marina Schmid*, euch kenne ich, abgesehen von meiner Familie, am längsten. Wir haben schon alles gemeinsam erlebt und durchgestanden. Vielen Dank für eure Freundschaft, dafür dass ihr immer für mich da seid und mich immer wieder aus meiner kleinen Chemiker-Blase entführt.

Ich möchte mich von tiefstem Herzen bei *Silvia*, *Gerhard*, *Adrian*, *Irena*, *Mateo* und *Angelo* bedanken, die mich so liebevoll und unterstützend aufgenommen haben und längst zu meiner eigenen Familie geworden sind.

Ohne meine wundervolle Familie wäre ich nicht dort, wo ich heute bin, und das nicht nur im übertragenen Sinne. Lieber *Papa*, du hast mich gelehrt, dass ich jeden Traum, egal wie groß und unerreichbar er auch scheinen mag, erreichen kann, und dass du mich bei jedem Schritt dorthin begleitest. Liebe *Mama*, du hast mir beigebracht, wie ich diese Träume mit Fleiß, Durchhaltevermögen und dennoch mit einer Leichtigkeit, positiven Einstellung und bester Laune verwirklichen kann. Liebe *Valentina*, wenn es mir an etwas fehlt, kann ich immer auf dich zählen und mit deiner Unterstützung das fehlende Puzzlestück einsetzen. Mit dir an meiner Seite lassen sich Berge versetzen. Ich danke euch unendlich für eure bedingungslose Liebe und dass ich mich immer auf euch verlassen kann.

Lieber *Gerhard*, du bist mein Fels in der Brandung, schenkst mir so viel Kraft und schaffst es, mir in jeder Situation ein Lächeln ins Gesicht zu zaubern. Wenn du mich umarmst, bleibt die Welt kurz stehen und ich weiß, alles wird gut. Ich freue mich unendlich auf unsere gemeinsame Zukunft und danke dir von ganzem Herzen für deine Motivation, Liebe und Geduld.

## Abbreviations and symbols

A	Pre-exponential factor of the Arrhenius equation
AAS	Atomic absorption spectroscopy
BAS	Brønsted acid site
BEA	Zeolite framework type code: Beta
BET	Brunauer-Emmet-Teller theory of physisorption
c	Concentration
c	Speed of light
CyEtOH	Cyclohexylethanol
CyOH	Cyclohexanol
d	Diameter
E <sub>a</sub>	Activation energy
FAME	Fatty acid methyl ester
FID	Flame ionization detector
ΔG°	Standard Gibbs free energy of activation
GC	Gas chromatograph(y)
h	Planck's constant
ΔH°	Standard enthalpy of activation
HDO	Hydrodeoxygenation
HTL	Hydrothermal liquefaction
IR	Infrared
K	Equilibrium constant
k	Rate constant
l	Length
LAS	Lewis acid site
M	Metal
M	Molecular weight
m	Mass
m	Monoclinic
McyOH	Methylcyclohexanol

MFI	Zeolite framework type code: Mordenite framework inverted
MS	Mass Spectrometry
N	Avogadro constant
n	Reaction order
n	Molar amount
p	Pressure
ppm	Parts per million
Py	Pyridine
$q_{\max}$	Saturation uptake
R	Universal gas constant
r	Reaction rate
rpm	Revolutions per minute
S	Selectivity
$\Delta S^\circ$	Standard entropy of activation
SI	Supporting information
T	Temperature
t	Tetragonal
t	Time
TOF	Turnover frequency
TPD	Temperature programmed desorption
V	Volume
wt%	Weight percent
X	Conversion
x	Molar fraction
XRD	X-ray diffraction
ZSM-5	Zeolite Socony Mobil-5

## **Abstract**

The conversion of biomass resources into hydrocarbon fuels was investigated, with an emphasis on the aqueous phase hydronium-ion-catalyzed dehydration of substituted cyclohexanols. The discovered compensation correlation between activation enthalpy and entropy allows to predict the trends of the catalytic reactivities for the alcohols. The turnover frequencies showed a volcano-shape dependency on the ionic strength, with the maximum consistently found at intermediate Si/Al ratios, independent of the reaction mechanism.

The second focus area is the optimization of catalysts for the conversion of microalgae. Stearic acid is successfully hydrodeoxygenated over bifunctional supported tungstate catalysts in both organic and aqueous solvents. The subsequent octadecanol dehydration step also showed a volcano-shaped rate dependency on the Brønsted acid site concentration, resulting from the occurrence of a most active species which correlates with the tetragonal zirconia phase.

## **Kurzzusammenfassung**

Die Umwandlung von Biomasse-Ressourcen zu Kohlenwasserstoff basierten Kraftstoffen wurde untersucht, wobei der Schwerpunkt auf der durch Hydronium-Ionen katalysierten Dehydratisierung von substituierten Cyclohexanolen in wässriger Phase lag. Die entdeckte Kompensationskorrelation zwischen Aktivierungsenthalpie und Entropie erlaubt es, die Trends der katalytischen Reaktivitäten für die Alkohole vorherzusagen. Die normierten Reaktionsraten zeigten eine vulkanförmige Abhängigkeit von der Ionenstärke, wobei das Maximum durchweg bei mittleren Si/Al-Verhältnissen gefunden wurde, unabhängig vom Reaktionsmechanismus.

Der zweite Fokusbereich ist die Optimierung von Katalysatoren für die Umwandlung von Mikroalgen. Stearinsäure wird erfolgreich mittels bifunktionellen geträgerten Wolframat-Katalysatoren sowohl in organischen als auch in wässrigen Lösungsmitteln hydrodesoxygeniert. Der anschließende Octadecanol-Dehydratisierungsschritt zeigte ebenfalls eine vulkanförmige Ratenabhängigkeit von der Konzentration der Brønsted-Säurestellen, was auf das Auftreten einer besonders aktiven Spezies zurückzuführen ist, die mit der tetragonalen Zirkoniumdioxidphase korreliert.



# Table of contents

<b>Acknowledgements</b> .....	<b>I</b>
<b>Abbreviations and symbols</b> .....	<b>III</b>
<b>Abstract</b> .....	<b>V</b>
<b>Kurzzusammenfassung</b> .....	<b>V</b>
<b>Chapter 1: INTRODUCTION</b> .....	<b>1</b>
1.1 A realistic assessment of the status quo.....	1
1.2 Biomass resources .....	5
1.2.1 Lignocellulose.....	5
1.2.2 Microalgae.....	7
1.3 Conversion of biomass to biofuels.....	10
1.3.1 Upgrading of lignocellulose-based pyrolysis oil .....	12
1.3.2 Catalytic conversion of microalgae oil .....	14
1.4 Catalysts.....	16
1.4.1 Zeolites.....	16
1.4.2 Supported tungstate catalysts .....	19
1.5 Scope of the thesis.....	21
1.6 References.....	22
<b>Chapter 2: TOWARDS UNDERSTANDING AND PREDICTING THE HYDRONIUM ION CATALYZED DEHYDRATION OF CYCLIC-PRIMARY, SECONDARY AND TERTIARY ALCOHOLS</b> .....	<b>29</b>
2.1 Introduction .....	30
2.2 Experimental methods.....	31
2.2.1 Chemicals.....	31
2.2.2 Zeolite catalysts .....	31
2.2.3 Reaction procedure.....	32
2.3 Results and discussion.....	32
2.3.1 Materials studied.....	32
2.3.2 Interactions of cyclic alcohols with MFI and BEA zeolites ..	33
2.3.3 Catalyzed dehydration .....	35

2.4	Conclusions .....	42
2.5	Author contributions .....	43
2.6	References .....	44
2.7	Supporting information .....	47
2.7.1	Methods .....	47
2.7.2	Figures and tables of the discussion part.....	48
2.7.3	References of the supporting information .....	76
<b>Chapter 3:</b>	<b>INFLUENCE OF INTRACRYSTALLINE IONIC STRENGTH IN MFI ZEOLITES ON AQUEOUS PHASE DEHYDRATION OF METHYLCYCLOHEXANOLS .....</b>	<b>77</b>
3.1	Introduction.....	78
3.2	Results and discussion .....	79
3.2.1	Characterization of MFI zeolites .....	79
3.2.2	Dehydration of 2- and 4-methylcyclohexanol.....	80
3.2.2.1	4-Methylcyclohexanol.....	81
3.2.2.2	<i>cis</i> -2-Methylcyclohexanol.....	83
3.2.2.3	Correlation of $\Delta S^{\ddagger}$ and $\Delta H^{\ddagger}$ .....	85
3.3	Conclusion .....	86
3.4	Acknowledgements.....	86
3.5	Author contributions .....	86
3.6	References .....	87
3.7	Supporting information .....	89
3.7.1	Experimental procedures.....	89
3.7.2	Figures and tables of the discussion part.....	92
3.7.3	References of the supporting information .....	103
<b>Chapter 4:</b>	<b>DEHYDRATION OF FATTY ALCOHOLS ON ZIRCONIA SUPPORTED TUNGSTATE CATALYSTS .....</b>	<b>105</b>
4.1	Introduction.....	106
4.2	Results and discussion .....	108
4.2.1	Characterization.....	108
4.2.2	Octadecanol dehydration .....	113
4.2.3	Promotion effect of platinum .....	114
4.3	Conclusion .....	115
4.4	Experimental .....	116

4.4.1	Chemicals.....	116
4.4.2	Catalyst preparation.....	116
4.4.3	Analysis Methods.....	116
4.4.4	Catalytic measurements.....	117
4.5	Acknowledgements.....	118
4.6	Author contributions.....	118
4.7	References.....	119
4.8	Supporting information.....	121
4.8.1	Figures of the results and discussion part.....	121
4.8.2	Aqueous phase.....	126
4.8.3	References of the supporting information.....	127
4.9	Extension of the carbon supported tungstate catalysts.....	128
4.9.1	Characterization.....	128
4.9.2	Octadecanol dehydration on WO <sub>3</sub> /C catalysts.....	129
<b>Chapter 5:</b>	<b>FATTY ACID HYDRODEOXYGENATION ON METAL SUPPORTED TUNGSTATE CATALYSTS (M/WO<sub>3</sub>/ZRO<sub>2</sub> OR M/WO<sub>3</sub>/C) IN ORGANIC AND AQUEOUS PHASE.....</b>	<b>131</b>
5.1	Introduction.....	132
5.2	Results and discussion.....	133
5.2.1	Zirconia supported tungstates.....	133
5.2.2	Carbon supported tungstates.....	139
5.3	Conclusion.....	144
5.4	Experimental.....	145
5.4.1	Chemicals.....	145
5.4.2	Catalyst preparation.....	145
5.4.3	Analysis Methods.....	146
5.4.4	Catalytic measurements.....	146
5.5	References.....	147
<b>Chapter 6:</b>	<b>CONCLUSIONS.....</b>	<b>149</b>
	<b>List of publications.....</b>	<b>152</b>
	<b>Statutory Declaration.....</b>	<b>153</b>



# Chapter 1

## Introduction

### 1.1 A realistic assessment of the status quo

"Is the end of the world near?" – This question has become a pressing concern, fueled by apocalyptic portrayals in the media. These portrayals often suggest that escaping Earth and populating other planets may be the only way to continue life as we know it. The primary scapegoat in these narratives is the human population and its seemingly unstoppable and exponentially increasing growth, especially in recent history, as depicted in Figure 1.1.<sup>1-3</sup>

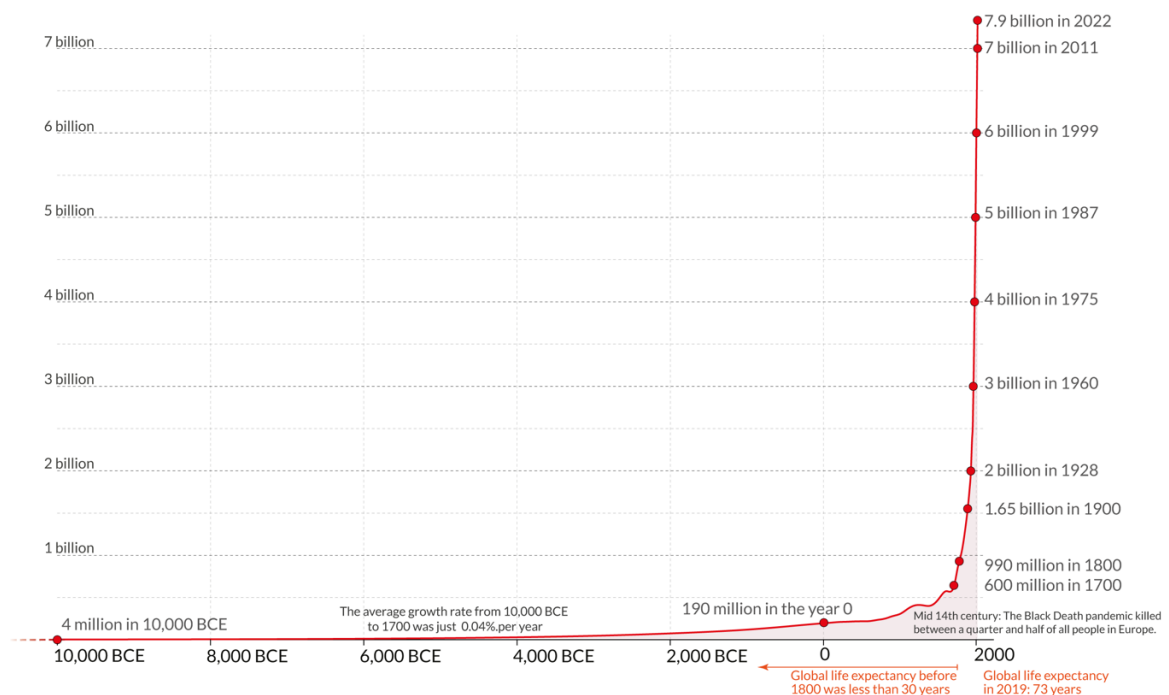


**Figure 1.1.** The size of the world population from 10,000 BCE to 2021 based on estimates by the History Database of the Global Environment (HYDE) and the United Nations.<sup>3</sup>

However, predictions indicate that this exponential growth will level off by the end of the century, as illustrated in Figure 1.2 (top). In fact, the growth rate has already been declining for decades (Figure 1.2 bottom).<sup>3</sup>

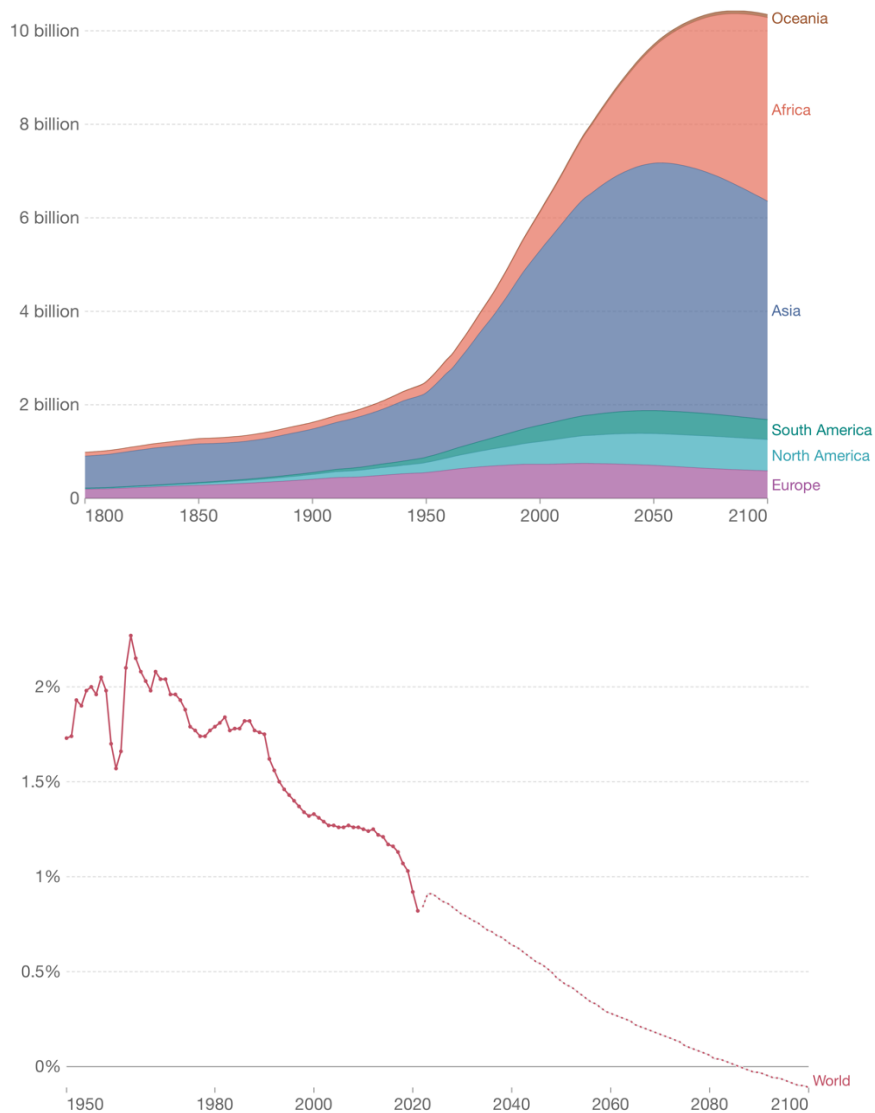


**Figure 1.2.** Population by world region (top) and world population growth rate (bottom) with historic estimates from 1950 to 2021, and projections to 2100 based on the UN medium-fertility scenario.<sup>3</sup>

The decrease in birth rates stems from increased human wealth. Global improvements in healthcare, education, and poverty reduction have resulted in lower mortality rates and better living standards, leading to fewer children being born. Essentially, a rise in wealth correlates with a decline in population growth.<sup>4</sup>

As wealth and living standards improve, the demand for energy increases. This increased demand poses a significant challenge due to our reliance on fossil fuels as the primary source of energy. This dependence on non-renewable energy sources bears environmental risks, including greenhouse gas emissions, which, in turn are the leading contributors to global warming. This has far-reaching consequences, such as more frequent and severe weather events, loss of biodiversity, and threats to food and water security.<sup>5</sup>

According to the 2018 World Energy Outlook by the International Energy Agency, the global energy demand is predicted to increase by over 25 % between 2017 and 2040. India is expected to become the main driver of global energy growth by doubling its demand by 2040. In contrast, China's growth, while still strong, is estimated to be only one-fifth of the rate seen in the period from 2000 to 2017. While the demand in the EU and Japan is even believed to decrease. All in line with their status of wealth.<sup>6</sup>

In 2018, the global energy consumption grew by 2.9%, thereby almost doubling its average growth rate of 1.5% during the previous ten years (2007 – 2017).<sup>7</sup> Figure 1.3 shows that in 2018, the transport sector accounted for the largest share of the global energy consumption with 29.1%, closely followed by the industry (28.8%) and residential sectors (21.1%).<sup>8</sup> The main energy sources in the same year were oil (31.5%), coal (27.0%) and natural gas (22.8%), while the remaining 18.8% came from biofuels and waste (9.3%), nuclear (4.9%), hydro (2.5%) and wind, solar, etc. (2.0%) energy.<sup>8</sup>

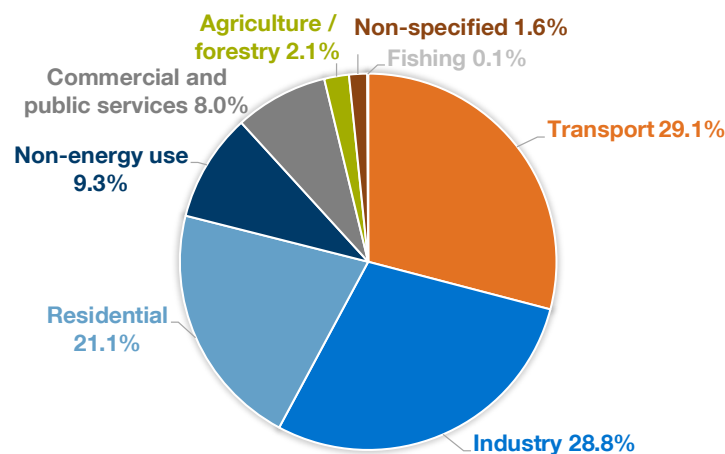


**Figure 1.3.** Total final energy consumption by sector in 2018.<sup>8</sup>

As a result of the higher energy consumption, CO<sub>2</sub> emissions as well increased substantially.<sup>7</sup> In 2018, energy-related CO<sub>2</sub> emissions experienced a growth of 1.7%, reaching a historic all-time high of 33.1 Gt CO<sub>2</sub>. This marked the fastest growth rate since 2013 and was 70% higher than the average rate observed since 2010.<sup>9</sup>

Figure 1.4 illustrates that the transport sector, accounting for 24.5% of CO<sub>2</sub> emissions, is the second largest contributor and thus presents both a significant potential for improvement and a pressing need for action.<sup>8</sup> Reducing the sector's reliance on fossil fuels and mitigating CO<sub>2</sub> emissions are critical. The need is further emphasized by the projected 80% growth in the global car fleet by 2040 and the assumption that aviation activity will more than triple by 2050.<sup>5,6,10</sup>

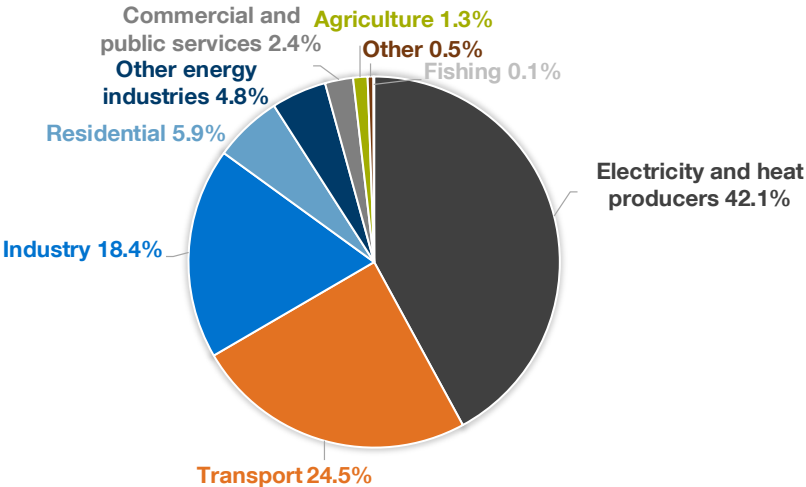


**Figure 1.4.** Global CO<sub>2</sub> emissions by sector in 2018.<sup>8</sup>

To address the issue of growing energy demand, particularly within the transport sector, and to lessen the environmental impact, it is crucial to invest in research, innovation, and development of sustainable and environmentally friendly alternatives to fossil fuels. Developing and employing biofuels emerges as one of the most promising strategies to tackle these challenges. This approach will help ensure the well-being of both our economies and future generations.

## 1.2 Biomass resources

In 2018, global biofuel production reached 95.4 million toe, a 9.7% increase from 2017, mainly driven by bioethanol.<sup>7,11</sup> Biofuels were primarily used in the transport sector, where they accounted for 3% of the energy demand.<sup>6</sup> However, to meet the objectives of the 2015 Paris Agreement, biofuel production and use needs to increase significantly, especially in aviation and shipping, where implementation remains limited.<sup>7,12</sup>

Biofuels are categorized into first, second, and third generations, depending on the feedstock material employed. First-generation biofuels (conventional biofuels), already produced at an industrial scale, are derived from terrestrial food crops and commodity vegetable oils such as rapeseed, soybean, palm, sunflower, corn, sugarcane, and sugar beet.<sup>13,14</sup> These biofuels contain minimal contaminants, facilitating relatively inexpensive and straightforward handling and treatment.<sup>6</sup> Nevertheless, their production is deemed unsustainable and ethically questionable due to the associated increase in food prices (food vs. fuel dilemma), contribution to water shortages, and accelerated deforestation, particularly impacting developing countries.<sup>15,16</sup>

### 1.2.1 Lignocellulose

Second-generation biofuels (advanced biofuels), on the other hand, originate from lignocellulosic agricultural, forest residues and non-food crops, avoiding the competition with food production.<sup>6</sup> These advanced biofuels also offer a higher lifecycle GHG emission reductions compared to first-generation biofuels. Around 10 billion tons of sustainable lignocellulosic feedstock is projected to be globally available for the production of second-generation biofuel.<sup>12</sup>

Lignocellulose, which is found in the cell walls of plants, is composed of three major biopolymers: cellulose (38 – 50%), hemicellulose (17 – 32%), and lignin (15 – 30%).<sup>17</sup> Cellulose consists of D-glucose monomers which are connected by  $\beta$ -1,4-glycoside linkages forming linear polysaccharides. Hemicellulose is a copolymer comprised of the monomers arabinose, galactose, glucose, glucuronic acid, mannose, and xylose, forming amorphous and heterogeneous, branched polysaccharides. As depicted in Figure 1.5, hemicellulose surrounds the cellulose fibers and serves as a linkage between cellulose and lignin.<sup>18</sup> Lignin is a highly complex three-dimensional polymer composed of various phenylpropane units linked by ether or C-C bonds and formed by an enzyme-initiated free-radical polymerization of the alcohol precursors, coniferyl, sinapyl, and coumaryl alcohol.<sup>18,19</sup> Lignin is predominantly found between the outer layers of the fibers, providing structural rigidity and facilitating the cohesion of polysaccharide fibers.<sup>18</sup>

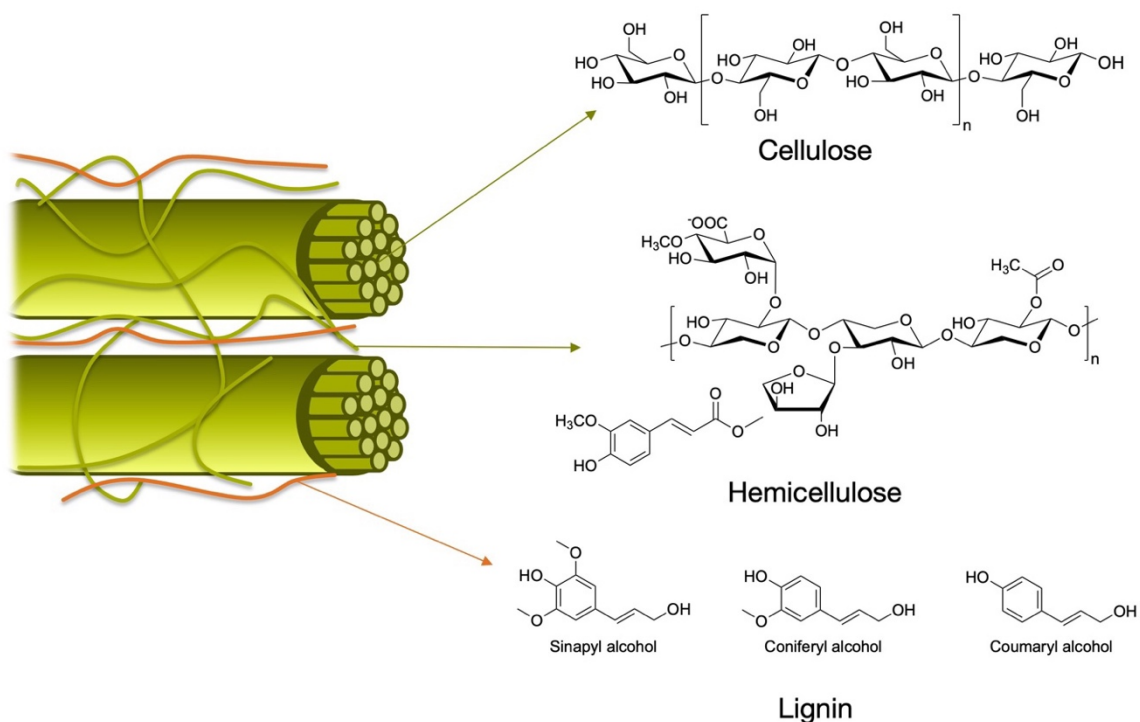


**Figure 1.5.** Schematic illustration of lignocellulose which consists of cellulose, hemicellulose, and lignin. Depicted are the alcohol precursors of the lignin polymer, coniferyl, sinapyl, and coumaryl alcohol.<sup>17</sup>

Despite the high abundance of lignocellulose, the feedstock grows less dense and, thus, requires substantial arable land and water resources for cultivation.<sup>6,14,15</sup> Moreover, the resulting fuel exhibits a lower energy content and variable quality compared to first-generation biofuels.<sup>6</sup>

## 1.2.2 Microalgae

Addressing the challenges of first and second-generation biofuels, such as regional economic constraints, insufficient agricultural expertise in developing countries, increased fertilizer use, and potential negative impacts on biodiversity, there has been a growing interest in the development of third-generation biofuels. These biofuels leverage microorganisms like microalgae as an innovative and sustainable feedstock.<sup>11</sup> Although still in the early stages of development and not yet commercially viable, microalgae-based biofuels show promise as a sustainable and environmentally friendly alternative to traditional fossil fuels, with the potential to transform the global energy landscape.

Algae are a diverse group of photosynthetic, heterotrophic organisms known for their adaptability to various environmental conditions.<sup>20</sup> This allows them to inhabit nearly any ecosystems worldwide, including freshwater, saline water, brackish water, and even terrestrial and subaerial environments.<sup>20,21</sup> Their remarkable biodiversity, which has led to the development of millions of algae species, is partially due to their diverse lipid profiles, which enable them to modify their cell membrane properties and, thus, to function effectively in various environments.<sup>20,22</sup>

Algae can be classified into microalgae and macroalgae, which exhibit distinct differences in terms of size, physical structure, and energy density.<sup>21</sup> Macroalgae are multicellular organisms that can grow up to 60 meters in length, while microalgae are unicellular organisms that typically measure between 1 to 50  $\mu\text{m}$ . The photosynthetic microorganisms of microalgae convert sunlight, water, and carbon dioxide into oxygen and various biomass components, such as proteins, carbohydrates, and lipids.<sup>23-25</sup> Microalgae are particularly noteworthy for their high lipid content, which ranges from 1 up to 70% of the dry biomass.<sup>26</sup> The lipids consist of triglycerides of saturated and unsaturated species-specific fatty acids with a typical length of 12 to 22 carbon atoms.<sup>27,28</sup> By storing energy in the triglycerides within their cells, microalgae can withstand unfavorable environmental conditions. Lipid induction, a process triggered by various stress factors such as nutrient limitations (nitrogen or phosphorus starvation), osmotic stress, radiation, extreme pH, temperature, and heavy metals, stimulates the production of these lipids.<sup>29</sup>

Microalgae have gained attention as renewable, carbon-neutral feedstock materials for various applications, including biofuels (biodiesel and renewable diesel), chemicals, biomaterials (bioplastics and industrial enzymes), and high-value products (cosmetics, food sources, and vitamins).

One of the most striking advantages of microalgae over conventional crop plants are their superior growth rates and lipid production capabilities. Microalgae boast biomass doubling times of just 1 – 6 days, and their lipid production rates are 10 – 20 times faster than those of terrestrial oil crop plants.<sup>20</sup> This impressive performance is primarily due to their exceptionally high photosynthetic efficiency (8.3%), which far surpasses that of terrestrial plants (2.4%).<sup>30</sup> As unicellular organisms, each microalgal cell is

photosynthetically active and can absorb nutrients and CO<sub>2</sub> from its surroundings. This characteristic provides microalgae with a larger active cellular surface area, shorter diffusion pathways, and eliminates the need for energy- and time-consuming transport processes.

Another significant advantage of microalgae is their ability to grow in areas unsuitable for conventional agriculture, as they do not compete for arable land or require large quantities of fresh water.<sup>20</sup> Additionally, microalgae can utilize nutrients from wastewater, making them a sustainable option for cultivation in various environments, including arid regions.<sup>15,27,31,32</sup> Their growth is also less affected by seasonal variations, and the need for herbicides and pesticides is eliminated.<sup>33,34</sup>

Furthermore, microalgae are highly efficient at capturing and converting atmospheric and dissolved CO<sub>2</sub> from flue gases, which can help mitigate carbon emissions and contribute to a greener future.<sup>35</sup> It is estimated that approximately 1.6 – 2 g of CO<sub>2</sub> is captured for each gram of produced microalgae biomass.<sup>36</sup> However, it should be noted that since algae-derived biofuels will eventually release CO<sub>2</sub> when combusted, the carbon credits come from the displacement of fossil fuels rather than the captured CO<sub>2</sub>.<sup>37</sup>

Despite these numerous advantages, the cultivation of microalgae as a feedstock material for biofuels presents a range of technological and economic challenges. Large-scale growth requires high atmospheric CO<sub>2</sub> concentrations, which are currently insufficient.<sup>15</sup> This issue could be addressed by dissolving large amounts of CO<sub>2</sub> in the growth medium, but there are only a limited number of large-scale CO<sub>2</sub> emitters located in regions suitable for year-round algae cultivation.<sup>38</sup> Furthermore, the presence of toxic SO<sub>x</sub> and NO<sub>x</sub> gases in industrial flue gases needs to be addressed before these gases can be used in microalgal growth media.<sup>15</sup>

Efficient distribution of CO<sub>2</sub> and other nutrients in microalgal cultivation systems demands an adequate mass transfer capacity, which typically involves rapid mixing of the algae solution through extensive pumping and circulation.<sup>31,39</sup> This mixing process is energy-intensive and contributes significantly to the overall energy consumption in microalgae cultivation. Artificial lighting, another energy-intensive factor, may be required for microalgae illumination due to diurnal cycles and seasonal variations, posing challenges for continuous year-round cultivation.<sup>15,40</sup>

The process of biomass recovery, another critical step in microalgae-based biofuel production, is also challenging due to factors such as the energy-intensive nature of harvesting methods, low microalgal cell concentration in commercial cultivation systems, and the need for efficient dewatering and extraction techniques.<sup>15,41-43</sup> For instance, centrifugal sedimentation, a commonly employed harvesting method, accounts for 20 – 30% of total production costs, emphasizing its energy-intensive nature.<sup>15,44</sup> Additionally, the typical water content of microalgae ranges from 80 to 90%, demanding the development of more sophisticated and costly dewatering methods beyond traditional sun drying.<sup>15,42,43</sup> Furthermore, the energy requirements for extracting

valuable products, such as lipids or other high-value compounds, are considerable. Given the high operating costs associated with mixing, illumination, harvesting, dewatering, and subsequent processing, commercial microalgae cultivation remains economically unviable under the current conditions.<sup>15,34,45-47</sup>

In comparison to traditional agricultural practices, microalgae cultivation presents unique challenges, including higher capital costs and the need for specialized infrastructure to ensure optimal growth conditions. Such infrastructure should provide a high surface-to-volume ratio (S/V ratio) and adequate process control to maximize cell concentrations and volumetric productivity while maintaining optimal temperature and pH levels for the specific organism.<sup>39</sup> Moreover, precise harvesting procedures are essential to preserving optimal cell density. Due to the high operating and capital costs, insufficient positive energy balance, and the lack of established sustainability in microalgae cultivation, no industrial-scale facilities for converting microalgal biomass into biofuels exist at present. Nevertheless, the potential benefits of microalgae-based biofuel production warrant continued and extensive research, even though the development of profitable and ecological technology may take at least another 10 to 15 years.

### 1.3 Conversion of biomass to biofuels

Biomass can be converted into useful energy through various processes. The choice of conversion process is influenced by factors such as the type, quantity, and characteristics of the biomass feedstock, the desired form of energy or end-use requirements, environmental standards, policies, economic conditions, and project-specific factors.<sup>42,48</sup> Bioenergy refers to the energy obtained from biomass feedstocks, which undergo several stages, including harvesting, drying, storage, transportation, and processing before they become useful energy sources. There are three main process technologies: biochemical, thermochemical, and physiochemical conversion, which are shown in Figure 1.6.<sup>48</sup>

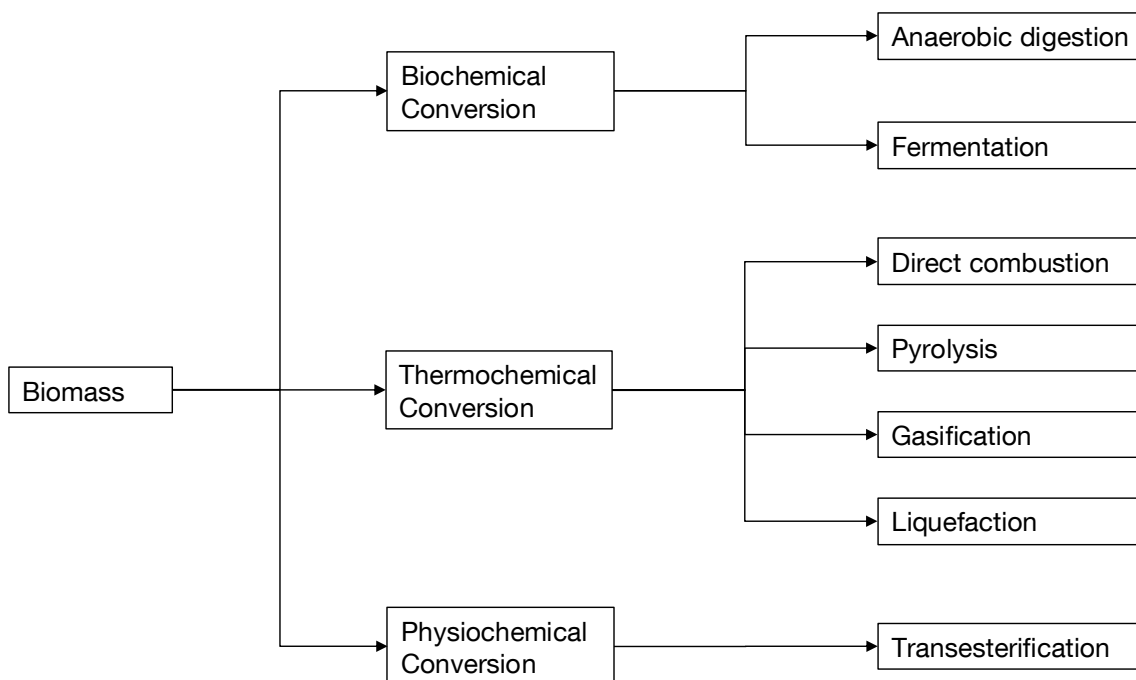
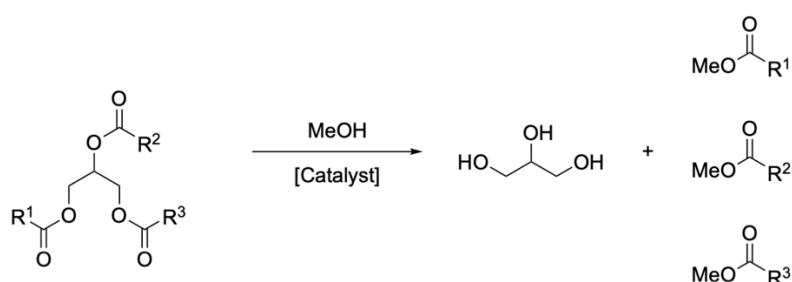


**Figure 1.6.** Process technologies for the conversion of biomass to biofuels classified by biochemical, thermochemical, and physiochemical conversion.

Biochemical conversion involves the use of bacteria or yeasts to convert biomass into gaseous or liquid fuels, typically within anaerobic digestion or fermentation processes. Anaerobic digestion is a biochemical process that utilizes bacteria to decompose the organic matter in biomass and produce biogas, a mixture of mainly methane and carbon dioxide. Fermentation, on the other hand, uses yeasts to convert the sugar content in the feedstock into ethanol. This diluted alcohol needs to be further distilled and, therefore, results in an overall lower process performance and incurs high plant cost. Despite this drawback, both anaerobic digestion and fermentation technologies have been tailored to suit various feedstocks, environmental conditions, and end-use purposes on a global scale.<sup>48-50</sup>

Thermochemical methods transform the biomass into various types of energy by employing heat and chemical reactions. The four main techniques are combustion, pyrolysis, gasification, and liquefaction.<sup>48,51</sup> Pyrolysis occurs in the absence of oxygen and thermally decomposes biomass into solid, liquid (referred to as bio-oil), and gaseous products depending on the applied mode (fast, intermediate or slow pyrolysis). Gasification converts the biomass feedstock at high gasification temperatures (above 1200°C) solely into gaseous products. At lower gasification temperatures by-products such as tar compounds can result and negatively influencing the performance.<sup>48</sup> Hydrothermal processing is a technique that involves heating aqueous biomass or organic waste in an aqueous solution at high pressure to increase its energy density. Hydrothermal liquefaction (HTL) is carried out at temperatures ranging from 250°C to 375°C and pressures up to 180 bar. The output is a liquid bio-crude that can be converted to a wide range of petroleum-based products using catalytic hydrotreatment.<sup>48,52,53</sup> Thermochemical processes generally have higher efficiencies than biochemical techniques, faster reaction times, and the ability to convert most of the organic compounds, e.g., lignin is typically non-fermentable and, thus, cannot be completely decomposed by biochemical conversion.<sup>48,54-56</sup>

Physiochemical conversion is a method that involves mechanical (physical) extraction of oil from biomass feedstock and subsequent chemical processes to obtain biofuels at near ambient temperature and pressure. The most prominent technique is the transesterification of extracted triglycerides such as vegetable oils, animal fats, and waste fats into fatty acid methyl ester (FAME), commonly known as biodiesel.<sup>48,50,57</sup> During transesterification the triglycerides are converted with a monohydric alcohol, typically methanol, in the presence of a catalyst, leading to the formation of biodiesel and glycerol as a byproduct as depicted in Scheme 1.1.<sup>58</sup> Basic catalysts such as sodium hydroxide, sodium methoxide or potassium hydroxide are most commonly used in biodiesel production.<sup>59</sup>



**Scheme 1.1.** Transesterification of triglyceride with methanol to glycerol and fatty acid methyl ester (FAME). R<sup>1</sup>, R<sup>2</sup> and R<sup>3</sup> represent saturated or unsaturated alkyl groups.

Biodiesel is typically blended with conventional diesel as it still faces disadvantages compared to the petroleum derived diesel.<sup>60</sup> FAMEs have a significant amount of oxygen and poor cold flow properties. Additionally, biodiesel lacks stability in terms of heat and oxidation, has lower energy content, and causes engines to run at slower speeds and with less power than conventional diesel.<sup>60,61</sup>

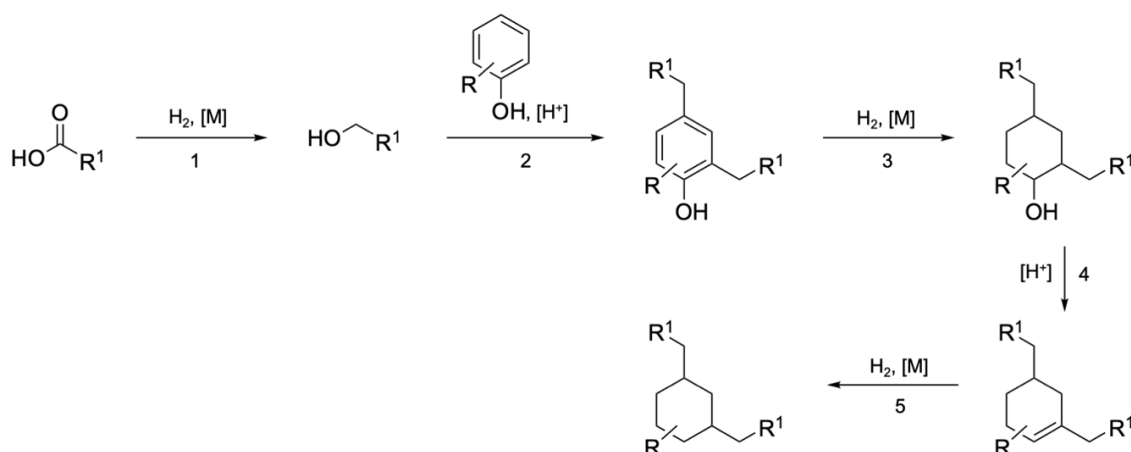
### 1.3.1 Upgrading of lignocellulose-based pyrolysis oil

Fast pyrolysis typically occurs at reaction conditions from 1 to 5 bar and 375 – 525°C in the absence of air with short residence times to convert biomass to bio-oils.<sup>19</sup> These bio-oils can contain more than 400 different compounds, depending on the converted feedstock.<sup>19,62</sup> Despite the need for additional upgrading, fast pyrolysis appears to be a promising technique due to its relatively low capital costs compared to other thermochemical conversion methods of biomass.<sup>19,63</sup>

Pyrolysis oil from lignocellulose is produced by depolymerizing and fragmenting its three main components: cellulose, hemicellulose and lignin. The most abundant molecules formed from cellulose and hemicellulose are short-chain acids such as acetic and propanoic acid, alcohols such as methanol and ethanol, aldehydes such as formaldehyde and acetaldehyde, miscellaneous oxygenates such as glycolaldehyde and acetol, sugars such as 1,6-anhydroglucose and acetol, and furans such as furfural and hydroxymethylfurfural. Lignin mainly results in the formation of (non-)substituted phenols such as phenol and catechol, guaiacols such as isoeugenol and eugenol, and syringols such as 2,6-dimethoxyphenol and syringaldehyde.<sup>19,64,65</sup>

Several characteristics of pyrolysis oil, including poor volatility, increased oxygen content, and high viscosity, negatively impact its fuel quality. A low heating value and high water content leads to difficult ignition, the presence of acids causes corrosiveness and thermally unstable components evoke coking. Consequently, pyrolysis oil requires upgrading before it can be effectively utilized as a biofuel.<sup>19,65</sup> The primary goal of the upgrading process is to transform the oxygen-rich, high molecular weight compounds into hydrocarbons that are comparable to petroleum-derived fuels. There are various techniques for upgrading pyrolysis oil, such as catalytic cracking, hydrodeoxygenation, steam reforming, esterification, and emulsification. Hydrodeoxygenation (HDO) appears to be one of the most promising routes as it offers economic viability with production costs comparable to conventional crude oil. However, challenges persist in this field as the reaction mechanism and the optimal catalyst formulation is not fully understood and requires further investigations.<sup>65</sup>

Scheme 1.2 demonstrates a reaction route of the hydrodeoxygenation of lignocellulose-based pyrolysis oil which allows to convert various compounds into high-value chemicals and transportation fuels.<sup>66</sup>



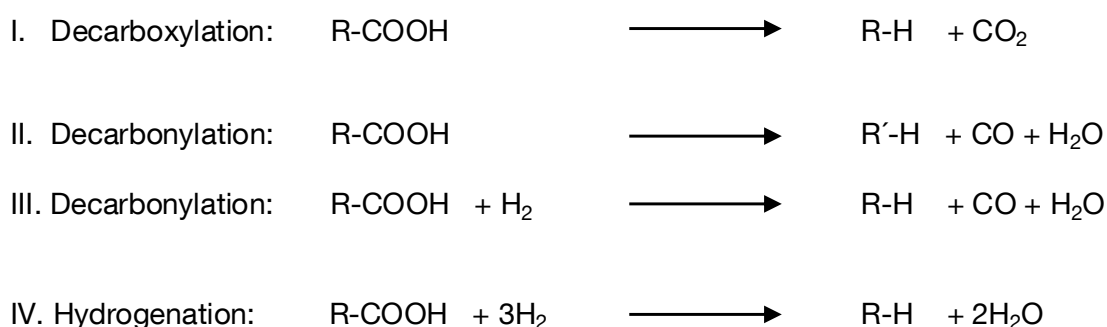
**Scheme 1.2.** Reaction mechanism of the hydrodeoxygenation of lignocellulose-based pyrolysis oil. 1 = Selective hydrogenation, 2 = alkylation, 3 = hydrogenation, 4 = dehydration, 5 = hydrogenation (adapted from reference 66). R and R<sup>1</sup> represent alkyl groups.

The first step of the reaction mechanism in Scheme 1.2 is the selective hydrogenation (1) of short-chain acids in the presence of hydrogen and supported metal catalysts. The resulting alcohols subsequently undergo alkylation (2) with the substituted phenolic compounds *via* acid-catalyzed electrophilic aromatic substitution, followed by the hydrogenation (3) of the alkylated phenolic compounds. The next step is the acid-catalyzed dehydration (4) of the substituted cyclohexanols, leading to the desired oxygen removal. The position of both the alcohol and the substituent has been shown to significantly affect the reactivity and product selectivity, making this an interesting area for further investigation and offering potential for better understanding and control of the reaction. The final step of the reaction mechanism is the hydrogenation (5) of the resulting unsaturated, substituted cyclohexenes.<sup>66</sup>

### 1.3.2 Catalytic conversion of microalgae oil

Catalytic hydrotreating addresses the drawbacks of other processes, e.g., the high oxygen content and poor oxidation stability of generated biofuels such as biodiesel from transesterification. During hydrodeoxygenation, the oxygen is removed from the organic molecules *via* hydrotreating catalysts in the presence of hydrogen.<sup>67,68</sup> The resulting saturated, long-chain hydrocarbons, referred to as renewable diesel, exhibit a high cetane number above 70.<sup>69-71</sup> This upgrading method of triglycerides has already been commercialized using existing infrastructures of petroleum refineries.<sup>72</sup> Typically, supported or unsupported transition metal sulfide catalysts (NiMo and CoMo sulfide) are employed, operating at reaction temperatures between 350 to 450°C and hydrogen pressures ranging from 40 to 150 bar.<sup>73-75</sup> The disadvantage of transition metal sulfide catalysts is that they tend to suffer from sulfur leaching, which causes contamination of the products and deactivation of the catalyst. Sulfur removal from the catalyst surface occurs via the reverse Mars-van-Krevelen mechanism, which is amplified by trace amounts of produced water.<sup>76,77</sup> Therefore, the development of stable and sulfur-free catalysts is a more appealing alternative to conventional sulfided catalysts.

Snåre et. al explored several sulfur-free supported metal catalysts for the deoxygenation of triglycerides and fatty acids derived from biomass, which were already active at milder reaction temperatures between 300 – 360°C and lower hydrogen pressures between 6 – 40 bar. The investigated catalysts were mainly noble metals such as Pd, Pt, Ru, and Rh on oxide supports, including Al<sub>2</sub>O<sub>3</sub>, Cr<sub>2</sub>O<sub>3</sub>, MgO, and SiO<sub>2</sub> as well as activated carbon. The highest activity was observed over Pt/C and Pd/C catalysts. Scheme 1.3 illustrates the different reaction pathways of the deoxygenation. Although decarbonylation and decarboxylation require less or no hydrogen, respectively, they suffer from a lower carbon efficiency compared to hydrodeoxygenation, since one carbon atom is released as CO or CO<sub>2</sub>.<sup>78-80</sup>



**Scheme 1.3.** Different fatty acid deoxygenation pathways, where R represents a saturated alkyl group and R' an unsaturated alkyl group.<sup>80</sup>

As previously discussed in Chapter 1.2.2, microalgae primarily comprise lipids, sugars, and proteins. Hydrodeoxygenation of sugars found in the microalgae yields short-chain hydrocarbons. Due to the complexity posed by the heteroatom nitrogen, proteins will not be further examined in this thesis. Among these components, microalgae oil offers

the highest potential for the conversion to biofuels since the hydrodeoxygenation of the lipids, typically consisting of 14 to 22 carbon atom chains, results in the production of long-chain, unbranched hydrocarbons ( $C_{15}$  to  $C_{22}$ ), i.e., renewable diesel-like transportation fuel.<sup>77,81-83</sup>

Recently, there has been growing interest in the conversion of biomass into hydrocarbons suitable for the kerosene range ( $C_8$  to  $C_{16}$ ), which could be utilized in the aviation sector.<sup>84-86</sup> To achieve this, an additional hydroisomerization or -cracking step needs be incorporated into the process. For this purpose, the catalyst should not only be active for the hydrodeoxygenation of triglycerides (e.g., Pt/C), but also requires acidic properties in the form of Brønsted acid sites. Identifying and designing such a bifunctional catalyst that enables the conversion of microalgae oil into hydrocarbons in the kerosene range within a single process, as depicted by the orange arrow in Figure 1.7, is one of the main objectives of this thesis.

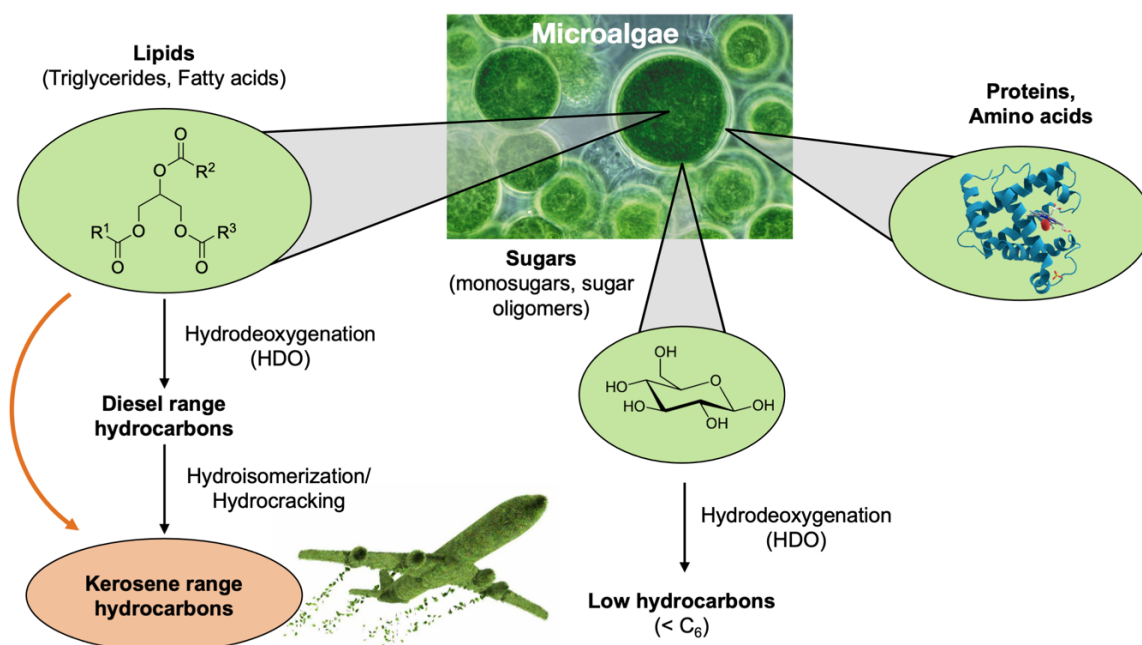


**Figure 1.7.** Microalgae composition comprising lipids, sugars and proteins; and the possible reaction network for the conversion into hydrocarbon transportation fuels *via* hydrodeoxygenation and hydroisomerization or -cracking.

## 1.4 Catalysts

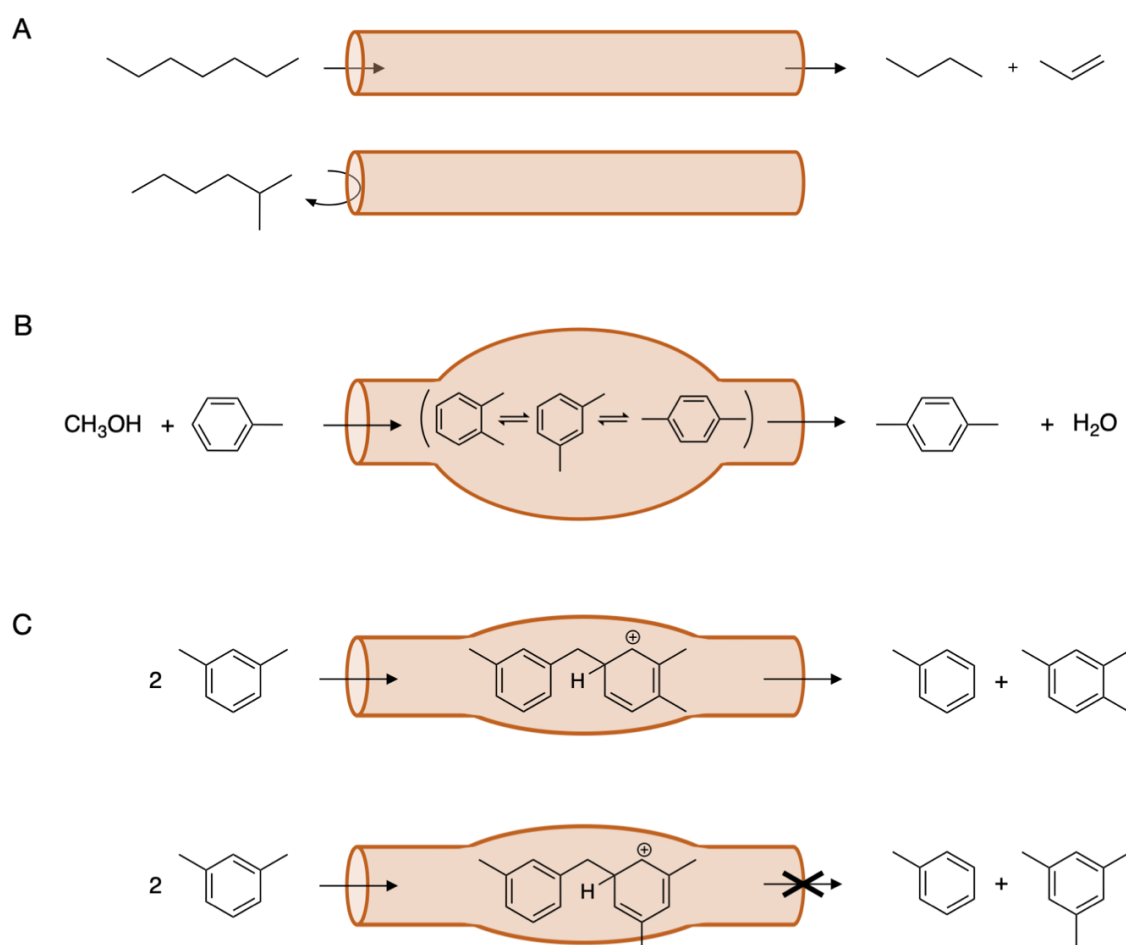
The choice of the catalyst plays a crucial role in the conversion of biomass to biofuels. The primary attributes that a catalyst should possess include activity, selectivity, and stability. Ensuring these criteria are met is fundamental for the successful and reliable execution of the process.

### 1.4.1 Zeolites

Zeolites are microporous crystalline aluminosilicates that feature both strong and weak Brønsted acid sites (BAS) as well as Lewis acid sites (LAS). Strong BAS are represented by hydroxyl groups adjacent to aluminum in the zeolite framework, which arise due to the charge-balancing necessity of the negative  $\text{AlO}_4$ -tetrahedra, while surface silica hydroxyl groups serve as weak BAS. Cationic extra-framework aluminum results in the formation of LAS.<sup>87</sup> Consequently, by altering the composition of the zeolite framework, such as by modifying the Si/Al ratio, the distribution of acid sites or defects, the properties of the catalyst can be tailored.<sup>88</sup>

The topology of the zeolite is also a crucial factor in determining the catalyst reactivity. The structure and dimensions formed by the channels and cavities (the void defined by channel intersections) directly influence the selectivity of chemical reactions.<sup>88</sup> Already in 1960, Weisz first proposed the concept of shape selectivity, which was then later extended by Csicsery.<sup>89-92</sup> Scheme 1.4 summarizes the three types of shape selectivity.

Reactant selectivity occurs when the entry size of the internal channel system restricts large molecules in a reactant mixture from diffusing into the catalyst pores. The size of these openings is determined by the number of atoms forming the channel, typically consisting of 8-, 10-, or 12-membered rings.<sup>88</sup> Scheme 1.4 A provides an example of reactant selectivity in heptane cracking, where only *n*-heptane can access the pore, while 2-methylhexane is left unreacted. Product selectivity is demonstrated when products formed within the pores are unable to diffuse out. For example, in a toluene methylation reaction, only *para* isomers of xylene can exit the cavities (Scheme 1.4 B). The third type occurs when the formation of a specific transition state demands more space than available within the channels or cavities. This is observed in the transalkylation of dialkylbenzenes, such as xylene, where an alkyl group is transferred from one molecule to another *via* a diphenylmethane-type transition state (Scheme 1.4 C). In this case, only certain positions of the alkyl group in the transition state are viable.<sup>89</sup>



**Scheme 1.4.** Illustrations of the three distinct types of shape selectivity, including reactant selectivity (A), product selectivity (B), and transition state selectivity (C).<sup>99</sup>

Zeolites are applied in various processes, including cracking, isomerization, hydrocarbon synthesis, synfuel production, refining, and production of chemicals. Far over 200 distinct zeolites structures have been identified to date, with MFI and BEA being among the ones most widely employed at industrial scale.<sup>93</sup>

H-ZSM-5 features a Mordenite Framework Inverted (MFI) topology. The structure consists of straight 10-membered ring channels measuring 0.53 nm x 0.56 nm along the [010] direction, and sinusoidal 10-membered ring channels with dimensions of 0.51 nm x 0.55 nm along the [100] direction (Figure 1.8).<sup>94</sup>

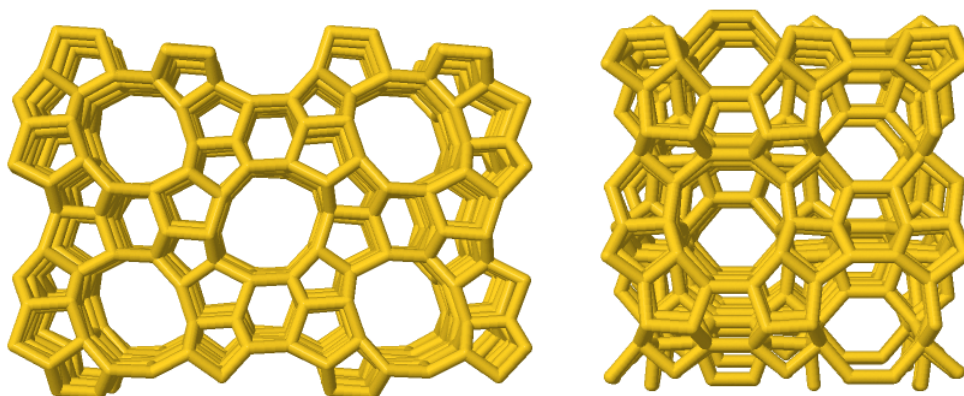


**Figure 1.8.** H-ZSM-5 (MFI) topology: straight 10-membered ring channels along the [010] direction (right) and sinusoidal 10-membered ring channels along the [010] direction (left).<sup>94</sup>

BEA zeolite, also known as Beta zeolite, has a disordered three-dimensional channel system with 12-membered ring channels. The void diameter in BEA zeolites is typically around 0.66 nm x 0.67 nm along the [100] direction and 0.56 nm x 0.56 nm along the [001] direction (Figure 1.9).<sup>94</sup>

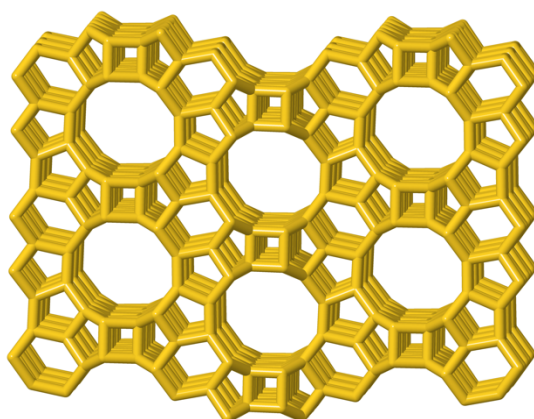


**Figure 1.9.** BEA topology: 12-membered ring channels along the [100] direction.<sup>94</sup>

While zeolites typically exhibit instability in aqueous phase at elevated temperatures,<sup>95,96</sup> recent studies have shown that zeolite frameworks can remain stable for extended durations in aqueous environments, as long as temperatures are maintained below 180°C.<sup>97,98</sup> Owing to their potential as solid acid catalysts in the conversion of oxo-functionalized molecules derived from renewable resources, and their unique selectivity properties, zeolites have been the subject of extensive research in such aqueous conditions.<sup>99-101</sup>

### 1.4.2 Supported tungstate catalysts

Since the discovery of hydrothermally stable  $\text{WO}_3/\text{ZrO}_2$  as a strong solid acid catalyst by Hino and Arata, its catalytic properties have garnered significant interest.<sup>102</sup> Tungstated zirconia has been studied as a catalyst for a variety of reactions, including light alkane isomerization,<sup>102-104</sup> selective catalytic reduction of  $\text{NO}_x$ ,<sup>105</sup> and dehydration of alcohols.<sup>106-108</sup>

The tungsten surface density is considered to be the primary determinant for the catalyst's activity, with a general consensus on the distinction between four different tungsten surface species.<sup>104,108-112</sup> At sub-monolayer surface coverage, octahedral isolated mono-oxo  $\text{W}=\text{O}$  species are present and transition to polymeric mono-oxo  $\text{W}=\text{O}$  species as the  $\text{W}$  surface density increases. Upon surpassing monolayer concentrations, crystalline, monoclinic  $\text{WO}_3$  nanoparticles are formed.<sup>108,113</sup> Under specific conditions, Zr-stabilized  $\text{WO}_3$  nanoparticles, which are speculated to be the most active species, can coexist with the aforementioned species (Figure 1.10).<sup>108,111,112</sup>

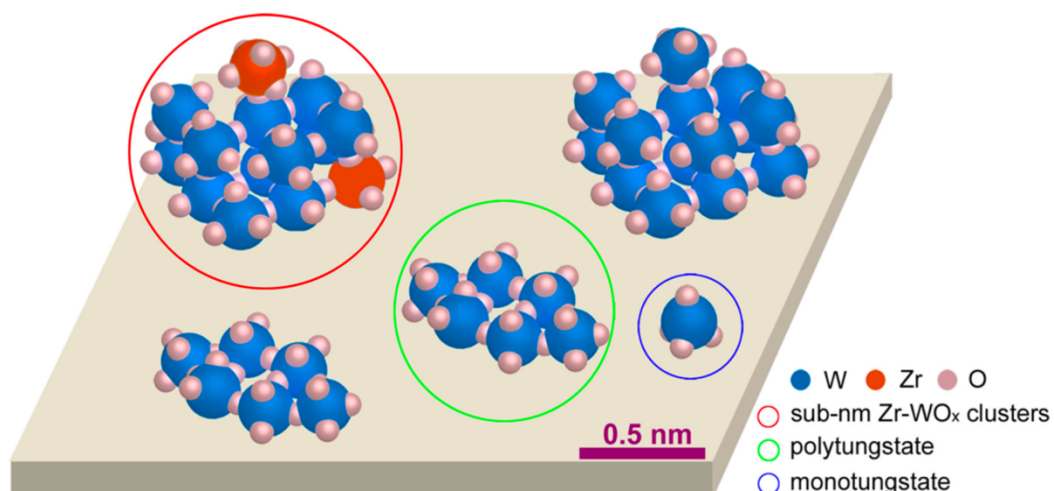


**Figure 1.10.** Illustration of the different tungsten surface species, including isolated surface monotungstate (blue circle), oligomeric two-dimensional polytungstate (green circle), three-dimensional Zr-stabilized  $\text{WO}_3$  nanoparticles (red circle), and crystalline  $\text{WO}_3$  nanoparticles (no circle) supported on  $\text{ZrO}_2$  surfaces. Reprinted from reference 114 Copyright (2023), with permission from Elsevier.

Tungstated zirconia exhibits both Lewis and Brønsted acid sites. Lewis acid sites are associated with coordinatively unsaturated  $\text{Zr}^{4+}$  sites, while Brønsted acid sites can originate from acidic hydroxyl groups linked to  $\text{W}-\text{O}-\text{W}$  and  $\text{W}-\text{O}-\text{Zr}$  bonds.<sup>115,116</sup> As the tungsten loading and consequently the  $\text{W}$  surface density increase, a higher concentration of these bonds and subsequently a higher concentration of Brønsted acid sites are observed.<sup>115,116</sup> In essence, the tungstate domain size increase enhances the conjugate base's ability to delocalize electrons upon acid deprotonation.<sup>112</sup> However, as tungsten loading continues to increase, larger crystalline  $\text{WO}_3$  particles start to form, making more  $\text{W}$  centers inaccessible and leading to a reduction in the concentration of Brønsted acid sites.<sup>113</sup>

Furthermore, recent studies have emphasized the significant impact of the tungstate support on the catalytic performance.<sup>117</sup> Employing activated carbon as the tungstate support, the turnover frequency in the aqueous phase dehydration of cyclohexanol was dramatically increased. It is expected that using activated carbon as a support will be especially beneficial for the conversion of the apolar microalgae oil, as it provides a sufficient catalytic surface while maintaining acidity.

Ultimately, to ensure that the catalyst is also active and suitable for the hydrodeoxygenation of microalgae oil, it is essential to incorporate a metal, e.g., a noble metal such as Pt, Rh or Ru, onto the supported tungstate catalyst.

## 1.5 Scope of the thesis

The overarching aim of this thesis is to contribute to a comprehensive and fundamental understanding of the catalytic conversion of biomass resources to hydrocarbon transportation fuels by examining the processes from a mechanistic perspective as well as adopting a more application-driven approach by proposing innovative pathways for the design of the heterogeneous catalysts and subsequently evaluating their performance.

The first objective of the thesis addresses the upgrading of pyrolysis oil, more specifically, the step of the acid-catalyzed dehydration of substituted cyclohexanols in aqueous phase (step 4 from Scheme 1.2). MFI and BEA zeolite catalysts were employed to investigate the effects of confinement, as well as the influence of the position of both the alcohol and the substituent on the reactivity and product selectivity. The aim is to gain a profound mechanistic understanding of the hydronium-ion-catalyzed dehydration of substituted cyclohexanols, ultimately allowing for the prediction of trends of the catalytic reactivity for various alcohols, independent of their specific substitution and the zeolite. Additionally, the impact of the BAS concentration on the reaction rate will be examined by varying the Si/Al ratios in MFI zeolites in the dehydration of substituted cyclic alcohols, following different reaction mechanisms. Thus, also reviewing whether variations in steric hindrance change the impact of the concentration of hydrated hydronium ions on the overall reaction rate.

The second objective of the thesis centers on the conversion of microalgae oil into hydrocarbon transportation fuels under mild conditions. In order to achieve the conversion of microalgae oil into kerosene range hydrocarbons, as depicted in Figure 1.7, a bifunctional catalyst is necessary that enables both hydrodeoxygenation and the subsequent hydroisomerization or hydrocracking step, while maintaining hydrothermal stability in aqueous phase, thereby avoiding the prior energy-demanding water separation. For this purpose, noble metal supported tungstate catalyst were employed, with either zirconia or activated carbon as the support ( $M/WO_3/ZrO_2$  or  $M/WO_3/C$ ;  $M = Pt, Rh, Ru$ ). Using stearic acid as model compound, the catalyst performance was investigated in terms of synthesis parameters, the influence of solvents and support differences, reaction conditions, and with a particular emphasis on the dehydration step of the reaction.

## 1.6 References

- (1) Ehrlich, P. R. *The Population Bomb*; Ballantine Books, 1968.
- (2) Kaku, M. *The Future of Humanity: Terraforming Mars, Interstellar Travel, Immortality, and Our Destiny Beyond Earth*; Knopf Doubleday Publishing Group, 2018.
- (3) Roser, M.; Ritchie, H.; Ortiz-Ospina, E.; Rod s-Guirao, L. World Population Growth. *Our World in Data 2013*, <https://ourworldindata.org/world-population-growth>.
- (4) Rosling, H.; R nnlund, A. R.; Rosling, O. *Factfulness: Ten Reasons We're Wrong About the World--and Why Things Are Better Than You Think*; Flatiron Books, 2018.
- (5) Agency, I. E. World Energy Outlook 2019. *IEA, Paris 2019*, <https://www.iea.org/reports/world-energy-outlook-2019>.
- (6) Agency, I. E. World Energy Outlook 2018. *IEA, Paris 2018*, <https://www.iea.org/reports/world-energy-outlook-2018>.
- (7) p.l.c, B. BP Statistical Review of World Energy. **2019**, <https://www.bp.com/content/dam/bp/business-sites/en/global/corporate/pdfs/energy-economics/statistical-review/bp-stats-review-2019-full-report.pdf>.
- (8) Agency, I. E. Energy Statistics Data Browser. *IEA, Paris 2022*, <https://www.iea.org/data-and-statistics/data-tools/energy-statistics-data-browser>.
- (9) Agency, I. E. Global Energy & CO2 Status Report 2019. *IEA, Paris 2019*, <https://www.iea.org/reports/global-energy-co2-status-report-2019>.
- (10) Agency, I. E. Technology Roadmap - Delivering Sustainable Bioenergy. *IEA, Paris 2017*, <https://www.iea.org/reports/world-energy-outlook-2018>.
- (11) Century, R. E. P. N. f. t. s. Renewables 2019 - Global Status Report. *REN21, Paris 2019*, [https://www.ren21.net/wp-content/uploads/2019/05/gsr\\_2019\\_full\\_report\\_en.pdf](https://www.ren21.net/wp-content/uploads/2019/05/gsr_2019_full_report_en.pdf).
- (12) Teter, J. L. F., P.; Gomer, M.; Scheffer, S. Tracking Transport 2019 – Analysis. *IEA, Paris 2020*, <https://www.iea.org/reports/tracking-transport-2019>.
- (13) Knothe, G., **2013**, 207.
- (14) Nations, F. a. A. O. o. t. U. The State of Food and Agriculture - Biofuels: prospects, risks and opportunities. *Food and Agriculture Organization of the United Nations, Rome 2008*, <https://www.fao.org/3/i0100e/i0100e.pdf>.
- (15) Brennan, L.; Owende, P. Biofuels from microalgae—A review of technologies for production, processing, and extractions of biofuels and co-products. *Renewable and Sustainable Energy Reviews 2010*, *14* (2), 557.
- (16) Lynch, J., **2017**, 261.
- (17) Sankaran, R.; Markandan, K.; Khoo, K. S.; Cheng, C. K.; Ashokkumar, V.; Deepanraj, B.; Show, P. L. The Expansion of Lignocellulose Biomass Conversion Into Bioenergy via Nanobiotechnology. *Frontiers in Nanotechnology 2021*, *3*.
- (18) St cker, M. Biofuels and Biomass-To-Liquid Fuels in the Biorefinery: Catalytic Conversion of Lignocellulosic Biomass using Porous Materials. *Angewandte Chemie International Edition 2008*, *47* (48), 9200.
- (19) Huber, G. W.; Iborra, S.; Corma, A. Synthesis of Transportation Fuels from Biomass: Chemistry, Catalysts, and Engineering. *Chemical Reviews 2006*, *106* (9), 4044.
- (20) Guschina, I. A.; Harwood, J. L. In *Algae for Biofuels and Energy*; Borowitzka, M. A.; Moheimani, N. R., Eds.; Springer Netherlands: Dordrecht, **2013**, 17.
- (21) Angelo, A. C.; Marujo, L., **2019**, 179.
- (22) Singh, J.; Saxena, R. C. In *Handbook of Marine Microalgae*; Kim, S.-K., Ed.; Academic Press: Boston, **2015**, 11.
- (23) Ruane, J.; Sonnino, A.; Agostini, A. Bioenergy and the potential contribution of agricultural biotechnologies in developing countries. *Biomass and Bioenergy 2010*, *34* (10), 1427.
- (24) Chisti, Y. Biodiesel from microalgae. *Biotechnology Advances 2007*, *25* (3), 294.
- (25) Spolaore, P.; Joannis-Cassan, C.; Duran, E.; Isambert, A. Commercial applications of microalgae. *Journal of Bioscience and Bioengineering 2006*, *101* (2), 87.
- (26) Metting, F. B. Biodiversity and application of microalgae. *Journal of Industrial Microbiology 1996*, *17* (5), 477.

- 
- (27) Mata, T.; Martins, A.; Caetano, N. Microalgae for biodiesel production and other applications: A review. *Renewable and Sustainable Energy Reviews* **2010**.
- (28) Thomas, W. H. T., T G; Weissman, J "Screening for lipid yielding microalgae: activities for 1983. Final subcontract report," 1984.
- (29) Sharma, K. K.; Schuhmann, H.; Schenk, P. M. High Lipid Induction in Microalgae for Biodiesel Production. *Energies* **2012**, 5 (5), 1532.
- (30) Chisti, Y. Raceways-based Production of Algal Crude Oil. *Green* **2013**, 3.
- (31) Tredici, M. R. Photobiology of microalgae mass cultures: understanding the tools for the next green revolution. *Biofuels* **2010**, 1 (1), 143.
- (32) Wijffels, R. H.; Barbosa, M. J. An outlook on microalgal biofuels. *Science* **2010**, 329 (5993), 796.
- (33) Rodolfi, L.; Chini Zittelli, G.; Bassi, N.; Padovani, G.; Biondi, N.; Bonini, G.; Tredici, M. R. Microalgae for oil: strain selection, induction of lipid synthesis and outdoor mass cultivation in a low-cost photobioreactor. *Biotechnology and Bioengineering* **2009**, 102 (1), 100.
- (34) Williams, P. R. D.; Inman, D.; Aden, A.; Heath, G. A. Environmental and Sustainability Factors Associated With Next-Generation Biofuels in the U.S.: What Do We Really Know? *Environmental Science & Technology* **2009**, 43 (13), 4763.
- (35) Wang, B.; Li, Y.; Wu, N.; Lan, C. Q. CO<sub>2</sub> bio-mitigation using microalgae. *Applied Microbiology and Biotechnology* **2008**, 79 (5), 707.
- (36) Pandit, S.; Das, D., **2015**, 375.
- (37) Flesch, A.; Beer, T.; Campbell, P.; Batten, D.; Grant, T., **2013**, 233.
- (38) Darzins, A. P., P.; Edey, L. "Current Status and Potential for Algal Biofuels Production," BioIndustry & NREL, 2010.
- (39) Posten, C. Design principles of photo-bioreactors for cultivation of microalgae. *Engineering in Life Sciences* **2009**, 9 (3), 165.
- (40) Janssen, M.; Tramper, J.; Mur, L. R.; Wijffels, R. H. Enclosed outdoor photobioreactors: light regime, photosynthetic efficiency, scale-up, and future prospects. *Biotechnology and Bioengineering* **2003**, 81 (2), 193.
- (41) Kalaitzidis, T. In *Algae for Biofuels and Energy*, **2013**, 165.
- (42) McKendry, P. Energy production from biomass (part 2): conversion technologies. *Bioresource Technology* **2002**, 83 (1), 47.
- (43) Prakash, J.; Pushparaj, B.; Carlozzi, P.; Torzillo, G.; Montaini, E.; Materassi, R. Microalgal Biomass Drying by a Simple Solar DEVICE. *International Journal of Solar Energy* **1997**, 18, 303.
- (44) Gudín, C. T., C.; Bioconversion of solar energy into organic chemicals by microalgae. *Advances in biotechnological processes* **1987**, 6, 73.
- (45) Borowitzka, M. A. Algal biotechnology products and processes — matching science and economics. *Journal of Applied Phycology* **1992**, 4 (3), 267.
- (46) Borowitzka, M. A.; Moheimani, N. R. Sustainable biofuels from algae. *Mitigation and Adaptation Strategies for Global Change* **2013**, 18 (1), 13.
- (47) Lardon, L.; Hélias, A.; Sialve, B.; Steyer, J. P.; Bernard, O. Life-cycle assessment of biodiesel production from microalgae. *Environmental Science and Technology* **2009**, 43 (17), 6475.
- (48) Adams, P.; Bridgwater, T.; Lea-Langton, A.; Ross, A.; Watson, I. In *Greenhouse Gas Balances of Bioenergy Systems*; Thornley, P.; Adams, P., Eds.; Academic Press, **2018**, 107.
- (49) Deublein, D.; Steinhauser, A. *Biogas from waste and renewable resources: an introduction*; John Wiley & Sons, 2011.
- (50) Food; department, a. o. o. t. U. N. F. *UBET-Unified bioenergy terminology*; Food and agriculture organization of the United States, 2004.
- (51) Patel, M.; Zhang, X.; Kumar, A. Techno-economic and life cycle assessment on lignocellulosic biomass thermochemical conversion technologies: A review. *Renewable and Sustainable Energy Reviews* **2016**, 53, 1486.
-

- (52) Biller, P.; Sharma, B. K.; Kunwar, B.; Ross, A. B. Hydroprocessing of bio-crude from continuous hydrothermal liquefaction of microalgae. *Fuel* **2015**, *159*, 197.
- (53) Elliott, D. C.; Biller, P.; Ross, A. B.; Schmidt, A. J.; Jones, S. B. Hydrothermal liquefaction of biomass: Developments from batch to continuous process. *Bioresource Technology* **2015**, *178*, 147.
- (54) Bridgwater, A. Thermal Conversion of Biomass and Waste: The Status. *Bio-Energy Research Group, Aston University, Birmingham, UK* **2001**.
- (55) Jenkins, B. M.; Baxter, L. L.; Miles, T. R.; Miles, T. R. Combustion properties of biomass. *Fuel Processing Technology* **1998**, *54* (1), 17.
- (56) Williams, R.; Jenkins, B.; Nguyen, D. Solid waste conversion: A review and database of current and emerging technologies. *Final report, Department of Biological and Agricultural Engineering, University of California, Davis* **2003**.
- (57) Bridgwater, A. V. Review of fast pyrolysis of biomass and product upgrading. *Biomass and Bioenergy* **2012**, *38*, 68.
- (58) Meher, L. C.; Vidya Sagar, D.; Naik, S. N. Technical aspects of biodiesel production by transesterification—a review. *Renewable and Sustainable Energy Reviews* **2006**, *10* (3), 248.
- (59) Vicente, G.; Martínez, M.; Aracil, J. Integrated biodiesel production: a comparison of different homogeneous catalysts systems. *Bioresource Technology* **2004**, *92* (3), 297.
- (60) Demirbas, A. Progress and recent trends in biodiesel fuels. *Energy Conversion and Management* **2009**, *50* (1), 14.
- (61) Benjumea, P.; Agudelo, J.; Agudelo, A. Basic properties of palm oil biodiesel–diesel blends. *Fuel* **2008**, *87* (10), 2069.
- (62) Elliott, D. C.; Beckman, D.; Bridgwater, A. V.; Diebold, J. P.; Gevert, S. B.; Solantausta, Y. Developments in direct thermochemical liquefaction of biomass: 1983-1990. *Energy & Fuels* **1991**, *5* (3), 399.
- (63) Czernik, S.; Bridgwater, A. V. Overview of Applications of Biomass Fast Pyrolysis Oil. *Energy & Fuels* **2004**, *18* (2), 590.
- (64) Bridgwater, A. V.; Boocock, D. G. B. *Developments in Thermochemical Biomass Conversion*; Blackie Academic & Professional, 1997.
- (65) Gollakota, A. R. K.; Kishore, N.; Gu, S. A review on hydrothermal liquefaction of biomass. *Renewable and Sustainable Energy Reviews* **2018**, *81*, 1378.
- (66) Hintermeier, P. H. Zeolite catalyzed dehydration of substituted cyclic alcohols in aqueous phase. Technische Universität München, 2017.
- (67) Kubička, D.; Horáček, J. Deactivation of HDS catalysts in deoxygenation of vegetable oils. *Applied Catalysis A: General* **2011**, *394* (1), 9.
- (68) Kubička, D.; Kaluža, L. Deoxygenation of vegetable oils over sulfided Ni, Mo and NiMo catalysts. *Applied Catalysis A: General* **2010**, *372* (2), 199.
- (69) Aatola, H.; Larmi, M.; Sarjovaara, T.; Mikkonen, S. Hydrotreated Vegetable Oil (HVO) as a Renewable Diesel Fuel: Trade-off between NO<sub>x</sub>, Particulate Emission, and Fuel Consumption of a Heavy Duty Engine. *SAE International Journal of Engines* **2008**, *1* (1), 1251.
- (70) Kuronen, M.; Mikkonen, S.; Aakko, P.; Murtonen, T.; SAE International, 2007.
- (71) Rantanen, L.; Linnaila, R.; Aakko, P.; Harju, T.; SAE International, 2005.
- (72) Veriansyah, B.; Han, J.; Kim, S.-K.; Hong, S.-A.; Kim, Y.; Lim, J. S.; Shu, Y.-W.; Oh, S.-G.; Kim, J. Production of renewable diesel by hydroprocessing of soybean oil: Effect of catalysts. *Fuel* **2011**, *94*.
- (73) Choudhary, T. V.; Phillips, C. B. Renewable fuels via catalytic hydrodeoxygenation. *Applied Catalysis A: General* **2011**, *397* (1), 1.
- (74) Donniss, B.; Egeberg, R. G.; Blom, P.; Knudsen, K. G. Hydroprocessing of Bio-Oils and Oxygenates to Hydrocarbons. Understanding the Reaction Routes. *Topics in Catalysis* **2009**, *52* (3), 229.

- 
- (75) Bezergianni, S.; Dimitriadis, A.; Meletidis, G. Effectiveness of CoMo and NiMo catalysts on co-hydroprocessing of heavy atmospheric gas oil–waste cooking oil mixtures. *Fuel* **2014**, *125*, 129.
- (76) Furimsky, E. Chemistry of Catalytic Hydrodeoxygenation. *Catalysis Reviews* **1983**, *25* (3), 421.
- (77) Peng, B.; Yao, Y.; Zhao, C.; Lercher, J. A. Towards Quantitative Conversion of Microalgae Oil to Diesel-Range Alkanes with Bifunctional Catalysts. *Angewandte Chemie International Edition* **2012**, *51* (9), 2072.
- (78) Kubičková, I.; Snåre, M.; Eränen, K.; Mäki-Arvela, P.; Murzin, D. Y. Hydrocarbons for diesel fuel via decarboxylation of vegetable oils. *Catalysis Today* **2005**, *106* (1), 197.
- (79) Snåre, M.; Kubičková, I.; Mäki-Arvela, P.; Chichova, D.; Eränen, K.; Murzin, D. Y. Catalytic deoxygenation of unsaturated renewable feedstocks for production of diesel fuel hydrocarbons. *Fuel* **2008**, *87* (6), 933.
- (80) Snåre, M.; Kubičková, I.; Mäki-Arvela, P.; Eränen, K.; Murzin, D. Y. Heterogeneous Catalytic Deoxygenation of Stearic Acid for Production of Biodiesel. *Industrial & Engineering Chemistry Research* **2006**, *45* (16), 5708.
- (81) Haas, M.; Wagner, K. Simplifying biodiesel production: The direct or in situ transesterification of algal biomass. *European Journal of Lipid Science and Technology* **2011**, *113*, 1219.
- (82) Zhao, C.; Brück, T.; Lercher, J. Catalytic deoxygenation of microalgae oil to green hydrocarbons. *Green Chemistry* **2013**, *15*.
- (83) Peng, B.; Yuan, X.; Zhao, C.; Lercher, J. A. Stabilizing Catalytic Pathways via Redundancy: Selective Reduction of Microalgae Oil to Alkanes. *Journal of the American Chemical Society* **2012**, *134* (22), 9400.
- (84) Busto, M.; Grau, J.; Vera, C. Screening of optimal pretreatment and reaction conditions for the isomerization-cracking of long paraffins over Pt/WO<sub>3</sub>-ZrO<sub>2</sub> catalysts. *Applied Catalysis A-general* **2010**, *387*, 35.
- (85) Lim, J. H. K.; Gan, Y. Y.; Ong, H. C.; Lau, B. F.; Chen, W.-H.; Chong, C. T.; Ling, T. C.; Klemeš, J. J. Utilization of microalgae for bio-jet fuel production in the aviation sector: Challenges and perspective. *Renewable and Sustainable Energy Reviews* **2021**, *149*, 111396.
- (86) Jiménez-Díaz, L.; Caballero, A.; Pérez-Hernández, N.; Segura, A. Microbial alkane production for jet fuel industry: motivation, state of the art and perspectives. *Microb Biotechnol* **2017**, *10* (1), 103.
- (87) Ertl, G.; Knözinger, H.; Schüth, F.; Weitkamp, J. *Handbook of Heterogeneous Catalysis*; Wiley-VCH Verlag GmbH & Co KGaA: Weinheim, 2008.
- (88) Olsbye, U.; Svelle, S.; Bjørgen, M.; Beato, P.; Janssens, T. V. W.; Joensen, F.; Bordiga, S.; Lillerud, K. P. Conversion of Methanol to Hydrocarbons: How Zeolite Cavity and Pore Size Controls Product Selectivity. *Angewandte Chemie International Edition* **2012**, *51* (24), 5810.
- (89) Csicsery, S. M. Catalysis by shape selective zeolites-science and technology. *Pure and Applied Chemistry* **1986**, *58* (6), 841.
- (90) Csicsery, S. M. *The future of shape selective catalysis*; Elsevier, 1995.
- (91) Marshall, J. F.; Weisz, P. B. Determination of diffusivities in catalyst particles. *Journal of Catalysis* **1988**, *111* (2), 460.
- (92) Weisz, P. B.; Frilette, V. J. INTRACRYSTALLINE AND MOLECULAR-SHAPE-SELECTIVE CATALYSIS BY ZEOLITE SALTS. *The Journal of Physical Chemistry* **1960**, *64* (3), 382.
- (93) Bingre, R.; Louis, B.; Nguyen, P. An Overview on Zeolite Shaping Technology and Solutions to Overcome Diffusion Limitations. *Catalysts* **2018**, *8* (4), 163.
- (94) Structure Commission of the International Zeolite Association. **2017**, <http://www.iza-structure.org/databases/>.
- (95) Vjunov, A.; Derewinski, M. A.; Fulton, J. L.; Camaioni, D. M.; Lercher, J. A. Impact of Zeolite Aging in Hot Liquid Water on Activity for Acid-Catalyzed Dehydration of Alcohols. *Journal of the American Chemical Society* **2015**, *137* (32), 10374.
-

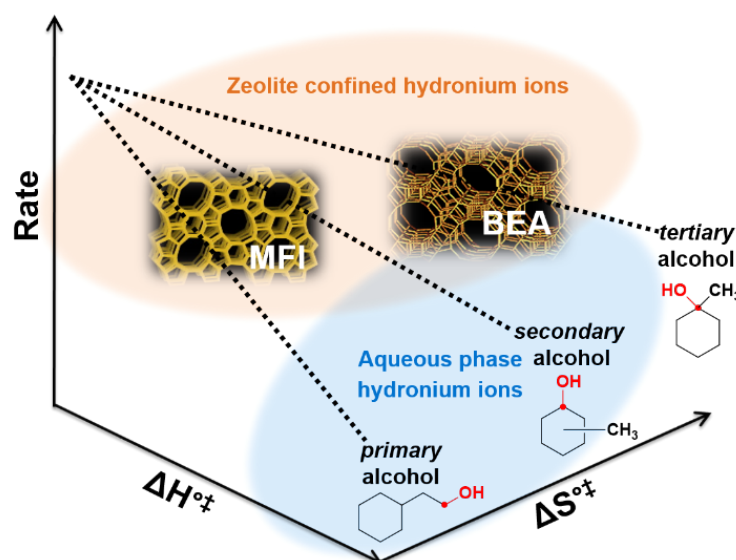
- (96) Vjunov, A.; Fulton, J. L.; Camaioni, D. M.; Hu, J. Z.; Burton, S. D.; Arslan, I.; Lercher, J. A. Impact of Aqueous Medium on Zeolite Framework Integrity. *Chemistry of Materials* **2015**, *27* (9), 3533.
- (97) Lutz, W.; Toufar, H.; Kurzhals, R.; Suckow, M. Investigation and Modeling of the Hydrothermal Stability of Technically Relevant Zeolites. *Adsorption* **2005**, *11* (3), 405.
- (98) Ravenelle, R. M.; Schüßler, F.; D'Amico, A.; Danilina, N.; van Bokhoven, J. A.; Lercher, J. A.; Jones, C. W.; Sievers, C. Stability of Zeolites in Hot Liquid Water. *The Journal of Physical Chemistry C* **2010**, *114* (46), 19582.
- (99) Liu, Y.; Vjunov, A.; Shi, H.; Eckstein, S.; Camaioni, D. M.; Mei, D.; Baráth, E.; Lercher, J. A. Enhancing the catalytic activity of hydronium ions through constrained environments. *Nature Communications* **2017**, *8* (1), 14113.
- (100) Shi, H.; Eckstein, S.; Vjunov, A.; Camaioni, D. M.; Lercher, J. A. Tailoring nanoscopic confines to maximize catalytic activity of hydronium ions. *Nature Communications* **2017**, *8* (1), 15442.
- (101) Zhao, C.; Lercher, J. A. Upgrading Pyrolysis Oil over Ni/HZSM-5 by Cascade Reactions. *Angewandte Chemie International Edition* **2012**, *51* (24), 5935.
- (102) Hino, M.; Arata, K. Synthesis of solid superacid of tungsten oxide supported on zirconia and its catalytic action for reactions of butane and pentane. *Journal of the Chemical Society, Chemical Communications* **1988**, (18), 1259.
- (103) Santiesteban, J. G.; Vartuli, J. C.; Han, S.; Bastian, R. D.; Chang, C. D. Influence of the Preparative Method on the Activity of Highly Acidic WO<sub>x</sub>/ZrO<sub>2</sub> and the Relative Acid Activity Compared with Zeolites. *Journal of Catalysis* **1997**, *168* (2), 431.
- (104) Soultanidis, N.; Zhou, W.; Psarras, A. C.; Gonzalez, A. J.; Iliopoulou, E. F.; Kiely, C. J.; Wachs, I. E.; Wong, M. S. Relating n-Pentane Isomerization Activity to the Tungsten Surface Density of WO<sub>x</sub>/ZrO<sub>2</sub>. *Journal of the American Chemical Society* **2010**, *132* (38), 13462.
- (105) Kantcheva, M.; Milanova, M.; Mametsheripov, S. In situ FT-IR spectroscopic investigation of gold supported on tungstated zirconia as catalyst for CO-SCR of NO<sub>x</sub>. *Catalysis Today* **2012**, *191* (1), 12.
- (106) Baertsch, C. D.; Komala, K. T.; Chua, Y.-H.; Iglesia, E. Genesis of Brønsted Acid Sites during Dehydration of 2-Butanol on Tungsten Oxide Catalysts. *Journal of Catalysis* **2002**, *205* (1), 44.
- (107) Macht, J.; Baertsch, C. D.; May-Lozano, M.; Soled, S. L.; Wang, Y.; Iglesia, E. Support effects on Brønsted acid site densities and alcohol dehydration turnover rates on tungsten oxide domains. *Journal of Catalysis* **2004**, *227* (2), 479.
- (108) Ross-Medgaarden, E. I.; Knowles, W. V.; Kim, T.; Wong, M. S.; Zhou, W.; Kiely, C. J.; Wachs, I. E. New insights into the nature of the acidic catalytic active sites present in ZrO<sub>2</sub>-supported tungsten oxide catalysts. *Journal of Catalysis* **2008**, *256* (1), 108.
- (109) Lee, J.-H.; Shin, C.-H.; Suh, Y.-W. Higher Brønsted acidity of WO<sub>x</sub>/ZrO<sub>2</sub> catalysts prepared using a high-surface-area zirconium oxyhydroxide. *Molecular Catalysis* **2017**, *438*, 272.
- (110) Piva, D. H.; Piva, R. H.; Pereira, C. A.; Silva, D. S. A.; Montedo, O. R. K.; Morelli, M. R.; Urquieta-González, E. A. Facile synthesis of WO<sub>x</sub>/ZrO<sub>2</sub> catalysts using WO<sub>3</sub>-H<sub>2</sub>O precipitate as synthetic precursor of active tungsten species. *Materials Today Chemistry* **2020**, *18*, 100367.
- (111) Zhou, W.; Ross-Medgaarden, E. I.; Knowles, W. V.; Wong, M. S.; Wachs, I. E.; Kiely, C. J. Identification of active Zr-WO<sub>x</sub> clusters on a ZrO<sub>2</sub> support for solid acid catalysts. *Nature Chemistry* **2009**, *1* (9), 722.
- (112) Zhou, W.; Soultanidis, N.; Xu, H.; Wong, M. S.; Neurock, M.; Kiely, C. J.; Wachs, I. E. Nature of Catalytically Active Sites in the Supported WO<sub>3</sub>/ZrO<sub>2</sub> Solid Acid System: A Current Perspective. *ACS Catalysis* **2017**, *7* (3), 2181.
- (113) Barton, D. G.; Shtein, M.; Wilson, R. D.; Soled, S. L.; Iglesia, E. Structure and Electronic Properties of Solid Acids Based on Tungsten Oxide Nanostructures. *The Journal of Physical Chemistry B* **1999**, *103* (4), 630.
-

- (114) Zhou, W.; Wachs, I. E.; Kiely, C. J. Nanostructural and chemical characterization of supported metal oxide catalysts by aberration corrected analytical electron microscopy. *Current Opinion in Solid State and Materials Science* **2012**, *16* (1), 10.
- (115) Baertsch, C. D.; Soled, S. L.; Iglesia, E. Isotopic and Chemical Titration of Acid Sites in Tungsten Oxide Domains Supported on Zirconia. *The Journal of Physical Chemistry B* **2001**, *105* (7), 1320.
- (116) Scheithauer, M.; Grasselli, R. K.; Knözinger, H. Genesis and Structure of WO<sub>x</sub>/ZrO<sub>2</sub> Solid Acid Catalysts. *Langmuir* **1998**, *14* (11), 3019.
- (117) Pfriem, N.; Liu, Y.; Zahn, F.; Shi, H.; Haller, G. L.; Lercher, J. A. Impact of the Local Concentration of Hydronium Ions at Tungstate Surfaces for Acid-Catalyzed Alcohol Dehydration. *Journal of the American Chemical Society* **2021**, *143* (48), 20133.



# Chapter 2

## Towards understanding and predicting the hydronium ion catalyzed dehydration of cyclic-primary, secondary and tertiary alcohols



### This work has been published

Reprinted with permission from: Milaković, L.; Hintermeier, P. H.; Liu, Q.; Shi, H.; Liu, Y.; Baráth, E.; Lercher, J. A. Towards understanding and predicting the hydronium ion catalyzed dehydration of cyclic-primary, secondary and tertiary alcohols. *Journal of Catalysis* **2020**, 390, 237. DOI: 10.1016/j.jcat.2020.08.009

Copyright (2023) Elsevier.

## Abstract

The varying steric environment of zeolites subtly influences the rates of hydronium-ion-catalyzed dehydration of alcohols containing a cyclohexyl group in aqueous phase. The investigated primary, secondary, and tertiary alcohols show an increasing stabilization of an ionic transition state in this sequence, i.e., an increasing tendency to move from a concerted (E2 mechanism) to a stepwise dehydration (E1 mechanism). Hydronium ions confined in the micropores of MFI and BEA zeolites induced much higher catalyzed rates than those in the aqueous phase. Independent of the reaction mechanism and the environment, however, all alcohols investigated follow one compensation correlation between activation enthalpy and entropy for primary, secondary, and tertiary alcohols, respectively. For a given transition enthalpy, the rate of dehydration is the higher the larger the reaction space (translated to the reaction entropy). Surprisingly, all compensation relations intersect in one point. These dependences for the different alcohols are also reflected in the turnover rates, for which all alcohols also intersect in a common point, which appears to mark the highest reaction rate for dehydration catalyzed by hydronium ions at the investigated temperature.

## 2.1 Introduction

Reaction pathways and catalytic activities in microporous zeolites are significantly affected by the fit between pore environment and the reacting molecules.<sup>1-5</sup> Increasing confinement tends to cause an increase in the heat of adsorption and a concomitant loss of entropy, shown exemplary for a series of *n*-alkanes and zeolites with varying pore radii.<sup>6-8</sup> As this confinement influences the ground and transition states along the reaction path differently, acid-catalyzed reactions on zeolites, such as alcohol dehydration, are in consequence also influenced by the local environment.<sup>9-21</sup> Carrying out the reactions in liquid phase brings about an additional level of complexity and transforms zeolite Brønsted acidic OH groups to hydrated hydronium ions<sup>22-27</sup> that protonate reactive substrates more basic than water and act in this environment as catalytically active sites.

Thus, the confines of zeolite pores facilitate dehydration compared to aqueous phase or in macroporous environment.<sup>28-30</sup> The site normalized rates (turnover frequencies, TOFs) decrease monotonically with increasing pore size (MFI and BEA zeolites).<sup>31</sup> The significantly higher dehydration rates of cyclohexanol (CyOH) in smaller pores was concluded to result from the greater enthalpic stabilization of the transition states (relative to the H-bonded alcohols), overcompensating the lower transition entropies in such tight confines.<sup>31-34</sup> However, the molecular structure of the alcohols was observed to induce strong variations in the rates. The associated standard transition enthalpies and entropies have been pointing to a subtle, but specific impact of the fit between the environment and the transition state.<sup>28</sup>

Based on the dehydration of substituted cyclohexanol molecules, it was concluded that not only the position of the alkyl substituent, but also the configuration (i.e., the position of the OH group relative to  $\beta$ -H and the substituent) of the substituted alcohol isomers

affect the elimination pathways and rates.<sup>28-30</sup> Dehydration of CyOH, *trans*-2-methylcyclohexanol (*trans*-2-McyOH), as well as *cis*- and *trans*-isomers of 4-methylcyclohexanol (*cis*-, *trans*-4-McyOH) were found to proceed predominantly *via* an E1 route, dehydration of *cis*-2-methylcyclohexanol (*cis*-2-McyOH) *via* an E2-type pathway. Interestingly, the mechanism did not depend on whether the reaction was catalyzed by hydronium ions in the aqueous solution or by those confined in the MFI pores.<sup>28</sup>

In order to better understand these influences and the potential interdependencies of mechanism and rate, we studied the impact of the steric environment (zeolites MFI and BEA in comparison to aqueous H<sub>3</sub>PO<sub>4</sub>) on the dehydration of primary (1°), secondary (2°), and tertiary (3°) alcohols. The systematic variation of the substrate structure and the size of confines allows to show the subtle interrelation between the fit and the catalyzed conversions and reveals a unique dependence of the catalyzed rates on the nature of the alcohol.

## 2.2 Experimental methods

### 2.2.1 Chemicals

The following chemicals were used: 1-methylcyclohexanol (96%, *Sigma-Aldrich*), 2-cyclohexylethanol (99%, *Sigma-Aldrich*), sodium sulfate (ACS reagent, >99%, *Sigma-Aldrich*) ethyl acetate (*Chromasolv*, 99.9%, *Sigma-Aldrich*), phosphoric acid (85% solution, *Sigma-Aldrich*) and sodium chloride (*ReagentPlus*, >99%, *Sigma-Aldrich*). All the chemicals were used directly without any further purifications. Hydrogen gas was obtained from *Westfalen* (>99.999%). Deionized water was treated with an *Easypure-II* system from *WERNER* to obtain ultrapure water (18.2 MΩ cm).

### 2.2.2 Zeolite catalysts

Commercial zeolites including H-MFI (Si/Al = 45 and 90) and H-BEA (Si/Al = 83) were obtained as H-form from *Clariant*. H-BEA (Si/Al = 12.5) was prepared by a calcination treatment of NH<sub>4</sub>-BEA (CP814E\*, *Zeolyst International*). All the zeolite samples were reactivated at 450°C for 4 h under 100 mL min<sup>-1</sup> synthetic air flow (80% N<sub>2</sub>, 20% O<sub>2</sub>, >99%) in a tube furnace.

It should be noted that acid-catalyzed water elimination reactions of different alcohols were intensively studied in aqueous phase using H-MFI-45 and H-BEA-83 zeolites. While H-BEA-12.5 and H-MFI-90 were selected as the comparative sample for H-MFI-45 and H-BEA-83, respectively, to evaluate the pore size effect on the saturation adsorption uptake.

### 2.2.3 Reaction procedure

All reactions were performed with a reactant and a catalyst in 100 mL ultrapure water as the solvent. Either 0.01/0.02 mol (1.28/2.56 g) of 2-cyclohexylethanol or 0.05 mol (5.71 g) of the secondary or tertiary methyl substituted cyclohexanols (2/4/1-methylcyclohexanol) and between 50 and 200 mg zeolite were dissolved and suspended, respectively. Homogeneously catalyzed experiments were performed with 0.02 mol (2.56 g) of 2-cyclohexylethanol and 0.07 mol (5 mL, 33.7 mg of 85 wt% H<sub>3</sub>PO<sub>4</sub>) phosphoric acid. 0.02 mol (2.28 g) of the secondary cyclohexanols (2/4-methylcyclohexanol) were converted with 0.29 mmol (20 μL, 8.4 g of 85 wt% H<sub>3</sub>PO<sub>4</sub>) phosphoric acid. For 0.01 mol (1.14 g) of 1-methylcyclohexanol, 0.51 mmol (35 μL, 0.06 g of 85 wt% H<sub>3</sub>PO<sub>4</sub>) phosphoric acid were used. 4.38 mmol (0.50 g) of the *trans*-2-methylcyclohexanol isomer were catalyzed with 5.00 mmol (0.34 mL, 0.58 g of 85 wt% H<sub>3</sub>PO<sub>4</sub>) phosphoric acid or with between 50 and 100 mg of the zeolites.

The autoclave (300 mL) was loaded with 100 mL water, the catalyst and the substituted cyclohexanol substrate. The reactor was purged two times with hydrogen (20 bar) and was heated to the reaction temperature (120 – 230°C) with a heating rate of 10°C per minute with 20 bar H<sub>2</sub> without stirring. Ten degrees below the reaction temperature the total pressure of the reactor was adjusted to 50 bar with hydrogen gas. As soon as the reaction temperature was reached, the stirring rate was set to 700 rpm. After the reaction time, the reactor was cooled down to room temperature by an ice bath. The pressure within the reactor was released below 5°C to prevent the loss of volatile products. The reaction mixture was extracted with 3 x 20 mL ethyl acetate. To improve the phase separation of the organic and the aqueous phases, a small amount of sodium chloride was added to the reaction mixture. After extraction, the organic phase was dried over sodium sulfate. The carbon balance was monitored by an internal standard (dodecane).

## 2.3 Results and discussion

### 2.3.1 Materials studied

Two zeolite frameworks with different pore diameters, channel topologies and dimensions (MFI, BEA; Table 2.1) were investigated to compare the impact of the steric environment on acid-catalyzed dehydration of substituted 1°, 2° and 3° cyclic alcohols (Figure S2.1-S2.41, Table S2.1-S2.36). The Si/Al ratios were chosen in order to ensure that the zeolites are sufficiently stable in hot liquid water on the timescale of kinetic measurements.<sup>32-34</sup> Table 2.1 compiles the acid properties of MFI (Si/Al = 45, MFI-45) and BEA (Si/Al = 83, BEA-83) used for catalytic studies. Additional sorption measurements were also conducted with two further zeolite samples (MFI-90 and BEA-12.5) in order to rule out dominating influences of the concentration of hydronium ions.

**Table 2.1.** Physicochemical properties and acid site concentrations of investigated MFI and BEA zeolites.

Zeolite	Si/Al	BET surface area (m <sup>2</sup> g <sup>-1</sup> )	Micropore Volume (cm <sup>3</sup> g <sup>-1</sup> )	Concentration (BAS) <sup>a</sup> (μmol g <sup>-1</sup> )	Concentration (LAS) <sup>a</sup> (μmol g <sup>-1</sup> )
MFI-45	45	389	0.12	360	50
MFI-90	90	365	0.11	150	45
BEA-12.5	12.5	492	0.15	402	378
BEA-83	83	523	0.18	120	20

<sup>a</sup>Determined by IR spectroscopy of adsorbed pyridine (see 2.7 Supporting information).

### 2.3.2 Interactions of cyclic alcohols with MFI and BEA zeolites

The ground state of adsorbed alcohols in the solvent filled zeolite pores is determined by the steric fit of the molecules and the density of the hydronium ions in the zeolite pores.<sup>28-30</sup> As the difference between this ground state and the transition state will determine the reaction rate, we explore here first the adsorption enthalpy and entropy of the reacting alcohols.<sup>28-30</sup> Compared to MFI, a larger uptake of the investigated alcohols on BEA was observed independently of the position of the substituent in the alcohols and of the concentration of BAS (Table 2.1, Figure S2.42). The saturation uptake increased with decreasing BAS concentration on BEA for all alcohols, whereas on MFI only for 2-CyEtOH (2-cyclohexylethanol) and 4-McyOH. For all other alcohols, similar and lower saturation uptakes were measured on MFI-90 with the lower BAS concentration (150 μmol g<sup>-1</sup>) than on MFI-45 (BAS / 360 μmol g<sup>-1</sup>). The smaller pore size of MFI zeolites is hypothesized to allow only for a less tight packing for the alcohols with a higher steric bulkiness. In line with this, *trans*-2-McyOH and *cis*-2-McyOH had in general a smaller uptake on MFI compared to the other alcohols (Table 2.2, Figure S2.42).

The adsorption enthalpy was higher for MFI than for BEA, i.e., the smaller diameter of the pores leads to stronger interactions *via* dispersion forces. Surprisingly, all adsorption entropies for substituted alcohols were positive for zeolite BEA, while for MFI lower and also negative values were obtained (Table 2.2). The substituted alcohols with higher steric hindrance tended to have a higher sorption entropy than CyOH. As it is hard to conceive that additional steric influence increases the sorption entropy other than by reducing the adsorption enthalpy, we speculate that the de-solvation of the alcohols led to the increase in the entropy of the solvating liquid phase. It is unclear at present whether desorption of loosely bound water at defect sites in the BEA pores plays an additional role for the entropy increase.

**Table 2.2.** Adsorption parameters for substituted cyclohexanols, uptake measurements from aqueous phase in MFI and BEA zeolites.

Zeolite	Alcohol	$q_{\max}$ (mmol g <sup>-1</sup> ) <sup>a</sup>	$K_{\text{ads}}^{\circ}$ <sup>b</sup>	$\Delta H_{\text{ads}}^{\circ}$ (kJ mol <sup>-1</sup> ) <sup>c</sup>	$\Delta S_{\text{ads}}^{\circ}$ (J mol <sup>-1</sup> K <sup>-1</sup> ) <sup>c</sup>
MFI-45	CyOH <sup>d</sup>	0.66	$1.6 \times 10^3$	-30	-55
BEA-83		1.60	$5.8 \times 10^2$	-22	-25
MFI-45	2-CyEtOH	0.51	$1.9 \times 10^3$	-24	-18
BEA-83		1.39	$4.6 \times 10^3$	-7.0	47
MFI-45	4-McyOH	0.54	$4.3 \times 10^3$	-26	-17
BEA-83		1.14	$4.9 \times 10^3$	-14	20
MFI-45	<i>trans</i> -2-McyOH	0.29	$4.4 \times 10^3$	-14	22
BEA-83		1.25	$1.2 \times 10^4$	-5.0	58
MFI-45	<i>cis</i> -2-McyOH	0.24	$5.6 \times 10^3$	-24	-7
BEA-83		1.25	$1.3 \times 10^4$	-11	42
MFI-45	1-McyOH	0.45	$2.1 \times 10^2$	-17	-11
BEA-83		1.35	$3.3 \times 10^3$	-7.0	24

<sup>a</sup>Saturation uptake in 298K. <sup>b</sup>Equilibrium adsorption constants were obtained by fitting the Langmuir isotherms. <sup>c</sup>Microcalorimetry was conducted to analyze the standard molar enthalpy changes of alcohols adsorption, while the standard molar entropy changes were derived from  $\Delta G_{\text{ads}}^{\circ} = -RT \ln K_{\text{ads}}^{\circ} = \Delta H_{\text{ads}}^{\circ} - T\Delta S_{\text{ads}}^{\circ}$ . All the standard states were set as 1 mol L<sup>-1</sup>. <sup>d</sup>Data from reference 31.

Figure 2.1 shows a linear correlation of the adsorption entropy and enthalpy for all investigated cyclohexanols independent of the position of the substitution and the position of the OH group. The only exception was found for the two molecules, which are having the smallest gyration radius, namely the tertiary 1-McyOH (1-methylcyclohexanol) and the non-substituted CyOH. Both follow also a linear correlation, but one that is shifted parallel by approximately 20 J mol<sup>-1</sup> K<sup>-1</sup> to lower adsorption entropies than the correlation of the other alcohols.

These parallel lines can be interpreted in two ways. One of the possibilities is that for a given heat of adsorption the configurational space of the molecules substituted not at the carbon atom also bearing the OH group allow more orientations in the pores, i.e., a larger configurational entropy of the alcohol in the solvated state (Figure 2.1, arrow A). Hence, they lose less entropy in the sorption process. It could also not be excluded that the solvation entropy of these molecules is significantly lower than the solvation entropy of cyclohexanol and 1-McyOH. The other equivalent interpretation is that despite a higher heat of adsorption for the 2-substituted cyclohexanol molecules (compared to 1-McyOH) their gain in entropy of de-solvation upon adsorption compensates the expected increase in entropy reduction upon a stronger interaction in the adsorbed state (Figure 2.1, arrow B).

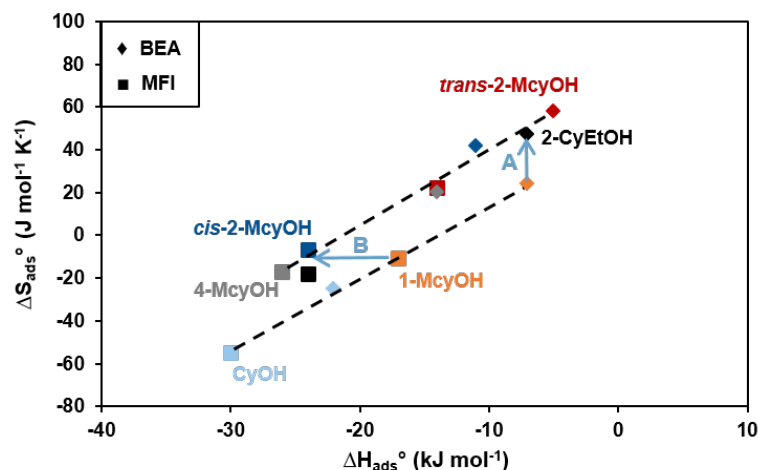


**Figure 2.1.** Correlation of  $\Delta S_{ads}^\circ$  and  $\Delta H_{ads}^\circ$  for cyclohexanol and substituted cyclohexanols from uptake measurements in aqueous phase on MFI and BEA zeolites.

More information on the solvation of such molecules would be needed in order to differentiate between the two possibilities and experiments in this direction are under way.

### 2.3.3 Catalyzed dehydration

Brønsted acid sites (BAS, hydrated hydronium ions) act as the active sites, while Lewis acid sites (LAS) hardly contribute to dehydration under these reaction conditions.<sup>31</sup> In all cases, (except for the 2-McyOH isomers in MFI-45 due to their higher steric hinderance), the concentration of the hydronium ions was significantly lower than the concentration of alcohol molecules in the pores, ensuring their sufficient utilization. A reaction order of one in the alcohol was determined for  $H_3PO_4$ -catalyzed dehydration, in contrast to a reaction order of zero for all zeolite-catalyzed reactions (see 2.7 Supporting information, Figure S2.1-S2.11, Table S2.1-S2.11). The activation entropies and enthalpies are compiled in detail in the supporting information (Figure S2.22 – S2.41, Table S2.22 – S2.36).

While the reaction order was one for  $H_3PO_4$  and zero for the zeolite catalysts, the activation parameters (Table 2.3) can be compared, because at least the enthalpy of interaction between hydronium ions and the alcohol is small.<sup>30</sup>

Table 2.3 compiles the rates and activation parameters for all alcohols converted in aqueous phase with  $H_3PO_4$ , as well as zeolites BEA and MFI added as acid catalysts. In agreement with earlier studies, the rates normalized to the concentration of hydronium ions (turnover frequency, TOF) were always the highest for the zeolite catalyzed reactions. However, the TOFs did not monotonically increase with decreasing pore diameter as reported for cyclohexanol, but rather showed an apparent random variation with MFI or BEA.

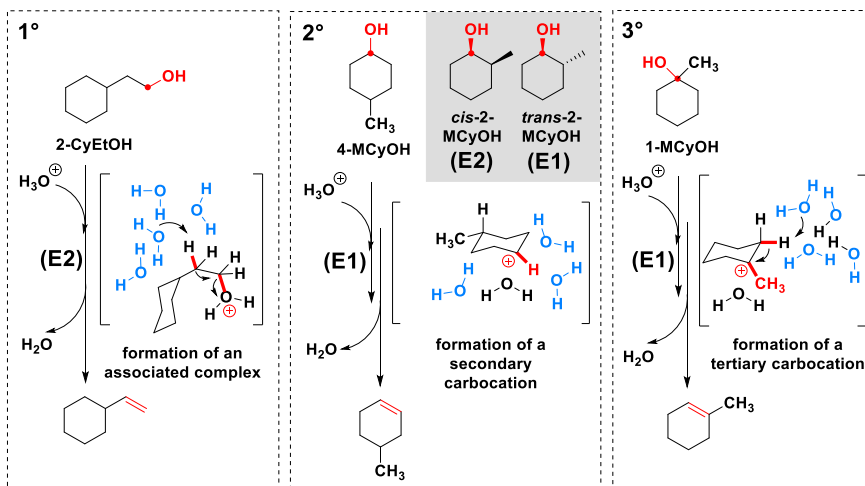
Chapter 2: Towards understanding and predicting the hydronium ion catalyzed dehydration of cyclic-primary, secondary and tertiary alcohols

**Table 2.3.** Activation parameters and TOFs categorized by reactant catalyzed by MFI, BEA and H<sub>3</sub>PO<sub>4</sub>.

Reactant	Catalyst	$\Delta H^{\ddagger}$ (kJ mol <sup>-1</sup> )	$\Delta S^{\ddagger}$ (J mol <sup>-1</sup> K <sup>-1</sup> )	$\Delta G^{\ddagger}(180^{\circ}\text{C})$ (kJ mol <sup>-1</sup> )	TOF (180°C) (s <sup>-1</sup> ) <sup>a</sup>	
1°-alcohol	2-CyEtOH <sup>b</sup>	H <sub>3</sub> PO <sub>4</sub>	159 (±3)	22 (±7)	149 (±1)	1.4 (±1)×10 <sup>-5c,d</sup>
		BEA	127 (±3)	-22 (±6)	137 (±1)	1.5 (±0.1)×10 <sup>-2d</sup>
		MFI	127 (±3)	-10 (±6)	132 (±1)	7.4 (±0.2)×10 <sup>-3d</sup>
2°-alcohol	4-McyOH <sup>e</sup>	H <sub>3</sub> PO <sub>4</sub>	151 (±2)	53 (±4)	127 (±1)	4.7 (±0.2)×10 <sup>-3</sup>
		BEA	164 (±3)	94 (±7)	121 (±1)	9.8 (±0.4)×10 <sup>-2</sup>
		MFI <sup>f</sup>	142 (±3)	53 (±6)	118 (±1)	2.2 (±0.1)×10 <sup>-1</sup>
	<i>trans</i> -2-McyOH <sup>g</sup>	H <sub>3</sub> PO <sub>4</sub>	163 (±3)	69 (±6)	132 (±1)	2.5 (±0.9)×10 <sup>-4</sup>
		BEA	178 (±5)	116 (±11)	125 (±1)	3.3 (±0.3)×10 <sup>-2</sup>
		MFI <sup>f,h</sup>	140 (±2)	41 (±2)	121 (±1)	3.2 (±0.1)×10 <sup>-2</sup>
2°-alcohol	<i>cis</i> -2-McyOH <sup>i</sup>	H <sub>3</sub> PO <sub>4</sub>	129 (±3)	18 (±7)	121 (±1)	2.3 (±0.2)×10 <sup>-2</sup>
		BEA	137 (±3)	57 (±6)	111 (±1)	1.4 (±0.1)×10 <sup>0</sup>
		MFI <sup>f</sup>	112 (±3)	-8 (±7)	116 (±1)	4.7 (±0.2)×10 <sup>-1</sup>
	CyOH <sup>j</sup>	H <sub>3</sub> PO <sub>4</sub>	157 (±3)	73 (±7)	124 (±1)	9.7 (±1)×10 <sup>-3c</sup>
		BEA	159 (±4)	87 (±9)	120 (±1)	1.5 (±1)×10 <sup>-1c</sup>
		MFI	140 (±5)	62 (±10)	112 (±1)	1.2 (±1)×10 <sup>0c</sup>
3°-alcohol	1-McyOH <sup>k</sup>	H <sub>3</sub> PO <sub>4</sub>	167 (±5)	167 (±12)	91 (±1)	2.6 (±1)×10 <sup>1c,l</sup>
		BEA	128 (±3)	76 (±7)	94 (±1)	1.6 (±1)×10 <sup>2c,l</sup>
		MFI	113 (±2)	30 (±5)	99 (±1)	3.4 (±1)×10 <sup>1c,l</sup>

<sup>a</sup>First order regime: H<sub>3</sub>PO<sub>4</sub>; zero order regime: BEA, MFI. <sup>b</sup>Reaction conditions: 190-230°C/H<sub>3</sub>PO<sub>4</sub>, 170-210°C/BEA, 160-200°C/MFI; 0.2M alcohol/H<sub>3</sub>PO<sub>4</sub>, MFI, 0.1M alcohol/BEA, 0.7M H<sub>3</sub>PO<sub>4</sub>, 0.2g BEA, 0.1g MFI, 100 mL H<sub>2</sub>O, 50 bar. <sup>c</sup>Extrapolated from Eyring equation. <sup>d</sup>Measured TOF (s<sup>-1</sup>) at 190°C: 3.7 (±0.2)×10<sup>-5</sup>/H<sub>3</sub>PO<sub>4</sub>, 2.8 (±0.2)×10<sup>-3</sup>/BEA, 1.4 (±0.1)×10<sup>-2</sup>/MFI. <sup>e</sup>Reaction conditions: 150-200°C/H<sub>3</sub>PO<sub>4</sub>, 160-200°C/BEA, 140-190°C/MFI; 0.2M alcohol/H<sub>3</sub>PO<sub>4</sub>, 0.5M alcohol/MFI, BEA, 2.9mM H<sub>3</sub>PO<sub>4</sub>, 0.15g BEA, 0.05g MFI, 100 mL H<sub>2</sub>O, 50 bar. <sup>f</sup>The original data were presented previously in reference 8 and 10. <sup>g</sup>Reaction conditions: 170-210°C/H<sub>3</sub>PO<sub>4</sub>, 160-200°C/BEA, 120-160°C/MFI; 44mM alcohol/H<sub>3</sub>PO<sub>4</sub>, BEA, MFI, 0.05M H<sub>3</sub>PO<sub>4</sub>, 0.1g BEA, 0.05g MFI, 100 mL H<sub>2</sub>O, 50 bar. <sup>h</sup>Additional data were measured at 180°C and 190°C. <sup>i</sup>Reaction conditions: 150-190°C/H<sub>3</sub>PO<sub>4</sub>, 150-190°C/BEA, 140-190°C/MFI; 0.2M alcohol/H<sub>3</sub>PO<sub>4</sub>, 0.5M alcohol/ BEA, MFI, 2.9mM H<sub>3</sub>PO<sub>4</sub>, 0.05g BEA, 0.05g MFI, 100 mL H<sub>2</sub>O, 50 bar. Since the *cis* isomer dominates the kinetic parameters,<sup>9</sup> the mixture of *cis/trans* 2-McyOH was used. <sup>j</sup>The original data were presented previously in reference 9. <sup>k</sup>Reaction conditions: 80-130°C/H<sub>3</sub>PO<sub>4</sub>, 90-130°C/BEA, 80-130°C/MFI; 0.1M alcohol/H<sub>3</sub>PO<sub>4</sub>, 0.5M alcohol/ BEA, MFI, 5.12mM H<sub>3</sub>PO<sub>4</sub>, 0.05g BEA, 0.05g MFI, 100 mL H<sub>2</sub>O, 50 bar. <sup>l</sup>Measured TOF (s<sup>-1</sup>) at 90°C: 4.0 (±0.2)×10<sup>-4</sup>/H<sub>3</sub>PO<sub>4</sub>, 3.0 (±0.1)×10<sup>-2</sup>/BEA, 1.7 (±0.1)×10<sup>-2</sup>/MFI.

Primary alcohols react *via* a concerted mechanism (E2), avoiding the energetically demanding formation of primary carbocations (Scheme 2.1), the dehydration of the tertiary alcohol is concluded to proceed stepwise (E1 mechanism, Scheme 2.1).

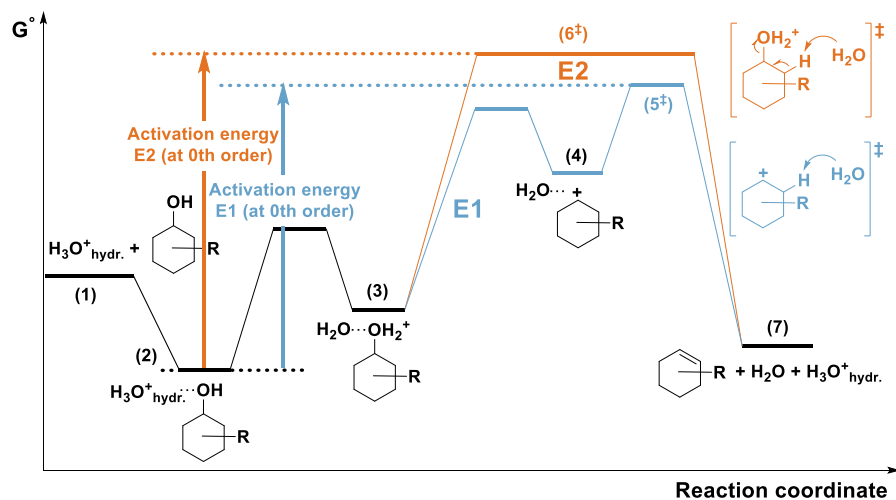


**Scheme 2.1.** Dehydration of cyclic alcohols *via* monomolecular (E1) and concerted way (E2).

The olefin formed by 2-CyEtOH dehydration is vinyl cyclohexane, and that formed from 1-McyOH is 1-methyl-1-cyclohexene (Scheme 2.1). The reactions were highly selective with negligible formation of side products, i.e., the total concentration of all double-bond-shifted and ring-annulated alkenes was lower than 1%. Dehydration of secondary cyclic alcohols is more complex (Scheme 2.1) as exemplified in an earlier study using MFI and  $\text{H}_3\text{PO}_4$ .<sup>28</sup> Dehydration of cyclohexanol, *trans*-2-methylcyclohexanol, as well as *cis*- and *trans*-isomers of 4-alkylcyclohexanols proceeded predominantly *via* an E1-type path, whereas dehydration of *cis*-2-methylcyclohexanol occurred mainly *via* an E2-type path.<sup>28</sup>

Scheme 2.2 shows the illustration of energy profiles for the E1 and E2 mechanisms. Both proceed stepwise via association with  $\text{H}_3\text{O}^+_{\text{hydr}}$ . (Step 2) and protonation of OH group (Step 3). While afterwards, it undergoes either C-O cleavage to form carbenium ion (Step 4) followed by deprotonation of cyclohexyl carbenium ion (Step 5) for E1 mechanism, or concerted C-O and C-H bond cleavage (Step 6) for E2 mechanism. The activation energy measured at reaction order of zero is the energy difference between ground state of adsorbed cyclohexanol associated with  $\text{H}_3\text{O}^+_{\text{hydr}}$ . ( $\text{H}_3\text{O}^+_{\text{hydr}} \cdots \text{C}_6\text{H}_{11}\text{OH}$ ) and transition state of the C-H bond cleavage in carbenium ion (Step 5) for E1 or concerted C-O and C-H bond cleavage (Step 6) for E2. For the reactions in aqueous phase with  $\text{H}_3\text{PO}_4$  the additional interaction with the hydronium ion has to be also considered. We would like to emphasize at this point that the activation parameters encompass all these steps until the rate determining formation of the alkene.

The detailed variation of rates and the underlying activation parameters do not follow a strict dependence on the pore diameter or the bulkiness of the molecule. In general, we use high transition entropies as indication for a late transition state and the prevalence of an E1 mechanism.



**Scheme 2.2.** Schematic illustration of energy profiles in the dehydration of cyclic alcohols via E1 (blue) and E2 (orange) pathways. (1) Reactant alcohol and  $\text{H}_3\text{O}^+_{\text{hydr.}}$ ; (2) alcohol associated with  $\text{H}_3\text{O}^+_{\text{hydr.}}$ ; (3) protonated alcohol; (4) carbenium ion in E1 pathway; (5 $^\ddagger$ ) transition state in E1 pathway; (6 $^\ddagger$ ) transition state in E2 pathway; (7) product alkene, water and  $\text{H}_3\text{O}^+_{\text{hydr.}}$ . The “ $\text{H}_2\text{O}\cdots$ ” represents the interactions with solvent water.

The 4-methyl substituent represents the least obtrusive substitution of cyclohexanol. Compared to 2-CyEtOH, the standard transition entropies, were markedly higher (Table 2.3). The high standard transition entropies of 4-McyOH point to a very late transition state, suggesting that elimination follows an E1 mechanism. The substitution at the 2 position in the cyclohexane ring has a significant importance. With increasing proximity to the leaving group, steric parameters markedly influence the reaction mechanism. In the case of *cis*-2- and *trans*-2-McyOH, the isomers followed two different reaction mechanisms, i.e., *cis*-2-McyOH the E2 and *trans*-2-McyOH the E1 mechanism. This difference has been discussed and explained by the fact that the antiperiplanar orientation of the  $\sigma\text{C-H}$  and  $\sigma^*\text{C-O}$  bond in the *cis* isomer forces the reaction to proceed via the E2 mechanism, avoiding the energetically demanding formation of the carbenium ion.<sup>28</sup> Indeed, the rates measured for the *cis* isomer were one order of magnitude higher than that for the *trans* isomer on BEA zeolite (Table 2.3, Figure S2.39 and S2.40).

Similar to 4-McyOH, the highest activation energies for the *trans*-2-McyOH dehydration were found with zeolite BEA. However, in this case, the significant gain in entropy (75  $\text{J mol}^{-1} \text{K}^{-1}$  difference between MFI and BEA) offsets the higher activation enthalpy resulting in comparable activities of the two zeolites. The most favorable activation enthalpy of the *cis*-2-McyOH dehydration was found for MFI. However, a significantly higher standard transition entropy with zeolite BEA more than offsets the higher enthalpic barrier, resulting in the highest rates and overall in an entropically driven reaction.

Also, for 1-McyOH, the highest dehydration rates (Table 2.3, Figure S2.41) were observed with zeolite BEA ( $3.0 \times 10^{-2} \text{ s}^{-1}$ ), despite of its ca.  $15 \text{ kJ mol}^{-1}$  higher activation enthalpy than other catalysts. In the temperature range studied, the less favorable enthalpic stabilization within the confined environment was frequently overcompensated by entropic gains in the larger reaction channels, which has not been observed in other cases in which the close environments influence the reaction rates.

The standard transition enthalpies ( $\Delta H^{\ddagger}$ ) and entropies ( $\Delta S^{\ddagger}$ ) for all alcohols are compared in Figure 2.2. Irrespective of the underlying elimination mechanism, the position and chirality of the substitution and the steric environment of the active hydrated hydronium ions, each group of the alcohols showed a characteristic linear correlation between enthalpy and entropy. Thus, we conclude that the mechanistic pathway is not the predominant factor that controls the standard free energy landscape, i.e., the stabilization of the cation neither favors nor disfavors a particular transition enthalpy or entropy.

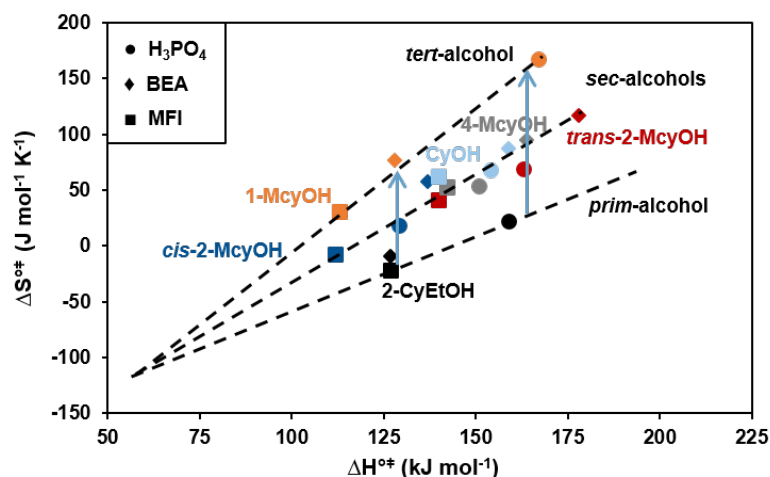


**Figure 2.2.** Correlation of  $\Delta S^{\ddagger}$  and  $\Delta H^{\ddagger}$  for primary, secondary and tertiary cyclic alcohols of the studied acid catalysts.

Analyzing the trends for the alcohols with respect to the compensation between entropy and enthalpy one notes that the rate of reaction increases sympathetically with the larger transition entropy, for a constant transition enthalpy (Figure 2.2 and Table 2.3, see arrows). The difficulty in this analysis comes, however, from the fact that this transition entropy is referenced either to the unbound solvated state or to the bound adsorbed state in case of zeolites. Thus, it is not solely the transition enthalpy and entropy of the rate determining step, but the sum of the activation parameters of all steps, i.e., also of the equilibrated steps until the highest position of the standard free energy along the reaction path.

In order to estimate the impact of the reaction path, we calculate the configurational entropy of the studied molecules in the ground state and compare it to the configurational entropy (which we hypothesize gives the largest contribution to the transition entropy) in the environment of both zeolites (Table 2.4, Table S2.37).<sup>35-37</sup>

**Table 2.4.** Calculated configurational entropy of the substituted alcohols in zeolite MFI and BEA.

Zeolite	Alcohol	$S_{\text{Ground State}}^{\circ}$ ( $\text{J mol}^{-1} \text{K}^{-1}$ ) <sup>a</sup>	$S_{\text{Transition State}}^{\circ}$ ( $\text{J mol}^{-1} \text{K}^{-1}$ ) <sup>a</sup>	$\Delta S^{\circ}$ ( $\text{J mol}^{-1} \text{K}^{-1}$ ) <sup>b</sup>
MFI-45	2-CyEtOH	13.6	7.1	-6.5
BEA-83		29.0	28.3	-0.7
MFI-45	<i>cis</i> -2-McyOH	9.3	5.3	-4.1
BEA-83		28.2	27.4	-0.8
MFI-45	4-McyOH	14.0	42.4	28.4
BEA-83		27.5	149.3	121.8
MFI-45	<i>trans</i> -2-McyOH	10.3	28.5	18.1
BEA-83		28.2	156.1	127.9
MFI-45	1-McyOH	12.9	35.7	22.8
BEA-83		28.8	161.9	133.1

<sup>a</sup> $\Delta S^{\circ}$  per mole BAS, calculated from  $S^{\circ} = -n R (x_1 \ln x_1 + x_2 \ln x_2 + \dots + x_n \ln x_n)$ <sup>35</sup> ( $x_i$ : molar fraction of species  $i$ ), see further steps in 2.7 supporting information, Table S2.37. <sup>b</sup> $\Delta S^{\circ} = S_{\text{Transition State}}^{\circ} - S_{\text{Ground State}}^{\circ}$ .

The highest difference in entropy is found with substrates following the E1 mechanism, because the separation of charge in this pathway gives the largest reaction volume and, hence, the largest configurational space. It could also be argued that the release/formation of a H<sub>2</sub>O molecule from C-O cleavage contributes to the increase of configurational entropy by increasing the complexity of the mixtures in the zeolite channel.

The lowest entropy difference is found for the alcohols following the E2 pathway, as the concerted mechanism in which H<sup>+</sup> and OH<sup>-</sup> are eliminated nearly simultaneously leads to the smallest reaction volume and in consequence the smallest configurational entropy. Thus, for a given standard transition enthalpy, the larger the total inscribed volume along the reaction path (total transition volume), the larger the transition entropy and, therefore, the larger the reaction rate.<sup>38-43</sup>

Within a group of alcohols, the dependence is subtler. Then, the overall transition enthalpy appears to be determined by the size of the molecule and the ability to fit into the zeolite pore. For a given molecule size, the weaker interaction in the sorbed state (i.e., the higher standard chemical potential) the lower the transition enthalpy (see e.g., the difference between CyOH and 1-McyOH, Figures 2.1 and 2.2 and the difference between BEA and MFI for all secondary alcohols).

The compensation effect shown in Figure 2.2 can, however, be also interpreted as lines of shared isokinetic temperatures. Such isokinetic temperatures have been interpreted as common (selective) energy transfers (heat bath theory).<sup>44-47</sup> In such a model, the catalyst is seen as the heat bath, which transfers energy to the reactant.<sup>44-47</sup> Reactant ( $\nu$ ) and catalyst ( $\omega$ ) oscillate with a specific vibrational frequency; the better these frequencies resonate, the higher the resulting rate enhancement will be.<sup>44-47</sup> A linear relationship of  $\ln A$  (the Arrhenius pre-exponential factor) and  $E_a$  (see 2.7 supporting information, Figure S2.43) or  $\Delta S^{\ddagger}$  and  $\Delta H^{\ddagger}$  (Figure 2.2) correspond to the fact that all dependencies of the logarithm of the rate constant and the inverse temperature

intersect at one common point, the so called isokinetic temperature, from which the vibrational frequency can be derived.<sup>44-47</sup> This temperature is corresponding to the slopes of the  $\Delta H^{\ddagger}$  and  $\Delta S^{\ddagger}$  correlations and are compiled in Table 2.5. 2-CyEtOH shows the highest isokinetic temperature (784K), followed by the secondary alcohols (510K) and then 1-McyOH (399K). Assuming full resonance of the system ( $\nu = \omega$ ), these correspond to vibrational frequencies ( $\nu_{FR}$ ) of 1089  $\text{cm}^{-1}$ , 710  $\text{cm}^{-1}$  and 555  $\text{cm}^{-1}$ , respectively.

**Table 2.5.** Approach of the selective energy transfer model to the individual alcohol classes.

Substrate	$T_{iso}$ (K) <sup>a</sup>	$\nu_{FR}$ ( $\text{cm}^{-1}$ ) <sup>b</sup>	$\omega$ ( $\text{cm}^{-1}$ ) <sup>c</sup>	$\nu$ ( $\text{cm}^{-1}$ ) <sup>c</sup>	$\nu/\omega$
Primary alcohol	784	1089	439	940	2.14
Secondary alcohols	510	710	405	672	1.66
Tertiary alcohol	399	555	412	556	1.35

<sup>a</sup>Resulting from the slope of the linear correlation of  $\Delta H^{\ddagger}$  vs.  $\Delta S^{\ddagger}$ . <sup>b</sup>Assuming full resonance between  $\nu$  and  $\omega$ , calculated from  $T_{iso} = Nhc\nu/2R$ .<sup>44-47</sup> <sup>c</sup>Assuming that  $\nu$  and  $\omega$  are not at full resonance, derived from  $T_{iso} = Nhc\nu/2R (\nu^2 - \omega^2) \omega^{-1} \{ \pm\pi/2 - \arctg [0.5 \nu \omega (\nu^2 - \omega^2)^{-1}] \}^{-1}$ ,<sup>44-47</sup> see further steps in 2.7 supporting information, Table S2.38 and S2.39.

Considering that the frequency of the oscillator of the catalysts might not be in full resonance with the vibration frequencies of the reactants, a more complex approach needs to be applied (Table S2.38).<sup>44-47</sup> In Table 2.5, the determined frequencies are summarized. All catalytic frequencies show similar values, which is in agreement to our studied reactions, as they were all catalyzed by hydronium-ions as the active species, even though on different catalysts. The ratios of  $\nu$  to  $\omega$  indicate that the tertiary alcohol is the closest to full resonance (ratio of 1), while the primary alcohol has the highest deviation. This in turn results in the highest rate enhancement for 1-McyOH and the least enhancement for 2-CyEtOH, which supports in good agreement with the experimental data.

The compensation of the transition entropy and enthalpy is correlated with the TOF, i.e., it increases linearly with the logarithm of the TOF with a slope that is the higher the lower the transition entropy is (Figure 2.3). Remarkably, all logarithmic rates lie on one plane and the trends for each of the groups of alcohols intersect also in one point, a turnover frequency, which is at least an order of magnitude higher than the highest value measure here.

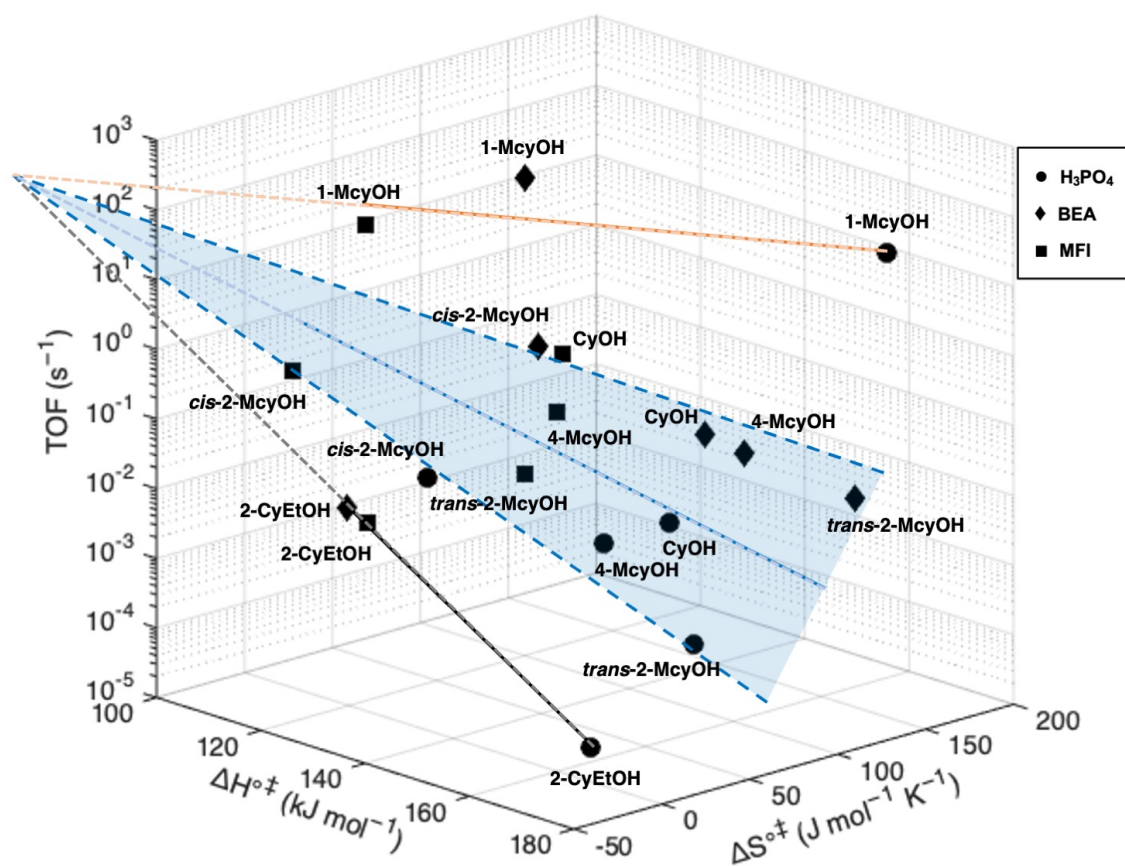


**Figure 2.3.** Reaction rates as a function of the correlation between transition enthalpy and entropy at 180°C; circles correspond to catalysis by hydronium ions in water (H<sub>3</sub>PO<sub>4</sub>), diamonds to catalysis in zeolite BEA and squares to catalysis in MFI at 180°C.

## 2.4 Conclusions

We have shown here that the apparent complexity of the hydronium-ion-catalyzed elimination of water of substituted cyclohexanol in aqueous phase on two zeolites with different pore size and aqueous phosphoric acid can be understood *via* the dependence of transition enthalpies and entropies of the reaction. This dependence is concluded to be primarily characteristic of the position of the OH group and the position of the substituent only subtly influences the elementary steps of the reaction. These correlations allow the prediction of catalytic reactivities for alcohols by defining the trends of catalyzed rates independent of the zeolite and the specific substitution of the alcohol.

The adsorption of the alcohols shows that the substitution leads to a weakening of the interaction with the pores, which is attributed to a less ideal fit. The bulkier molecules tend to have a lower heat of adsorption, but also lose less entropy. It is remarkable that the molecules with the smallest radius of gyration lose more entropy on adsorption. The reasons for such a behaviour lie in the differences between the solvation in the liquid phase and the interactions in the pores. Substituted molecules are hypothesized to have a lower solvation enthalpy in the solvent and, therefore, lose less or gain entropy upon

adsorption. However, substantially more measurements are needed to probe this hypothesis.

The catalytic activity for dehydration depends, at large, directly on the transition enthalpy. This dependence is the stronger the lower the transition entropy is. It is independent whether dehydration occurs concerted or stepwise, i.e., whether it follows an E1 or E2 mechanism. It is also independent of the reaction order and whether it occurs within the zeolite pores or in the plain aqueous phase. The rates are dependent on the location of the alcohol OH group, with tertiary alcohols showing the highest transition entropy and primary alcohols the lowest.

Such experimentally derived dependencies offer the possibility to predict rates in a way hitherto not possible to our knowledge. The dependencies offer also benchmarks to calibrate theory at the complex liquid solid interfaces.

## **2.5 Author contributions**

L.M. and P.H.H. contributed equally to this work. P.H.H., E.B. and J.A.L. conceived the initial idea. L.M. conducted synthesis, adsorption measurements, kinetic experiments and calculations. P.H.H. carried out synthesis, kinetic experiments and kinetic calculations. The manuscript was written through contributions of all authors. All authors have given approval to the final version of the manuscript. The authors declare no competing financial interest.

## **Acknowledgements**

L.M., P.H.H., and J.A.L. were supported by the U.S. Department of Energy (DOE), Office of Science, Office of Basic Energy Sciences (BES), Division of Chemical Sciences, Geosciences and Biosciences (Transdisciplinary Approaches to Realize Novel Catalytic Pathways to Energy Carriers, FWP 47319). We thank Prof. Gary L. Haller (Yale University), for fruitful and extensive discussions.

## 2.6 References

- (1) Sastre, G.; Corma, A. The confinement effect in zeolites. *Journal of Molecular Catalysis A: Chemical* **2009**, *305* (1), 3.
- (2) Margarit, V. J.; Osman, M.; Al-Khattaf, S.; Martínez, C.; Boronat, M.; Corma, A. Control of the Reaction Mechanism of Alkylaromatics Transalkylation by Means of Molecular Confinement Effects Associated to Zeolite Channel Architecture. *ACS Catalysis* **2019**, *9* (7), 5935.
- (3) Wu, S.-M.; Yang, X.-Y.; Janiak, C. Confinement Effects in Zeolite-Confined Noble Metals. *Angewandte Chemie International Edition* **2019**, *58* (36), 12340.
- (4) Lesthaeghe, D.; Van Speybroeck, V.; Waroquier, M. Theoretical evaluation of zeolite confinement effects on the reactivity of bulky intermediates. *Physical Chemistry Chemical Physics* **2009**, *11* (26), 5222.
- (5) Yumura, T.; Takeuchi, M.; Kobayashi, H.; Kuroda, Y. Effects of ZSM-5 zeolite confinement on reaction intermediates during dioxygen activation by enclosed dicopper cations. *Inorganic Chemistry* **2009**, *48* (2), 508.
- (6) Eder, F.; Lercher, J. A. On the Role of the Pore Size and Tortuosity for Sorption of Alkanes in Molecular Sieves. *The Journal of Physical Chemistry B* **1997**, *101* (8), 1273.
- (7) Eder, F.; Stockenhuber, M.; Lercher, J. A. Brønsted Acid Site and Pore Controlled Siting of Alkane Sorption in Acidic Molecular Sieves. *The Journal of Physical Chemistry B* **1997**, *101* (27), 5414.
- (8) Eder, F.; Lercher, J. A. Alkane sorption in molecular sieves: The contribution of ordering, intermolecular interactions, and sorption on Brønsted acid sites. *Zeolites* **1997**, *18* (1), 75.
- (9) Chiang, H.; Bhan, A. Catalytic consequences of hydroxyl group location on the rate and mechanism of parallel dehydration reactions of ethanol over acidic zeolites. *Journal of Catalysis* **2010**, *271* (2), 251.
- (10) Kang, M.; DeWilde, J. F.; Bhan, A. Kinetics and Mechanism of Alcohol Dehydration on  $\gamma$ -Al<sub>2</sub>O<sub>3</sub>: Effects of Carbon Chain Length and Substitution. *ACS Catalysis* **2015**, *5* (2), 602.
- (11) Zhi, Y.; Shi, H.; Mu, L.; Liu, Y.; Mei, D.; Camaioni, D. M.; Lercher, J. A. Dehydration Pathways of 1-Propanol on HZSM-5 in the Presence and Absence of Water. *Journal of the American Chemical Society* **2015**, *137* (50), 15781.
- (12) Vjunov, A.; Hu, M. Y.; Feng, J.; Camaioni, D. M.; Mei, D.; Hu, J. Z.; Zhao, C.; Lercher, J. A. Following Solid-Acid-Catalyzed Reactions by MAS NMR Spectroscopy in Liquid Phase—Zeolite-Catalyzed Conversion of Cyclohexanol in Water. *Angewandte Chemie International Edition* **2014**, *53* (2), 479.
- (13) Makarova, M. A.; Williams, C.; Romannikov, V. N.; Zamaraev, K. I.; Thomas, J. M. Influence of pore confinement on the catalytic dehydration of isobutyl alcohol on H-ZSM-5. *Journal of the Chemical Society, Faraday Transactions* **1990**, *86* (3), 581.
- (14) Makarova, M. A.; Paukshtis, E. A.; Thomas, J. M.; Williams, C.; Zamaraev, K. I. Dehydration of n-Butanol on Zeolite H-ZSM-5 and Amorphous Aluminosilicate: Detailed Mechanistic Study and the Effect of Pore Confinement. *Journal of Catalysis* **1994**, *149* (1), 36.
- (15) Jones, A. J.; Zones, S. I.; Iglesia, E. Implications of Transition State Confinement within Small Voids for Acid Catalysis. *The Journal of Physical Chemistry C* **2014**, *118* (31), 17787.
- (16) Simonetti, D. A.; Carr, R. T.; Iglesia, E. Acid strength and solvation effects on methylation, hydride transfer, and isomerization rates during catalytic homologation of C1 species. *Journal of Catalysis* **2012**, *285* (1), 19.
- (17) Macht, J.; Carr, R. T.; Iglesia, E. Consequences of Acid Strength for Isomerization and Elimination Catalysis on Solid Acids. *Journal of the American Chemical Society* **2009**, *131* (18), 6554.
- (18) Deshlahra, P.; Carr, R. T.; Iglesia, E. Ionic and Covalent Stabilization of Intermediates and Transition States in Catalysis by Solid Acids. *Journal of the American Chemical Society* **2014**, *136* (43), 15229.

- (19) Gounder, R.; Iglesia, E. The catalytic diversity of zeolites: confinement and solvation effects within voids of molecular dimensions. *Chemical Communications* **2013**, 49 (34), 3491.
- (20) Jones, A. J.; Carr, R. T.; Zones, S. I.; Iglesia, E. Acid strength and solvation in catalysis by MFI zeolites and effects of the identity, concentration and location of framework heteroatoms. *Journal of Catalysis* **2014**, 312, 58.
- (21) Deshlahra, P.; Carr, R. T.; Chai, S.-H.; Iglesia, E. Mechanistic Details and Reactivity Descriptors in Oxidation and Acid Catalysis of Methanol. *ACS Catalysis* **2015**, 5 (2), 666.
- (22) Eckstein, S.; Hintermeier, P. H.; Zhao, R.; Baráth, E.; Shi, H.; Liu, Y.; Lercher, J. A. Influence of Hydronium Ions in Zeolites on Sorption. *Angewandte Chemie International Edition* **2019**, 58 (11), 3450.
- (23) Markovitch, O.; Agmon, N. Structure and Energetics of the Hydronium Hydration Shells. *The Journal of Physical Chemistry A* **2007**, 111 (12), 2253.
- (24) Eigen, M. Proton Transfer, Acid-Base Catalysis, and Enzymatic Hydrolysis. Part I: ELEMENTARY PROCESSES. *Angewandte Chemie International Edition in English* **1964**, 3 (1), 1.
- (25) Termath, V.; Haase, F.; Sauer, J.; Hutter, J.; Parrinello, M. Understanding the Nature of Water Bound to Solid Acid Surfaces. Ab Initio Simulation on HSAPO-34. *Journal of the American Chemical Society* **1998**, 120 (33), 8512.
- (26) Limtrakul, J.; Chuichay, P.; Nokbin, S. Effect of high coverages on proton transfer in the zeolite/water system. *Journal of Molecular Structure* **2001**, 560 (1), 169.
- (27) Smith, L.; Cheetham, A. K.; Morris, R. E.; Marchese, L.; Thomas, J. M.; Wright, P. A.; Chen, J. On the Nature of Water Bound to a Solid Acid Catalyst. *Science* **1996**, 271 (5250), 799.
- (28) Hintermeier, P. H.; Eckstein, S.; Mei, D.; Olarte, M. V.; Camaioni, D. M.; Baráth, E.; Lercher, J. A. Hydronium-Ion-Catalyzed Elimination Pathways of Substituted Cyclohexanols in Zeolite H-ZSM5. *ACS Catalysis* **2017**, 7 (11), 7822.
- (29) Liu, Y.; Baráth, E.; Shi, H.; Hu, J.; Camaioni, D. M.; Lercher, J. A. Solvent-determined mechanistic pathways in zeolite-H-BEA-catalysed phenol alkylation. *Nature Catalysis* **2018**, 1 (2), 141.
- (30) Liu, Y.; Vjunov, A.; Shi, H.; Eckstein, S.; Camaioni, D. M.; Mei, D.; Baráth, E.; Lercher, J. A. Enhancing the catalytic activity of hydronium ions through constrained environments. *Nature Communications* **2017**, 8 (1), 14113.
- (31) Shi, H.; Eckstein, S.; Vjunov, A.; Camaioni, D. M.; Lercher, J. A. Tailoring nanoscopic confines to maximize catalytic activity of hydronium ions. *Nature Communications* **2017**, 8 (1), 15442.
- (32) Proding, S.; Derewinski, M. A.; Vjunov, A.; Burton, S. D.; Arslan, I.; Lercher, J. A. Improving Stability of Zeolites in Aqueous Phase via Selective Removal of Structural Defects. *Journal of the American Chemical Society* **2016**, 138 (13), 4408.
- (33) Vjunov, A.; Derewinski, M. A.; Fulton, J. L.; Camaioni, D. M.; Lercher, J. A. Impact of Zeolite Aging in Hot Liquid Water on Activity for Acid-Catalyzed Dehydration of Alcohols. *Journal of the American Chemical Society* **2015**, 137 (32), 10374.
- (34) Lutz, W.; Toufar, H.; Kurzhals, R.; Suckow, M. Investigation and Modeling of the Hydrothermal Stability of Technically Relevant Zeolites. *Adsorption* **2005**, 11 (3), 405.
- (35) Karplus, M.; Kushick, J. N. Method for estimating the configurational entropy of macromolecules. *Macromolecules* **1981**, 14 (2), 325.
- (36) Leffler, J. E. Parameters for the description of transition states. *Science* **1953**, 117 (3039), 340.
- (37) Hammond, G. S. A correlation of reaction rates. *Journal of the American Chemical Society* **1955**, 77 (2), 334.
- (38) Muller, P. Glossary of terms used in physical organic chemistry (IUPAC Recommendations 1994). *Pure and Applied Chemistry* **1994**, 66 (5), 1077.
- (39) Eyring, H. The Activated Complex in Chemical Reactions. *The Journal of Chemical Physics* **1935**, 3 (2), 107.
-

- (40) Evans, M. G.; Polanyi, M. Some applications of the transition state method to the calculation of reaction velocities, especially in solution. *Transactions of the Faraday Society* **1935**, *31*, 875.
- (41) Chen, B.; Hoffmann, R.; Cammi, R. The Effect of Pressure on Organic Reactions in Fluids—a New Theoretical Perspective. *Angewandte Chemie International Edition* **2017**, *56* (37), 11126.
- (42) Drljaca, A.; Hubbard, C. D.; van Eldik, R.; Asano, T.; Basilevsky, M. V.; le Noble, W. J. Activation and Reaction Volumes in Solution. 3. *Chem Rev* **1998**, *98* (6), 2167.
- (43) Van Eldik, R.; Asano, T.; Le Noble, W. Activation and reaction volumes in solution. 2. *Chemical Reviews* **1989**, *89* (3), 549.
- (44) Bratlie, K. M.; Li, Y.; Larsson, R.; Somorjai, G. A. Compensation Effect of Benzene Hydrogenation on Pt(111) and Pt(100) Analyzed by the Selective Energy Transfer Model. *Catalysis Letters* **2008**, *121* (3), 173.
- (45) Larsson, R. Catalysis as a resonance effect, V. Factors that determine the isokinetic temperature in catalytic reactions. *Reaction Kinetics and Catalysis Letters* **1999**, *68* (1), 115.
- (46) Larsson, R. On the compensation effect and selective oxidation reactions. *Catalysis Today* **1987**, *1* (1), 93.
- (47) Galwey, A. K. In *Advances in Catalysis*; Eley, D. D.; Pines, H.; Weisz, P. B., Eds.; Academic Press, **1977**; Vol. 26, 247.

## 2.7 Supporting information

### 2.7.1 Methods

**Reactor:** All reactions were performed in an autoclave (300 mL) from *Parr Instruments Co.* (type: *PST FS*, material: HASTELLOY C) with a temperature and stirring controlling device (*Parr Instruments Co. 4848 Reactor Controller*).

**GC-MS FID:** Quantification and qualification of the dehydration reactions was analyzed by GC/MS (*Agilent Technologies 7890 B GC*, column: *Agilent 19091S-433UI INV02* (30 m x 250  $\mu\text{m}$  x 0.25  $\mu\text{m}$ ), heating program: 10°C min<sup>-1</sup> from 80°C to 280°C). Data was analyzed with *MassHunter Workstation Software, Qualitative Analysis, Version B.06.00, Agilent Technologies (2012)*.

**AAS:** The Si and Al content for each zeolite was measured by atomic absorption spectroscopy (AAS) on a *UNICAM 939 AA-Spectrometer*.

**N<sub>2</sub> physisorption:** The surface area and micropore volume of the zeolites was measured by nitrogen physisorption at 77K. The zeolite sample was activated at 473K for 2 h to remove water or any other impurities before each analysis. The specific surface area was calculated by using the *Brunauer-Emmett-Teller (BET)* method, while the micropore volume was determined by the *t*-plot mode.

**IR spectroscopy:** The concentration of acid sites in terms of Lewis acid site and Brønsted acid site on the zeolites was measured by IR spectroscopy of adsorbed pyridine with a *Perkin-Elmer 2000* spectrometer at a resolution of 4 cm<sup>-1</sup>. The zeolite catalyst was pelleted into a self-supporting wafer and activated in vacuum (ca. 10<sup>-7</sup> mbar) at 450°C for 1 h. After cooling down to 150°C, the sample was dosed and equilibrated with 0.1 mbar of pyridine until saturation. Then the spectrum with chemisorbed pyridine was collected after degassing to remove physically adsorbed pyridine at 150°C for 1 h. Finally, the sample was heated up to 450°C for 0.5 h to desorb the chemisorbed pyridine. The concentration of Brønsted (1540 cm<sup>-1</sup>) and Lewis (1450 cm<sup>-1</sup>) acid sites was quantitatively calculated using molar integral extinction coefficients of 0.73 cm  $\mu\text{mol}^{-1}$  and 0.96 cm  $\mu\text{mol}^{-1}$ , respectively.

**Adsorption uptake and adsorption heat measurements:** Aqueous phase adsorption uptake of the alcohols on different zeolites was carried out at room temperature. Typically, 1-60 mg of the zeolite sample was immersed into the alcohol aqueous solutions with certain concentrations under vigorous stirring for 24 h. The saturated concentration of the aqueous solution of primary, secondary and tertiary alcohols was prepared as 12 mmol L<sup>-1</sup>, 5.0 mmol L<sup>-1</sup> and 39 mmol L<sup>-1</sup>, respectively. The mixtures were separated from the zeolite by using syringe filters (Nylon or Polypropylene membrane, 25 mm, 0.2  $\mu\text{m}$ ), then extracted using dichloromethane (*Sigma-Aldrich*, >99% purity) and finally analyzed on a GC-MS FID after the addition of an internal standard (*n*-dodecane). The adsorption uptake was calculated based on the alcohol concentration

change for a certain amount of the zeolite. The saturation uptake ( $q_{\max}$ ) of the alcohols on each zeolite was derived from the fitted adsorption isotherms using the Langmuir equation  $q = q_{\max} K_{\text{ads}} c (1 + K_{\text{ads}} c)^{-1}$ , where  $c$  represents the equilibrium concentration of the alcohols after adsorption,  $K_{\text{ads}}$  is the adsorption constant with the standard state set as 1 mol L<sup>-1</sup>.

Aqueous phase adsorption heat of substituted alcohols on MFI-45 and BEA-83 were measured on a microcalorimetry equipment (*Setaram Calvet C80*) containing two separate cells. Each cell has two compartments. 0.8 mL of the aqueous solution of alcohol was added into the lower compartment, while the upper compartment was filled by 0.2 mL of water dispersed with 2 – 10 mg of zeolites. The same method was used to prepare the reference cell except for the addition of zeolite. All the experiments were conducted at room temperature.

## 2.7.2 Figures and tables of the discussion part

Reaction order of aqueous phase dehydration

1° alcohol: 2-cyclohexylethanol

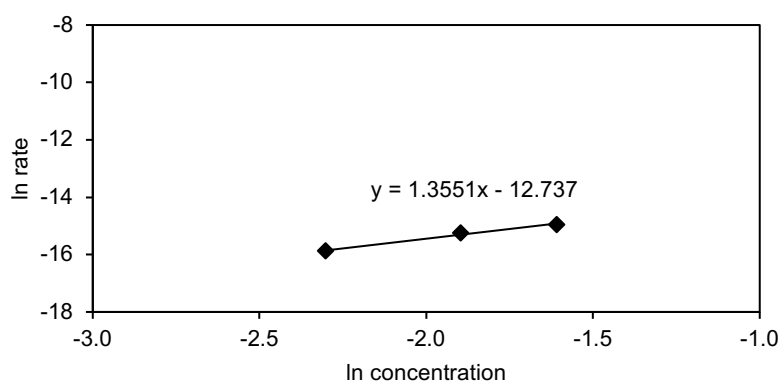


**Figure S2.1.** Reaction order: 2-cyclohexylethanol dehydration (210°C, 50 bar, H<sub>3</sub>PO<sub>4</sub>).

**Table S2.1.** 2-cyclohexylethanol dehydration rates and different initial concentrations (210°C, 50 bar, H<sub>3</sub>PO<sub>4</sub>).

rate (mol s <sup>-1</sup> )	c (mol L <sup>-1</sup> )	ln rate	ln c
1.3×10 <sup>-7</sup>	0.10	-15.88	-2.30
2.4×10 <sup>-7</sup>	0.15	-15.26	-1.90
3.2×10 <sup>-7</sup>	0.20	-14.95	-1.61

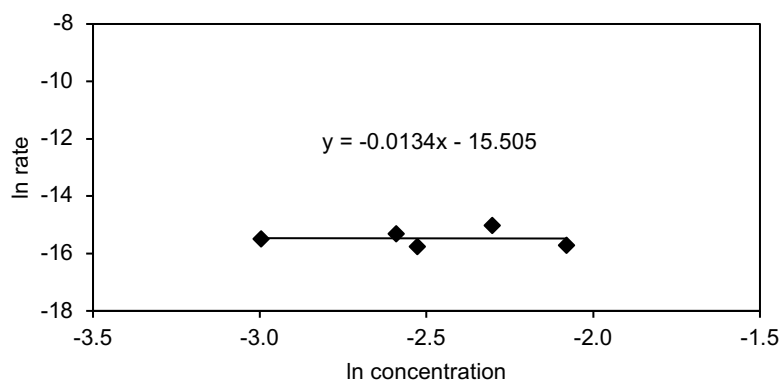


**Figure S2.2.** Reaction order: **2-cyclohexylethanol** dehydration (190°C, 50 bar, **BEA**).

**Table S2.2.** **2-cyclohexylethanol** dehydration rates and different initial concentrations (190°C, 50 bar, **BEA**).

rate (mol g <sup>-1</sup> s <sup>-1</sup> )	c (mol L <sup>-1</sup> )	ln rate	ln c
1.9×10 <sup>-7</sup>	0.050	-15.50	-3.00
2.2×10 <sup>-7</sup>	0.075	-15.33	-2.59
1.4×10 <sup>-7</sup>	0.080	-15.78	-2.53
3.0×10 <sup>-7</sup>	0.100	-15.03	-2.30
1.5×10 <sup>-7</sup>	0.125	-15.71	-2.08

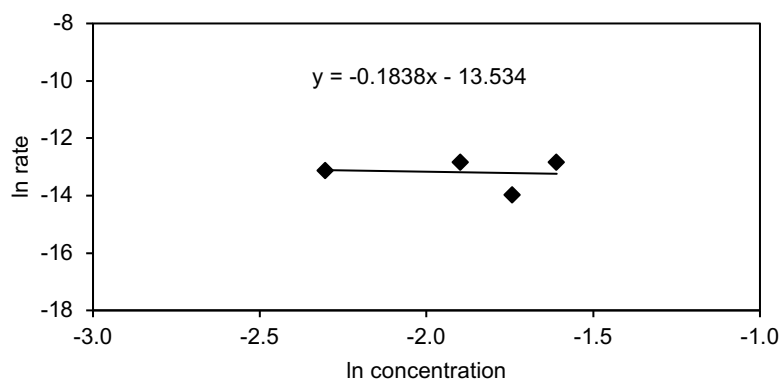


**Figure S2.3.** Reaction order: **2-cyclohexylethanol** dehydration (180°C, 50 bar, **MFI**).

**Table S2.3.** **2-cyclohexylethanol** dehydration rates and different initial concentrations (180°C, 50 bar, **MFI**).

rate (mol g <sup>-1</sup> s <sup>-1</sup> )	c (mol L <sup>-1</sup> )	ln rate	ln c
2.0×10 <sup>-6</sup>	0.10	-13.11	-2.30
2.7×10 <sup>-6</sup>	0.15	-12.83	-1.90
8.6×10 <sup>-7</sup>	0.18	-13.97	-1.74
2.7×10 <sup>-6</sup>	0.20	-12.84	-1.61

**2° alcohol: 4-methylcyclohexanol**

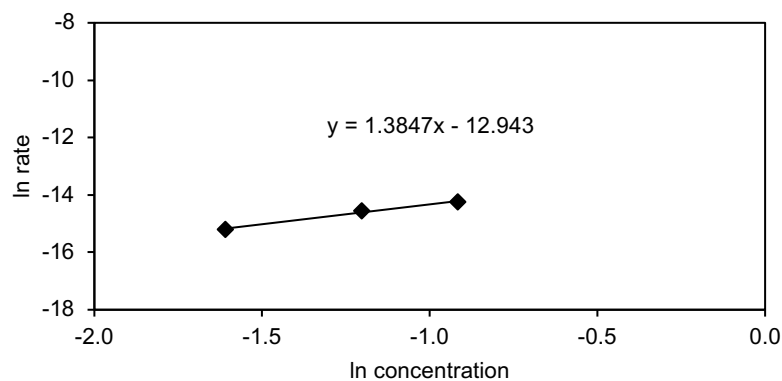


**Figure S2.4.** Reaction order: **4-methylcyclohexanol** dehydration (170°C, 50 bar, **H<sub>3</sub>PO<sub>4</sub>**).

**Table S2.4.** **4-methylcyclohexanol** dehydration rates and different initial concentrations (170°C, 50 bar, **H<sub>3</sub>PO<sub>4</sub>**).

rate (mol s <sup>-1</sup> )	c (mol L <sup>-1</sup> )	ln rate	ln c
$2.5 \times 10^{-7}$	0.20	-15.19	-1.61
$4.8 \times 10^{-7}$	0.30	-14.56	-1.20
$6.5 \times 10^{-7}$	0.40	-14.24	-0.92

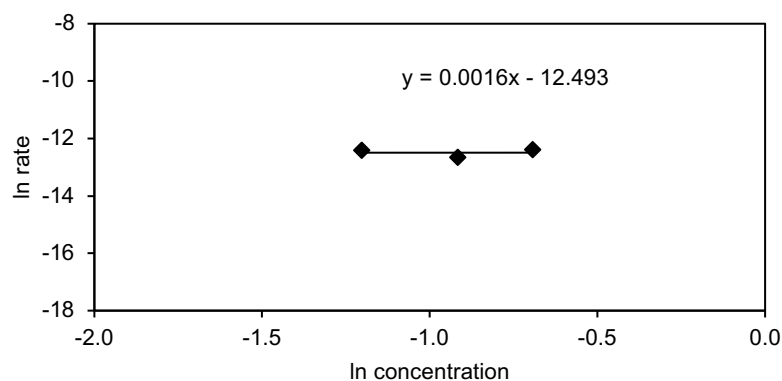


**Figure S2.5.** Reaction order: **4-methylcyclohexanol** dehydration (170°C, 50 bar, **BEA**).

**Table S2.5.** **4-methylcyclohexanol** dehydration rates and different initial concentrations (170°C, 50 bar, **BEA**).

rate (mol g <sup>-1</sup> s <sup>-1</sup> )	c (mol L <sup>-1</sup> )	ln rate	ln c
$4.0 \times 10^{-6}$	0.30	-12.42	-1.20
$3.2 \times 10^{-6}$	0.40	-12.67	-0.92
$4.1 \times 10^{-6}$	0.50	-12.40	-0.69

**2° alcohol: 2-methylcyclohexanol**

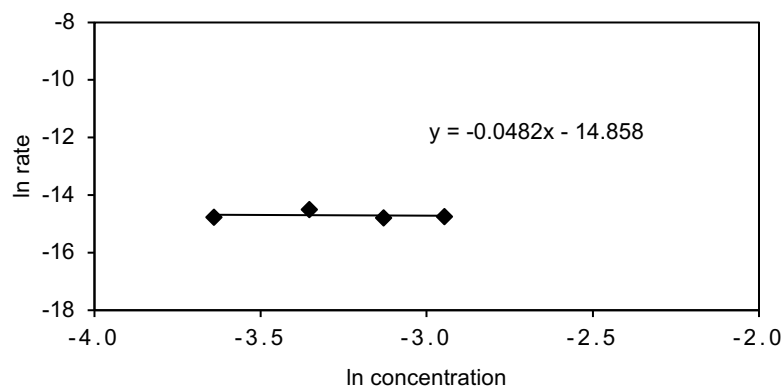


**Figure S2.6.** Reaction order: *trans*-2-methylcyclohexanol dehydration (170°C, 50 bar, **BEA**).

**Table S2.6.** *trans*-2-methylcyclohexanol dehydration rates and different initial concentrations (170°C, 50 bar, **BEA**).

rate (mol g <sup>-1</sup> s <sup>-1</sup> )	c (mol L <sup>-1</sup> )	ln rate	ln c
3.8×10 <sup>-7</sup>	0.026	-14.77	-3.64
5.0×10 <sup>-7</sup>	0.035	-14.51	-3.35
3.8×10 <sup>-7</sup>	0.044	-14.78	-3.13
4.0×10 <sup>-7</sup>	0.052	-14.74	-2.95

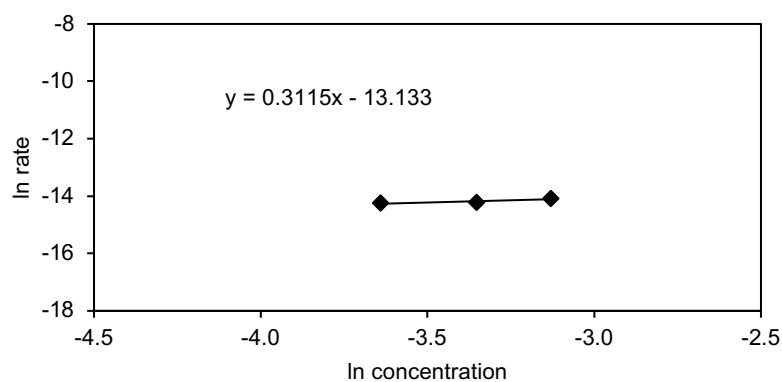


**Figure S2.7.** Reaction order: *trans*-2-methylcyclohexanol dehydration (140°C, 50 bar, **MFI**).

**Table S2.7.** *trans*-2-methylcyclohexanol dehydration rates and different initial concentrations (140°C, 50 bar, **MFI**).

rate (mol g <sup>-1</sup> s <sup>-1</sup> )	c (mol L <sup>-1</sup> )	ln rate	ln c
6.5×10 <sup>-7</sup>	0.026	-14.25	-3.64
6.7×10 <sup>-7</sup>	0.035	-14.21	-3.35
7.6×10 <sup>-7</sup>	0.044	-14.09	-3.13

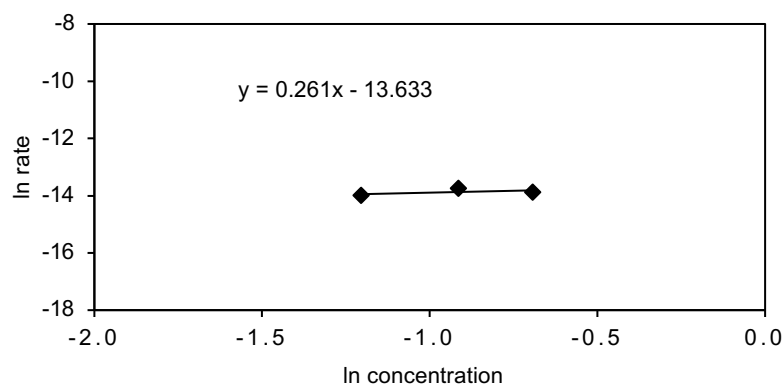


**Figure S2.8.** Reaction order: **2-methylcyclohexanol** dehydration (170°C, 50 bar, **BEA**).

**Table S2.8.** **2-methylcyclohexanol** dehydration rates and different initial concentrations (170°C, 50 bar, **BEA**).

rate (mol g <sup>-1</sup> s <sup>-1</sup> )	c (mol L <sup>-1</sup> )	ln rate	ln c
7.8×10 <sup>-7</sup>	0.30	-14.00	-1.21
1.0×10 <sup>-6</sup>	0.40	-13.75	-0.92
9.4×10 <sup>-7</sup>	0.50	-13.88	-0.69

### 3° alcohol: 1-methylcyclohexanol

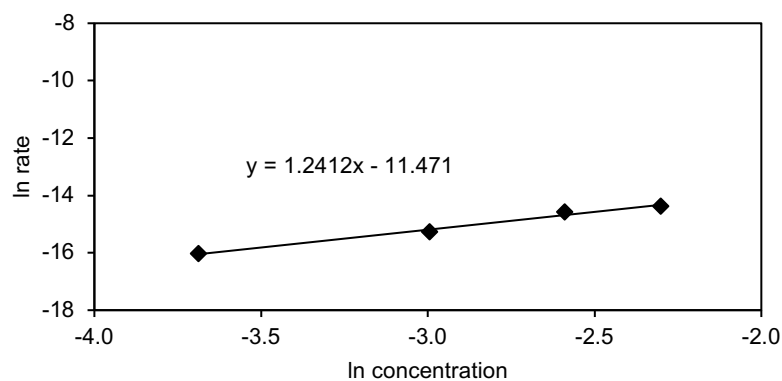


**Figure S2.9.** Reaction order: **1-methylcyclohexanol** dehydration (100°C, 50 bar, **H<sub>3</sub>PO<sub>4</sub>**).

**Table S2.9.** **1-methylcyclohexanol** dehydration rates and different initial concentrations (100°C, 50 bar, **H<sub>3</sub>PO<sub>4</sub>**).

rate (mol s <sup>-1</sup> )	c (mol L <sup>-1</sup> )	ln rate	ln c
1.1×10 <sup>-7</sup>	0.025	-16.03	-3.69
2.3×10 <sup>-7</sup>	0.050	-15.27	-3.00
4.7×10 <sup>-7</sup>	0.075	-14.57	-2.59
5.7×10 <sup>-7</sup>	0.100	-14.38	-2.30

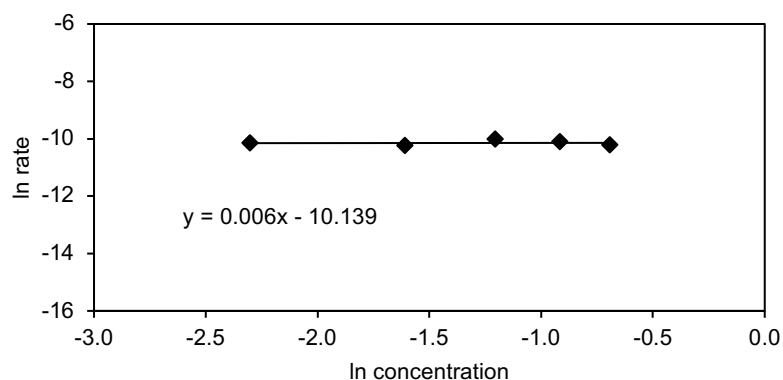


**Figure S2.10.** Reaction order: **1-methylcyclohexanol** dehydration (110°C, 50 bar, **BEA**).

**Table S2.10.** **1-methylcyclohexanol** dehydration rates and different initial concentrations (110°C, 50 bar, **BEA**).

rate (mol g <sup>-1</sup> s <sup>-1</sup> )	c (mol L <sup>-1</sup> )	ln rate	ln c
3.9×10 <sup>-5</sup>	0.10	-10.15	-2.30
3.6×10 <sup>-5</sup>	0.20	-10.24	-1.61
4.5×10 <sup>-5</sup>	0.30	-10.02	-1.20
4.1×10 <sup>-5</sup>	0.40	-10.10	-0.92
3.6×10 <sup>-5</sup>	0.50	-10.23	-0.69

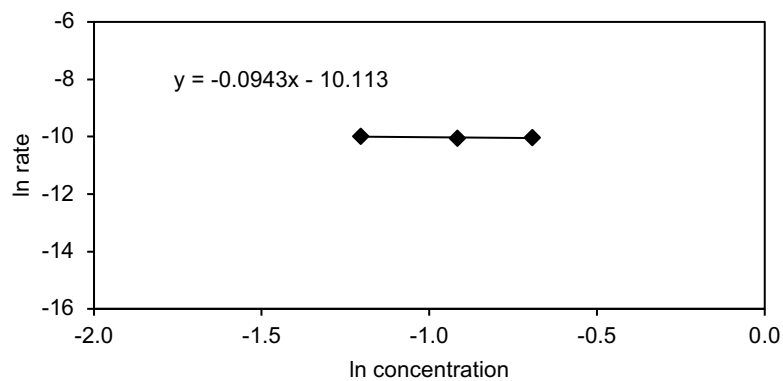


**Figure S2.11.** Reaction order: **1-methylcyclohexanol** dehydration (110°C, 50 bar, **MFI**).

**Table S2.11.** **1-methylcyclohexanol** dehydration rates and different initial concentrations (110°C, 50 bar, **MFI**).

rate (mol g <sup>-1</sup> s <sup>-1</sup> )	c (mol L <sup>-1</sup> )	ln rate	ln c
4.6×10 <sup>-5</sup>	0.30	-10.00	-1.20
4.3×10 <sup>-5</sup>	0.40	-10.05	-0.92
4.4×10 <sup>-5</sup>	0.50	-10.04	-0.69

Activation energy of aqueous phase dehydration

1° alcohol: 2-cyclohexylethanol

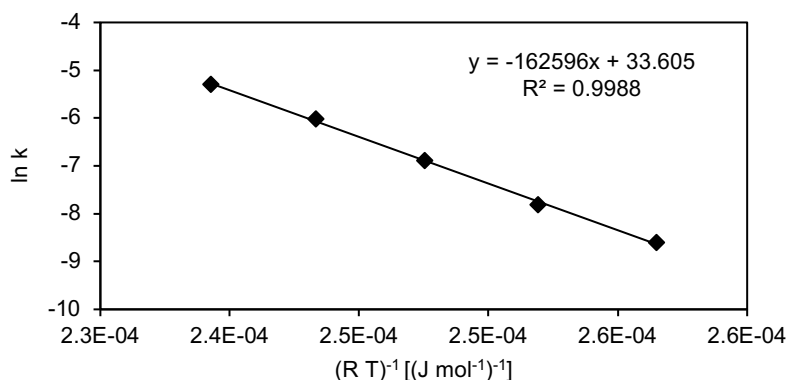


Figure S2.12. Arrhenius-plot: 2-cyclohexylethanol (0.2 M) dehydration ( $E_a \approx 163 \text{ kJ mol}^{-1}$ ),  $\text{H}_3\text{PO}_4$ .

Table S2.12. 2-cyclohexylethanol (0.2 M) dehydration rates at different reaction temperatures,  $\text{H}_3\text{PO}_4$ .

T (°C)	T (K)	rate (mol s <sup>-1</sup> )	n H <sup>+</sup> (mol)	k (L mol <sup>-1</sup> s <sup>-1</sup> )	TOF (s <sup>-1</sup> )	ln k	(R T) <sup>-1</sup> [(J mol <sup>-1</sup> ) <sup>-1</sup> ]
190	463	7.22×10 <sup>-8</sup>	1.95×10 <sup>-3</sup>	1.85×10 <sup>-4</sup>	3.70×10 <sup>-5</sup>	-8.59	2.60×10 <sup>-4</sup>
200	473	1.43×10 <sup>-7</sup>	1.76×10 <sup>-3</sup>	4.06×10 <sup>-4</sup>	8.12×10 <sup>-5</sup>	-7.81	2.54×10 <sup>-4</sup>
210	483	3.22×10 <sup>-7</sup>	1.58×10 <sup>-3</sup>	1.02×10 <sup>-3</sup>	2.03×10 <sup>-4</sup>	-6.89	2.49×10 <sup>-4</sup>
220	493	6.94×10 <sup>-7</sup>	1.42×10 <sup>-3</sup>	2.44×10 <sup>-3</sup>	4.87×10 <sup>-4</sup>	-6.02	2.44×10 <sup>-4</sup>
230	503	1.29×10 <sup>-6</sup>	1.28×10 <sup>-3</sup>	5.04×10 <sup>-3</sup>	1.01×10 <sup>-3</sup>	-5.29	2.39×10 <sup>-4</sup>

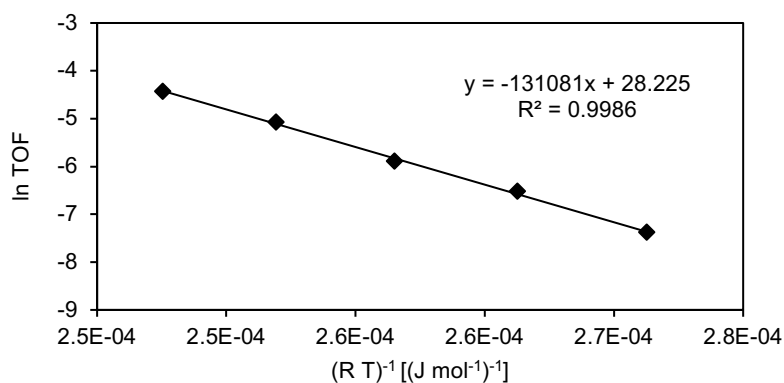
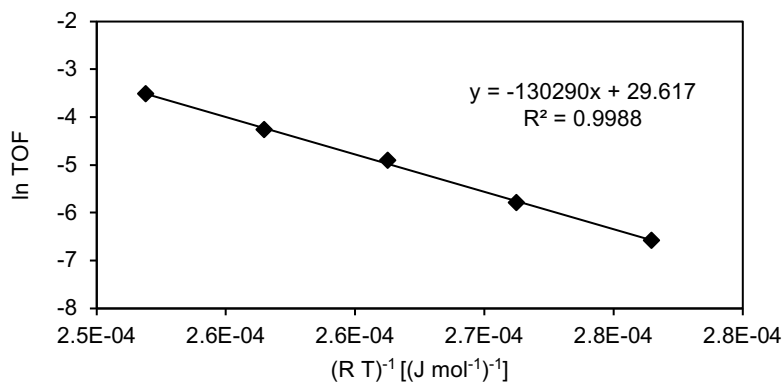


Figure S2.13. Arrhenius-plot: 2-cyclohexylethanol (0.1 M) dehydration ( $E_a \approx 131 \text{ kJ mol}^{-1}$ ), BEA.

**Table S2.13.** 2-cyclohexylethanol (0.1 M) dehydration rates at different reaction temperatures, **BEA**.

T (°C)	T (K)	rate (mol g <sup>-1</sup> s <sup>-1</sup> )	TOF (s <sup>-1</sup> )	ln TOF	(R T) <sup>-1</sup> [(J mol <sup>-1</sup> ) <sup>-1</sup> ]
170	443	7.45×10 <sup>-8</sup>	6.21×10 <sup>-4</sup>	-7.38	2.72×10 <sup>-4</sup>
180	453	1.76×10 <sup>-7</sup>	1.47×10 <sup>-3</sup>	-6.52	2.66×10 <sup>-4</sup>
190	463	3.34×10 <sup>-7</sup>	2.78×10 <sup>-3</sup>	-5.89	2.60×10 <sup>-4</sup>
200	473	7.50×10 <sup>-7</sup>	6.25×10 <sup>-3</sup>	-5.08	2.54×10 <sup>-4</sup>
210	483	1.44×10 <sup>-6</sup>	1.20×10 <sup>-2</sup>	-4.43	2.49×10 <sup>-4</sup>



**Figure S2.14.** Arrhenius-plot: 2-cyclohexylethanol (0.2 M) dehydration ( $E_a \approx 130$  kJ mol<sup>-1</sup>), **MFI**.

**Table S2.14.** 2-cyclohexylethanol (0.2 M) dehydration rates at different reaction temperatures, **MFI**.

T (°C)	T (K)	rate (mol g <sup>-1</sup> s <sup>-1</sup> )	TOF (s <sup>-1</sup> )	ln TOF	(R T) <sup>-1</sup> [(J mol <sup>-1</sup> ) <sup>-1</sup> ]
160	433	5.00×10 <sup>-7</sup>	1.39×10 <sup>-3</sup>	-6.58	2.78×10 <sup>-4</sup>
170	443	1.11×10 <sup>-6</sup>	3.07×10 <sup>-3</sup>	-5.79	2.72×10 <sup>-4</sup>
180	453	2.66×10 <sup>-6</sup>	7.39×10 <sup>-3</sup>	-4.91	2.66×10 <sup>-4</sup>
190	463	5.06×10 <sup>-6</sup>	1.41×10 <sup>-2</sup>	-4.26	2.60×10 <sup>-4</sup>
200	473	1.07×10 <sup>-5</sup>	2.97×10 <sup>-2</sup>	-3.52	2.54×10 <sup>-4</sup>

**2° alcohol: 4-methylcyclohexanol**

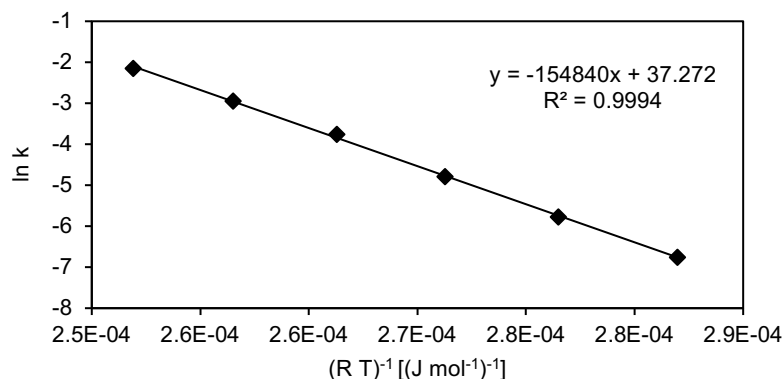


**Figure S2.15.** Arrhenius-plot: **4-methylcyclohexanol** (0.2 M) dehydration ( $E_a \approx 155 \text{ kJ mol}^{-1}$ ),  $\text{H}_3\text{PO}_4$ .

**Table S2.15.** **4-methylcyclohexanol** (0.2 M) dehydration rates at different reaction temperatures,  $\text{H}_3\text{PO}_4$ .

T (°C)	T (K)	rate (mol s <sup>-1</sup> )	n H <sup>+</sup> (mol)	k (L mol <sup>-1</sup> s <sup>-1</sup> )	TOF (s <sup>-1</sup> )	ln k	(R T) <sup>-1</sup> [(J mol <sup>-1</sup> ) <sup>-1</sup> ]
150	423	4.26×10 <sup>-8</sup>	1.83×10 <sup>-4</sup>	1.17×10 <sup>-3</sup>	2.33×10 <sup>-4</sup>	-6.75	2.84×10 <sup>-4</sup>
160	433	1.03×10 <sup>-7</sup>	1.66×10 <sup>-4</sup>	3.11×10 <sup>-3</sup>	6.23×10 <sup>-4</sup>	-5.77	2.78×10 <sup>-4</sup>
170	443	2.52×10 <sup>-7</sup>	1.51×10 <sup>-4</sup>	8.36×10 <sup>-3</sup>	1.67×10 <sup>-3</sup>	-4.78	2.72×10 <sup>-4</sup>
180	453	6.34×10 <sup>-7</sup>	1.36×10 <sup>-4</sup>	2.32×10 <sup>-2</sup>	4.65×10 <sup>-3</sup>	-3.76	2.66×10 <sup>-4</sup>
190	463	1.30×10 <sup>-6</sup>	1.23×10 <sup>-4</sup>	5.27×10 <sup>-2</sup>	1.05×10 <sup>-2</sup>	-2.94	2.60×10 <sup>-4</sup>
200	473	2.60×10 <sup>-6</sup>	1.11×10 <sup>-4</sup>	1.17×10 <sup>-1</sup>	2.34×10 <sup>-2</sup>	-2.15	2.54×10 <sup>-4</sup>

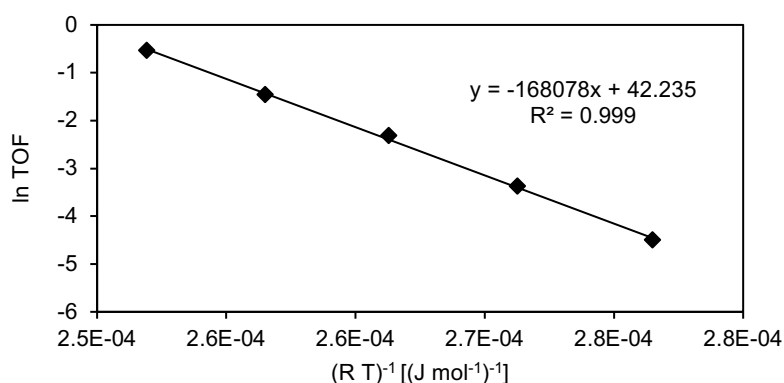


**Figure S2.16.** Arrhenius-plot: **4-methylcyclohexanol** (0.5 M) dehydration ( $E_a \approx 168 \text{ kJ mol}^{-1}$ ),  $\text{BEA}$ .

**Table S2.16.** 4-methylcyclohexanol (0.5 M) dehydration rates at different reaction temperatures, **BEA**.

T (°C)	T (K)	rate (mol g <sup>-1</sup> s <sup>-1</sup> )	TOF (s <sup>-1</sup> )	ln TOF	(R T) <sup>-1</sup> [(J mol <sup>-1</sup> ) <sup>-1</sup> ]
160	433	1.33×10 <sup>-6</sup>	1.11×10 <sup>-2</sup>	-4.50	2.78×10 <sup>-4</sup>
170	443	4.13×10 <sup>-6</sup>	3.44×10 <sup>-2</sup>	-3.37	2.72×10 <sup>-4</sup>
180	453	1.18×10 <sup>-5</sup>	9.81×10 <sup>-2</sup>	-2.32	2.66×10 <sup>-4</sup>
190	463	2.79×10 <sup>-5</sup>	2.33×10 <sup>-1</sup>	-1.46	2.60×10 <sup>-4</sup>
200	473	7.07×10 <sup>-5</sup>	5.89×10 <sup>-1</sup>	-0.53	2.54×10 <sup>-4</sup>

**2° alcohol: 2-methylcyclohexanol**

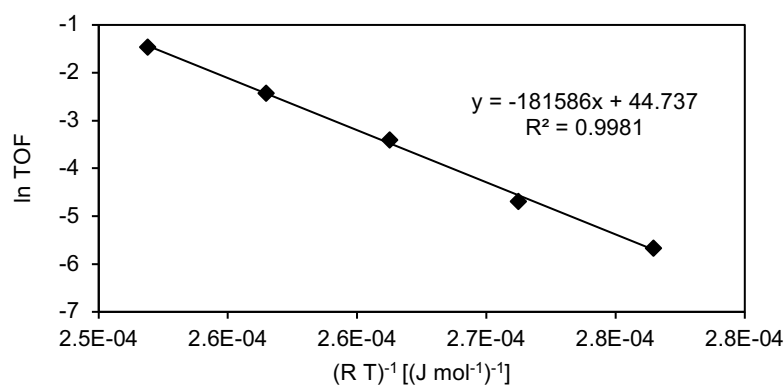


**Figure S2.17.** Arrhenius-plot: *trans*-2-methylcyclohexanol (44 mM) dehydration ( $E_a \approx 182$  kJ mol<sup>-1</sup>), **BEA**.

**Table S2.17.** *trans*-2-methylcyclohexanol (44 mM) dehydration rates at different reaction temperatures, **BEA**.

T (°C)	T (K)	rate (mol g <sup>-1</sup> s <sup>-1</sup> )	TOF (s <sup>-1</sup> )	ln TOF	(R T) <sup>-1</sup> [(J mol <sup>-1</sup> ) <sup>-1</sup> ]
160	433	4.20×10 <sup>-7</sup>	3.50×10 <sup>-3</sup>	-5.66	2.78×10 <sup>-4</sup>
170	443	1.11×10 <sup>-6</sup>	9.27×10 <sup>-3</sup>	-4.68	2.72×10 <sup>-4</sup>
180	453	3.98×10 <sup>-6</sup>	3.32×10 <sup>-2</sup>	-3.41	2.66×10 <sup>-4</sup>
190	463	1.06×10 <sup>-5</sup>	8.83×10 <sup>-2</sup>	-2.43	2.60×10 <sup>-4</sup>
200	473	2.81×10 <sup>-5</sup>	2.34×10 <sup>-1</sup>	-1.45	2.54×10 <sup>-4</sup>

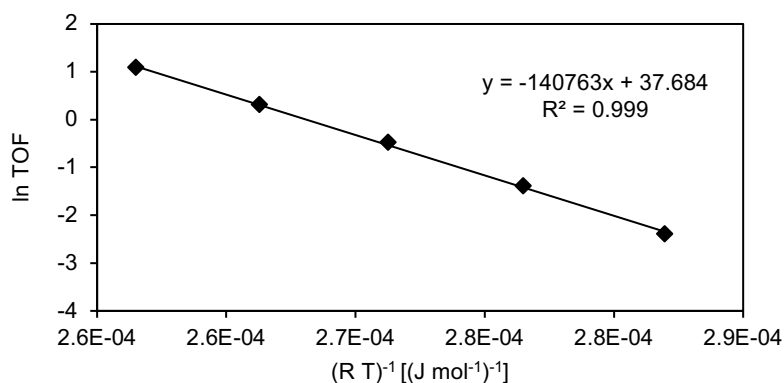


**Figure S2.18.** Arrhenius-plot: **2-methylcyclohexanol** (0.5 M) dehydration ( $E_a \approx 141 \text{ kJ mol}^{-1}$ ), **BEA**.

**Table S2.18.** **2-methylcyclohexanol** (0.5 M) dehydration rates at different reaction temperatures, **BEA**.

T (°C)	T (K)	rate (mol g <sup>-1</sup> s <sup>-1</sup> )	TOF (s <sup>-1</sup> )	ln TOF	(R T) <sup>-1</sup> [(J mol <sup>-1</sup> ) <sup>-1</sup> ]
150	423	1.10×10 <sup>-5</sup>	9.17×10 <sup>-2</sup>	-2.39	2.84×10 <sup>-4</sup>
160	433	3.00×10 <sup>-5</sup>	2.50×10 <sup>-1</sup>	-1.39	2.78×10 <sup>-4</sup>
170	443	7.42×10 <sup>-5</sup>	6.18×10 <sup>-1</sup>	-0.48	2.72×10 <sup>-4</sup>
180	453	1.63×10 <sup>-4</sup>	1.36	0.31	2.66×10 <sup>-4</sup>
190	463	3.54×10 <sup>-4</sup>	2.95	1.08	2.60×10 <sup>-4</sup>

### 3° alcohol: 1-methylcyclohexanol

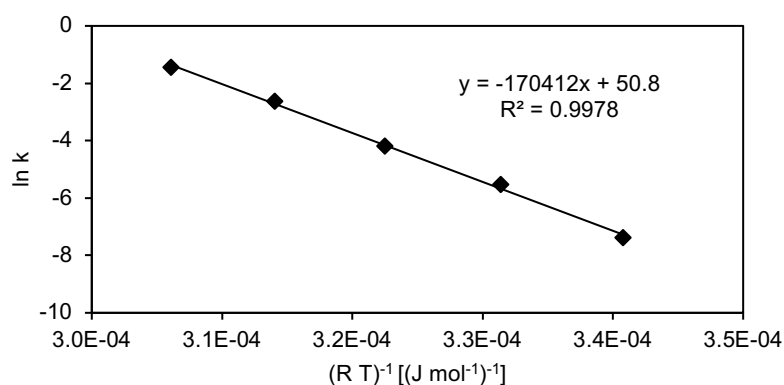


**Figure S2.19.** Arrhenius-plot: **1-methylcyclohexanol** (0.1 M) dehydration ( $E_a \approx 170 \text{ kJ mol}^{-1}$ ), **H<sub>3</sub>PO<sub>4</sub>**.

**Table S2.19.** 1-methylcyclohexanol (0.1 M) dehydration rates at different reaction temperatures,  $\text{H}_3\text{PO}_4$ .

T (°C)	T (K)	rate (mol s <sup>-1</sup> )	n H <sup>+</sup> (mol)	k (L mol <sup>-1</sup> s <sup>-1</sup> )	TOF (s <sup>-1</sup> )	ln k	(R T) <sup>-1</sup> [(J mol <sup>-1</sup> ) <sup>-1</sup> ]
80	353	2.75×10 <sup>-8</sup>	4.36×10 <sup>-4</sup>	6.31×10 <sup>-4</sup>	6.31×10 <sup>-5</sup>	-7.37	3.41×10 <sup>-4</sup>
90	363	1.60×10 <sup>-7</sup>	4.05×10 <sup>-4</sup>	3.95×10 <sup>-3</sup>	3.95×10 <sup>-4</sup>	-5.53	3.31×10 <sup>-4</sup>
100	373	5.69×10 <sup>-7</sup>	3.74×10 <sup>-4</sup>	1.52×10 <sup>-2</sup>	1.52×10 <sup>-3</sup>	-4.19	3.22×10 <sup>-4</sup>
110	383	2.51×10 <sup>-6</sup>	3.45×10 <sup>-4</sup>	7.28×10 <sup>-2</sup>	7.28×10 <sup>-3</sup>	-2.62	3.14×10 <sup>-4</sup>
120	393	7.44×10 <sup>-6</sup>	3.17×10 <sup>-4</sup>	2.35×10 <sup>-1</sup>	2.35×10 <sup>-2</sup>	-1.45	3.06×10 <sup>-4</sup>

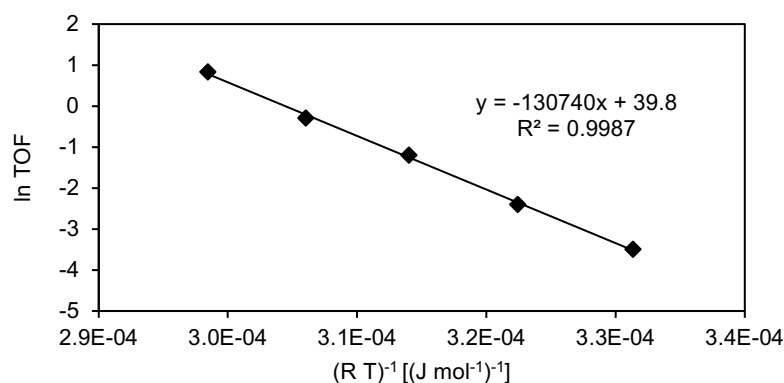


**Figure S2.20.** Arrhenius-plot: 1-methylcyclohexanol (0.5 M) dehydration ( $E_a \approx 131$  kJ mol<sup>-1</sup>), BEA.

**Table S2.20.** 1-methylcyclohexanol (0.5 M) dehydration rates at different reaction temperatures, BEA.

T (°C)	T (K)	rate (mol g <sup>-1</sup> s <sup>-1</sup> )	TOF (s <sup>-1</sup> )	ln TOF	(R T) <sup>-1</sup> [(J mol <sup>-1</sup> ) <sup>-1</sup> ]
90	363	3.63×10 <sup>-6</sup>	3.03×10 <sup>-2</sup>	-3.50	3.31×10 <sup>-4</sup>
100	373	1.09×10 <sup>-5</sup>	9.08×10 <sup>-2</sup>	-2.40	3.22×10 <sup>-4</sup>
110	383	3.61×10 <sup>-5</sup>	3.01×10 <sup>-1</sup>	-1.20	3.14×10 <sup>-4</sup>
120	393	8.91×10 <sup>-5</sup>	7.43×10 <sup>-1</sup>	-0.30	3.06×10 <sup>-4</sup>
130	403	2.74×10 <sup>-4</sup>	2.28	0.83	2.98×10 <sup>-4</sup>

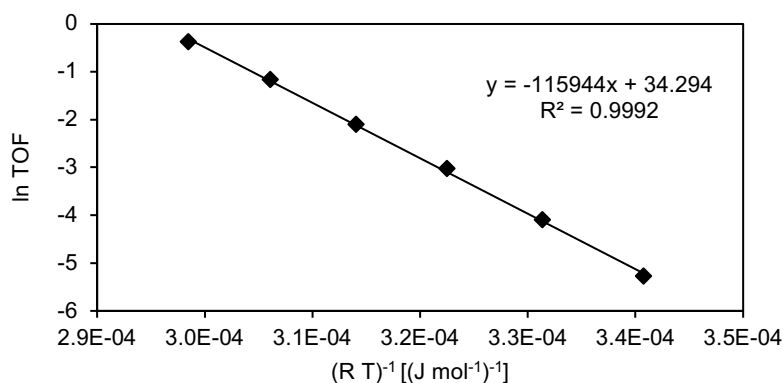


**Figure S2.21.** Arrhenius-plot: **1-methylcyclohexanol** (0.5 M) dehydration ( $E_a \approx 116 \text{ kJ mol}^{-1}$ ), **MFI**.

**Table S2.21.** **1-methylcyclohexanol** (0.5 M) dehydration rates at different reaction temperatures, **MFI**.

T (°C)	T (K)	rate (mol g <sup>-1</sup> s <sup>-1</sup> )	TOF (s <sup>-1</sup> )	ln TOF	(R T) <sup>-1</sup> [(J mol <sup>-1</sup> ) <sup>-1</sup> ]
80	353	1.84×10 <sup>-6</sup>	5.11×10 <sup>-3</sup>	-5.28	3.41×10 <sup>-4</sup>
90	363	5.94×10 <sup>-6</sup>	1.65×10 <sup>-2</sup>	-4.10	3.31×10 <sup>-4</sup>
100	373	1.75×10 <sup>-5</sup>	4.86×10 <sup>-2</sup>	-3.02	3.22×10 <sup>-4</sup>
110	383	4.38×10 <sup>-5</sup>	1.22×10 <sup>-1</sup>	-2.11	3.14×10 <sup>-4</sup>
120	393	1.12×10 <sup>-4</sup>	3.11×10 <sup>-1</sup>	-1.17	3.06×10 <sup>-4</sup>
130	403	2.48×10 <sup>-4</sup>	6.89×10 <sup>-1</sup>	-0.37	2.98×10 <sup>-4</sup>

### Determination of $\Delta H^{\ddagger}$ and $\Delta S^{\ddagger}$

#### 1° alcohol: **2-cyclohexylethanol**

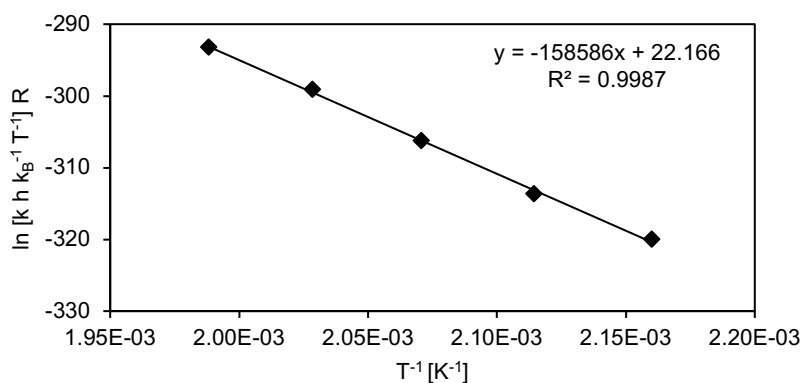


**Figure S2.22.**  $\Delta H^{\ddagger}$  (159 kJ mol<sup>-1</sup>) and  $\Delta S^{\ddagger}$  (+22 J mol<sup>-1</sup> K<sup>-1</sup>) for **2-cyclohexylethanol** (0.2 M) dehydration, **H<sub>3</sub>PO<sub>4</sub>**.

**Table S2.22.** Kinetic data for **2-cyclohexylethanol** (0.2 M) dehydration, **H<sub>3</sub>PO<sub>4</sub>**.

T (°C)	T (K)	k (L mol <sup>-1</sup> s <sup>-1</sup> )	TOF (s <sup>-1</sup> )	ln [k h k <sub>B</sub> <sup>-1</sup> T <sup>-1</sup> ] R	T <sup>-1</sup> (K <sup>-1</sup> )
190	463	1.85×10 <sup>-4</sup>	3.70×10 <sup>-5</sup>	-320.02	2.16×10 <sup>-3</sup>
200	473	4.06×10 <sup>-4</sup>	8.12×10 <sup>-5</sup>	-313.67	2.11×10 <sup>-3</sup>
210	483	1.02×10 <sup>-3</sup>	2.03×10 <sup>-4</sup>	-306.21	2.07×10 <sup>-3</sup>
220	493	2.44×10 <sup>-3</sup>	4.87×10 <sup>-4</sup>	-299.11	2.03×10 <sup>-3</sup>
230	503	5.04×10 <sup>-3</sup>	1.01×10 <sup>-3</sup>	-293.25	1.99×10 <sup>-3</sup>

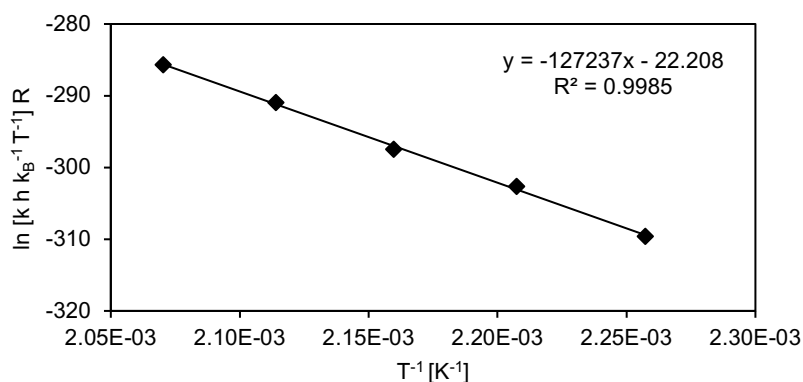


**Figure S2.23.**  $\Delta H^{\ddagger}$  (127 kJ mol<sup>-1</sup>) and  $\Delta S^{\ddagger}$  (-22 J mol<sup>-1</sup> K<sup>-1</sup>) for **2-cyclohexylethanol** (0.1 M) dehydration, **BEA**.

**Table S2.23.** Kinetic data for **2-cyclohexylethanol** (0.1 M) dehydration, **BEA**.

T (°C)	T (K)	TOF (s <sup>-1</sup> )	ln [k h k <sub>B</sub> <sup>-1</sup> T <sup>-1</sup> ] R	T <sup>-1</sup> (K <sup>-1</sup> )
170	443	6.21×10 <sup>-4</sup>	-309.59	2.26×10 <sup>-3</sup>
180	453	1.47×10 <sup>-3</sup>	-302.63	2.21×10 <sup>-3</sup>
190	463	2.78×10 <sup>-3</sup>	-297.50	2.16×10 <sup>-3</sup>
200	473	6.25×10 <sup>-3</sup>	-290.94	2.11×10 <sup>-3</sup>
210	483	1.20×10 <sup>-2</sup>	-285.72	2.07×10 <sup>-3</sup>

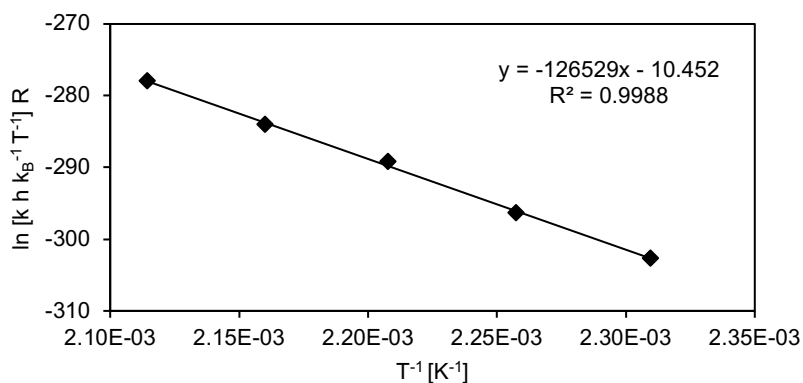


**Figure S2.24.**  $\Delta H^{\ddagger}$  (127 kJ mol<sup>-1</sup>) and  $\Delta S^{\ddagger}$  (-10 J mol<sup>-1</sup> K<sup>-1</sup>) for **2-cyclohexylethanol** (0.2 M) dehydration, **MFI**.

**Table S2.24.** Kinetic data for **2-cyclohexylethanol** (0.2 M) dehydration, **MFI**.

T (°C)	T (K)	TOF (s <sup>-1</sup> )	$\ln [k h k_B^{-1} T^{-1}] R$	$T^{-1} (K^{-1})$
160	433	$1.39 \times 10^{-3}$	-302.71	$2.31 \times 10^{-3}$
170	443	$3.07 \times 10^{-3}$	-296.30	$2.26 \times 10^{-3}$
180	453	$7.39 \times 10^{-3}$	-289.19	$2.21 \times 10^{-3}$
190	463	$1.41 \times 10^{-2}$	-284.02	$2.16 \times 10^{-3}$
200	473	$2.97 \times 10^{-2}$	-277.97	$2.11 \times 10^{-3}$

## 2° alcohol: 4-methylcyclohexanol

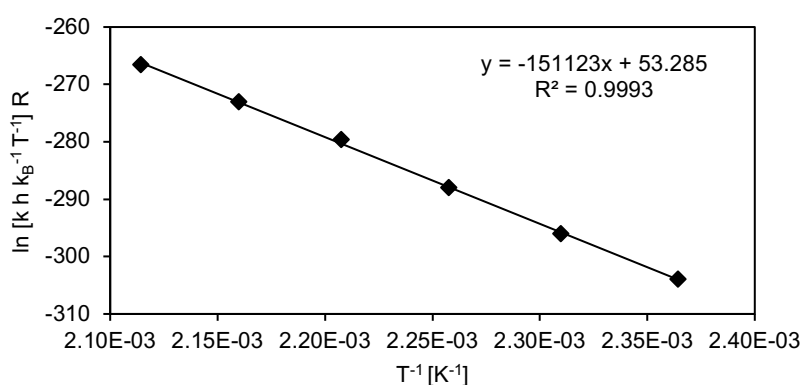


**Figure S2.25.**  $\Delta H^{\ddagger}$  (151 kJ mol<sup>-1</sup>) and  $\Delta S^{\ddagger}$  (+53 J mol<sup>-1</sup> K<sup>-1</sup>) for **4-methylcyclohexanol** (0.2 M) dehydration, **H<sub>3</sub>PO<sub>4</sub>**.

**Table S2.25.** Kinetic data for **4-methylcyclohexanol** (0.2 M) dehydration, **H<sub>3</sub>PO<sub>4</sub>**.

T (°C)	T (K)	k (L mol <sup>-1</sup> s <sup>-1</sup> )	TOF (s <sup>-1</sup> )	ln [k h k <sub>B</sub> <sup>-1</sup> T <sup>-1</sup> ] R	T <sup>-1</sup> (K <sup>-1</sup> )
150	423	1.17×10 <sup>-3</sup>	2.33×10 <sup>-4</sup>	-303.97	2.36×10 <sup>-3</sup>
160	433	3.11×10 <sup>-3</sup>	6.23×10 <sup>-4</sup>	-296.00	2.31×10 <sup>-3</sup>
170	443	8.36×10 <sup>-3</sup>	1.67×10 <sup>-3</sup>	-287.97	2.26×10 <sup>-3</sup>
180	453	2.32×10 <sup>-2</sup>	4.65×10 <sup>-3</sup>	-279.66	2.21×10 <sup>-3</sup>
190	463	5.27×10 <sup>-2</sup>	1.05×10 <sup>-2</sup>	-273.03	2.16×10 <sup>-3</sup>
200	473	1.17×10 <sup>-1</sup>	2.34×10 <sup>-2</sup>	-266.59	2.11×10 <sup>-3</sup>

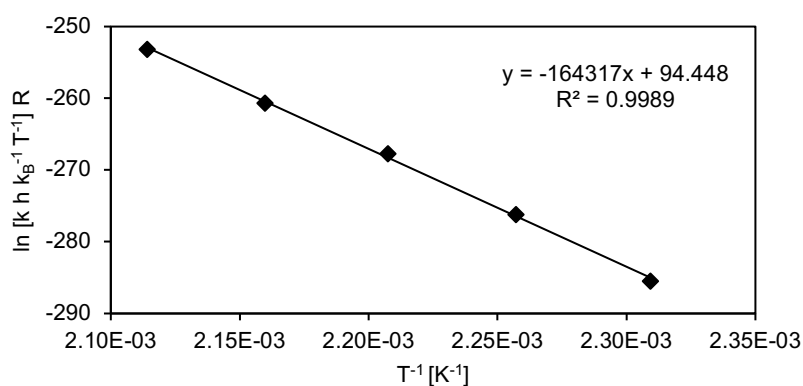


**Figure S2.26.**  $\Delta H^{\ddagger}$  (164 kJ mol<sup>-1</sup>) and  $\Delta S^{\ddagger}$  (+94 J mol<sup>-1</sup> K<sup>-1</sup>) for **4-methylcyclohexanol** (0.5 M) dehydration, **BEA**.

**Table S2.26.** Kinetic data for **4-methylcyclohexanol** (0.5 M) dehydration, **BEA**.

T (°C)	T (K)	TOF (s <sup>-1</sup> )	ln [k h k <sub>B</sub> <sup>-1</sup> T <sup>-1</sup> ] R	T <sup>-1</sup> (K <sup>-1</sup> )
160	433	1.11×10 <sup>-2</sup>	-285.46	2.31×10 <sup>-3</sup>
170	443	3.44×10 <sup>-2</sup>	-276.20	2.26×10 <sup>-3</sup>
180	453	9.81×10 <sup>-2</sup>	-267.69	2.21×10 <sup>-3</sup>
190	463	2.33×10 <sup>-1</sup>	-260.68	2.16×10 <sup>-3</sup>
200	473	5.89×10 <sup>-1</sup>	-253.15	2.11×10 <sup>-3</sup>

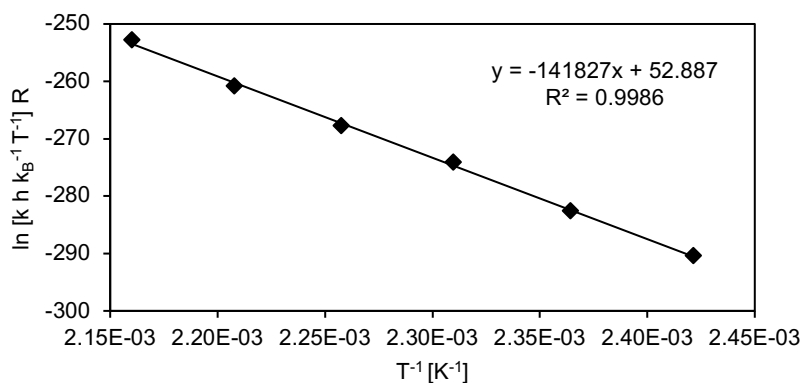


**Figure S2.27.**  $\Delta H^{\ddagger}$  (142 kJ mol<sup>-1</sup>) and  $\Delta S^{\ddagger}$  (+53 J mol<sup>-1</sup> K<sup>-1</sup>) for **4-methylcyclohexanol** (0.5 M) dehydration, **MFI**.

**Table S2.27.** Kinetic data for **4-methylcyclohexanol** (0.5 M) dehydration, **MFI**.

T (°C)	T (K)	TOF (s <sup>-1</sup> )	$\ln [k h k_B^{-1} T^{-1}] R$	$T^{-1} (K^{-1})$
140	413	$5.83 \times 10^{-3}$	-290.38	$2.42 \times 10^{-3}$
150	423	$1.53 \times 10^{-2}$	-282.55	$2.36 \times 10^{-3}$
160	433	$4.31 \times 10^{-2}$	-274.16	$2.31 \times 10^{-3}$
170	443	$9.50 \times 10^{-2}$	-267.77	$2.26 \times 10^{-3}$
180	453	$2.24 \times 10^{-1}$	-260.84	$2.21 \times 10^{-3}$
190	463	$6.03 \times 10^{-1}$	-252.77	$2.16 \times 10^{-3}$

## 2° alcohol: 2-methylcyclohexanol

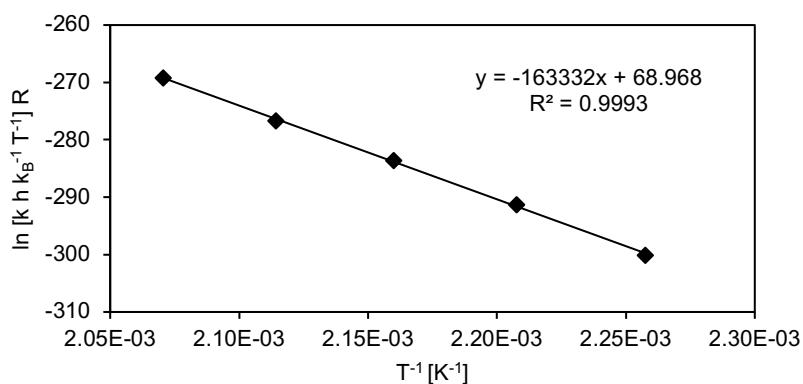


**Figure S2.28.**  $\Delta H^{\ddagger}$  (163 kJ mol<sup>-1</sup>) and  $\Delta S^{\ddagger}$  (+69 J mol<sup>-1</sup> K<sup>-1</sup>) for **trans-2-methylcyclohexanol** (44 mM) dehydration, **H<sub>3</sub>PO<sub>4</sub>**.

**Table S2.28.** Kinetic data for *trans*-2-methylcyclohexanol (44 mM) dehydration,  $\text{H}_3\text{PO}_4$ .

T (°C)	T (K)	k (L mol <sup>-1</sup> s <sup>-1</sup> )	TOF (s <sup>-1</sup> )	ln [k h k <sub>B</sub> <sup>-1</sup> T <sup>-1</sup> ] R	T <sup>-1</sup> (K <sup>-1</sup> )
170	443	1.96×10 <sup>-3</sup>	8.58×10 <sup>-5</sup>	-300.04	2.26×10 <sup>-3</sup>
180	453	5.78×10 <sup>-3</sup>	2.53×10 <sup>-4</sup>	-291.23	2.21×10 <sup>-3</sup>
190	463	1.49×10 <sup>-2</sup>	6.52×10 <sup>-4</sup>	-283.54	2.16×10 <sup>-3</sup>
200	473	3.48×10 <sup>-2</sup>	1.52×10 <sup>-3</sup>	-276.66	2.11×10 <sup>-3</sup>
210	483	8.74×10 <sup>-2</sup>	3.83×10 <sup>-3</sup>	-269.18	2.07×10 <sup>-3</sup>

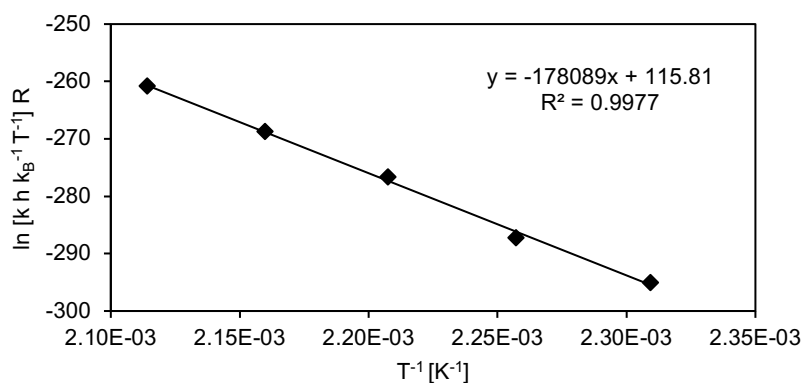


**Figure S2.29.**  $\Delta H^{\ddagger}$  (178 kJ mol<sup>-1</sup>) and  $\Delta S^{\ddagger}$  (+116 J mol<sup>-1</sup> K<sup>-1</sup>) for *trans*-2-methylcyclohexanol (44 mM) dehydration, **BEA**.

**Table S2.29.** Kinetic data for *trans*-2-methylcyclohexanol (44 mM) dehydration, **BEA**.

T (°C)	T (K)	TOF (s <sup>-1</sup> )	ln [k h k <sub>B</sub> <sup>-1</sup> T <sup>-1</sup> ] R	T <sup>-1</sup> (K <sup>-1</sup> )
160	433	3.50×10 <sup>-3</sup>	-295.03	2.31×10 <sup>-3</sup>
170	443	9.27×10 <sup>-3</sup>	-287.25	2.26×10 <sup>-3</sup>
180	453	3.32×10 <sup>-2</sup>	-276.69	2.21×10 <sup>-3</sup>
190	463	8.83×10 <sup>-2</sup>	-268.74	2.16×10 <sup>-3</sup>
200	473	2.34×10 <sup>-1</sup>	-260.81	2.11×10 <sup>-3</sup>

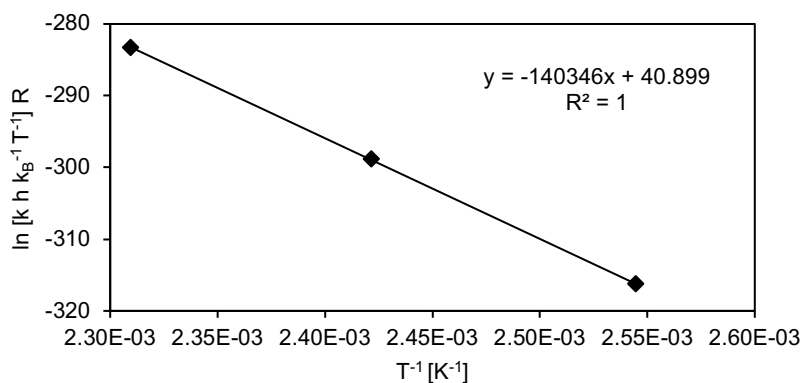


**Figure S2.30.**  $\Delta H^{\ddagger}$  (140 kJ mol<sup>-1</sup>) and  $\Delta S^{\ddagger}$  (+41 J mol<sup>-1</sup> K<sup>-1</sup>) for *trans*-2-methylcyclohexanol (44 mM) dehydration, MFI.

**Table S2.30.** Kinetic data for *trans*-2-methylcyclohexanol (44 mM) dehydration, MFI.

T (°C)	T (K)	TOF (s <sup>-1</sup> )	$\ln [k h k_B^{-1} T^{-1}] R$	$T^{-1} (K^{-1})$
120	413	$2.74 \times 10^{-4}$	-316.26	$2.54 \times 10^{-3}$
140	413	$2.11 \times 10^{-3}$	-298.82	$2.42 \times 10^{-3}$
160	433	$1.44 \times 10^{-3}$	-283.28	$2.31 \times 10^{-3}$

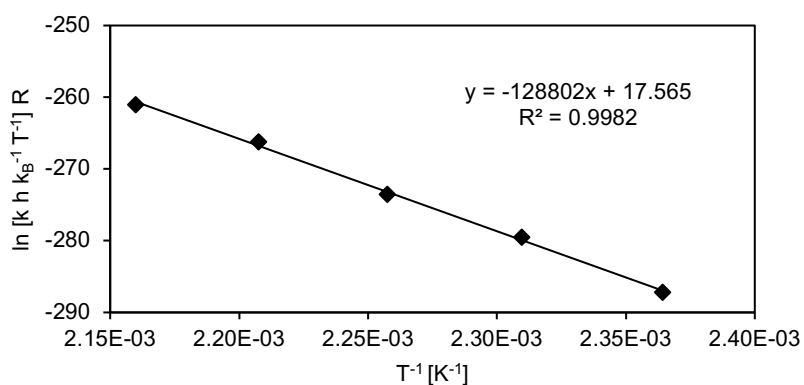


**Figure S2.31.**  $\Delta H^{\ddagger}$  (129 kJ mol<sup>-1</sup>) and  $\Delta S^{\ddagger}$  (+18 J mol<sup>-1</sup> K<sup>-1</sup>) for 2-methylcyclohexanol (0.2 M) dehydration, H<sub>3</sub>PO<sub>4</sub>.

**Table S2.31.** Kinetic data for **2-methylcyclohexanol** (0.2 M) dehydration, **H<sub>3</sub>PO<sub>4</sub>**.

T (°C)	T (K)	k (L mol <sup>-1</sup> s <sup>-1</sup> )	TOF (s <sup>-1</sup> )	ln [k h k <sub>B</sub> <sup>-1</sup> T <sup>-1</sup> ] R	T <sup>-1</sup> (K <sup>-1</sup> )
150	423	8.76×10 <sup>-3</sup>	1.75×10 <sup>-3</sup>	-287.20	2.36×10 <sup>-3</sup>
160	433	2.26×10 <sup>-2</sup>	4.52×10 <sup>-3</sup>	-279.52	2.31×10 <sup>-3</sup>
170	443	4.79×10 <sup>-2</sup>	9.57×10 <sup>-3</sup>	-273.47	2.26×10 <sup>-3</sup>
180	453	1.17×10 <sup>-1</sup>	2.35×10 <sup>-2</sup>	-266.20	2.21×10 <sup>-3</sup>
190	463	2.24×10 <sup>-1</sup>	4.48×10 <sup>-2</sup>	-261.01	2.16×10 <sup>-3</sup>

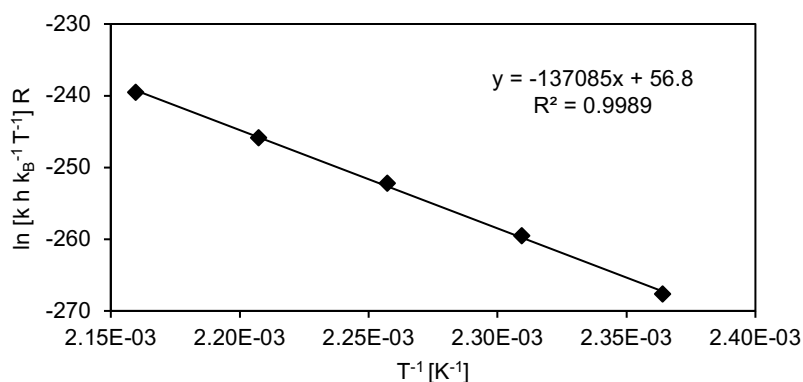


**Figure S2.32.**  $\Delta H^{\ddagger}$  (137 kJ mol<sup>-1</sup>) and  $\Delta S^{\ddagger}$  (+57 J mol<sup>-1</sup> K<sup>-1</sup>) for **2-methylcyclohexanol** (0.5 M) dehydration, **BEA**.

**Table S2.32.** Kinetic data for **2-methylcyclohexanol** (0.5 M) dehydration, **BEA**.

T (°C)	T (K)	TOF (s <sup>-1</sup> )	ln [k h k <sub>B</sub> <sup>-1</sup> T <sup>-1</sup> ] R	T <sup>-1</sup> (K <sup>-1</sup> )
150	423	9.17×10 <sup>-2</sup>	-267.68	2.36×10 <sup>-3</sup>
160	433	2.50×10 <sup>-1</sup>	-259.53	2.31×10 <sup>-3</sup>
170	443	6.18×10 <sup>-1</sup>	-252.20	2.26×10 <sup>-3</sup>
180	453	1.36	-245.84	2.21×10 <sup>-3</sup>
190	463	2.95	-239.57	2.16×10 <sup>-3</sup>

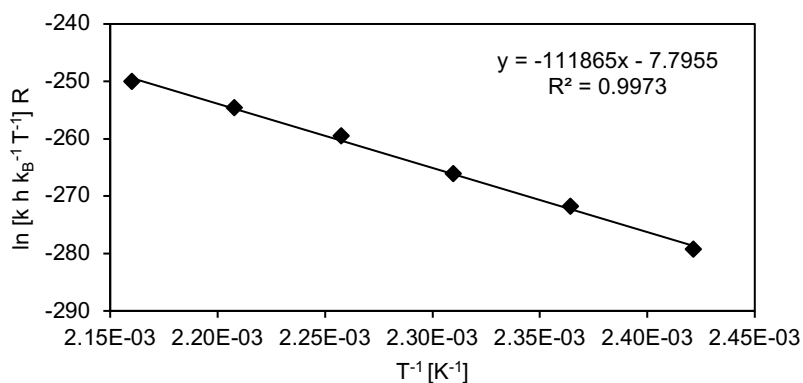


**Figure S2.33.**  $\Delta H^{\ddagger}$  (112 kJ mol<sup>-1</sup>) and  $\Delta S^{\ddagger}$  (-8 J mol<sup>-1</sup> K<sup>-1</sup>) for **2-methylcyclohexanol** (0.5 M) dehydration, **MFI**.

**Table S2.33.** Kinetic data for **2-methylcyclohexanol** (0.5 M) dehydration, **MFI**.

T (°C)	T (K)	TOF (s <sup>-1</sup> )	$\ln [k h k_B^{-1} T^{-1}] R$	$T^{-1} (K^{-1})$
140	413	$2.21 \times 10^{-2}$	-279.33	$2.42 \times 10^{-3}$
150	423	$5.61 \times 10^{-2}$	-271.76	$2.36 \times 10^{-3}$
160	433	$1.13 \times 10^{-1}$	-266.13	$2.31 \times 10^{-3}$
170	443	$2.54 \times 10^{-1}$	-259.59	$2.26 \times 10^{-3}$
180	453	$4.69 \times 10^{-1}$	-254.67	$2.21 \times 10^{-3}$
190	463	$8.39 \times 10^{-1}$	-250.03	$2.16 \times 10^{-3}$

### 3° alcohol: 1-methylcyclohexanol

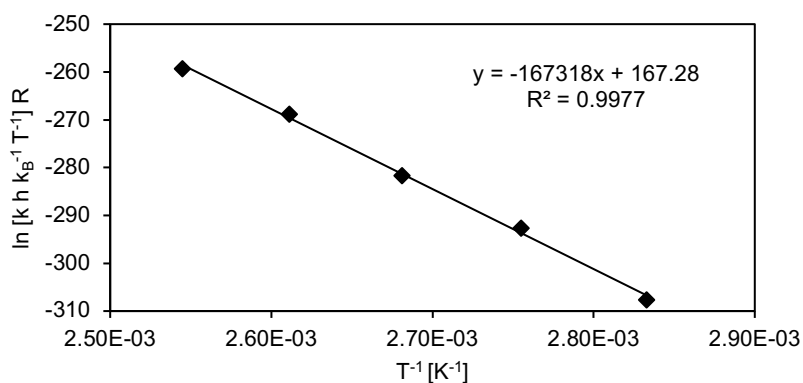


**Figure S2.34.**  $\Delta H^{\ddagger}$  (167 kJ mol<sup>-1</sup>) and  $\Delta S^{\ddagger}$  (+167 J mol<sup>-1</sup> K<sup>-1</sup>) for **1-methylcyclohexanol** (0.1 M) dehydration, **H<sub>3</sub>PO<sub>4</sub>**.

**Table S2.34.** Kinetic data for **1-methylcyclohexanol** (0.1 M) dehydration, **H<sub>3</sub>PO<sub>4</sub>**.

T (°C)	T (K)	k (L mol <sup>-1</sup> s <sup>-1</sup> )	TOF (s <sup>-1</sup> )	ln [k h k <sub>B</sub> <sup>-1</sup> T <sup>-1</sup> ] R	T <sup>-1</sup> (K <sup>-1</sup> )
80	353	6.31×10 <sup>-4</sup>	6.31×10 <sup>-5</sup>	-307.58	2.83×10 <sup>-3</sup>
90	363	3.95×10 <sup>-3</sup>	3.95×10 <sup>-4</sup>	-292.55	2.76×10 <sup>-3</sup>
100	373	1.52×10 <sup>-2</sup>	1.52×10 <sup>-3</sup>	-281.57	2.68×10 <sup>-3</sup>
110	383	7.28×10 <sup>-2</sup>	7.28×10 <sup>-3</sup>	-268.77	2.61×10 <sup>-3</sup>
120	393	2.35×10 <sup>-1</sup>	2.35×10 <sup>-2</sup>	-259.25	2.55×10 <sup>-3</sup>

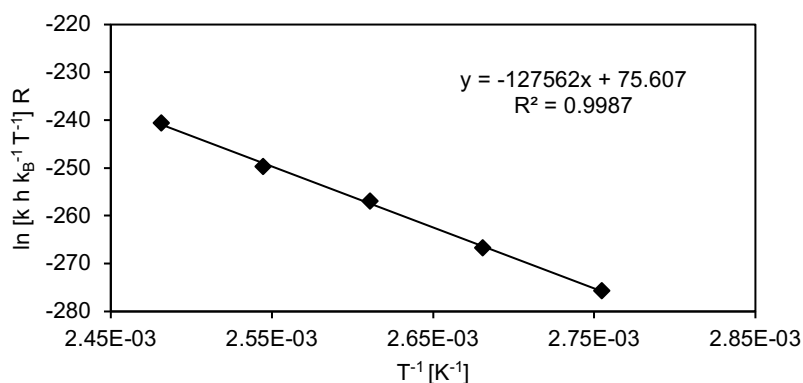


**Figure S2.35.**  $\Delta H^{\ddagger}$  (128 kJ mol<sup>-1</sup>) and  $\Delta S^{\ddagger}$  (+76 J mol<sup>-1</sup> K<sup>-1</sup>) for **1-methylcyclohexanol** (0.5 M) dehydration, **BEA**.

**Table S2.35.** Kinetic data for **1-methylcyclohexanol** (0.5 M) dehydration, **BEA**.

T (°C)	T (K)	TOF (s <sup>-1</sup> )	ln [k h k <sub>B</sub> <sup>-1</sup> T <sup>-1</sup> ] R	T <sup>-1</sup> (K <sup>-1</sup> )
90	363	3.03×10 <sup>-2</sup>	-275.63	2.75×10 <sup>-3</sup>
100	373	9.08×10 <sup>-2</sup>	-266.71	2.68×10 <sup>-3</sup>
110	383	3.01×10 <sup>-1</sup>	-256.98	2.61×10 <sup>-3</sup>
120	393	7.43×10 <sup>-1</sup>	-249.68	2.54×10 <sup>-3</sup>
130	403	2.28	-240.55	2.48×10 <sup>-3</sup>

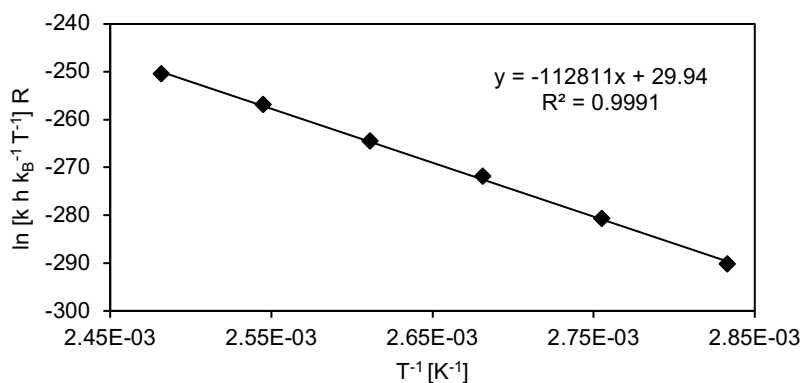


**Figure S2.36.**  $\Delta H^{\ddagger}$  (113 kJ mol<sup>-1</sup>) and  $\Delta S^{\ddagger}$  (+30 J mol<sup>-1</sup> K<sup>-1</sup>) for **1-methylcyclohexanol** (0.5 M) dehydration, **MFI**.

**Table S2.36.** Kinetic data for **1-methylcyclohexanol** (0.5 M) dehydration, **MFI**.

T (°C)	T (K)	TOF (s <sup>-1</sup> )	$\ln [k h k_B^{-1} T^{-1}] R$	$T^{-1} (K^{-1})$
80	353	$5.11 \times 10^{-3}$	-290.18	$2.83 \times 10^{-3}$
90	363	$1.65 \times 10^{-2}$	-280.67	$2.75 \times 10^{-3}$
100	373	$4.86 \times 10^{-2}$	-271.91	$2.68 \times 10^{-3}$
110	383	$1.22 \times 10^{-1}$	-264.50	$2.61 \times 10^{-3}$
120	393	$3.11 \times 10^{-1}$	-256.91	$2.54 \times 10^{-3}$
130	403	$6.89 \times 10^{-1}$	-250.51	$2.48 \times 10^{-3}$

Summary of Arrhenius plots and correlation of  $\Delta H^{\ddagger}$  and  $\Delta S^{\ddagger}$

1° alcohol: 2-cyclohexylethanol

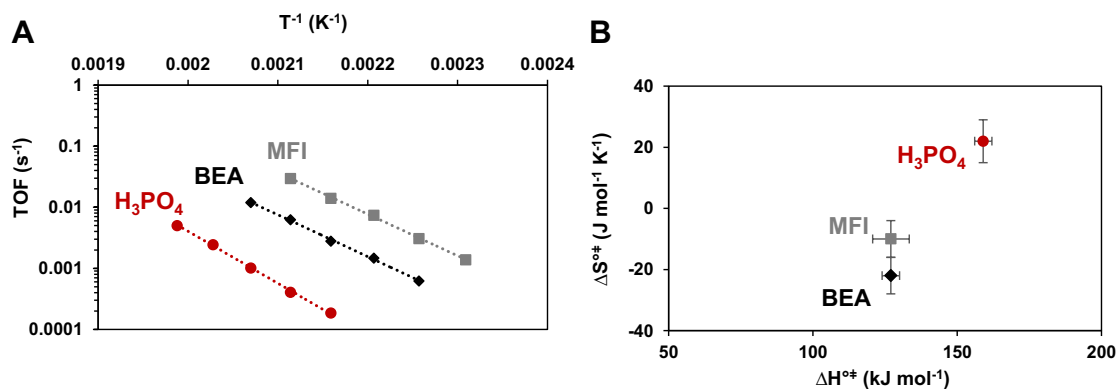


**Figure S2.37.** Arrhenius plots for **2-cyclohexylethanol** dehydration catalyzed by zeolites and H<sub>3</sub>PO<sub>4</sub> (A); Correlation of  $\Delta H^{\ddagger}$  and  $\Delta S^{\ddagger}$  values for the dehydration of **2-cyclohexylethanol** (B).

2° alcohol: 4-methylcyclohexanol

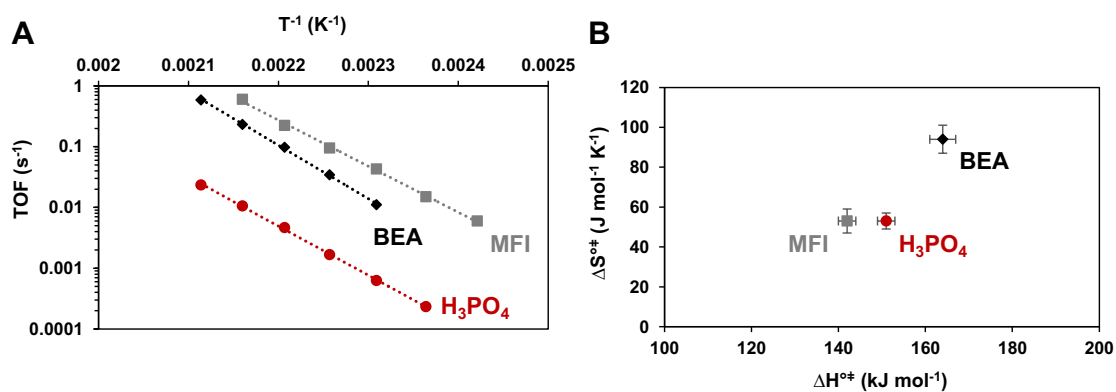


**Figure S2.38.** Arrhenius plots for **4-methylcyclohexanol** dehydration catalyzed by zeolites and H<sub>3</sub>PO<sub>4</sub> (A); Correlation of  $\Delta H^{\ddagger}$  and  $\Delta S^{\ddagger}$  values for the dehydration of **4-methylcyclohexanol** (B).

2° alcohol: 2-methylcyclohexanol

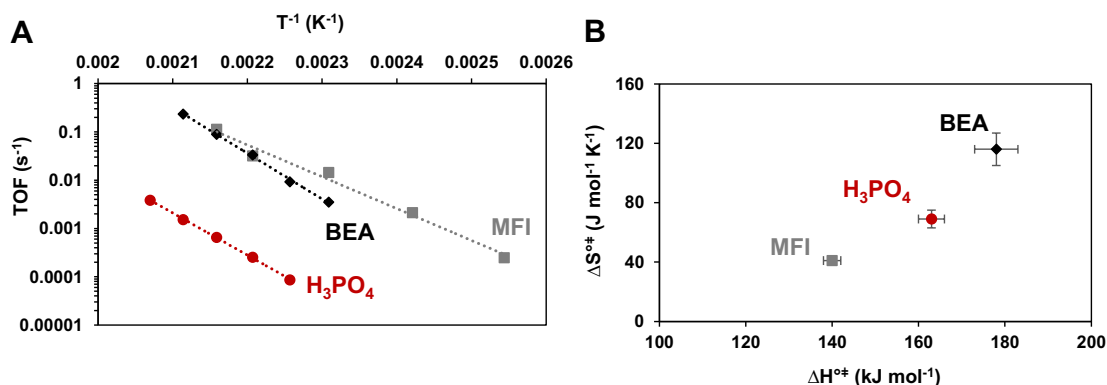


**Figure S2.39.** Arrhenius plots for *trans*-2-methylcyclohexanol dehydration catalyzed by zeolites and H<sub>3</sub>PO<sub>4</sub> (A) (for MFI the original data was presented previously in reference 1, additional data was measured at 180°C and 190°C); Correlation of ΔH<sup>‡</sup> and ΔS<sup>‡</sup> values for the dehydration of *trans*-2-methylcyclohexanol (B) (for MFI the original data were presented previously in reference 1).

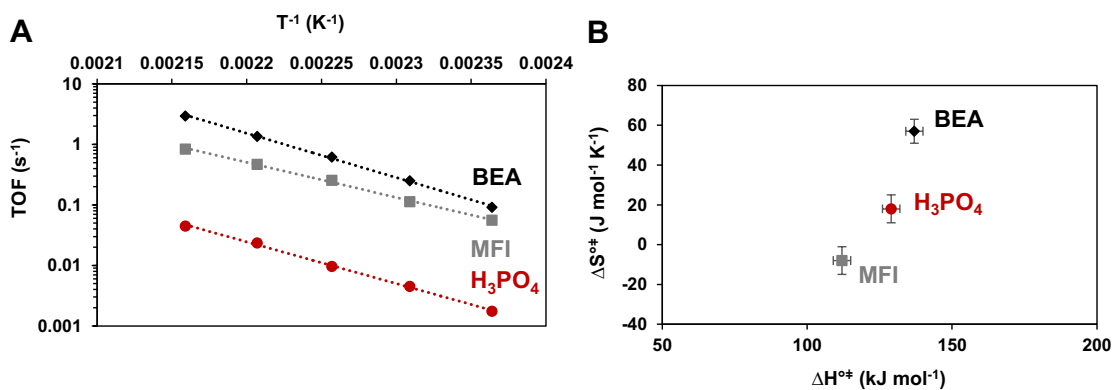


**Figure S2.40.** Arrhenius plots for *cis*-2-methylcyclohexanol dehydration catalyzed by zeolites and H<sub>3</sub>PO<sub>4</sub> (A); Correlation of ΔH<sup>‡</sup> and ΔS<sup>‡</sup> values for the dehydration of *cis*-2-methylcyclohexanol (B).

3° alcohol: 1-methylcyclohexanol

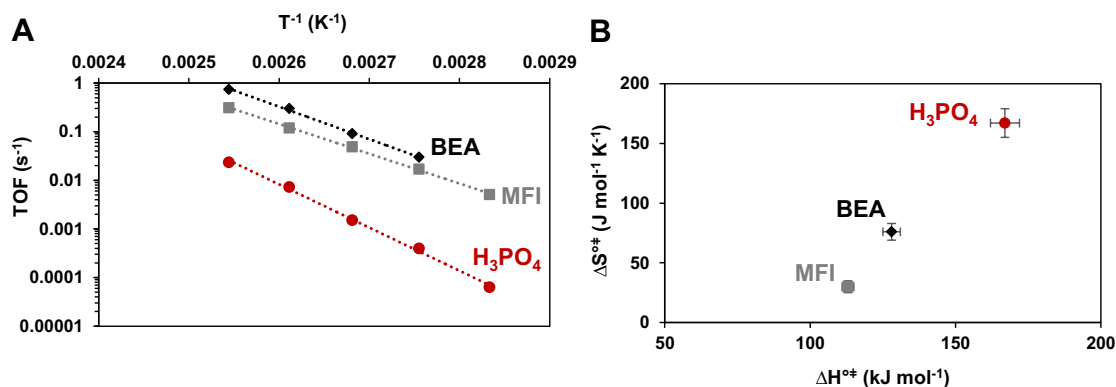


**Figure S2.41.** Arrhenius plots for **1-methylcyclohexanol** dehydration catalyzed by zeolites and H<sub>3</sub>PO<sub>4</sub> (A); Correlation of ΔH<sup>‡</sup> and ΔS<sup>‡</sup> values for the dehydration of **1-methylcyclohexanol** (B).

Adsorption measurements

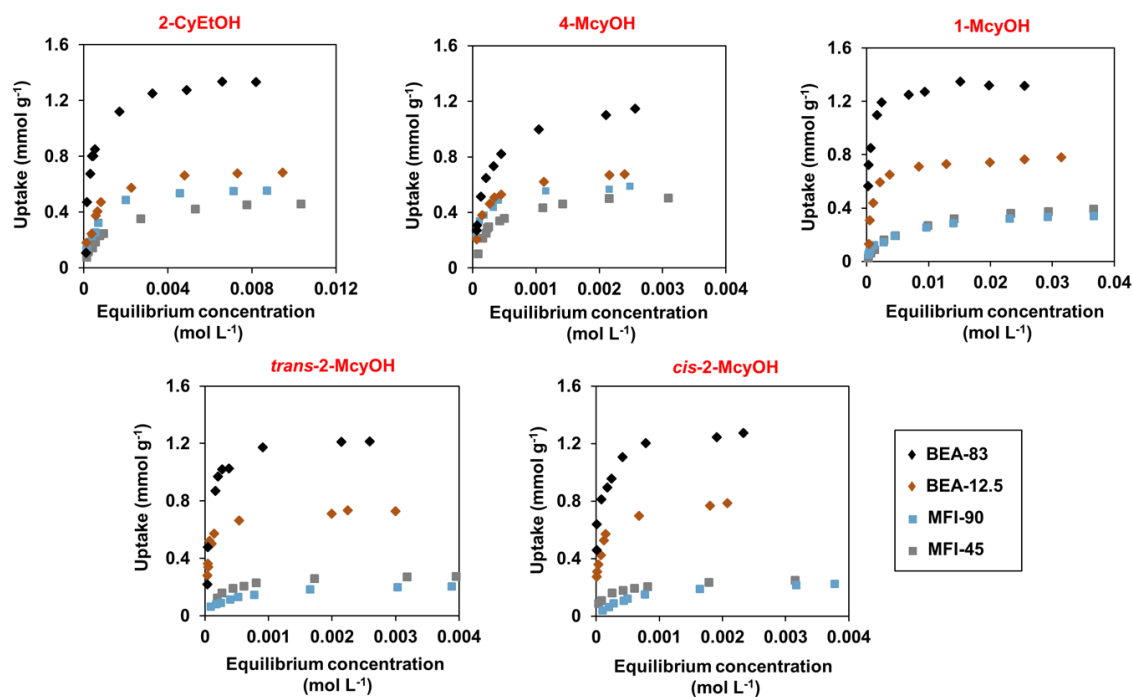


**Figure S2.42.** Adsorption measurements of primary, secondary and tertiary alcohols on MFI-45 (BAS/360 μmol g<sup>-1</sup>), MFI-90 (BAS/150 μmol g<sup>-1</sup>), BEA-12.5 (BAS/402 μmol g<sup>-1</sup>) and BEA-83 (BAS/120 μmol g<sup>-1</sup>).

## Configurational entropy

**Table S2.37.** Estimates for the calculation of the configurational entropy.

		2-CyEtOH	<i>cis</i> -2-McyOH	4-McyOH	<i>trans</i> -2-McyOH	1-McyOH
<b>Ground State</b>						
MFI-45	Substrate/BAS ratio in the pores	1.42	0.67	1.50	0.81	1.25
BEA-83		11.58	10.42	9.50	10.42	11.25
MFI-45	Number of hydrated hydronium ion clusters	1	1	1	1	1
BEA-83		1	1	1	1	1
MFI-45	n: total number of molecules	2.42	1.67	2.50	1.81	2.25
BEA-83		12.58	11.42	10.50	11.42	12.25
<b>Transition State</b>						
MFI-45	Number of released water molecules	0	0	8 <sup>a</sup>	6.48 <sup>a</sup>	8 <sup>a</sup>
BEA-83		0	0	12 <sup>b</sup>	12 <sup>b</sup>	12 <sup>b</sup>
MFI-45	Number of transition complex	1	0.67	1	0.81	1
BEA-83		1	1	1	1	1
MFI-45	Number of residual substrate	0.42	0	0.50	0	0.25
BEA-83		10.58	9.42	8.50	9.42	10.25
MFI-45	Number of residual hydronium ion	0	0.33	0	0.19	0
BEA-83		0	0	0	0	0
MFI-45	n: total number of molecules	1.42	1	9.50	7.48	9.25
BEA-83		11.58	10.42	21.50	22.42	23.25

<sup>a</sup>Number of water molecules involved in a hydrated hydronium ion cluster from reference 2. <sup>b</sup>Estimated based on results from reference 2.

Selective energy transfer

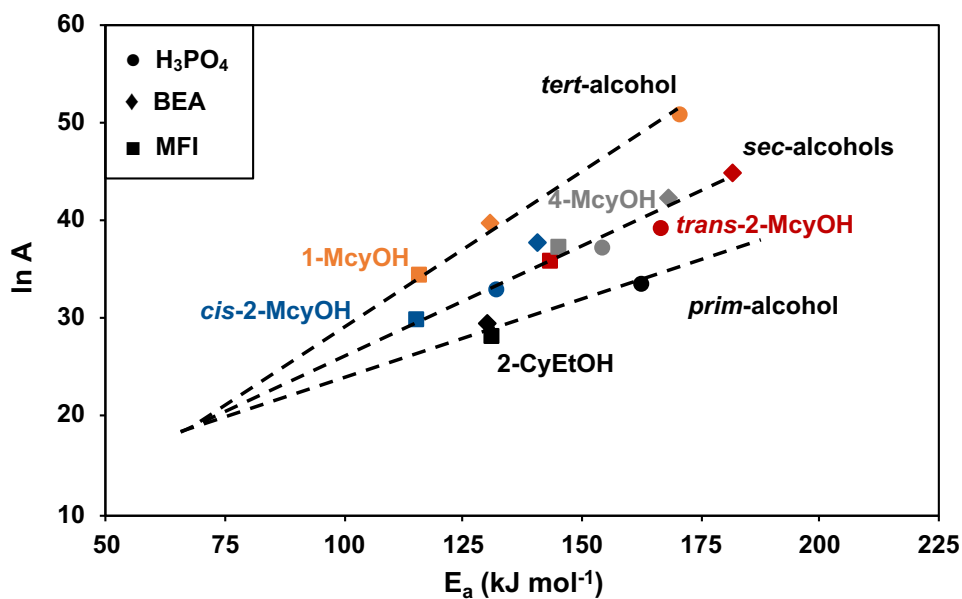


**Figure S2.43.** Compensation effect by the linear correlation of  $\ln A$  (the Arrhenius pre-exponential factor) and  $E_a$  for primary, secondary and tertiary cyclic alcohols of the studied acid catalysts.

**Table S2.38.** Application of the selective energy transfer model<sup>3</sup>, in the case of no full resonance.

Substrate	$\Delta(\Delta H^{\ddagger})$ (kJ/mol)	$\Delta_{\text{abbreviated}}$ (kJ/mol)	$n'$	$E_0: \frac{\sum \Delta(\Delta H^{\ddagger})}{\sum n'}$ (kJ/mol)	$\Delta H^{\ddagger} / E_0$	$n$
	0	0	0		23.81	24
2-CyEtOH	32	30	6	5.33	23.81	24
	32	30	6		29.81	30
Sum	64		12			
	38	40	8		28.57	29
4-MCyOH	15	15	3		36.33	36
	51	50	10		33.27	33
	25	25	5		22.86	23
trans-2-MCyOH	8	10	2	4.90	27.96	28
	13	15	3		26.33	26
	22	20	4		28.98	29
cis-2-MCyOH	13	15	3		33.47	34
	11	10	2		30.82	31
Sum	196		40			
	15	15	3		23.02	23
1-MCyOH	39	40	8	4.91	26.07	26
	54	55	11		34.02	34
Sum	108		22			

**Table S2.39.** Parameters after fitting  $\Delta H^{\ddagger}$  to a second-order function of  $n$ ,  $\Delta H^{\ddagger} = M_0 + M_1n + M_2n^2$ , including the origin (0,0).  $M_1$  corresponds to  $\omega$ .

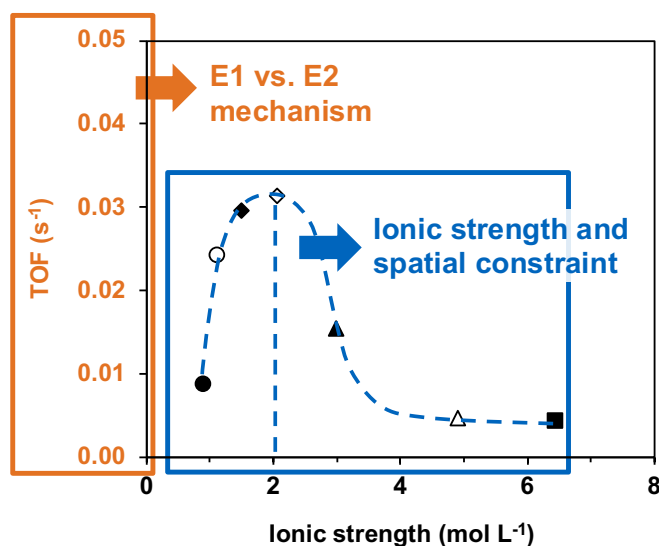
Substrate	$M_0$ (kJ/mol)	$M_1$ (kJ/mol)	$M_2$ (kJ/mol)
Primary alcohol	$1.4211 \times 10^{-14}$	5.2583	0.0014
Secondary alcohols	0.0519	4.8435	0.0015
Tertiary alcohol	-0.0048	4.9314	-0.0005

### 2.7.3 References of the supporting information

- (1) Hintermeier, P. H.; Eckstein, S.; Mei, D.; Olarte, M. V.; Camaioni, D. M.; Baráth, E.; Lercher, J. A. Hydronium-Ion-Catalyzed Elimination Pathways of Substituted Cyclohexanols in Zeolite H-ZSM5. *ACS Catalysis* **2017**, 7 (11), 7822.
- (2) Eckstein, S.; Hintermeier, P. H.; Zhao, R.; Baráth, E.; Shi, H.; Liu, Y.; Lercher, J. A. Influence of Hydronium Ions in Zeolites on Sorption. *Angewandte Chemie International Edition* **2019**, 58 (11), 3450.
- (3) Bratlie, K. M.; Li, Y.; Larsson, R.; Somorjai, G. A. Compensation Effect of Benzene Hydrogenation on Pt(111) and Pt(100) Analyzed by the Selective Energy Transfer Model. *Catalysis Letters* **2008**, 121 (3), 173.

# Chapter 3

## Influence of intracrystalline ionic strength in MFI zeolites on aqueous phase dehydration of methylcyclohexanols



### This work has been published

Reprinted with permission from: Milaković, L.; Hintermeier, P. H.; Liu, Y.; Baráth, E.; Lercher, J. A. Influence of Intracrystalline Ionic Strength in MFI Zeolites on Aqueous Phase Dehydration of Methylcyclohexanols. *Angewandte Chemie International Edition* **2021**, 60 (47), 24806. DOI: 10.1002/anie.202107947

Copyright (2023) Wiley.

## Abstract

The impact of the concentration of hydrated hydronium ions and in turn of the local ionic strength in MFI zeolites has been investigated for the aqueous phase dehydration of 4-methylcyclohexanol (E1 mechanism) and *cis*-2-methylcyclohexanol (E2 mechanism). The E2 pathway with the latter alcohol led to a 2.5-fold higher activity. The catalytic activity normalized to the hydronium ions (turnover frequency, TOF) passed through a pronounced maximum, which is attributed to the increasing excess chemical potential of the alcohols in the pores, increasing in parallel with the ionic strength and the additional work caused by repulsive interactions and charge separation induced by the bulky alcohols. While the maximum in rate observed is invariant with the mechanism or substitution, the reaction pathway is influencing the activation parameters differently.

## 3.1 Introduction

Zeolitic Brønsted acid sites (BAS) are generated by substitution of metal cations with a 3+ charge to the framework Si<sup>4+</sup>-oxygen tetrahedra. Although often denoted as a “proton”, i.e., a H<sup>+</sup>, the acid site is intrinsically a charge-neutral hydroxyl group in which the hydrogen atom is covalently bonded to the oxygen bridging between Si and Al based tetrahedra. In gas phase, BAS of a specific type of zeolite tend to have a similar acid strength and, therefore, act catalytically similarly on reactive substrates.<sup>1,2</sup> Stronger deviations occur, if the zeolite has pronounced differences in the Al locations, a substantial concentration of extra-framework Al, and Al concentrations that lead to substantial concentration of aluminum as next nearest neighbors.<sup>3-6</sup>

Zeolites tend to be unstable in aqueous phase at elevated temperatures.<sup>7,8</sup> Recent studies showed, however, that the zeolite frameworks tend to be stable for a prolonged time in aqueous phase, if temperatures do not exceed 180°C.<sup>9,10</sup> The suitability of the solid acids as catalyst for converting oxo-functionalized molecules derived from renewable resources, has led to a quite intense exploration of molecular sieves in such aqueous environment.<sup>11-13</sup>

It has been shown that in presence of water the covalently bound OH group balancing the charge of aluminum-oxygen tetrahedron is deprotonated, forming a hydrated hydronium ion (abbreviated as H<sub>3</sub>O<sup>+</sup><sub>hydr.</sub>).<sup>14,15</sup> The hydration shell forms a fluxional, positively charged cluster that remains close to the anion in the zeolite lattice. The size of the cluster depends on the micropore size of the zeolite. We have shown its composition to be H<sup>+</sup>(H<sub>2</sub>O)<sub>8</sub> in MFI, creating an empty void between these clusters.<sup>16</sup> Sorbed organic substrates, e.g., cyclohexanol or phenol, may be sorbed in these voids between neighboring hydrated hydronium ions.<sup>16,17</sup>

This transforms the zeolite pores in water into a strongly ionic environment, with the concentration of hydronium ions in the volume of the zeolite pores, approximating liquids with high ionic strength. We have shown that a high intracrystalline ionic strength induces a strong non-ideality and destabilizes a sorbed organic substrate by increasing its excess chemical potential compared to a zeolite pore without acid sites, similarly to

the increase in the excess chemical potential as the ionic strength of an electrolyte solution is increased. The intracrystalline ionic strength increases proportionally to the  $\text{H}_3\text{O}^+$  concentration, leading to a monotonic increase of the standard free energy of adsorption of nonpolar or less polar substrates in zeolite pores.<sup>18</sup>

Using cyclohexanol dehydration to cyclohexene catalyzed by MFI and BEA in water, it was shown recently that the ionic environment in zeolite crystallites stabilizes the cationic transition state, thus, decreasing the reaction barrier and enhancing the reaction rate.<sup>18</sup> This provides a new path to influence the catalytic activity of Brønsted acidic zeolites.

In this work, we investigate, how the intracrystalline ionic strength influences the reaction rate in the dehydration of substituted cyclic alcohols, independent of the reaction mechanism (E1 vs. E2 elimination) respond to the ionic strength and whether variations in the steric hindrance changes the impact of ionic strength.

Two isomers of methylcyclohexanol were chosen for the study, i.e., 4-methylcyclohexanol (4-McyOH) and *cis*-2-methylcyclohexanol (*cis*-2-McyOH). The former is shown to dehydrate *via* an E1 mechanism and can access to all micropore space in MFI channels, while the latter dehydrates *via* an E2 mechanism<sup>19</sup> and can only access part of the MFI micropore space due to its bulkiness. The comparison of the dehydration rates of the two substrates catalyzed by a series of MFI zeolites with varying BAS concentrations allows to address the role of steric challenges and of the nature of the transition state.

## 3.2 Results and discussion

### 3.2.1 Characterization of MFI zeolites

The most important physicochemical properties of the zeolites are compiled in Table 3.1 (additional in 3.6 supporting information, Table S3.1). With increasing Si/Al ratio, the BAS (and hence  $\text{H}_3\text{O}^+_{\text{hydr.}}$ ) decreased from 1.14 to 0.09 mmol g<sup>-1</sup>. The micropore volumes ( $V_{\text{micro}}$ ) were found to be low for MFI with high Si/Al ratio and tended to increase with decreasing Si/Al ratio. The calculated unit cell volumes in Table 3.1 show that the unit cell does not change significantly across all samples studied. Thus, the differences in  $V_{\text{micro}}$  are tentatively attributed to (presumably silica) debris in the pores. By normalizing the BAS concentration (forming quantitatively hydrated hydronium ions) to the micropore volumes the intracrystalline ionic strength was calculated to range from 0.89 to 6.44 mol L<sup>-1</sup> ( $\text{Ionic strength} = c(\text{BAS}) V_{\text{micro}}^{-1}$ ).

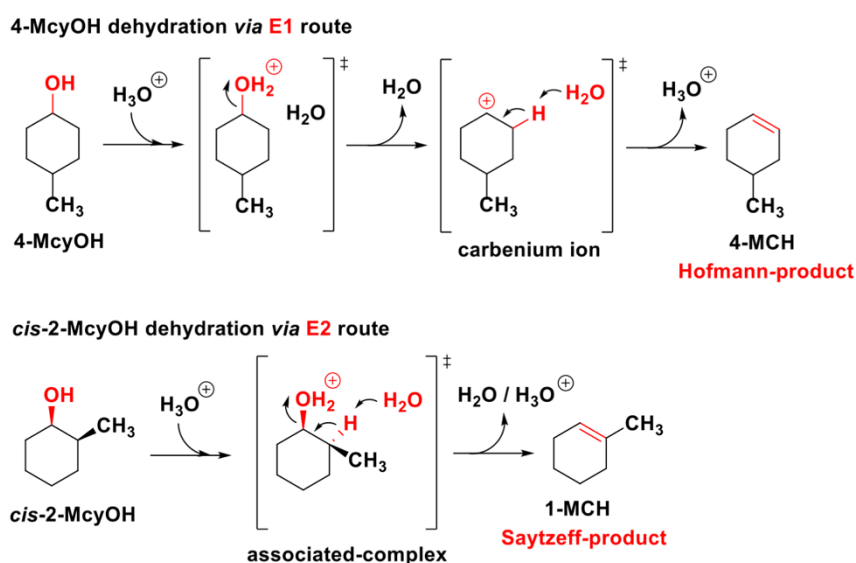
**Table 3.1.** Characterization of the investigated MFI zeolites, measured kinetic (150°C) and activation parameters of 4-McyOH dehydration over MFI zeolites.

Entry	Zeolite	$V_{\text{micro}}$ ( $\text{cm}^3$ $\text{g}^{-1}$ )	Unit cell volume ( $\text{\AA}^3$ ) <sup>[a]</sup>	c (BAS) ( $\text{mmol g}^{-1}$ )	Ionic strength ( $\text{mol L}^{-1}$ )	TOF ( $\text{s}^{-1}$ )	$\Delta G^{\ddagger}$ ( $\text{kJ mol}^{-1}$ )	$\Delta H^{\ddagger}$ ( $\text{kJ mol}^{-1}$ )	$\Delta S^{\ddagger}$ ( $\text{J mol}^{-1} \text{K}^{-1}$ )
1	MFI-193	0.10	5374.4	0.09	0.89	0.009	121 ( $\pm 2$ )	149 ( $\pm 1$ )	66 ( $\pm 3$ )
2	MFI-90 <sup>[b]</sup>	0.13	5376.8	0.15	1.12	0.024	-	-	-
3	MFI-60	0.15	5376.8	0.23	1.51	0.030	117 ( $\pm 6$ )	143 ( $\pm 3$ )	60 ( $\pm 6$ )
4	MFI-45	0.12	5376.7	0.36	3.00	0.015	120 ( $\pm 2$ )	145 ( $\pm 1$ )	59 ( $\pm 3$ )
5	MFI-40	0.15	5372.8	0.31	2.07	0.031	117 ( $\pm 9$ )	141 ( $\pm 5$ )	56 ( $\pm 10$ )
6	MFI-15	0.18	5380.9	0.86	4.92	0.005	124 ( $\pm 7$ )	157 ( $\pm 4$ )	77 ( $\pm 8$ )
7	MFI-12	0.18	5377.3	1.14	6.44	0.004	124 ( $\pm 6$ )	153 ( $\pm 3$ )	68 ( $\pm 7$ )

[a] Derived from XRD (lattice parameters a,b,c in 3.6 supporting information, Table S3.1). [b] Experiment conducted only at 150°C.

### 3.2.2 Dehydration of 2- and 4-methylcyclohexanol

Previous investigations have established that *trans*-2-McyOH and 4-McyOH (*cis/trans*) dehydrate *via* carbenium ion intermediates following an E1 mechanism.<sup>19</sup> 4-McyOH is thereby predominately dehydrated to 4-methylcyclohexene (4-MCH), which represents the Hofmann-product (Scheme 3.1).<sup>19,20</sup>



**Scheme 3.1.** Dehydration mechanism of 4-McyOH (E1) and *cis*-2-McyOH (E2).<sup>19</sup>

In contrast, the concerted E2 mechanism was concluded to dominate in the dehydration of *cis*-2-McyOH, which almost exclusively resulted in the formation of the Saytzeff-product 1-methylcyclohexene (1-MCH) (Scheme 3.1).<sup>19,21</sup> The *cis* isomer shows a 30  $\text{kJ mol}^{-1}$  lower activation barrier than the *trans* isomer and, therefore, is converted preferentially in a racemic mixture of both isomers. The reaction order in 2- and 4-McyOH was zero for MFI zeolites; consequently, it is assumed that the measured activation parameters are representing intrinsic values, i.e., the energy difference between transition state and sorbed substrate (Figures S3.1 – S3.2 and Tables S3.2 – S3.3).<sup>19</sup>

### 3.2.2.1 4-Methylcyclohexanol

The turnover frequencies (TOF) of 4-McyOH dehydration at 150°C on all MFI zeolites are compiled in Table 3.1. The highest TOFs appeared on zeolites (MFI-40 and MFI-60) with BAS concentrations of 0.23 – 0.31 mmol g<sup>-1</sup> and ionic strengths of 1.51 – 2.07 mol L<sup>-1</sup>, respectively. Figure 3.1 A shows a volcano-shaped dependence of the TOF on the ionic strength. A similar trend is also seen when correlating the TOF with the concentration of the hydrated hydronium ions (H<sub>3</sub>O<sup>+</sup><sub>hydr.</sub>) (Figure S3.3). While for lower ionic strength a sharp increase of the TOF was observed, a decreasing trend is present for catalysts with high ionic strength. The volcano-shaped dependence of the TOF on the ionic strength was also consistently found at other reaction temperatures (160 – 190°C, Figure S3.4).

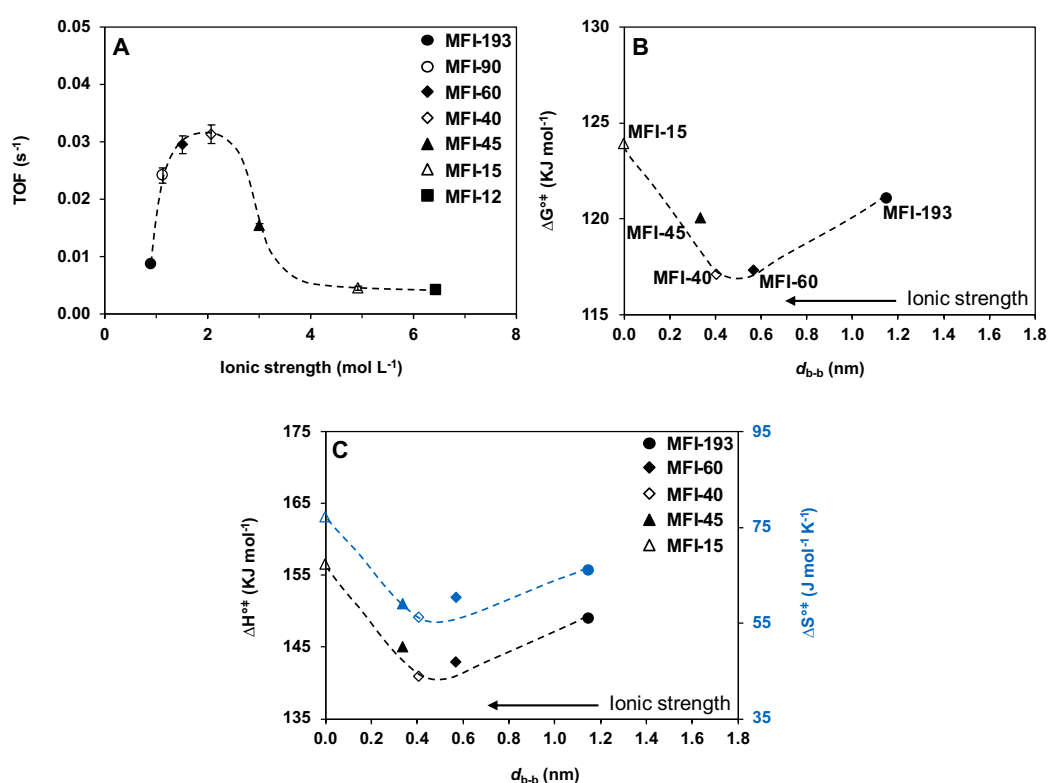


**Figure 3.1.** (A) TOF as a function of ionic strength in the dehydration of 4-McyOH at 150°C. (B)  $\Delta G^{\ddagger}$  and (C)  $\Delta H^{\ddagger}$  (black) and  $\Delta S^{\ddagger}$  (blue) as a function of the distance between hydronium ions ( $d_{b-b}$ ).

As we demonstrated previously,<sup>18</sup> the increasing local ionic strength in the zeolite pores causes the increase in TOFs. This conclusion was drawn unequivocally from a series of Na<sup>+</sup> partly exchanged H-MFI, in which the ionic strength was kept constant while at the same time the H<sub>3</sub>O<sup>+</sup><sub>hydr.</sub> concentration was decreased.<sup>18</sup> Consequently, we conclude that also in the present study, the high ionic strength is responsible for the increasing TOFs by inducing non-ideality to the system. More precisely, the induced ionic environment destabilizes the uncharged sorbed reactant and simultaneously stabilizes the positively charged transition state intermediate (carbenium ion), which in turn results in an overall lowering of the free energy barrier and, therefore, in higher TOFs (Table 3.1).

The marked decrease of the TOF at very high ionic strengths, however, is hypothesized to result from reorganization of the ion pair by the spatial constraints brought by the neighboring  $\text{H}_3\text{O}^+_{\text{hydr.}}$  to the organic substrate residing in between. In order to explore this hypothesis, the distance between the boundaries of neighboring  $\text{H}_3\text{O}^+_{\text{hydr.}}$  ( $d_{b-b}$ ) in the investigated MFIs is plotted against the corresponding activation parameters (Figure 3.1 B and C).  $d_{b-b}$  is calculated by subtracting the length of a hydrated hydronium ion cluster consisting of eight water molecules  $\text{H}^+(\text{H}_2\text{O})_8$ <sup>16</sup> from the distance between two centers of the clusters ( $d_{h-h}$ )<sup>22</sup> (Figure 3.2 A), which is decreasing with decreasing Si/Al ratios and increasing  $\text{H}_3\text{O}^+_{\text{hydr.}}$  concentrations, respectively (Figure 3.2 B). Figure 3.1 B illustrates that for the dehydration of 4-McyOH,  $\Delta G^{\ddagger}$  reaches a minimum at a  $d_{b-b}$  between 0.4 and 0.6 nm. For zeolites with smaller  $d_{b-b}$ , the free energy is increasing although featuring a higher ionic strength.

Once the void space between the hydronium ions is smaller than the volume of one substrate molecule, the repulsion induced by the sorption of molecules and the partial separation of charge *via* a rearrangement of the hydronium ions (combination of electrostatic, hydrogen bonding, and dispersion interactions) sets in in constrained systems forcing reorganization in the highly ionic strength environment.<sup>18</sup> The additional work resulting from the partial separation of the negative charge at the zeolite lattice and the positive charge (particularly for the transition state) that has to be overcome, causes an increase of the free energy and, therefore, a decrease of the TOF.

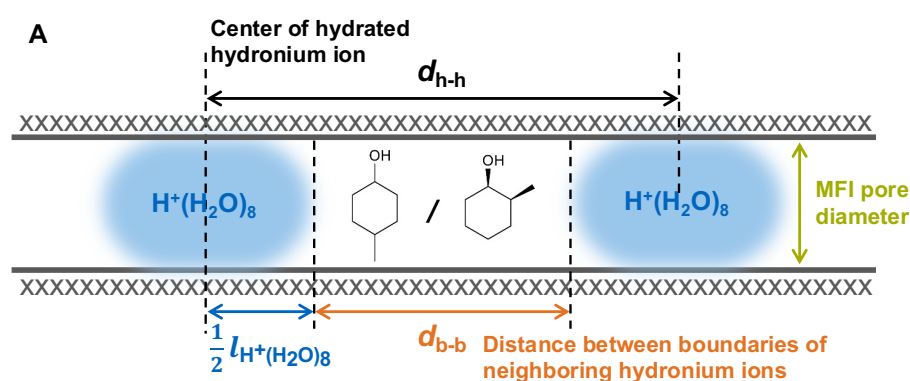


**Figure 3.2 A.** Illustration of the distance between the boundaries of neighboring hydronium ions ( $d_{b-b}$ ) in the MFI pores adapted from reference 16. The distance between the centers of hydrated hydronium ions ( $d_{h-h}$ ) is estimated by the cubic root of the average zeolite volume normalized to the number of hydronium ions.<sup>16,22</sup> The  $\text{H}^+(\text{H}_2\text{O})_8$  cluster is assumed to be cylindrical with the diameter of the H-MFI zeolite micropore channel.<sup>23</sup>

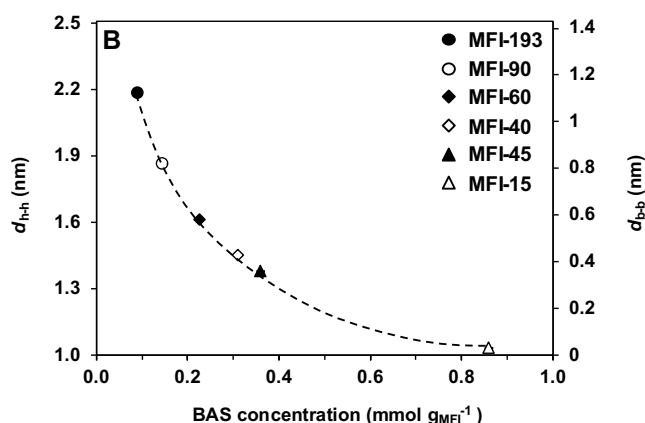


**Figure 3.2 B.**  $d_{h-h}$  and  $d_{b-b}$  as function of the BAS concentration.

In open systems<sup>18</sup> the TOF increased monotonically with increasing ionic strength without passing through a maximum. The sorption in the environment of higher ionic strength is compensated by volume expansion, which causes minimal additional work.

Alcohol adsorption measurements (Figure S3.17, Table S3.16) confirm that the uptake of 4-McyOH starts to decrease on zeolites with ionic strength higher than 2 mol L<sup>-1</sup>. However, it should be noted that the reaction is not transport limited despite steric constraints as also on these zeolites the reaction order in the alcohol was zero. In parallel with the variations of the free energy, the activation enthalpy and entropy obtained with the investigated MFI zeolites show an equal dependency on  $d_{b-b}$ . As soon as  $d_{b-b}$  falls below 0.4 nm, a sharp increase in  $\Delta H^{\ddagger}$  and  $\Delta S^{\ddagger}$  is observed. Despite the beneficial gain in entropy, the high enthalpic barrier more than offsets this contribution, resulting in the aforementioned increase in  $\Delta G^{\ddagger}$ . Longer  $d_{b-b}$  again favor  $\Delta S^{\ddagger}$ , but suffer from a lower stabilization of  $\Delta H^{\ddagger}$  than for zeolites with higher ionic strength.

### 3.2.2.2 *cis*-2-Methylcyclohexanol

The dehydration of *cis*-2-McyOH shows a similar volcano-shaped dependency of the TOF on the ionic strength and the BAS concentration, respectively (Table 3.3, Figure 3.3 A, Figure S3.3). The highest TOFs are again obtained at ionic strengths between 1.51 – 2.07 mol L<sup>-1</sup>. As also in a concerted E2 dehydration pathway, the  $\beta$ -H abstraction (and simultaneous C-O bond cleavage) is the kinetically relevant step, the rate enhancement shows that also transition states in a concerted elimination benefit from a high ionic strength.

Interestingly, the drop of the reaction rates occurs at the symmetric situation as for 4-McyOH and prior for the non-substituted CyOH,<sup>18</sup> irrespective of the higher steric hindrance through the position and orientation of the substituted group or the mechanism pathway.  $\Delta G^{\ddagger}$  is increasing for all three substrates at the same boundary (Figure 3.1 B and 3.3 B), suggesting that the cyclohexyl ring determines the critical size (distance) after which the contribution of the repulsions exceeds the gain from the high local ionic strength. The reorganization penalty seems to have a less severe impact on the associated-complex than on the carbenium ion intermediate. This is demonstrated

by the not as sharply decreasing volcano-plot for the E2 compared to the E1 mechanism (TOF decrease from MFI-40 to MFI-45 ~31% for E2 vs. ~52% for E1).

**Table 3.3.** Characterization of the investigated MFI zeolites, measured kinetic (150°C) and activation parameters of *cis*-2-McyOH dehydration over MFI zeolites.

Entry	Zeolite	Ionic strength (mol L <sup>-1</sup> )	TOF (s <sup>-1</sup> )	$\Delta G^{\ddagger}$ (kJ mol <sup>-1</sup> )	$\Delta H^{\ddagger}$ (kJ mol <sup>-1</sup> )	$\Delta S^{\ddagger}$ (J mol <sup>-1</sup> K <sup>-1</sup> )
1	MFI-193	0.89	0.019	118 (±6)	113 (±3)	-13 (±7)
2	MFI-60	1.51	0.076	114 (±4)	115 (±2)	2 (±4)
3	MFI-45	3.00	0.056	115 (±7)	111 (±4)	-10 (±8)
4	MFI-40	2.07	0.081	114 (±6)	114 (±3)	0 (±7)
5	MFI-15	4.92	0.045	116 (±4)	103 (±2)	-30 (±4)
6	MFI-12	6.44	0.021	119 (±4)	103 (±2)	-37 (±4)

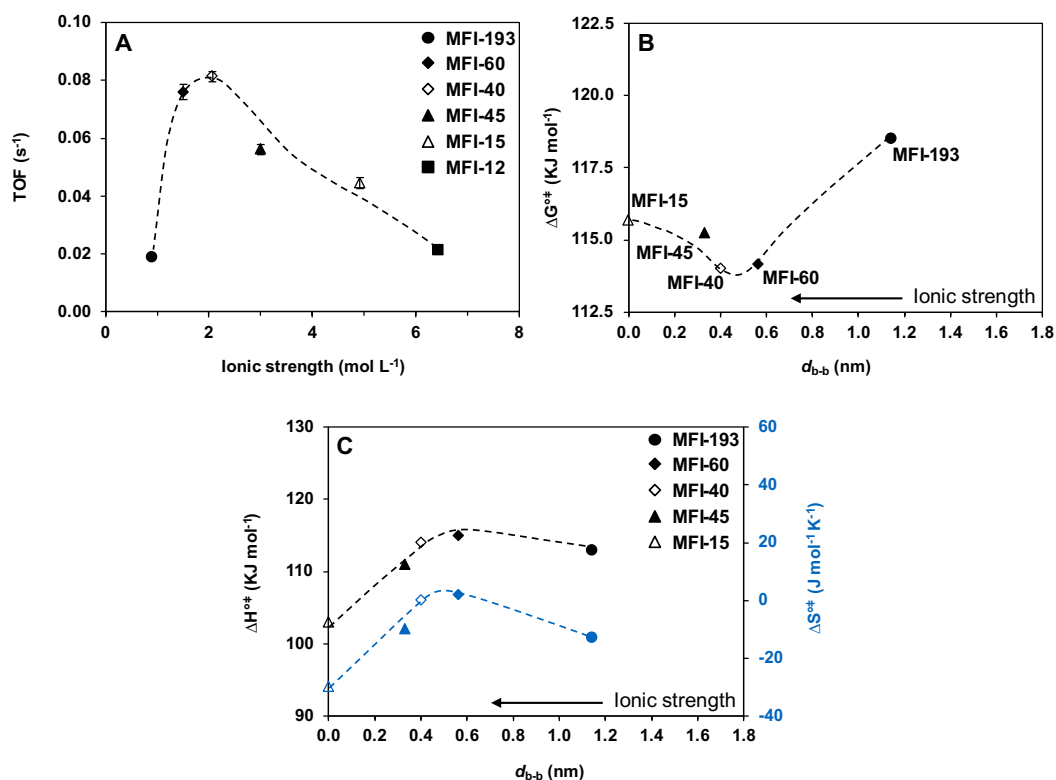


**Figure 3.3.** (A) TOF as a function of ionic strength in dehydration of *cis*-2-McyOH at 150°C. (B)  $\Delta G^{\ddagger}$  and (C)  $\Delta H^{\ddagger}$  (black) and  $\Delta S^{\ddagger}$  (blue) as a function of the distance between hydronium ions ( $d_{b-b}$ ).

Moreover, for the dehydration of *cis*-2-McyOH, the dependency of the activation enthalpy and entropy on  $d_{b-b}$  shows an opposite trend (Figure 3.3 C). The enthalpic stabilization is now increasing for distances below 0.4 nm and above 0.6 nm, while a significant decrease of the entropy to negative values is observed. This loss in entropy is caused by the associated complex formed in the transition state of the concerted elimination consisting of a proton, the alcohol and water acting as the proton-abstracting base (Scheme 3.1).

The adsorption uptake of *cis*-2-McyOH is reduced, in line with the TOF decrease, after an ionic strength of 2.07 mol L<sup>-1</sup> (Figure S3.17, Table S3.16). This isomer showed an overall lower uptake than 4-McyOH due to its higher steric hindrance (on MFI-40: 0.34 mmol g<sup>-1</sup> for *cis*-2-McyOH vs. 1.08 mmol g<sup>-1</sup> for 4-McyOH). Nevertheless, the dehydration of *cis*-2-McyOH results in more than 2.5-fold higher TOFs (Table 3.1 and 3.3). As it was concluded previously, the antiperiplanar arrangement of the protonated hydroxyl group and the adjacent β-H allows the *cis*-2-McyOH to proceed *via* a concerted E2 mechanism, thereby resulting in an increased selectivity towards the energetically more favored Saytzeff-product (1-MCH) and simultaneously avoiding the energetically demanding formation of a carbenium ion (Table S3.17).<sup>19</sup>

### 3.2.2.3 Correlation of $\Delta S^{\ddagger}$ and $\Delta H^{\ddagger}$

Figure 3.4 displays that all tested zeolites follow a linear correlation between the entropy and enthalpy. Remarkably, the correlation even falls on the same line as all other secondary alcohols converted over various catalysts as reported recently.<sup>24</sup> This reflects the significant influence of the position of the OH-group on the overall catalytic activity (Figure S3.18).

Furthermore, Figure 3.4 highlights again that an increasing ionic strength has a different influence on the enthalpy and entropy when following an E1 or E2 mechanism. While a pronounced stabilization of  $\Delta H^{\ddagger}$  is characteristic for the E2 mechanism (absence of a carbenium ion), this pathway suffers from low or even negative  $\Delta S^{\ddagger}$  due to a highly ordered and multicomponent transition state. An increasing ionic strength has, in this case, a stronger beneficial impact on the entropy and shifts the parameters towards a more E1-like character (Figure 3.4, blue arrow). In contrast, an increasing ionic strength seems to shift an E1 mechanism more towards E2-like parameters by reducing the characteristic high enthalpic barrier at the expense of a lowering in entropy (Figure 3.4, black arrow).

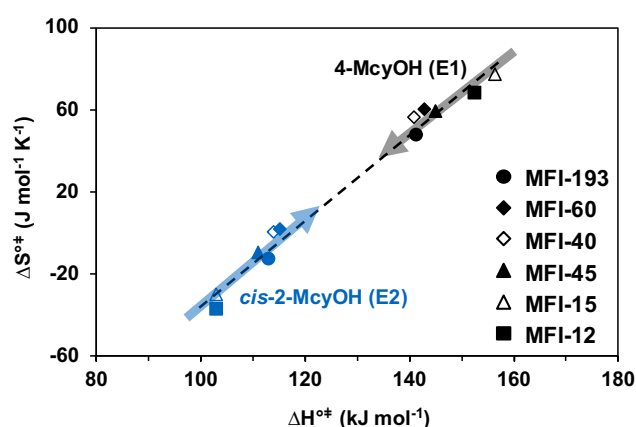


**Figure 3.4.** Correlation of the activation entropy ( $\Delta S^{\ddagger}$ ) and enthalpy ( $\Delta H^{\ddagger}$ ) in the dehydration of 4-McyOH (E1, black) and *cis*-2-McyOH (E2, blue).

### 3.3 Conclusion

In conclusion, we investigated the impact of the concentration of  $\text{H}_3\text{O}^+_{\text{hydr}}$  and the intracrystalline ionic strength on the aqueous phase dehydration of 2- and 4-methylcyclohexanol. The increase of the turnover frequency in the demonstrated volcano-plot is caused by increasing local ionic strength in the zeolite pores. The highest dehydration rates were obtained by zeolites of moderate Si/Al ratios, i.e., on MFI-40 and MFI-60. The decrease, on the other hand, is arising from the additional work to overcome the strong repulsions once the void space between neighboring hydronium ions falls below the critical distance of 0.4 nm and a reorganization of the ion pairs is required. The position of the maximum is consistently found regardless of the substitution or whether the dehydration proceeds via an E1 or E2 mechanism. The reaction pathway strongly affects the activation entropy and enthalpy and the mode by which they are influenced by the ionic strength. While the formation of the carbenium ion primarily resulted in an enthalpic stabilization at high ionic strength, the formation of the associated complex was mainly entropically supported. The significantly higher rates for the *cis*-2-McyOH over the 4-McyOH dehydration, despite the higher steric bulkiness, are a consequence of the E2 pathway and the selective conversion to the Saytzeff-product.

### 3.4 Acknowledgements

This work was supported by the U.S. Department of Energy (DOE), Office of Science, Office of Basic Energy Sciences (BES), Division of Chemical Sciences, Geosciences and Biosciences (Transdisciplinary Approaches to Realize Novel Catalytic Pathways to Energy Carriers, FWP 47319). Special gratitude is expressed to Prof. Gary L. Haller for fruitful discussions and P. Waligorski and P. Pfäuser for their help in performing experiments.

### 3.5 Author contributions

L.M. and P.H.H. contributed equally to this work. P.H.H., E.B. and J.A.L. conceived the initial idea. L.M. conducted synthesis, adsorption measurements, kinetic experiments and calculations. P.H.H. carried out synthesis, kinetic experiments and kinetic calculations. The manuscript was written through contributions of all authors. All authors have given approval to the final version of the manuscript.

### 3.6 References

- (1) Haag, W. O. In *Studies in Surface Science and Catalysis*; Weitkamp, J.; Karge, H. G.; Pfeifer, H.; Hölderich, W., Eds.; Elsevier, **1994**; Vol. 84, 1375.
- (2) Haag, W. O.; Lago, R. M.; Weisz, P. B. The active site of acidic aluminosilicate catalysts. *Nature* **1984**, 309 (5969), 589.
- (3) Schallmoser, S.; Ikuno, T.; Wagenhofer, M. F.; Kolvenbach, R.; Haller, G. L.; Sanchez-Sanchez, M.; Lercher, J. A. Impact of the local environment of Brønsted acid sites in ZSM-5 on the catalytic activity in n-pentane cracking. *Journal of Catalysis* **2014**, 316, 93.
- (4) Janda, A.; Bell, A. T. Effects of Si/Al Ratio on the Distribution of Framework Al and on the Rates of Alkane Monomolecular Cracking and Dehydrogenation in H-MFI. *Journal of the American Chemical Society* **2013**, 135 (51), 19193.
- (5) Gounder, R.; Iglesia, E. Catalytic Consequences of Spatial Constraints and Acid Site Location for Monomolecular Alkane Activation on Zeolites. *Journal of the American Chemical Society* **2009**, 131 (5), 1958.
- (6) Kazanskii, V. The nature of adsorbed carbenium ions as active intermediates in catalysis by solid acids. *Accounts of Chemical Research* **1991**, 24 (12), 379.
- (7) Vjunov, A.; Derewinski, M. A.; Fulton, J. L.; Camaioni, D. M.; Lercher, J. A. Impact of Zeolite Aging in Hot Liquid Water on Activity for Acid-Catalyzed Dehydration of Alcohols. *Journal of the American Chemical Society* **2015**, 137 (32), 10374.
- (8) Vjunov, A.; Fulton, J. L.; Camaioni, D. M.; Hu, J. Z.; Burton, S. D.; Arslan, I.; Lercher, J. A. Impact of Aqueous Medium on Zeolite Framework Integrity. *Chemistry of Materials* **2015**, 27 (9), 3533.
- (9) Ravenelle, R. M.; Schüßler, F.; D'Amico, A.; Danilina, N.; van Bokhoven, J. A.; Lercher, J. A.; Jones, C. W.; Sievers, C. Stability of Zeolites in Hot Liquid Water. *The Journal of Physical Chemistry C* **2010**, 114 (46), 19582.
- (10) Lutz, W.; Toufar, H.; Kurzhals, R.; Suckow, M. Investigation and Modeling of the Hydrothermal Stability of Technically Relevant Zeolites. *Adsorption* **2005**, 11 (3), 405.
- (11) Zhao, C.; Lercher, J. A. Upgrading Pyrolysis Oil over Ni/HZSM-5 by Cascade Reactions. *Angewandte Chemie International Edition* **2012**, 51 (24), 5935.
- (12) Shi, H.; Eckstein, S.; Vjunov, A.; Camaioni, D. M.; Lercher, J. A. Tailoring nanoscopic confines to maximize catalytic activity of hydronium ions. *Nature Communications* **2017**, 8 (1), 15442.
- (13) Liu, Y.; Vjunov, A.; Shi, H.; Eckstein, S.; Camaioni, D. M.; Mei, D.; Baráth, E.; Lercher, J. A. Enhancing the catalytic activity of hydronium ions through constrained environments. *Nature Communications* **2017**, 8 (1), 14113.
- (14) Zundel, G. Hydration Structure and Intermolecular Interaction in Polyelectrolytes. *Angewandte Chemie International Edition in English* **1969**, 8 (7), 499.
- (15) Eigen, M. Proton Transfer, Acid-Base Catalysis, and Enzymatic Hydrolysis. Part I: ELEMENTARY PROCESSES. *Angewandte Chemie International Edition in English* **1964**, 3 (1), 1.
- (16) Eckstein, S.; Hintermeier, P. H.; Zhao, R.; Baráth, E.; Shi, H.; Liu, Y.; Lercher, J. A. Influence of Hydronium Ions in Zeolites on Sorption. *Angewandte Chemie International Edition* **2019**, 58 (11), 3450.
- (17) Eckstein, S.; Hintermeier, P. H.; Olarte, M. V.; Liu, Y.; Baráth, E.; Lercher, J. A. Elementary steps and reaction pathways in the aqueous phase alkylation of phenol with ethanol. *Journal of Catalysis* **2017**, 352, 329.
- (18) Pfriem, N.; Hintermeier, P. H.; Eckstein, S.; Kim, S.; Liu, Q.; Shi, H.; Milakovic, L.; Liu, Y.; Haller, G. L.; Baráth, E. et al. Role of the ionic environment in enhancing the activity of reacting molecules in zeolite pores. *Science* **2021**, 372 (6545), 952.
- (19) Hintermeier, P. H.; Eckstein, S.; Mei, D.; Olarte, M. V.; Camaioni, D. M.; Baráth, E.; Lercher, J. A. Hydronium-Ion-Catalyzed Elimination Pathways of Substituted Cyclohexanols in Zeolite H-ZSM5. *ACS Catalysis* **2017**, 7 (11), 7822.
- (20) Hofmann, A. W. Beiträge zur Kenntniss der flüchtigen organischen Basen. *Justus Liebigs Annalen der Chemie* **1851**, 79 (1), 11.

- (21) Saytzeff, A. Zur Kenntniss der Reihenfolge der Analgerung und Ausscheidung der Jodwasserstoffelemente in organischen Verbindungen. *Justus Liebigs Annalen der Chemie* **1875**, 179 (3), 296.
- (22) Kokotailo, G. T.; Lawton, S. L.; Olson, D. H.; Meier, W. M. Structure of synthetic zeolite ZSM-5. *Nature* **1978**, 272 (5652), 437.
- (23) Olson, D. H.; Kokotailo, G. T.; Lawton, S. L.; Meier, W. M. Crystal structure and structure-related properties of ZSM-5. *The Journal of Physical Chemistry* **1981**, 85 (15), 2238.
- (24) Milakovic, L.; Hintermeier, P. H.; Liu, Q.; Shi, H.; Liu, Y.; Baráth, E.; Lercher, J. A. Towards understanding and predicting the hydronium ion catalyzed dehydration of cyclic-primary, secondary and tertiary alcohols. *Journal of Catalysis* **2020**, 390, 237.

## 3.7 Supporting information

### 3.7.1 Experimental procedures

#### Chemicals

The following chemicals were used: 4-methylcyclohexanol (4-McyOH) (mixture of *cis* and *trans* (25%:75%), 98%, *Sigma-Aldrich*), 2-methylcyclohexanol (2-McyOH) (mixture of *cis* and *trans* (48%:52%), 99%, *Sigma-Aldrich*), sodium sulfate (ACS reagent, >99%, *Sigma-Aldrich*), ethyl acetate (*Chromasolv*, 99.9%, *Sigma-Aldrich*). Hydrogen gas was obtained from *Westfalen* (>99.999%). Deionized water was treated with an *Easypure-II* system from *WERNER* to obtain ultrapure water (18.2 M $\Omega$  cm).

#### Zeolite catalysts

All zeolites are referred to as MFI-X, where “X” is the Si/Al ratio as determined by atomic absorption spectroscopy. MFI-193 was synthesized according to the recipe described below. Zeolite MFI-90 (Si/Al = 90), MFI-60 (Si/Al = 60) and MFI-45 (Si/Al = 45) were obtained from *CLARIANT AG* in H-form. The MFI zeolites CBV8014 (referred to MFI-40; Si/Al = 40), CBV3024E (referred to MFI-15; Si/Al = 15) and CBV2314 (referred to as MFI-12; Si/Al = 11.5) were obtained from *ZEOLYST* in H-form. All zeolites were treated at 550°C (rate: 10°C min<sup>-1</sup>) for six hours in 100 mL min<sup>-1</sup> synthetic air (80% nitrogen, 20% oxygen; >99%) before they were tested.

#### Zeolite synthesis of MFI-193

The MFI zeolite (desired Si/Al ratio: 200) had the following gel-composition: 10.75 Na<sub>2</sub>O : 0.25 Al<sub>2</sub>O<sub>3</sub> : 100 SiO<sub>2</sub> : 2000 H<sub>2</sub>O : 20 TPABr. At first, 1.38 g NaOH was dissolved in 35.34 g H<sub>2</sub>O. Step by step 8.55 g tetrapropylammonium bromide, 0.25 g Al<sub>2</sub>(SO<sub>4</sub>)<sub>3</sub> × H<sub>2</sub>O and 32.1 g LUDOX-30 (*Sigma-Aldrich*, AS-30) were added to the solution under vigorously stirring. The zeolite gel was stirred over night at room temperature to increase homogeneity. The gel crystallized during 60 hours of slow axial rotation (30 rpm) in autoclaves at 170°C. After drying overnight, the template was removed by thermal treatment at 550°C (heating rate: 10°C min<sup>-1</sup>) for six hours and 100 mL min<sup>-1</sup> flow of synthetic air. Catalytically active H-form was obtained after NH<sub>4</sub><sup>+</sup>-exchange, where approximately 2 g of Na-form MFI-193 were stirred with 50 mL of 1M NH<sub>4</sub>NO<sub>3</sub> (*Sigma-Aldrich*, >99%) solution at 80°C for 2 h. The treated zeolite was centrifuged and washed with deionized water. The exchange procedure was repeated two further times before the zeolite was dried overnight and calcined as described above.

### Reaction procedure

All reactions were performed with the same molar amount of reactant, catalyst and solvent. In 100 mL ultrapure water 0.05 mol of substrate (5.71 g of 2-/4-methylcyclohexanol) and 50 mg of zeolite MFI-193, MFI-90, MFI-60, MFI-45, MFI-40, MFI-15 or MFI-12 were dissolved and suspended, respectively.

### Catalytic reactions

The autoclave (300 mL) was loaded with 100 mL water, the given amount of zeolite catalyst (see above) and 0.05 mol of substituted cyclohexanol substrate. The reactor was purged two times with 20 bar with hydrogen and was heated to the desired temperature with a heating rate of 10°C per minute under a starting pressure of 20 bar H<sub>2</sub> without stirring. Ten degrees below the reaction temperature the total pressure of the reactor was adjusted to 50 bar with hydrogen gas and as soon as the reaction temperature was reached the stirring rate was set to 700 rpm. The usage of H<sub>2</sub> is replaceable with an inert gas (N<sub>2</sub>) in terms of reaction rates. It was used to enable a faster heating profile.

After the reaction time, the reactor was cooled down from reaction temperature to room temperature within two minutes using an ice bath. The pressure within the reactor was released at a temperature of 5°C to prevent the loss of volatile products (cyclohexene). The reaction mixture was extracted with 3 × 20 mL ethyl acetate. To improve the phase separation of the organic and the aqueous phases, a small amount of sodium chloride was added to the reaction mixture. After extraction, the organic phase was dried over sodium sulfate. The carbon-balance was monitored by an internal standard (dodecane).

### Methods

**Reactor:** All reactions were performed in an autoclave (300 mL) from *Parr Instruments Co.* (type: *PST FS*, material: HASTELLOY C) with a temperature and stirring controlling device (*Parr Instruments Co. 4848 Reactor Controller*).

**GC-MS FID:** Quantification and qualification of the dehydration reactions was analyzed by GC/MS (*Agilent Technologies 7890 B GC*, column: *Agilent 19091S-433UI INV02* (30 m × 250 μm × 0.25 μm), heating program: 10°C min<sup>-1</sup> from 80°C to 280°C). Data was analyzed with *MassHunter Workstation Software, Qualitative Analysis, Version B.06.00, Agilent Technologies (2012)*.

**AAS:** The Si and Al content of the zeolite samples was measured by atomic absorption spectroscopy (AAS) on a *UNICAM 939 AA-Spectrometer*.

**N<sub>2</sub> physisorption:** The BET specific surface area and micropore volume of the zeolites were determined by nitrogen physisorption. The isotherms were measured at liquid nitrogen temperature (-196°C) using a *PMI Automatic Sorptometer*. The catalyst was activated in vacuum at 200°C for two hours before measurement. Apparent surface area was calculated by applying the *Brunauer-Emmett-Teller (BET) theory*, and the *t-plot method* was used to determine the micropore volumes.

**IR:** Infrared spectroscopy of adsorbed pyridine was performed with a *Perkin–Elmer 2000* spectrometer at a resolution of  $4\text{ cm}^{-1}$ . The catalyst sample was prepared as wafer and activated in vacuum (ca.  $10^{-6}$  mbar) at  $450^{\circ}\text{C}$  for one hour (heating rate =  $10^{\circ}\text{C min}^{-1}$ ). After cooling to  $150^{\circ}\text{C}$ , the sample was equilibrated with 0.1 mbar of pyridine for 30 min followed by outgassing for one hour. A spectrum with the chemisorbed pyridine was recorded thereafter. Adsorbed pyridine was desorbed finally by heating up to  $450^{\circ}\text{C}$  with  $10^{\circ}\text{C min}^{-1}$  for half an hour, the spectra were recorded at equilibrium. For quantification, molar integral extinction coefficients of  $0.73\text{ cm } \mu\text{mol}^{-1}$  and  $0.96\text{ cm } \mu\text{mol}^{-1}$  were used for Brønsted and Lewis acid sites, respectively.

**NH<sub>3</sub>-TPD:** Temperature-programmed desorption (TPD) of ammonia was performed in a 6-fold parallel reactor system. The catalysts were activated under reduced pressure at  $450^{\circ}\text{C}$  (heating rate:  $5^{\circ}\text{C min}^{-1}$ ) for one hour. NH<sub>3</sub> was adsorbed for one hour with partial pressures of 1 mbar at  $100^{\circ}\text{C}$ , respectively. Subsequently, the samples were evacuated for two hours to remove physisorbed probe molecules. For the temperature-programmed desorption experiments, six samples were sequentially heated from  $100$  to  $770^{\circ}\text{C}$  with a heating rate of  $10^{\circ}\text{C min}^{-1}$  to desorb ammonia. The rates of desorbing species were monitored by mass spectrometry (*Balzers QME 200*). For the quantification of the amount of acidity, a standard MFI-zeolite with known acid site concentration was used to calibrate the signal.

**XRD:** X-ray diffraction measurements were performed on a *PANalytical Empyrean* diffractometer in a Bragg–Brentano geometry ( $\theta$ -  $2\theta$ -goniometer), equipped with a Cu- $K\alpha$  radiation source operating at 45 kV and 40 mA. The scanning range was  $5^{\circ}$ – $70^{\circ}$   $2\theta$  with increments of  $0.017^{\circ}$ . Diffractogram and unit cell refinement analysis was performed using *PANalytical Highscore Plus* software.

**Adsorption uptake and adsorption heat measurements:** Aqueous phase adsorption uptake of the alcohols on different zeolites was carried out at room temperature. Typically, 30–80 mg of the zeolite sample was immersed into the alcohol aqueous solutions with certain concentrations under vigorous stirring for 24 h. The mixtures were separated from the zeolite by using syringe filters (Nylon or Polypropylene membrane, 25 mm,  $0.2\text{ }\mu\text{m}$ ), then extracted using dichloromethane (*Sigma-Aldrich*, >99% purity) and finally analyzed on a GC-MS FID after the addition of an internal standard (*n*-dodecane). The adsorption uptake was calculated based on the alcohol concentration change for a certain amount of the zeolite. The saturation uptake ( $q_{max}$ ) of the alcohols on each zeolite was derived from the fitted adsorption isotherms using the Langmuir equation  $q = q_{max} K_{ads} c (1 + K_{ads} c)^{-1}$ , where  $c$  represents the equilibrium concentration of the alcohols after adsorption,  $K_{ads}$  is the adsorption constant with the standard state set as  $1\text{ mol L}^{-1}$ .

### 3.7.2 Figures and tables of the discussion part

#### Materials

**Table S3.1.** Physicochemical properties of the investigated MFI zeolites.

Entry	Zeolite	Si / Al	Surface area (m <sup>2</sup> g <sup>-1</sup> )	c (BAS) <sup>[a]</sup> (mmol g <sup>-1</sup> )	c(LAS) <sup>[a]</sup> (mmol g <sup>-1</sup> )	c (BAS+ LAS) <sup>[b]</sup> (mmol g <sup>-1</sup> )	Unit cell parameters <sup>[c]</sup>		
							a (Å)	b (Å)	c (Å)
1	MFI-193	193	379	0.09	0.02	0.11	20.107	19.929	13.412
2	MFI-90	90	388	0.15	0.04	0.13	20.109	19.939	13.410
3	MFI-60	60	460	0.23	0.08	0.28	20.087	19.943	13.422
4	MFI-45	45	389	0.36	0.05	0.40	20.078	19.956	13.419
5	MFI-40	40	478	0.31	0.08	0.41	20.075	19.949	13.416
6	MFI-15	15	419	0.86	0.16	0.76	20.087	19.948	13.429
7	MFI-12	12	432	1.14	0.20	0.83	20.079	19.956	13.420

[a] Determined by IR spectroscopy of adsorbed pyridine. [b] Determined by NH<sub>3</sub>-TPD. [c] Calculated from XRD (MFI: orthorhombic structure with  $\alpha = \beta = \gamma = 90^\circ$ ).

#### Reaction order

The reaction order for both substrates over MFI-45 was previously published in reference 1.

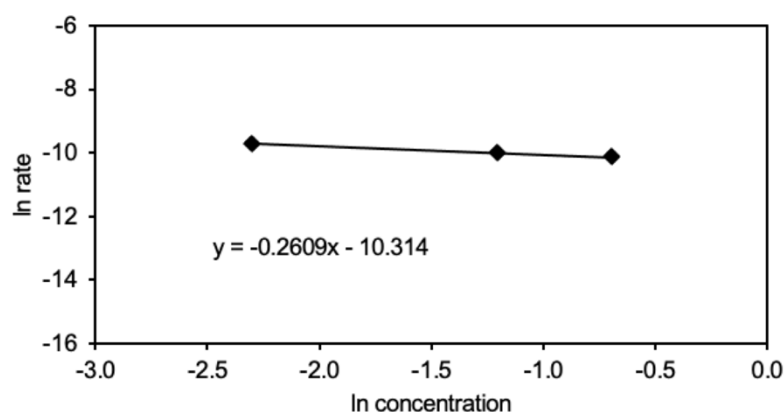


**Figure S3.1.** Reaction order: **4-methylcyclohexanol** dehydration (170°C, 50 bar, **MFI-12**).

**Table S3.2.** Dehydration rates and initial concentrations of **4-methylcyclohexanol** (170°C, 50 bar, **MFI-12**).

rate (mol g <sup>-1</sup> s <sup>-1</sup> )	c (mol L <sup>-1</sup> )	ln rate	ln c
6.1×10 <sup>-5</sup>	0.10	- 9.7	-2.30
4.5×10 <sup>-5</sup>	0.30	- 10.0	-1.20
4.0×10 <sup>-5</sup>	0.50	- 10.1	-0.69

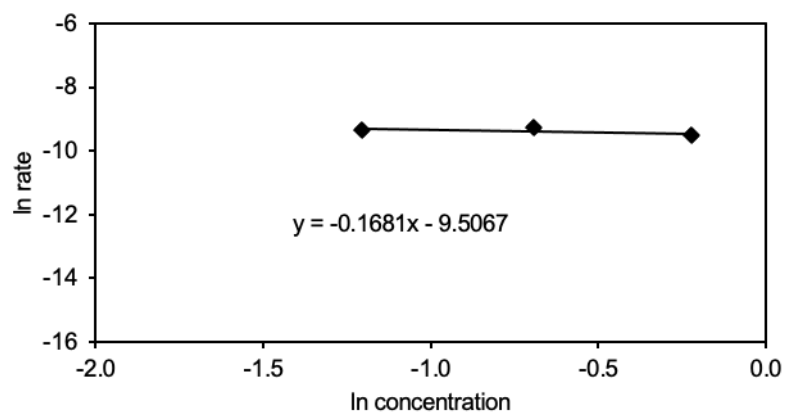


**Figure S3.2.** Reaction order: **2-methylcyclohexanol** dehydration (170°C, 50 bar, **MFI-12**).

**Table S3.3.** Dehydration rates and initial concentrations of **2-methylcyclohexanol** (170°C, 50 bar, **MFI-12**).

rate (mol g <sup>-1</sup> s <sup>-1</sup> )	c (mol L <sup>-1</sup> )	ln rate	ln c
8.6×10 <sup>-5</sup>	0.30	- 9.4	-1.20
9.4×10 <sup>-5</sup>	0.50	- 9.3	-0.69
7.3×10 <sup>-5</sup>	0.80	- 9.5	-0.22

### BAS dependent volcano plot

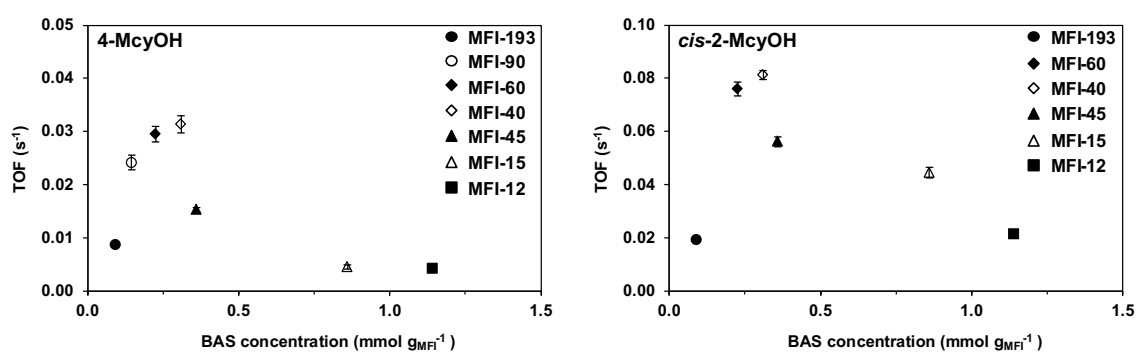


**Figure S3.3.** TOF as a function of BAS concentration in the dehydration of 4-methylcyclohexanol (left) and *cis*-2-methylcyclohexanol (right).

Volcano plot at different temperatures

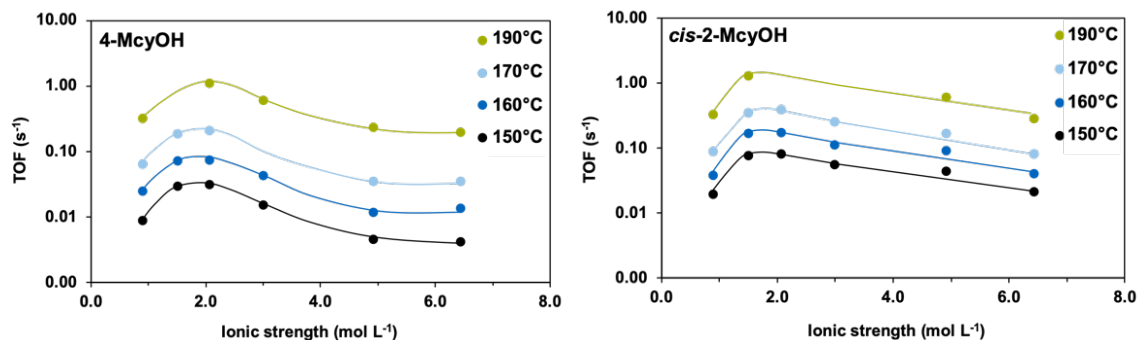


**Figure S3.4.** TOF as a function of ionic strength in the dehydration of 4-methylcyclohexanol (left) and 2-methylcyclohexanol (right) at different temperatures.

$\Delta S^{\ddagger}$  and  $\Delta H^{\ddagger}$ : 4-methylcyclohexanol

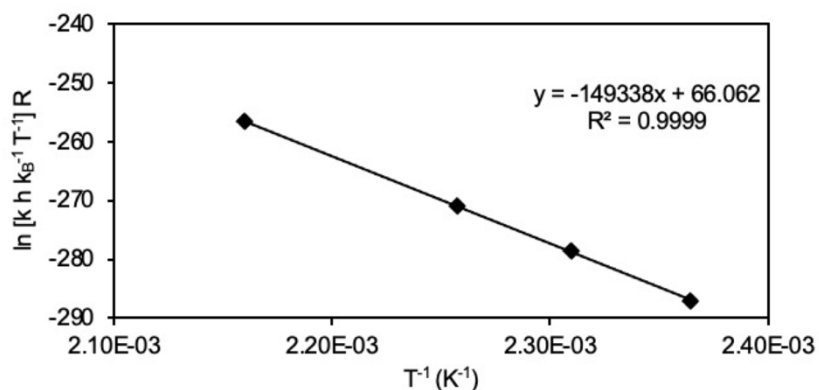


**Figure S3.5.**  $\Delta H^{\ddagger}$  (149 kJ mol<sup>-1</sup>) and  $\Delta S^{\ddagger}$  (66 J mol<sup>-1</sup> K<sup>-1</sup>) for 4-methylcyclohexanol (0.5 M) dehydration, MFI-193.

**Table S3.4.** Kinetic data for 4-methylcyclohexanol (0.5 M) dehydration, MFI-193.

T (°C)	T (K)	TOF (s <sup>-1</sup> )	ln [k h kg <sup>-1</sup> T <sup>-1</sup> ] R	T <sup>-1</sup> (K <sup>-1</sup> )
150	423	8.8×10 <sup>-3</sup>	-287.15	2.36×10 <sup>-3</sup>
160	433	2.5×10 <sup>-2</sup>	-278.67	2.31×10 <sup>-3</sup>
170	443	6.5×10 <sup>-2</sup>	-270.95	2.26×10 <sup>-3</sup>
190	463	3.8×10 <sup>-1</sup>	-256.58	2.16×10 <sup>-3</sup>

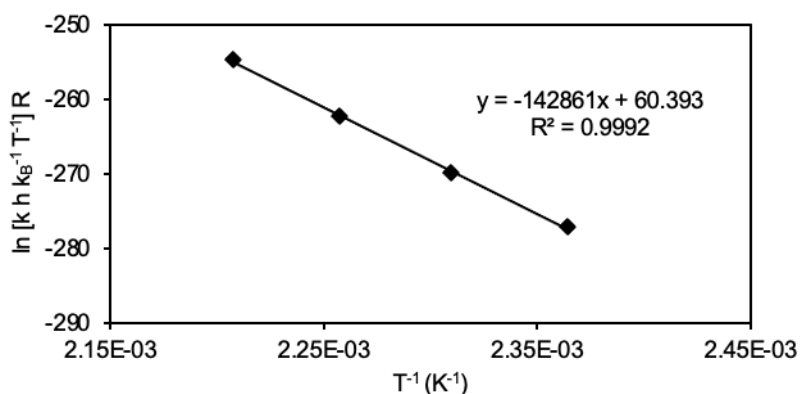


**Figure S3.6.**  $\Delta H^{\ddagger}$  (143 kJ mol<sup>-1</sup>) and  $\Delta S^{\ddagger}$  (60 J mol<sup>-1</sup> K<sup>-1</sup>) for **4-methylcyclohexanol** (0.5 M) dehydration, **MFI-60**.

**Table S3.5.** Kinetic data for **4-methylcyclohexanol** (0.5 M) dehydration, **MFI-60**.

T (°C)	T (K)	TOF (s <sup>-1</sup> )	$\ln [k h k_B^{-1} T^{-1}] R$	$T^{-1} (K^{-1})$
150	423	$3.0 \times 10^{-2}$	-277.10	$2.36 \times 10^{-3}$
160	433	$7.3 \times 10^{-2}$	-269.82	$2.31 \times 10^{-3}$
170	443	$1.8 \times 10^{-1}$	-262.27	$2.26 \times 10^{-3}$
180	453	$4.7 \times 10^{-1}$	-254.76	$2.21 \times 10^{-3}$

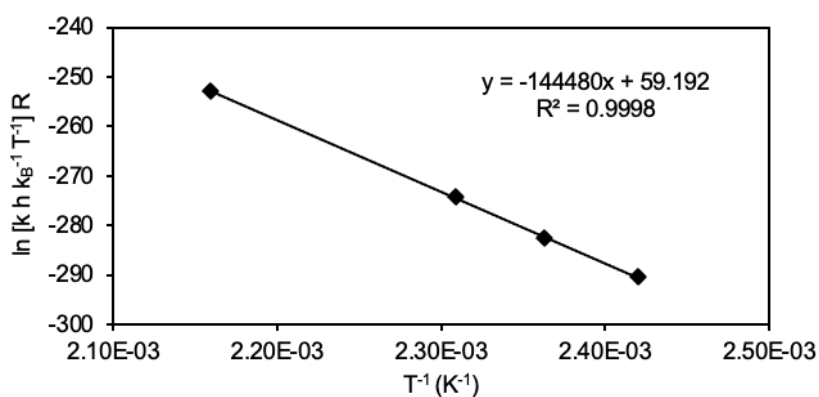


**Figure S3.7.**  $\Delta H^{\ddagger}$  (145 kJ mol<sup>-1</sup>) and  $\Delta S^{\ddagger}$  (59 J mol<sup>-1</sup> K<sup>-1</sup>) for **4-methylcyclohexanol** (0.5 M) dehydration, **MFI-45**.

**Table S3.6.** Kinetic data for **4-methylcyclohexanol** (0.5 M) dehydration, **MFI-45**.

T (°C)	T (K)	TOF (s <sup>-1</sup> )	ln [k h k <sub>B</sub> <sup>-1</sup> T <sup>-1</sup> ] R	T <sup>-1</sup> (K <sup>-1</sup> )
140	413	5.8×10 <sup>-3</sup>	-290.39	2.42×10 <sup>-3</sup>
150	423	1.5×10 <sup>-2</sup>	-282.55	2.36×10 <sup>-3</sup>
160	433	4.3×10 <sup>-2</sup>	-274.16	2.31×10 <sup>-3</sup>
190	463	6.0×10 <sup>-1</sup>	-252.78	2.16×10 <sup>-3</sup>

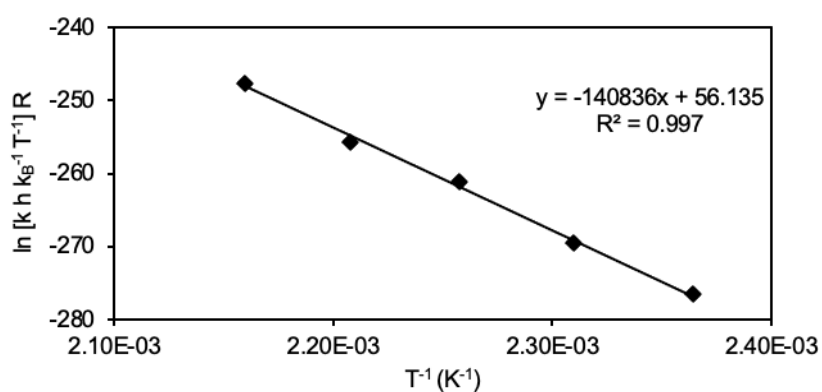


**Figure S3.8.**  $\Delta H^{\ddagger}$  (141 kJ mol<sup>-1</sup>) and  $\Delta S^{\ddagger}$  (56 J mol<sup>-1</sup> K<sup>-1</sup>) for **4-methylcyclohexanol** (0.5 M) dehydration, **MFI-40**.

**Table S3.7.** Kinetic data for **4-methylcyclohexanol** (0.5 M) dehydration, **MFI-40**.

T (°C)	T (K)	TOF (s <sup>-1</sup> )	ln [k h k <sub>B</sub> <sup>-1</sup> T <sup>-1</sup> ] R	T <sup>-1</sup> (K <sup>-1</sup> )
150	423	3.1×10 <sup>-2</sup>	-276.61	2.36×10 <sup>-3</sup>
160	433	7.5×10 <sup>-2</sup>	-269.56	2.31×10 <sup>-3</sup>
170	443	2.1×10 <sup>-1</sup>	-261.11	2.26×10 <sup>-3</sup>
180	453	4.2×10 <sup>-1</sup>	-255.61	2.21×10 <sup>-3</sup>
190	463	1.2×10 <sup>0</sup>	-247.63	2.16×10 <sup>-3</sup>

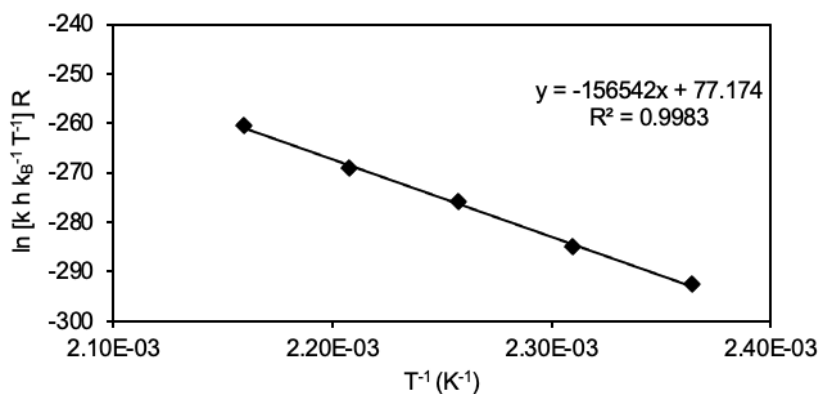


**Figure S3.9.**  $\Delta H^{\ddagger}$  (157 kJ mol<sup>-1</sup>) and  $\Delta S^{\ddagger}$  (77 J mol<sup>-1</sup> K<sup>-1</sup>) for **4-methylcyclohexanol** (0.5 M) dehydration, **MFI-15**.

**Table S3.8.** Kinetic data for **4-methylcyclohexanol** (0.5 M) dehydration, **MFI-15**.

T (°C)	T (K)	TOF (s <sup>-1</sup> )	ln [k h kg <sup>-1</sup> T <sup>-1</sup> ] R	T <sup>-1</sup> (K <sup>-1</sup> )
150	423	4.6 × 10 <sup>-3</sup>	-292.52	2.36 × 10 <sup>-3</sup>
160	433	1.2 × 10 <sup>-2</sup>	-284.90	2.31 × 10 <sup>-3</sup>
170	443	3.6 × 10 <sup>-2</sup>	-275.87	2.26 × 10 <sup>-3</sup>
180	453	8.4 × 10 <sup>-2</sup>	-268.98	2.21 × 10 <sup>-3</sup>
190	463	2.4 × 10 <sup>-1</sup>	-260.51	2.16 × 10 <sup>-3</sup>

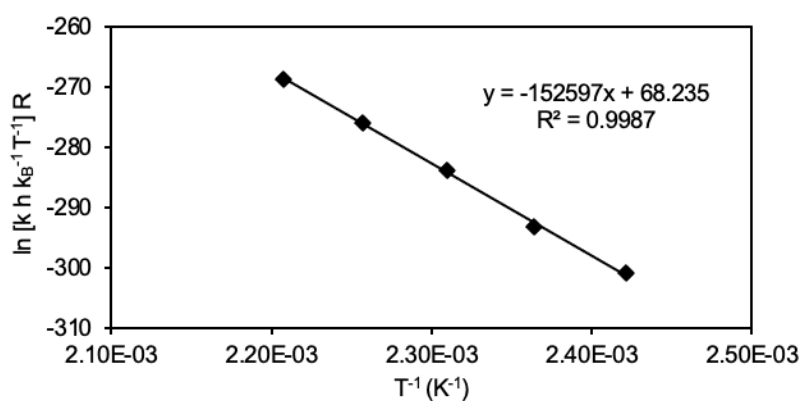


**Figure S3.10.**  $\Delta H^{\ddagger}$  (153 kJ mol<sup>-1</sup>) and  $\Delta S^{\ddagger}$  (68 J mol<sup>-1</sup> K<sup>-1</sup>) for **4-methylcyclohexanol** (0.5 M) dehydration, **MFI-12**.

**Table S3.9.** Kinetic data for **4-methylcyclohexanol** (0.5 M) dehydration, **MFI-12**.

T (°C)	T (K)	TOF (s <sup>-1</sup> )	ln [k h k <sub>B</sub> <sup>-1</sup> T <sup>-1</sup> ] R	T <sup>-1</sup> (K <sup>-1</sup> )
140	413	1.7×10 <sup>-3</sup>	-300.89	2.42×10 <sup>-3</sup>
150	423	4.2×10 <sup>-3</sup>	-293.27	2.36×10 <sup>-3</sup>
160	433	1.3×10 <sup>-2</sup>	-283.86	2.31×10 <sup>-3</sup>
170	443	3.5×10 <sup>-2</sup>	-276.06	2.26×10 <sup>-3</sup>
180	453	8.7×10 <sup>-2</sup>	-268.72	2.21×10 <sup>-3</sup>

$\Delta S^{\ddagger}$  and  $\Delta H^{\ddagger}$ : 2-methylcyclohexanol

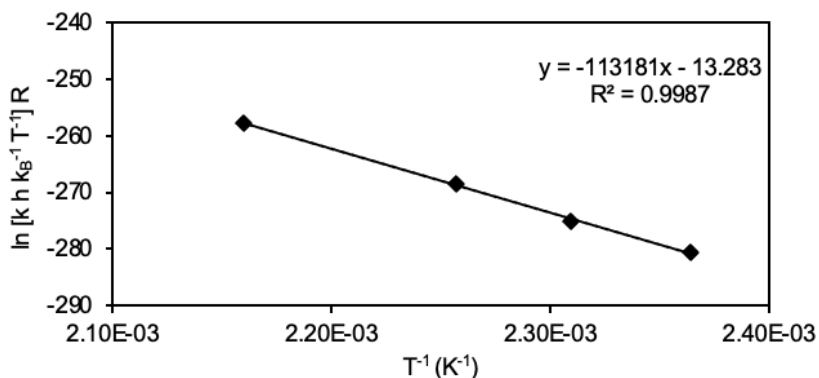


**Figure S3.11.**  $\Delta H^{\ddagger}$  (113 kJ mol<sup>-1</sup>) and  $\Delta S^{\ddagger}$  (-13 J mol<sup>-1</sup> K<sup>-1</sup>) for **2-methylcyclohexanol** (0.5 M) dehydration, **MFI-193**.

**Table S3.10.** Kinetic data for **2-methylcyclohexanol** (0.5 M) dehydration, **MFI-193**.

T (°C)	T (K)	TOF (s <sup>-1</sup> )	ln [k h k <sub>B</sub> <sup>-1</sup> T <sup>-1</sup> ] R	T <sup>-1</sup> (K <sup>-1</sup> )
150	423	1.9×10 <sup>-2</sup>	-280.64	2.36×10 <sup>-3</sup>
160	433	3.8×10 <sup>-2</sup>	-275.16	2.31×10 <sup>-3</sup>
170	443	8.7×10 <sup>-2</sup>	-268.46	2.26×10 <sup>-3</sup>
190	463	3.3×10 <sup>-1</sup>	-257.76	2.16×10 <sup>-3</sup>

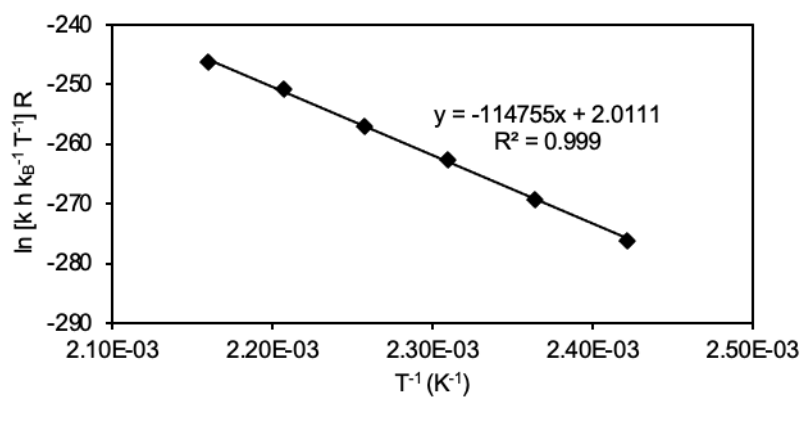


**Figure S3.12.**  $\Delta H^{\ddagger}$  (115 kJ mol<sup>-1</sup>) and  $\Delta S^{\ddagger}$  (2 J mol<sup>-1</sup> K<sup>-1</sup>) for **2-methylcyclohexanol** (0.5 M) dehydration, **MFI-60**.

**Table S3.11.** Kinetic data for **2-methylcyclohexanol** (0.5 M) dehydration, **MFI-60**.

T (°C)	T (K)	TOF (s <sup>-1</sup> )	ln [k h kB <sup>-1</sup> T <sup>-1</sup> ] R	T <sup>-1</sup> (K <sup>-1</sup> )
140	413	3.2×10 <sup>-2</sup>	-276.12	2.42×10 <sup>-3</sup>
150	423	7.6×10 <sup>-2</sup>	-269.24	2.36×10 <sup>-3</sup>
160	433	1.7×10 <sup>-1</sup>	-262.72	2.31×10 <sup>-3</sup>
170	443	3.5×10 <sup>-1</sup>	-257.04	2.26×10 <sup>-3</sup>
180	453	7.5×10 <sup>-1</sup>	-250.83	2.21×10 <sup>-3</sup>
190	463	1.3×10 <sup>0</sup>	-246.35	2.16×10 <sup>-3</sup>

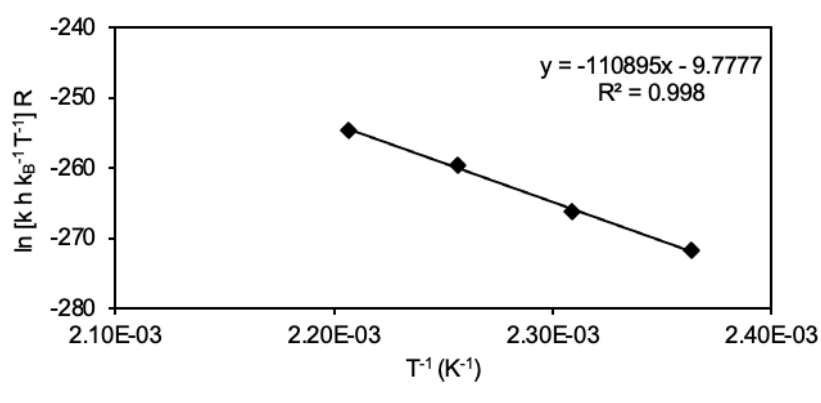


**Figure S3.13.**  $\Delta H^{\ddagger}$  (111 kJ mol<sup>-1</sup>) and  $\Delta S^{\ddagger}$  (-10 J mol<sup>-1</sup> K<sup>-1</sup>) for **2-methylcyclohexanol** (0.5 M) dehydration, **MFI-45**.

**Table S3.12.** Kinetic data for **2-methylcyclohexanol** (0.5 M) dehydration, **MFI-45**.

T (°C)	T (K)	TOF (s <sup>-1</sup> )	ln [k h k <sub>B</sub> <sup>-1</sup> T <sup>-1</sup> ] R	T <sup>-1</sup> (K <sup>-1</sup> )
150	423	5.6×10 <sup>-2</sup>	-271.77	2.36×10 <sup>-3</sup>
160	433	1.1×10 <sup>-1</sup>	-266.14	2.31×10 <sup>-3</sup>
170	443	2.5×10 <sup>-1</sup>	-259.59	2.26×10 <sup>-3</sup>
180	453	4.7×10 <sup>-1</sup>	-254.67	2.21×10 <sup>-3</sup>

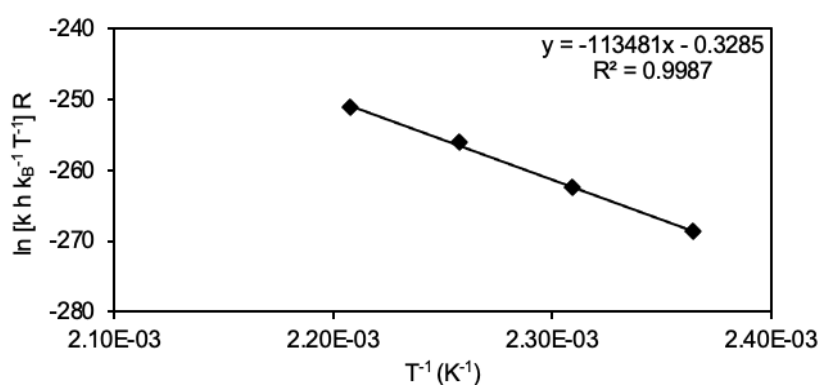


**Figure S3.14.**  $\Delta H^{\ddagger}$  (114 kJ mol<sup>-1</sup>) and  $\Delta S^{\ddagger}$  (0 J mol<sup>-1</sup> K<sup>-1</sup>) for **2-methylcyclohexanol** (0.5 M) dehydration, **MFI-40**.

**Table S3.13.** Kinetic data for **2-methylcyclohexanol** (0.5 M) dehydration, **MFI-40**.

T (°C)	T (K)	TOF (s <sup>-1</sup> )	ln [k h k <sub>B</sub> <sup>-1</sup> T <sup>-1</sup> ] R	T <sup>-1</sup> (K <sup>-1</sup> )
150	423	8.1×10 <sup>-2</sup>	-268.68	2.36×10 <sup>-3</sup>
160	433	1.8×10 <sup>-1</sup>	-262.49	2.31×10 <sup>-3</sup>
170	443	3.8×10 <sup>-1</sup>	-256.09	2.26×10 <sup>-3</sup>
180	453	7.2×10 <sup>-1</sup>	-251.09	2.21×10 <sup>-3</sup>

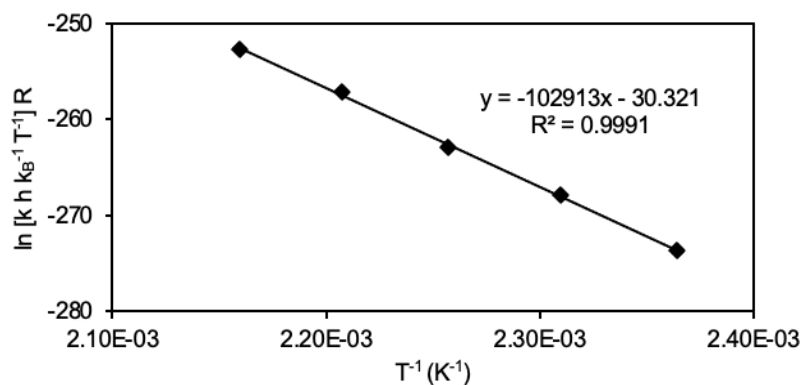


**Figure S3.15.**  $\Delta H^{\ddagger}$  (103 kJ mol<sup>-1</sup>) and  $\Delta S^{\ddagger}$  (-30 J mol<sup>-1</sup> K<sup>-1</sup>) for **2-methylcyclohexanol** (0.5 M) dehydration, **MFI-15**.

**Table S3.14.** Kinetic data for **2-methylcyclohexanol** (0.5 M) dehydration, **MFI-15**.

T (°C)	T (K)	TOF (s <sup>-1</sup> )	ln [k h kg <sup>-1</sup> T <sup>-1</sup> ] R	T <sup>-1</sup> (K <sup>-1</sup> )
150	423	4.5 × 10 <sup>-2</sup>	-273.63	2.36 × 10 <sup>-3</sup>
160	433	9.1 × 10 <sup>-2</sup>	-267.92	2.31 × 10 <sup>-3</sup>
170	443	1.7 × 10 <sup>-1</sup>	-262.90	2.26 × 10 <sup>-3</sup>
180	453	3.5 × 10 <sup>-1</sup>	-257.14	2.21 × 10 <sup>-3</sup>
190	463	6.0 × 10 <sup>-1</sup>	-252.75	2.16 × 10 <sup>-3</sup>

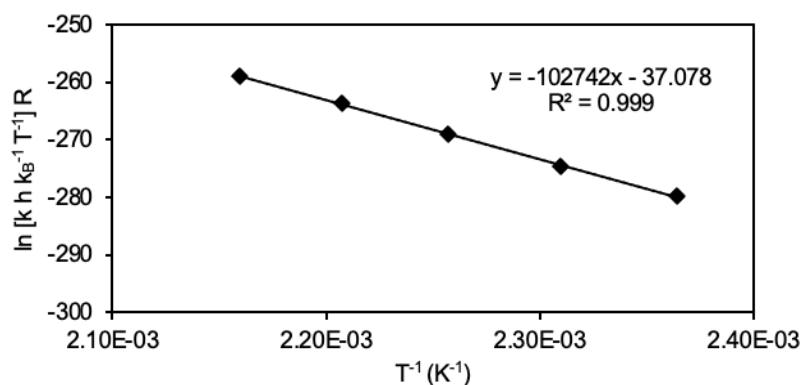


**Figure S3.16.**  $\Delta H^{\ddagger}$  (103 kJ mol<sup>-1</sup>) and  $\Delta S^{\ddagger}$  (-37 J mol<sup>-1</sup> K<sup>-1</sup>) for **2-methylcyclohexanol** (0.5 M) dehydration, **MFI-12**.

**Table S3.15.** Kinetic data for **2-methylcyclohexanol** (0.5 M) dehydration, **MFI-12**.

T (°C)	T (K)	TOF (s <sup>-1</sup> )	ln [k h k <sub>B</sub> <sup>-1</sup> T <sup>-1</sup> ] R	T <sup>-1</sup> (K <sup>-1</sup> )
150	423	2.2×10 <sup>-2</sup>	-279.74	2.36×10 <sup>-3</sup>
160	433	4.0×10 <sup>-2</sup>	-274.75	2.31×10 <sup>-3</sup>
170	443	8.2×10 <sup>-2</sup>	-269.00	2.26×10 <sup>-3</sup>
180	453	1.6×10 <sup>-1</sup>	-263.63	2.21×10 <sup>-3</sup>
190	463	2.8×10 <sup>-1</sup>	-259.07	2.16×10 <sup>-3</sup>

### Alcohol adsorption on MFI zeolites

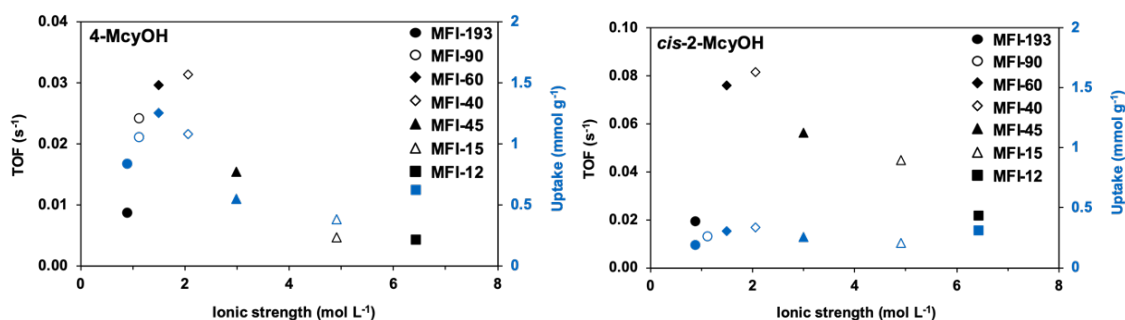


**Figure S3.17.** TOF (black) and substrate uptake (blue) as a function of ionic strength in the dehydration of 4-methylcyclohexanol (left) and 2-methylcyclohexanol (right).

**Table S3.16.** Adsorption measurements on investigated MFI zeolites at room temperature.

Entry	Zeolite	Ionic strength (mol L <sup>-1</sup> )	4-McyOH	cis-2-McyOH
			Substrate uptake (mmol g <sup>-1</sup> )	Substrate uptake (mmol g <sup>-1</sup> )
1	MFI-193	0.89	0.84	0.19
2	MFI-90	1.12	1.05	0.26
3	MFI-60	1.51	1.25	0.30
4	MFI-45	3.00	0.55	0.26
5	MFI-40	2.07	1.08	0.34
6	MFI-15	4.92	0.38	0.20
7	MFI-12	6.44	0.62	0.31

## Hofmann vs. Saytzeff product

**Table S3.17.** Distinction of TOFs to Hofmann and Saytzeff products of 4-McyOH and *cis*-2-McyOH dehydration over MFI zeolites at 150°C.

Entry	Zeolite	Ionic strength (mol L <sup>-1</sup> )	4-McyOH		<i>cis</i> -2-McyOH	
			TOF to Hofmann product (s <sup>-1</sup> )	TOF to Saytzeff product (s <sup>-1</sup> )	TOF to Hofmann product (s <sup>-1</sup> )	TOF to Saytzeff product (s <sup>-1</sup> )
1	MFI-193	0.89	0.007	0.002	0.003	0.016
2	MFI-90	1.12	0.020	0.004	-	-
3	MFI-60	1.51	0.027	0.003	0.010	0.061
4	MFI-45	3.00	0.011	0.004	0.007	0.047
5	MFI-40	2.07	0.026	0.006	0.011	0.066
6	MFI-15	4.92	0.004	0.001	0.005	0.038
7	MFI-12	6.44	0.003	0.001	0.002	0.018

## Correlation of $\Delta S^{\ddagger}$ and $\Delta H^{\ddagger}$

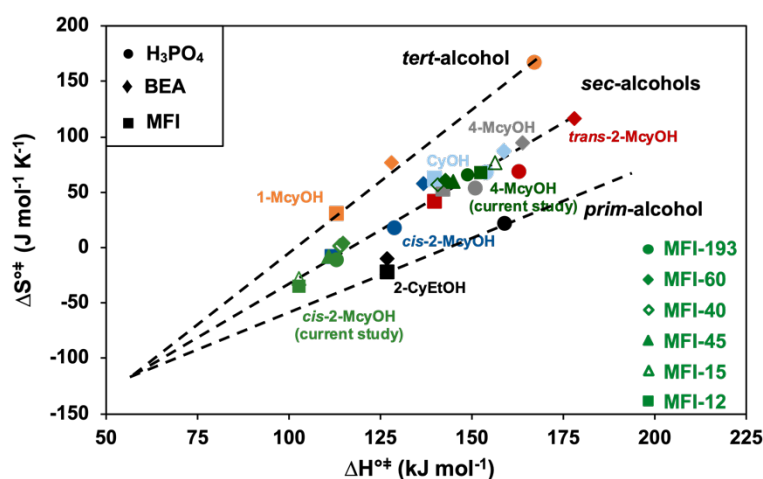


**Figure S3.18.** Correlation of  $\Delta S^{\ddagger}$  and  $\Delta H^{\ddagger}$  for primary, secondary and tertiary cyclic alcohols of previous published and currently studied acid catalysts.<sup>2</sup>

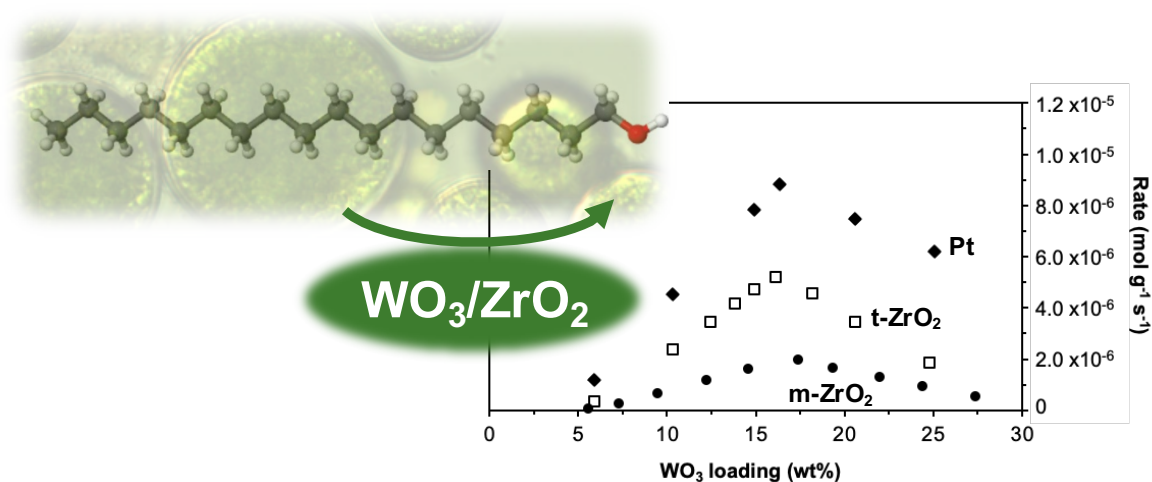
### 3.7.3 References of the supporting information

- (1) Hintermeier, P. H.; Eckstein, S.; Mei, D.; Olarte, M. V.; Camaioni, D. M.; Baráth, E.; Lercher, J. A. Hydronium-Ion-Catalyzed Elimination Pathways of Substituted Cyclohexanols in Zeolite H-ZSM5. *ACS Catalysis* **2017**, 7 (11), 7822.
- (2) Milakovic, L.; Hintermeier, P. H.; Liu, Q.; Shi, H.; Liu, Y.; Baráth, E.; Lercher, J. A. Towards understanding and predicting the hydronium ion catalyzed dehydration of cyclic-primary, secondary and tertiary alcohols. *Journal of Catalysis* **2020**, 390, 237.



# Chapter 4

## Dehydration of fatty alcohols on zirconia supported tungstate catalysts



**This work has been published**

Reprinted with permission from: Milaković, L.; Liu, Y.; Baráth, E.; Lercher, J. A. Dehydration of fatty alcohols on zirconia supported tungstate catalysts. *Catalysis Science & Technology* **2022**, 12 (20), 6084. DOI: 10.1039/D2CY00785A

Copyright (2023) Royal Society of Chemistry.

## Abstract

Zirconia supported tungstates catalyze octadecanol dehydration, an important step in the carbon preserving conversion of triglycerides to fuels. This study shows the dependence of the tetragonal zirconia phase of  $\text{WO}_3/\text{ZrO}_2$  on the formation of Zr-stabilized  $\text{WO}_3$  clusters, leading to the highest Brønsted acid site concentrations and in turn to the highest octadecanol dehydration rates. Small concentrations of Pt increased the Brønsted acid site concentrations by stabilizing partly reduced tungstates.

## 4.1 Introduction

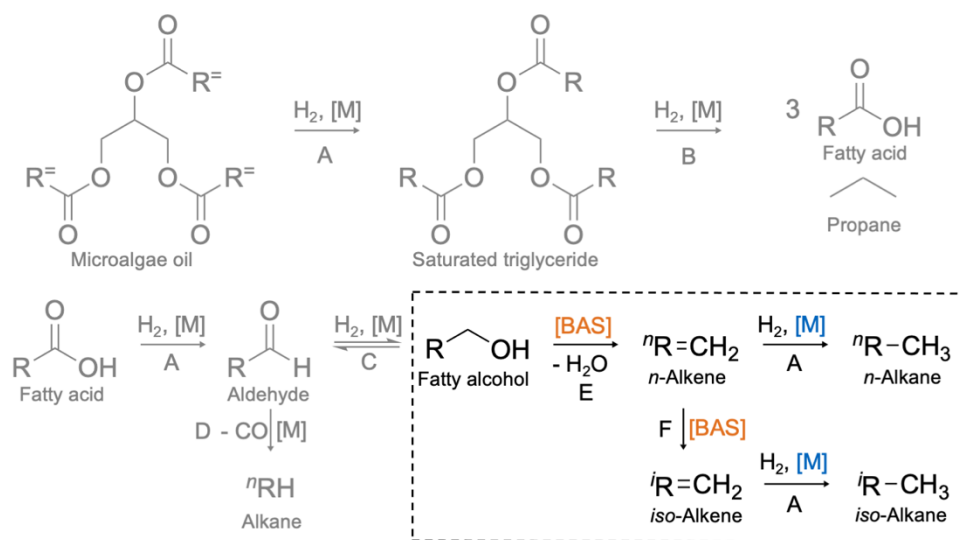
Since Hino and Arata discovered the hydrothermally stable  $\text{WO}_3/\text{ZrO}_2$  as a strong solid acid catalyst, considerable interest was raised in its catalytic properties.<sup>1</sup> Extensive research has been conducted employing tungstated zirconia as catalyst for various reactions such as isomerization of light alkanes,<sup>1-3</sup> selective catalytic reduction of  $\text{NO}_x$ <sup>4</sup> and dehydration of alcohols.<sup>5-7</sup> In general, the tungsten surface density is presumed to be the key indicator for the catalytic activity. There is a general agreement on the differentiation between four tungsten surface species.<sup>3,7-11</sup> In sub-monolayer concentrations octahedral isolated mono-oxo  $\text{W}=\text{O}$  species grow with increasing  $\text{W}$  surface density to polymeric mono-oxo  $\text{W}=\text{O}$  species. After reaching monolayer surface coverage, crystalline, monoclinic  $\text{WO}_3$  nanoparticles start to form.<sup>7,12</sup> Under certain conditions Zr-stabilized  $\text{WO}_3$  nanoparticles can co-exist with monomeric and polymeric  $\text{W}=\text{O}$  containing species.<sup>7-9</sup>

Our recent study, moreover, revealed the significant influence of the tungstate support.<sup>13</sup> The aqueous phase dehydration of cyclohexanol showed a drastically increase of the turnover frequency for the activated carbon support induced by changes of the local ionic strength and in turn the excess chemical potential. Besides, differences between two polymorphs of the zirconia support were indicated, which has also been previously addressed.<sup>7,14</sup> However, there are still discrepancies regarding the source of the catalytic activity.<sup>3,7,14-17</sup> For instance, while Lebarbier et al.<sup>14</sup> attribute the different activity of the two polymorphs mainly to the crystalline composition (tetragonal vs. monoclinic zirconia), Ross-Medgaarden et al.<sup>7</sup> reason that the catalytic differences are primarily based on the presence of Zr-stabilized  $\text{WO}_3$  nanoparticles.

In this study, we investigate the origin of the surface differences of the zirconia support by examining the fatty alcohol dehydration (highlighted in Scheme 4.1) with octadecanol as the model compound on two different zirconia supported tungstate catalysts and additional platinum promotion in organic phase.

Dehydration of fatty alcohols is an important step in the hydrodeoxygenation of microalgae oil to hydrocarbon fuel which is considered an important alternative to petroleum-based fuels due to the promising properties of microalgae such as their high abundance and rapid growth.<sup>18,19</sup> The fatty acids of microalgae oil consist typically of a chain length between 14 – 22 carbon atoms.<sup>19,20</sup> Thus, their hydrodeoxygenation produces diesel-like transportation fuel.<sup>19,21,22</sup> In recent years, the further conversion to

hydrocarbons in the kerosene range for utilization in the aviation sector has attracted increasing interest.<sup>23</sup> This can be implemented by incorporating additionally a hydroisomerization or -cracking step. The reaction mechanism of the hydrodeoxygenation of microalgae oil to hydrocarbon fuel with a bifunctional catalyst is depicted in Scheme 4.1. The first step is the metal ([M]) catalyzed hydrogenation (A) of the unsaturated bonds in the triglyceride, followed by hydrogenolysis (B) to fatty acids and propane.



**Scheme 4.1.** Reaction mechanism of the microalgae oil hydrodeoxygenation to hydrocarbon fuel with a bifunctional catalyst, and highlighted the fatty alcohol dehydration. A = hydrogenation, B = hydrogenolysis, C = (de-)hydrogenation, D = decarbonylation, E = dehydration, F = isomerization.

The fatty acid is then hydrogenated (A) to an aldehyde which is in equilibrium with the corresponding fatty alcohol (C) or can undergo decarbonylation (D) to a *n*-alkane.

In the presence of Brønsted acid sites (BAS), the fatty alcohol is dehydrated (E) to a *n*-alkene. This is in turn either isomerized (F) and then further hydrogenated (A) to an *iso*-alkane or is just directly hydrogenated (A) to the saturated and unbranched *n*-alkane.<sup>21</sup> As the microalgae are cultivated in an aqueous environment, the zirconia supported tungstate catalysts fulfill the requirement of being stable in water and at the same time provide the needed Brønsted acidity.<sup>1</sup>

## 4.2 Results and discussion

### 4.2.1 Characterization

WO<sub>3</sub>/ZrO<sub>2</sub> catalysts with different tungsten oxide loading in the range between 5.9 to 27.4 wt% were synthesized via two methods. One method incorporated the WO<sub>3</sub> onto a pre-calcined crystalline zirconia (ZrO<sub>2</sub>) support (subsequently referred to as xWZrO<sub>2</sub>(y), with x indicating the WO<sub>3</sub> loading and y the W surface density), while for the other an incipient wetness impregnation directly onto the amorphous zirconium hydroxide (Zr(OH)<sub>4</sub>) was conducted (xWZrOH(y)). Further details of the synthesis can be found in the 4.4 Experimental section. The physiochemical properties of the investigated catalyst are summarized in Table 4.1. The tungsten surface density is calculated based on the WO<sub>3</sub> loadings and the specific surface areas (detailed calculation in the 4.4 Experimental section).<sup>7</sup> As the surface area depends on the calcination temperature, it also influences the WO<sub>x</sub> surface density.<sup>7,24</sup> This study uses a pre-calcination temperature of 800°C. While the W surface density increased expectedly with increasing W loadings (Table 4.1, SI, Figure S4.1), the specific surface areas of the final materials passed through a maximum. The increase of the BET surface area is attributed to stabilization of the zirconia support by direct interaction with the octahedral tungstates via covalent W-O-Zr bonds<sup>7</sup> that block nucleation sites, reduce surface diffusivity and inhibit so sintering of the ZrO<sub>2</sub> support.<sup>16,24,25</sup> The specific surface area decreased once the monolayer coverage was reached.<sup>26</sup> Using the maximum as indication, a W surface density above 4.6 and 4.0 W nm<sup>-2</sup> for the WZrO<sub>2</sub> and WZrOH catalysts was considered to be monolayer coverage.<sup>7,12,27-30</sup> In general, the WZrOH catalysts showed higher BET surface areas than the WZrO<sub>2</sub> catalysts, which is attributed to the more facile surface stabilization in presence of the higher concentration of hydroxyl groups to develop W-O-Zr bonds.

**Table 4.1.** Physiochemical properties of the studied WZrO<sub>2</sub> and WZrOH catalysts.

WZrO <sub>2</sub>	BET surface area (m <sup>2</sup> g <sup>-1</sup> )	W surface density (W nm <sup>-2</sup> ) <sup>a</sup>	c (BAS) (mmol g <sup>-1</sup> ) <sup>b</sup>	WZrOH	BET surface area (m <sup>2</sup> g <sup>-1</sup> )	W surface density (W nm <sup>-2</sup> ) <sup>a</sup>	c (BAS) (mmol g <sup>-1</sup> ) <sup>b</sup>
7.3 wt% WO <sub>3</sub> /ZrO <sub>2</sub>	66	2.8	0.008	5.9 wt% WO <sub>3</sub> /ZrO <sub>2</sub>	63	2.4	0.004
12.2 wt% WO <sub>3</sub> /ZrO <sub>2</sub>	70	4.6	0.015	10.3 wt% WO <sub>3</sub> /ZrO <sub>2</sub>	71	3.7	0.023
14.6 wt% WO <sub>3</sub> /ZrO <sub>2</sub>	66	5.7	0.019	13.8 wt% WO <sub>3</sub> /ZrO <sub>2</sub>	91	4.0	0.033
17.4 wt% WO <sub>3</sub> /ZrO <sub>2</sub>	64	7.1	0.023	14.9 wt% WO <sub>3</sub> /ZrO <sub>2</sub>	87	4.5	0.035
19.4 wt% WO <sub>3</sub> /ZrO <sub>2</sub>	60	8.5	0.022	16.2 wt% WO <sub>3</sub> /ZrO <sub>2</sub>	78	5.4	0.038
22.0 wt% WO <sub>3</sub> /ZrO <sub>2</sub>	53	10.9	0.020	18.2 wt% WO <sub>3</sub> /ZrO <sub>2</sub>	77	6.2	0.035
24.4 wt% WO <sub>3</sub> /ZrO <sub>2</sub>	49	13.0	0.016	20.6 wt% WO <sub>3</sub> /ZrO <sub>2</sub>	63	8.6	0.029
27.4 wt% WO <sub>3</sub> /ZrO <sub>2</sub>	44	16.1	0.011	24.8 wt% WO <sub>3</sub> /ZrO <sub>2</sub>	60	10.7	0.018

<sup>a</sup>Detailed calculation in the 4.4 Experimental section. <sup>b</sup>Determined from IR spectroscopy of adsorbed pyridine.

In order to better understand the surface composition of the catalysts Raman spectroscopy was used. The Raman spectra of the  $\text{WZrO}_2$  are presented in Figure 4.1 A. Most bands below  $700\text{ cm}^{-1}$  are attributed to monoclinic  $\text{ZrO}_2$  with bands at  $180, 192, 220, 308, 335, 349, 383, 476, 503, 539, 561, 617,$  and  $638\text{ cm}^{-1}$ .<sup>7,31</sup>

The intensity of these bands, however, decreased with increasing tungsten coverage. Above a W surface density of  $4.6\text{ W nm}^{-2}$  the characteristic bands of crystalline m- $\text{WO}_3$  at  $272, 713,$  and  $804\text{ cm}^{-1}$  were detected.<sup>12,14,28,30</sup> The broad bands around  $960 - 970\text{ cm}^{-1}$  are attributed to isolated mono-oxo  $\text{W}=\text{O}$  species, shifting toward  $1000\text{ cm}^{-1}$  when polymeric mono-oxo  $\text{W}=\text{O}$  species evolve with increasing tungsten loading.<sup>12,14,28,30</sup>

On  $\text{WZrOH}$  catalysts (Figure 4.1 B), the appearance of characteristic bands of crystalline m- $\text{WO}_3$  ( $272, 713,$  and  $804\text{ cm}^{-1}$ ) suggest that monolayer coverage is reached above  $4.0\text{ W nm}^{-2}$ . Below  $700\text{ cm}^{-1}$  mainly bands of t- $\text{ZrO}_2$  at  $149, 319, 464, 476,$  and  $647\text{ cm}^{-1}$  were detected, which were also decreasing with higher W surface density.<sup>7,31</sup> As these bands partly overlap with those of monoclinic  $\text{ZrO}_2$  the phase composition was additionally probed by XRD. Further, also bands of isolated and polymeric mono-oxo  $\text{W}=\text{O}$  species are presented around  $960 - 970\text{ cm}^{-1}$  and  $1000\text{ cm}^{-1}$ , respectively.<sup>12,14,28,30</sup> The  $13.8\text{WZrOH}(4.0)$  catalyst showed additional bands at  $835\text{ cm}^{-1}$  and a wider less intense at  $905\text{ cm}^{-1}$ , assigned to three-dimensional distorted  $\text{Zr-WO}_3$  clusters.<sup>8</sup> As their characteristic band ( $835\text{ cm}^{-1}$ ) overlaps with the strong band of m- $\text{WO}_3$  ( $804\text{ cm}^{-1}$ ), it can only be hypothesized that the Zr-stabilized  $\text{WO}_3$  clusters are also present in the other catalysts. Due to the fact that Raman-spectroscopy is not perfectly suited for the identification of the  $\text{Zr-WO}_3$  species above monolayer coverage, their existence has not been experimentally observed. In 2009, however, Zhou et al. provided direct imaging of this species with the help of high-angle annular dark-field imaging in an aberration-corrected STEM.<sup>8</sup>

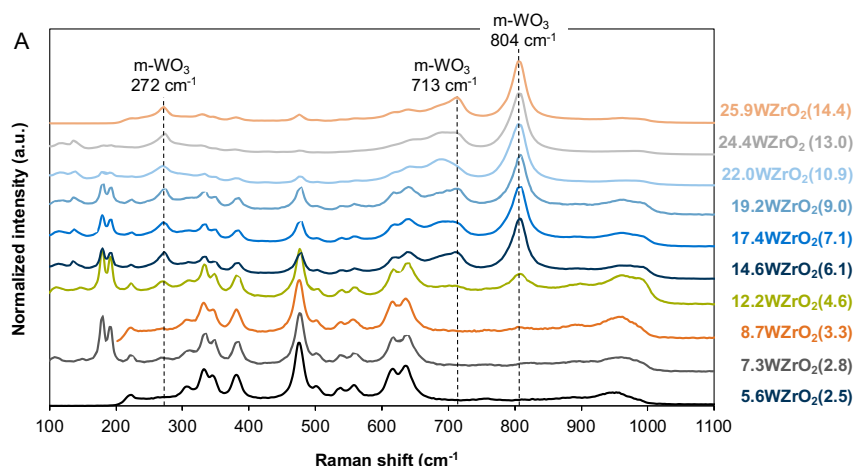


**Figure 4.1 A.** Raman shift of the  $\text{WZrO}_2$  (A) catalysts with different  $\text{WO}_3$  loadings with identification of the characteristic bands of m- $\text{WO}_3$ .

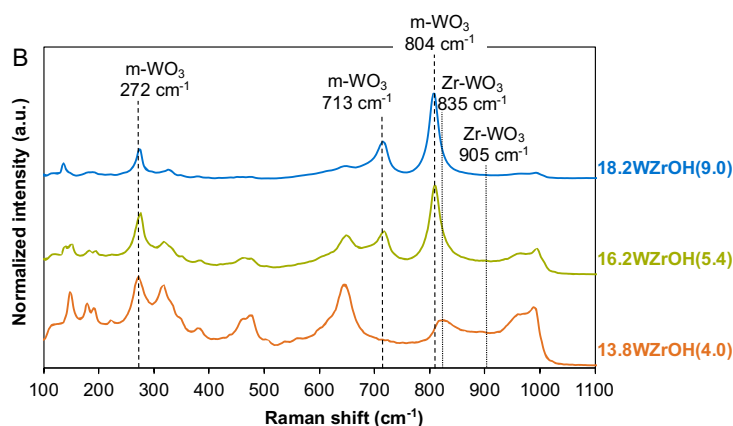


**Figure 4.1 B.** Raman shift of the WZrOH (B) catalysts with different  $\text{WO}_3$  loadings with identification of the characteristic bands of m- $\text{WO}_3$  and Zr- $\text{WO}_3$ .

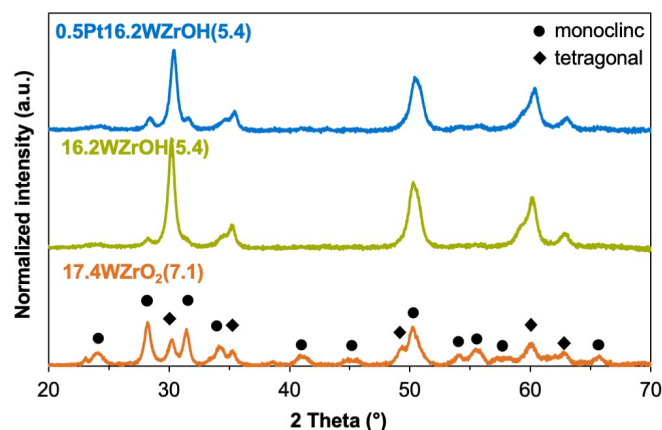
At high temperature pure zirconia is transformed from the metastable tetragonal to the thermodynamically stable monoclinic phase.<sup>32</sup> This transformation is retarded by the stabilizing interaction with the tungstates.<sup>24,25</sup> Table 4.2 summarizes the fractions of these two phases determined by X-ray diffraction (all XRD patterns in SI, Figure S4.2 and S4.3).

Figure 4.2 assigns the reflections of the XRD patterns of the 17.4WZrO<sub>2</sub>(7.1), 16.2WZrOH(5.4), and 0.5Pt16.2WZrOH(5.4) catalysts to either monoclinic or tetragonal phases. The WZrO<sub>2</sub> catalysts have a significantly higher fraction of m-ZrO<sub>2</sub> than the WZrOH catalysts, because of the lack of stabilization by tungstates during the pre-calcination of the zirconia support at 400°C, where the t-ZrO<sub>2</sub> was already partly transformed.

The 0.5Pt16.2WZrOH(5.4) catalyst on the contrary, only suffers a minor loss of the tetragonal phase despite the repeated thermal treatment. With increasing  $\text{WO}_3$  loading, the fraction of t-ZrO<sub>2</sub> is growing and levels off at high loadings. It is interesting to note that this decrease occurs, in contrast to the BET surface area, above monolayer coverage.

**Table 4.2.** Content of the monoclinic or tetragonal phase in the WZrO<sub>2</sub> and WZrOH catalysts derived from XRD.

WZrO <sub>2</sub>	m-ZrO <sub>2</sub> (%)	t-ZrO <sub>2</sub> (%)	WZrOH	m-ZrO <sub>2</sub> (%)	t-ZrO <sub>2</sub> (%)
ZrO <sub>2</sub> (400°C)	63	37	5.9 wt% $\text{WO}_3/\text{ZrO}_2$	73	28
ZrO <sub>2</sub> (800°C)	92	8	10.3 wt% $\text{WO}_3/\text{ZrO}_2$	54	46
5.6 wt% $\text{WO}_3/\text{ZrO}_2$	90	10	12.5 wt% $\text{WO}_3/\text{ZrO}_2$	41	59
8.7 wt% $\text{WO}_3/\text{ZrO}_2$	88	12	14.9 wt% $\text{WO}_3/\text{ZrO}_2$	25	75
12.2 wt% $\text{WO}_3/\text{ZrO}_2$	85	15	16.2 wt% $\text{WO}_3/\text{ZrO}_2$	23	77
17.4 wt% $\text{WO}_3/\text{ZrO}_2$	81	19	18.2 wt% $\text{WO}_3/\text{ZrO}_2$	26	74
22.0 wt% $\text{WO}_3/\text{ZrO}_2$	84	16	0.5 wt% Pt 16.2 wt% $\text{WO}_3/\text{ZrO}_2$	33	67



**Figure 4.2.** XRD patterns of a WZrO<sub>2</sub>, WZrOH and PtWZrOH catalyst with the assignment of the reflections to the monoclinic or tetragonal phase.

The Brønsted acid site concentration of the catalysts, which is summarized in Table 4.1, is presented as a function of the tungsten loading in Figure 4.3. It is shown that the BAS concentration passes through a maximum by increasing the tungsten loading (analogous dependency of BAS concentration by increasing the W surface density, SI, Figure S4.4). As BAS can originate from acidic hydroxyl groups associated with W-O-W and W-O-Zr bonds, an increase of the tungsten loading, and in turn the W surface density, will result in a higher concentration of these bonds and, therefore, a higher concentration of Brønsted acid sites.<sup>33</sup> In other words, by increasing the tungstate domain size the associated ability of the conjugate base to delocalize electrons upon deprotonation of the acid is increased.<sup>9</sup> However, with increasing tungsten loading large crystalline WO<sub>3</sub> particles start to form. Therefore, more and more W centers become inaccessible which results in a decrease of the BAS concentration.<sup>12</sup> It should be noted in passing that when discussing the dependency of the W surface density on the BAS concentration, the impact of the surface area is also being taken into account as these two parameters are interdependent.

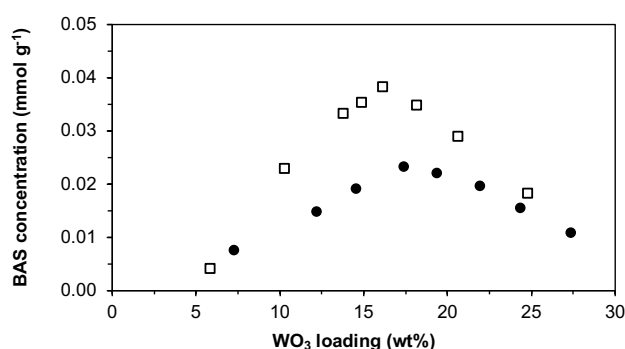


**Figure 4.3.** BAS concentrations as function of the WO<sub>3</sub> loading of different WZrO<sub>2</sub> (●) and WZrOH (□) catalysts.

The highest concentrations were observed above monolayer coverage on the 17.4WZrO<sub>2</sub>(7.1) and 16.2WZrOH(5.4) catalyst with 0.023 and 0.038 mmol g<sup>-1</sup>, respectively, which is in line with the highest fraction of t-ZrO<sub>2</sub>. Thus, the BAS concentration continues to increase, even after crystalline WO<sub>3</sub> particles are formed. This indicates that an additional species could exist, namely Zr-stabilized WO<sub>3</sub> nanoparticles, which contribute to the acidity of the catalysts. In literature it is speculated that Zr-stabilized WO<sub>3</sub> nanoparticles are the most active species.<sup>7,8</sup> In line, density functional theory calculations of the Brønsted acidity of these Zr-WO<sub>3</sub> nanoparticles have shown that they have the lowest deprotonation energy.<sup>9, 34</sup>

Remarkably, the BAS concentration correlates positively with the fraction of t-ZrO<sub>2</sub> (Figure 4.4). While the origin of this correlation needs further investigations, empirically it explains the significantly higher BAS concentrations in WZrOH compared to WZrO<sub>2</sub> catalysts. The BAS concentration, which is maximized by increasing the concentration of Zr-WO<sub>3</sub> clusters, has, therefore, a direct relation with the tetragonal phase of the zirconia support.

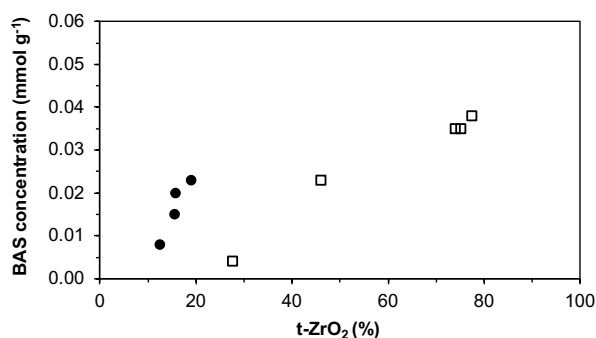


**Figure 4.4.** Correlation of the BAS concentration and the fraction of the tetragonal phase for both WZrO<sub>2</sub> (●) and WZrOH (□) catalysts.

It is assumed that the clusters can only be formed on the t-ZrO<sub>2</sub>. This could be due to their different lattice structures. While the monoclinic polymorph has heptacoordinated Zr<sup>4+</sup> cations and either tri- or tetraordinated O<sup>2-</sup> anions, the lattice of tetragonal zirconia consists of octacoordinated Zr<sup>4+</sup> cations and exclusively of tetraordinated O<sup>2-</sup> anions.<sup>35</sup> Recognizing that the presence of Zr-stabilized WO<sub>3</sub> nanoparticles and the tetragonal zirconia phase are interdependent, also harmonizes some conflicts in literature where it was believed that predominantly only one of these parameters is the main source of the catalytic activity.<sup>3,7,14-17</sup>

## 4.2.2 Octadecanol dehydration

The time-dependent conversion of octadecanol in a batch reactor with 17.4WZrO<sub>2</sub>(7.1) and 16.2WZrOH(5.4) are shown in Figure 4.5 A and B, respectively. With both catalysts *iso*-octadecene was selectively formed. Small amounts of *n*-octadecene and octadecanal were detected. The reaction order in the alcohol was zero (SI, Figure S4.5). After 240 min around 77% of octadecanol were converted with 17.4WZrO<sub>2</sub>(7.1) catalyst, 83% with 16.2WZrOH(5.4) catalyst already after 60 min reaction time. This superior catalytic activity of the zirconium hydroxide-based catalyst is also demonstrated in Figure 4.5 C, in which octadecanol dehydration rates are plotted versus the WO<sub>3</sub> loading for both series of catalysts. At equal tungstate concentrations, WZrO<sub>2</sub> (●) catalysts had an almost three-fold lower rate than the corresponding WZrOH (□) catalysts. The highest rate within a series was observed on 17.4WZrO<sub>2</sub>(7.1) catalyst with 2.0 × 10<sup>-6</sup> mol g<sup>-1</sup> s<sup>-1</sup> and on 16.2WZrOH(5.4) with 5.2 × 10<sup>-6</sup> mol g<sup>-1</sup> s<sup>-1</sup>. The rates show a volcano-shaped dependency on the WO<sub>3</sub> loading and on the tungstate surface density which also parallels the BAS concentrations (Figure 4.3 and 4.5 C, SI, Figure S4.4 and S4.6), coinciding to the hypothesis of the presence of Zr-stabilized WO<sub>3</sub> nanoparticles as the most active species. From a practical point it appears, therefore, that the highest activity is achieved with amorphous zirconium hydroxide support loaded with a medium W surface density.<sup>3,5,6,9,10</sup>

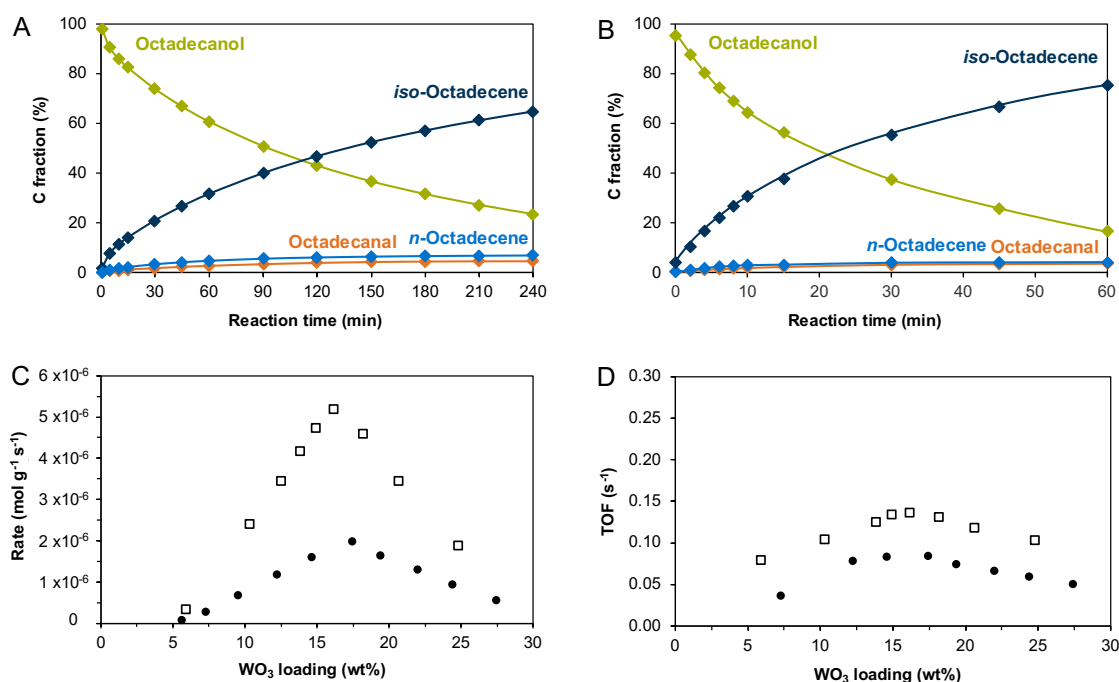


**Figure 4.5.** Product distribution of the octadecanol dehydration with 17.4WZrO<sub>2</sub>(7.1) (A) and 16.2WZrOH(5.4) (B) catalysts. Rate (C) and TOF (D) of the octadecanol dehydration as function of the WO<sub>3</sub> loading on different WZrO<sub>2</sub> (●) and WZrOH (□) catalysts. Reaction conditions: catalyst (0.2 g), octadecanol (0.5 g), decalin (100 mL), 180°C,  $p(\text{H}_2) = 40$  bar, 700 rpm.

Analyzing the turnover frequency (TOF), by normalizing the weight-based rate by the BAS concentration, it would be expected to see a constant dependency of the TOF on the tungsten loading. Figure 4.5 D shows a slight increase of the TOF for medium tungsten loadings (also for medium W surface densities, SI, Figure S4.7). Therefore, further investigations are necessary to differentiate between the strength of the acid sites of the Zr-WO<sub>3</sub> nanoparticles which cause this deviation in TOF plot. The activation energy is rather constant throughout the varying WO<sub>3</sub> content, however, is more than twice as high for the WZrO<sub>2</sub> catalysts in comparison to the WZrOH (e.g., SI, 14.6WZrO<sub>2</sub>(5.6): 97 kJ mol<sup>-1</sup> vs. 14.9WZrOH(4.5.): 38 kJ mol<sup>-1</sup>, Figure S4.8).

### 4.2.3 Promotion effect of platinum

As the conversion of triglycerides requires bifunctional, metal containing catalysts, the impact of Pt on the WZrOH catalysts was explored for dehydration. In order to exclude dehydration activity of the platinum, octadecanol was tested with a non-acidic Pt on carbon catalyst, which showed no conversion. Additionally, the results from our previous studies, investigating the HDO reaction network of long chain fatty acids with Ni on SiO<sub>2</sub> and ZrO<sub>2</sub>, support this hypothesis.<sup>36-38</sup>

Figure 4.6 A shows that the main product of the conversion over the 0.5Pt16.2WZrOH(5.4) catalyst was (expectedly) *n*-octadecane, while only small amounts of *iso*-octadecane and traces of octadecanal were detected. This allows to conclude that the hydrogenation rate was higher under the explored experimental conditions compared to the isomerization rate. Additionally, the pressure and the relatively low reaction temperature led to a low concentration of alkenes and, hence, to a very low rate of hydroisomerization. Indeed, experiments with a constant total pressure but varying H<sub>2</sub> partial pressure showed that lower H<sub>2</sub> pressures led to a higher *iso*-octadecane formation rate, while the dehydration rate was unchanged (SI, Figure S4.9). The rate of dehydration was also unaffected by varying the total pressure (SI, Figure S4.10).

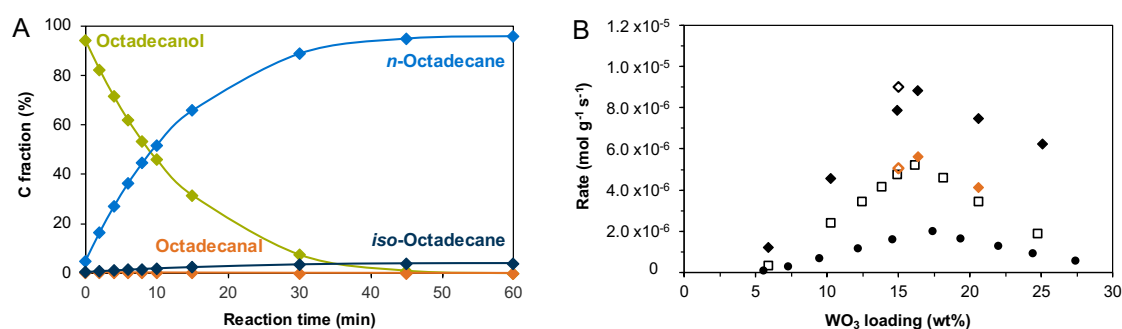


**Figure 4.6.** (A) Product distribution of the octadecanol dehydration over the 0.5Pt16.2WZrOH(5.4) catalyst. (B) Rate of the octadecanol dehydration as function of the WO<sub>3</sub> loading on different WZrO<sub>2</sub> (●), WZrOH (□), 0.5PtWZrOH (◆) and 1.5PtWZrOH (◇) catalysts in H<sub>2</sub>; and marked in orange in N<sub>2</sub>. Reaction conditions: catalyst (0.1 g), octadecanol (0.5 g), decalin (100 mL), 180°C,  $p(\text{H}_2/\text{N}_2) = 40$  bar, 700 rpm.

The reaction order was determined to be zero in the alcohol (SI, Figure S4.11). The weight normalized dehydration rate was as well independent of the carbon chain length of the converted substrate (C15 – C18, SI, Figure S4.12).

Also for the 0.5PtWZrOH (◆) catalysts a volcano-shaped rate dependency on the  $\text{WO}_3$  loading was found (Figure 4.6 B). The highest dehydration rate was measured with the catalyst having the same tungsten density as on the one without Pt. Although Pt is not actively participating in the dehydration reaction, the dehydration rates were enhanced by 40% up to 70% in presence of Pt (e.g.,  $5.2 \times 10^{-6} \text{ mol g}^{-1} \text{ s}^{-1}$  without Pt increased to  $8.8 \times 10^{-6} \text{ mol g}^{-1} \text{ s}^{-1}$  with 0.5Pt16.2WZrOH(5.4)). The same was observed for 0.5PtWZrO<sub>2</sub> catalysts (SI, Note S4.1). It is hypothesized and has previously been reported that Pt in the presence of  $\text{H}_2$  enables a partial reduction of the tungstates increasing the concentration of Brønsted acid sites (SI, Scheme S4.1).<sup>16,26</sup> Indeed, when the reaction was conducted in  $\text{N}_2$ , the rates were identical in presence and absence of Pt (marked in orange, Figure 4.6 B). Expectedly, the product distribution of the Pt containing catalysts reverted to *iso*-octadecene as main product (SI, Figure S4.13). Moreover, Figure 4.6 B shows that increasing the amount of platinum to 1.5 wt% (◇) slightly enhances the rate further. When conducting the reactions in nitrogen, this promotion again disappears (e.g., 14.9WZrOH(4.5):  $4.7 \times 10^{-6} \text{ mol g}^{-1} \text{ s}^{-1}$ , 0.5Pt14.9WZrOH(4.5):  $7.8 \times 10^{-6} \text{ mol g}^{-1} \text{ s}^{-1}$ , 1.5Pt14.9WZrOH(4.5):  $9.0 \times 10^{-6} \text{ mol g}^{-1} \text{ s}^{-1}$  ( $\text{H}_2$ ),  $5.0 \times 10^{-6} \text{ mol g}^{-1} \text{ s}^{-1}$  ( $\text{N}_2$ )). In general, the dehydration rate was increasing with an increasing Pt loading, while the *iso*-octadecane formation rate was decreasing (SI, Figure S4.14).

### 4.3 Conclusion

The octadecanol dehydration over  $\text{WO}_3$  supported zirconia catalysts showed on volcano-shaped rate dependency on the tungsten loading independent of the initial crystallinity of the support (crystalline zirconia or amorphous zirconium hydroxide) or a metal promotion (with or without Pt). The maximum was consistently found above monolayer coverage, confirming the presence of a most active species.

Even though, Raman spectroscopy could only detect the presence of Zr-stabilized  $\text{WO}_3$  clusters on the 13.8WZrOH(4.0) catalyst, following the evidence and conclusions of the work of Zhou et al.<sup>8</sup> in analogy to our results, it is hypothesized that Zr- $\text{WO}_3$  clusters as the most active species also exist on the other investigated catalysts.

Further, XRD measurements revealed the dependency of the occurrence of Zr-stabilized  $\text{WO}_3$  clusters on the tetragonal zirconia phase. By maximizing this polymorph, the highest BAS concentrations were generated and in turn the highest octadecanol dehydration rates were obtained. During the pre-calcination of the crystalline zirconia support, t-ZrO<sub>2</sub> was already partly transformed to the monoclinic phase due to the absence of stabilizing interactions with the tungstates. Consequently, the WZrO<sub>2</sub> catalysts had a lower activity than the WZrOH catalysts.

Incorporating platinum onto the WZrOH catalysts resulted in a rate enhancement, even though it is not involved in the reaction and has a similar t-ZrO<sub>2</sub> content as the sole WZrOH catalyst. The enhancement was presumably caused by a Pt facilitated reduction of the tungstates already at moderate temperatures in the presence of hydrogen.

## 4.4 Experimental

### 4.4.1 Chemicals

All chemicals were purchased commercially and were not further purified. The following chemicals were used: Nitrogen 5.0, hydrogen 5.0 and synthetic air (20.5 vol% oxygen, 79.5 vol% nitrogen) were obtained from *Westfalen*.  $\text{Zr}(\text{OH})_4 \cdot x\text{H}_2\text{O}$  (XZO880/01) was supplied by *MEL Chemicals*.  $(\text{NH}_4)_6\text{H}_2\text{W}_{12}\text{O}_{40} \cdot x\text{H}_2\text{O}$  (99.99% trace metals basis),  $\text{Pt}(\text{NH}_3)_4(\text{NO}_3)_2$  (99.995% trace metals basis), 1-octadecanol (*ReagentPlus*, 99%), 1-heptadecanol (98%), 1-hexadecanol (*ReagentPlus*, 99%) and 1-pentadecanol (99%) were acquired from *Sigma-Aldrich*. Decahydronaphthalene (mixture of *cis*- and *trans* isomers,  $\geq 99.0\%$ , for synthesis) was purchased from *Merck*.

### 4.4.2 Catalyst preparation

**$\text{WO}_3/\text{ZrO}_2$ :** For the synthesis of the  $\text{WZrO}_2$  catalysts, the zirconium hydroxide was pre-calcined in synthetic air (flow rate:  $100 \text{ mL min}^{-1}$ ) at  $400^\circ\text{C}$  for 4 h (heating rate:  $10^\circ\text{C min}^{-1}$ ). The  $(\text{NH}_4)_6\text{H}_2\text{W}_{12}\text{O}_{40} \cdot x\text{H}_2\text{O}$  precursor solution was added dropwise onto the  $\text{ZrO}_2$  ( $\text{WZrO}_2$ ) or  $\text{Zr}(\text{OH})_4 \cdot x\text{H}_2\text{O}$  ( $\text{WZrOH}$ ) support by incipient wetness impregnation, dried overnight at  $110^\circ\text{C}$ , and subsequently calcined in synthetic air (flow rate:  $100 \text{ mL min}^{-1}$ ) at  $800^\circ\text{C}$  for 3 h (heating rate:  $10^\circ\text{C min}^{-1}$  until  $700^\circ\text{C}$ , afterwards  $5^\circ\text{C min}^{-1}$ ).

**$\text{Pt}/\text{WO}_3/\text{ZrO}_2$ :** Platinum was incorporated onto the  $\text{WZrOH}$  catalysts also by incipient wetness impregnation with the tetraammineplatinum(II) nitrate precursor solution. The catalyst was thermally treated in  $\text{N}_2$  (flow rate:  $100 \text{ mL min}^{-1}$ ) at  $400^\circ\text{C}$  for 3 h (heating rate:  $3^\circ\text{C min}^{-1}$ ) and then reduced in  $\text{H}_2$  (flow rate:  $100 \text{ mL min}^{-1}$ ) at  $400^\circ\text{C}$  for 3 h (heating rate:  $3^\circ\text{C min}^{-1}$ ).

### 4.4.3 Analysis Methods

**Elemental analysis:** The tungsten and platinum content was determined photometrically using a *Shimadzu UV-160 UV-VIS-NIR* spectrometer. 25 mg of the tungsten sample was prepared by an alkaline pulping and analyzed by the absorbance of a trithiocyanatotungsten(V)-complex at 405 nm, while for the determination of the platinum content 100 mg of the sample were prepared by an acidic pulping and subsequently measured by the absorbance of a trichlorostannatoplatinum-complex at 403 nm.

**$\text{N}_2$  physisorption:** The specific surface area of the catalysts was determined by using a *Thermo Fisher Scientific Sorptomatic 1990 series* instrument. First, 150 mg of sample were outgassed at  $300^\circ\text{C}$  for two hours at  $1.3 \times 10^{-5}$  bar. The adsorption-desorption isotherms were collected at  $-196^\circ\text{C}$  in a  $\text{N}_2$  pressure range from 0.9613 to 0.9626 bar. The specific surface areas were calculated by means of *Brunauer-Emmett-Teller* (BET) theory.

**Tungsten surface density:** The W surface densities were determined by the following equation adapted from Ross-Medgaarden et al.<sup>7</sup>:

$$\text{W surface density} \left[ \frac{\text{W}}{\text{nm}^2} \right] = \frac{\left( \frac{\text{WO}_3 \text{ loading [wt\%]}}{100} \right) \cdot N_A \left[ \frac{1}{\text{mol}} \right]}{M_{\text{WO}_3} \left[ \frac{\text{g}}{\text{mol}} \right] \cdot \text{BET surface area} \left[ \frac{\text{m}^2}{\text{g}} \right] \cdot 10^{18}}$$

where  $N_A$  is the Avogadro constant and  $M_{\text{WO}_3}$  represents the molar mass of tungsten trioxide.

**IR spectra of adsorbed pyridine (Py-IR):** The Brønsted acid site concentration was determined by measuring Py-IR with a *Thermo Nicolet 5700* FT-IR spectrometer at a resolution of  $4 \text{ cm}^{-1}$ . The catalyst was pelleted into a thin wafer and activated at  $450^\circ\text{C}$  (heating rate =  $10^\circ\text{C min}^{-1}$ ) for one hour in vacuum (ca.  $10^{-6}$  mbar). After cooling down to  $150^\circ\text{C}$ , the apparatus was filled with pyridine until the sample was fully saturated and subsequently equilibrated for one hour. Next, the system was outgassed for one hour to remove physically adsorbed pyridine and a spectrum with the chemisorbed pyridine was collected. Finally, the system was heated again to  $450^\circ\text{C}$  (heating rate =  $10^\circ\text{C min}^{-1}$ ) for one hour in vacuum to desorb the pyridine. The concentration of the Brønsted ( $1540 \text{ cm}^{-1}$ ) acid sites was quantitatively calculated by using a molar integral extinction coefficients of  $0.73 \text{ cm } \mu\text{mol}^{-1}$ .

**Raman spectroscopy:** The Raman spectra of the catalysts were acquired by a *Via Reflex Raman System* which comprises a research grade optical microscope (*Leica DM2700M*, Magnification 5x, 20x, 50x) coupled to a high-performance Raman spectrometer (*Renishaw*) and a 532 nm diode laser as excitation source (*RL532C*, Class 3B).

**X-ray powder diffraction (XRD):** XRD measurements were performed on a *PANalytical Empyrean* diffractometer equipped with a Cu-K $\alpha$  radiation of  $\lambda = 1.54 \text{ \AA}$  operating at 45 kV and 40 mA. The scanning range was  $5 - 70^\circ 2\theta$  with a step size of  $0.017^\circ$ . For the analysis of the diffractograms as well as the determination of the monoclinic and tetragonal phases, the *PANalytical Highscore Plus* software was used.

#### 4.4.4 Catalytic measurements

All reactions were performed in an autoclave (300 mL) from *Parr Instruments Co.* (type: *PST FS*, material: HASTELLOY C) with a temperature and stirring controlling device (*Parr Instruments Co. 4848 Reactor Controller*). The liquid samples were analyzed by a gas chromatography (GC) system (*Agilent Technologies 7890B GC*, *HP-5* capillary column (30 m, 0.32 mm inner diameter, 0.25  $\mu\text{m}$  film), equipped with a flame ionization detector (FID) and a mass spectrometer (MS) (*Agilent Technologies 5977 MS*). Data was analyzed with *MassHunter Workstation Software, Qualitative Analysis, Version B.06.00*, *Agilent Technologies (2012)*.

The reactant and the catalyst were dissolved in 100 mL decalin. After purging the reactor two times with  $\text{H}_2$  or  $\text{N}_2$ , the pressure was set to 6 bar and heated to the desired temperature with a heating rate of  $10^\circ\text{C per minute}$  without stirring.  $10^\circ\text{C}$  below the

reaction temperature, the total pressure was adjusted and as soon as the target temperature was reached, the stirring rate was set to 700 rpm to start the experiment. During the reaction, in situ sampling was applied. The reaction conditions included a high hydrogen pressure in order to be consistent with the experiments investigating the hydrodeoxygenation of microalgae.

The weight normalized dehydration rate was independent of the employed catalyst amount (SI, Figure S4.15) and refers to the initial rates which were determined by plotting the conversion of octadecanol versus the reaction time. The slope of the linear fit at low conversions (< 20%) is then multiplied with the initial molar amount of octadecanol and divided by the mass of the catalyst.

## 4.5 Acknowledgements

This work was funded by the Alpines AlgenKerosin (FKZ LaBay89A) project by the Bavarian State Ministry for Economic Affairs, Regional Development and Energy and the Bavarian State Ministry of Science and the Arts.

J. A. L. was supported by the U.S. Department of Energy (DOE), Office of Science, Office of Basic Energy Sciences (BES), Division of Chemical Sciences, Geosciences and Biosciences (Transdisciplinary Approaches to Realize Novel Catalytic Pathways to Energy Carriers, FWP 47319). Special gratitude is expressed to A. Brenig and A. Mühlbach for their help in performing experiments.

## 4.6 Author contributions

L.M., E.B., Y. L. and J.A.L. conceived the initial idea. L.M. conducted synthesis, characterization, experiments and calculations. The manuscript was written through contributions of all authors.

## 4.7 References

- (1) Hino, M.; Arata, K. Synthesis of solid superacid of tungsten oxide supported on zirconia and its catalytic action for reactions of butane and pentane. *Journal of the Chemical Society, Chemical Communications* **1988**, (18), 1259.
- (2) Santiesteban, J. G.; Vartuli, J. C.; Han, S.; Bastian, R. D.; Chang, C. D. Influence of the Preparative Method on the Activity of Highly Acidic  $WO_x/ZrO_2$  and the Relative Acid Activity Compared with Zeolites. *Journal of Catalysis* **1997**, *168* (2), 431.
- (3) Soultanidis, N.; Zhou, W.; Psarras, A. C.; Gonzalez, A. J.; Iliopoulou, E. F.; Kiely, C. J.; Wachs, I. E.; Wong, M. S. Relating n-Pentane Isomerization Activity to the Tungsten Surface Density of  $WO_x/ZrO_2$ . *Journal of the American Chemical Society* **2010**, *132* (38), 13462.
- (4) Kantcheva, M.; Milanova, M.; Mametsheripov, S. In situ FT-IR spectroscopic investigation of gold supported on tungstated zirconia as catalyst for CO-SCR of NOx. *Catalysis Today* **2012**, *191* (1), 12.
- (5) Baertsch, C. D.; Komala, K. T.; Chua, Y.-H.; Iglesia, E. Genesis of Brønsted Acid Sites during Dehydration of 2-Butanol on Tungsten Oxide Catalysts. *Journal of Catalysis* **2002**, *205* (1), 44.
- (6) Macht, J.; Baertsch, C. D.; May-Lozano, M.; Soled, S. L.; Wang, Y.; Iglesia, E. Support effects on Brønsted acid site densities and alcohol dehydration turnover rates on tungsten oxide domains. *Journal of Catalysis* **2004**, *227* (2), 479.
- (7) Ross-Medgaarden, E. I.; Knowles, W. V.; Kim, T.; Wong, M. S.; Zhou, W.; Kiely, C. J.; Wachs, I. E. New insights into the nature of the acidic catalytic active sites present in  $ZrO_2$ -supported tungsten oxide catalysts. *Journal of Catalysis* **2008**, *256* (1), 108.
- (8) Zhou, W.; Ross-Medgaarden, E. I.; Knowles, W. V.; Wong, M. S.; Wachs, I. E.; Kiely, C. J. Identification of active Zr- $WO_x$  clusters on a  $ZrO_2$  support for solid acid catalysts. *Nature Chemistry* **2009**, *1* (9), 722.
- (9) Zhou, W.; Soultanidis, N.; Xu, H.; Wong, M. S.; Neurock, M.; Kiely, C. J.; Wachs, I. E. Nature of Catalytically Active Sites in the Supported  $WO_3/ZrO_2$  Solid Acid System: A Current Perspective. *ACS Catalysis* **2017**, *7* (3), 2181.
- (10) Lee, J.-H.; Shin, C.-H.; Suh, Y.-W. Higher Brønsted acidity of  $WO_x/ZrO_2$  catalysts prepared using a high-surface-area zirconium oxyhydroxide. *Molecular Catalysis* **2017**, *438*, 272.
- (11) Piva, D. H.; Piva, R. H.; Pereira, C. A.; Silva, D. S. A.; Montedo, O. R. K.; Morelli, M. R.; Urquieta-González, E. A. Facile synthesis of  $WO_x/ZrO_2$  catalysts using  $WO_3 \cdot H_2O$  precipitate as synthetic precursor of active tungsten species. *Materials Today Chemistry* **2020**, *18*, 100367.
- (12) Barton, D. G.; Shtein, M.; Wilson, R. D.; Soled, S. L.; Iglesia, E. Structure and Electronic Properties of Solid Acids Based on Tungsten Oxide Nanostructures. *The Journal of Physical Chemistry B* **1999**, *103* (4), 630.
- (13) Pfriem, N.; Liu, Y.; Zahn, F.; Shi, H.; Haller, G. L.; Lercher, J. A. Impact of the Local Concentration of Hydronium Ions at Tungstate Surfaces for Acid-Catalyzed Alcohol Dehydration. *Journal of the American Chemical Society* **2021**, *143* (48), 20133.
- (14) Lebarbier, V.; Clet, G.; Houalla, M. A Comparative Study of the Surface Structure, Acidity, and Catalytic Performance of Tungstated Zirconia Prepared from Crystalline Zirconia or Amorphous Zirconium Oxyhydroxide. *The Journal of Physical Chemistry B* **2006**, *110* (28), 13905.
- (15) Gonell, F.; Portehault, D.; Julián-López, B.; Vallé, K.; Sanchez, C.; Corma, A. One step microwave-assisted synthesis of nanocrystalline  $WO_x-ZrO_2$  acid catalysts. *Catalysis Science & Technology* **2016**, *6* (23), 8257.
- (16) Barton, D. G.; Soled, S. L.; Meitzner, G. D.; Fuentes, G. A.; Iglesia, E. Structural and Catalytic Characterization of Solid Acids Based on Zirconia Modified by Tungsten Oxide. *Journal of Catalysis* **1999**, *181* (1), 57.
- (17) Di Gregorio, F.; Keller, V. Activation and isomerization of hydrocarbons over  $WO_3/ZrO_2$  catalysts: I. Preparation, characterization, and X-ray photoelectron spectroscopy studies. *Journal of Catalysis* **2004**, *225* (1), 45.

- (18) Guschina, I. A.; Harwood, J. L. In *Algae for Biofuels and Energy*; Borowitzka, M. A.; Moheimani, N. R., Eds.; Springer Netherlands: Dordrecht, **2013**, 17.
- (19) Zhao, C.; Brück, T.; Lercher, J. Catalytic deoxygenation of microalgae oil to green hydrocarbons. *Green Chemistry* **2013**, 15.
- (20) Haas, M.; Wagner, K. Simplifying biodiesel production: The direct or in situ transesterification of algal biomass. *European Journal of Lipid Science and Technology* **2011**, 113, 1219.
- (21) Peng, B.; Yao, Y.; Zhao, C.; Lercher, J. A. Towards Quantitative Conversion of Microalgae Oil to Diesel-Range Alkanes with Bifunctional Catalysts. *Angewandte Chemie International Edition* **2012**, 51 (9), 2072.
- (22) Peng, B.; Yuan, X.; Zhao, C.; Lercher, J. A. Stabilizing Catalytic Pathways via Redundancy: Selective Reduction of Microalgae Oil to Alkanes. *Journal of the American Chemical Society* **2012**, 134 (22), 9400.
- (23) Jiménez-Díaz, L.; Caballero, A.; Pérez-Hernández, N.; Segura, A. Microbial alkane production for jet fuel industry: motivation, state of the art and perspectives. *Microb Biotechnol* **2017**, 10 (1), 103.
- (24) Scheithauer, M.; Grasselli, R. K.; Knözinger, H. Genesis and Structure of W<sub>2</sub>O<sub>3</sub>/ZrO<sub>2</sub> Solid Acid Catalysts. *Langmuir* **1998**, 14 (11), 3019.
- (25) Scheithauer, M.; Cheung, T. K.; Jentoft, R. E.; Grasselli, R. K.; Gates, B. C.; Knözinger, H. Characterization of W<sub>2</sub>O<sub>3</sub>/ZrO<sub>2</sub> by Vibrational Spectroscopy and n-Pentane Isomerization Catalysis. *Journal of Catalysis* **1998**, 180 (1), 1.
- (26) Barton, D. G.; Soled, S. L.; Iglesia, E. Solid acid catalysts based on supported tungsten oxides. *Topics in Catalysis* **1998**, 6 (1), 87.
- (27) Ross-Medgaarden, E. I.; Wachs, I. E. Structural Determination of Bulk and Surface Tungsten Oxides with UV-vis Diffuse Reflectance Spectroscopy and Raman Spectroscopy. *The Journal of Physical Chemistry C* **2007**, 111 (41), 15089.
- (28) Kim, D. S.; Ostromecki, M.; Wachs, I. E. Surface structures of supported tungsten oxide catalysts under dehydrated conditions. *Journal of Molecular Catalysis A: Chemical* **1996**, 106 (1), 93.
- (29) Kim, T.; Burrows, A.; Kiely, C. J.; Wachs, I. E. Molecular/electronic structure-surface acidity relationships of model-supported tungsten oxide catalysts. *Journal of Catalysis* **2007**, 246 (2), 370.
- (30) Wachs, I. E. Raman and IR studies of surface metal oxide species on oxide supports: Supported metal oxide catalysts. *Catalysis Today* **1996**, 27 (3), 437.
- (31) Keramidis, V. G.; White, W. B. Raman Scattering Study of the Crystallization and Phase Transformations of ZrO<sub>2</sub>. *Journal of the American Ceramic Society* **1974**, 57 (1), 22.
- (32) Subbarao, E. C. *Zirconia - an overview*, 1981.
- (33) Baertsch, C. D.; Soled, S. L.; Iglesia, E. Isotopic and Chemical Titration of Acid Sites in Tungsten Oxide Domains Supported on Zirconia. *The Journal of Physical Chemistry B* **2001**, 105 (7), 1320.
- (34) Macht, J.; Carr, R. T.; Iglesia, E. Functional assessment of the strength of solid acid catalysts. *Journal of Catalysis* **2009**, 264 (1), 54.
- (35) Jacob, K.-H.; Knözinger, E.; Benier, S. Adsorption sites on polymorphic zirconia. *Journal of Materials Chemistry* **1993**, 3 (6), 651.
- (36) Denk, C.; Foraita, S.; Kovarik, L.; Stoerzinger, K.; Liu, Y.; Baráth, E.; Lercher, J. A. Rate enhancement by Cu in Ni<sub>x</sub>Cu<sub>1-x</sub>/ZrO<sub>2</sub> bimetallic catalysts for hydrodeoxygenation of stearic acid. *Catalysis Science & Technology* **2019**, 9 (10), 2620.
- (37) Foraita, S.; Fulton, J. L.; Chase, Z. A.; Vjunov, A.; Xu, P.; Baráth, E.; Camaioni, D. M.; Zhao, C.; Lercher, J. A. Impact of the Oxygen Defects and the Hydrogen Concentration on the Surface of Tetragonal and Monoclinic ZrO<sub>2</sub> on the Reduction Rates of Stearic Acid on Ni/ZrO<sub>2</sub>. *Chemistry – A European Journal* **2015**, 21 (6), 2423.
- (38) Foraita, S.; Liu, Y.; Haller, G. L.; Baráth, E.; Zhao, C.; Lercher, J. A. Controlling Hydrodeoxygenation of Stearic Acid to n-Heptadecane and n-Octadecane by Adjusting the Chemical Properties of Ni/SiO<sub>2</sub>-ZrO<sub>2</sub> Catalyst. *ChemCatChem* **2017**, 9 (1), 195.

## 4.8 Supporting information

### 4.8.1 Figures of the results and discussion part

Zirconia supported tungstates

Characterization

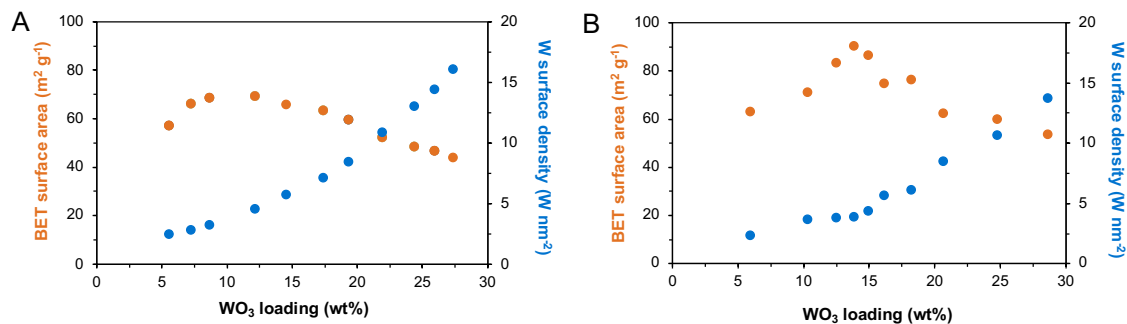


**Figure S4.1.** BET surface area (●) and W surface density (●) as function of the  $\text{WO}_3$  loading of different  $\text{WZrO}_2$  (A) and  $\text{WZrOH}$  (B) catalysts.

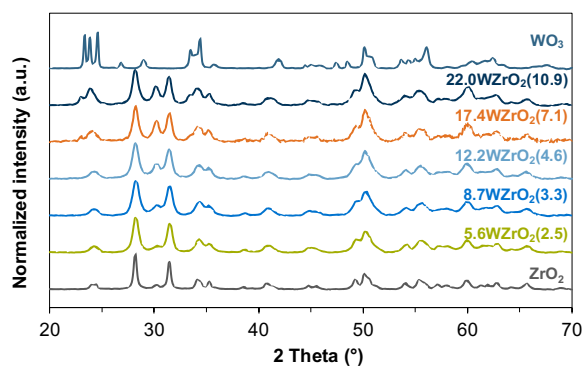


**Figure S4.2.** XRD patterns of the  $\text{WZrO}_2$  catalysts with different  $\text{WO}_3$  loadings.

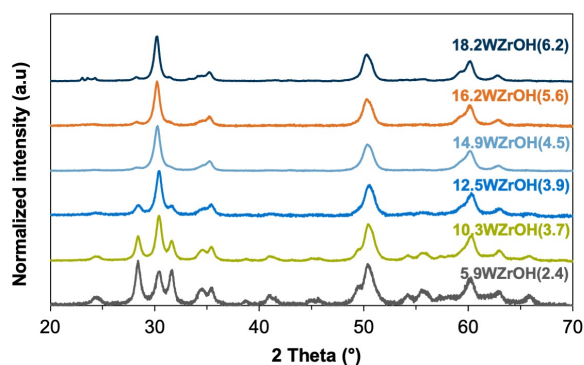


**Figure S4.3.** XRD patterns of the  $\text{WZrOH}$  catalysts with different  $\text{WO}_3$  loadings.

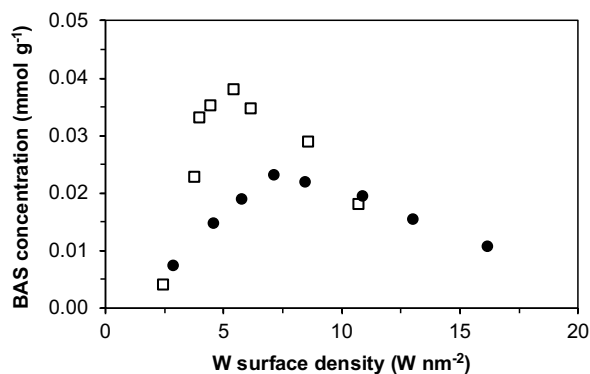


**Figure S4.4.** BAS concentrations as function of the W surface density of different WZrO<sub>2</sub> (●) and WZrOH (□) catalysts.

Octadecanol dehydration over WZrO<sub>2</sub> vs. WZrOH catalysts

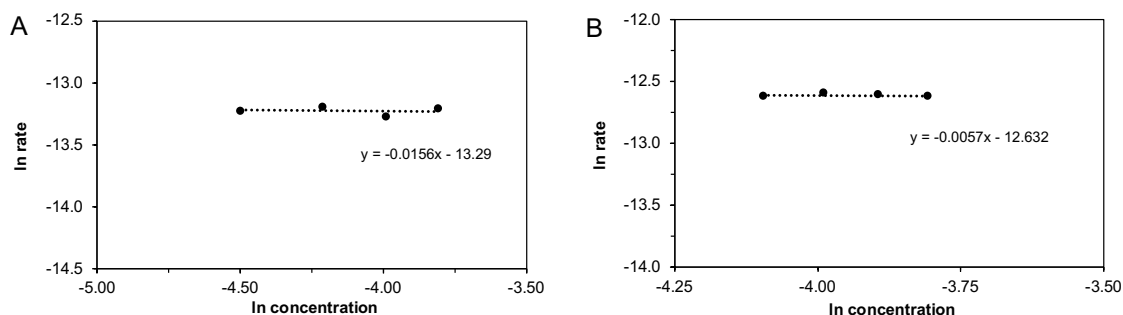


**Figure S4.5.** Rate dependency on the octadecanol concentration over the 14.6WZrO<sub>2</sub>(5.7) (A) and 12.5WZrOH(3.9) (B) catalysts. Reaction conditions: catalyst (0.2 g), decalin (100 mL), 180°C,  $p(\text{H}_2) = 40$  bar, 700 rpm.

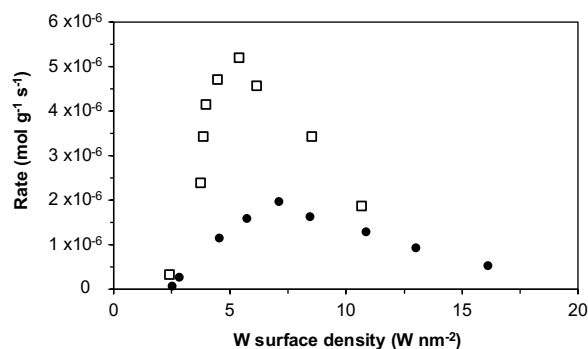


**Figure S4.6.** Rate of the octadecanol dehydration as function of the W surface density on different WZrO<sub>2</sub> (●) and WZrOH (□) catalysts. Reaction conditions: catalyst (0.2 g), octadecanol (0.5 g), decalin (100 mL), 180°C,  $p(\text{H}_2) = 40$  bar, 700 rpm.

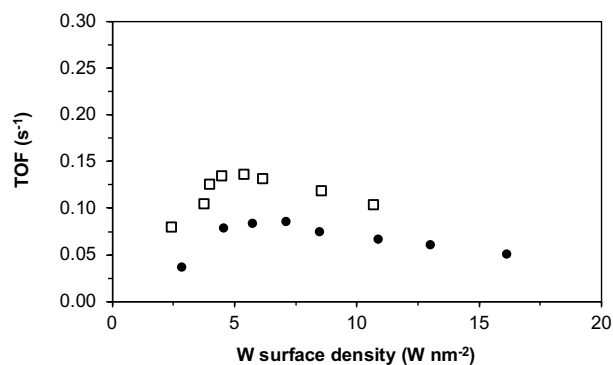


**Figure S4.7.** TOF of the octadecanol dehydration as function of the W surface density on different WZrO<sub>2</sub> (●) and WZrOH (□) catalysts. Reaction conditions: catalyst (0.2 g), octadecanol (0.5 g), decalin (100 mL), 180°C,  $p(\text{H}_2) = 40$  bar, 700 rpm.

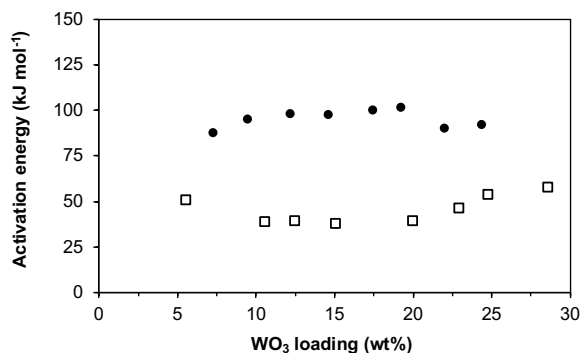


**Figure S4.8.** Activation energy of the octadecanol dehydration as function of the WO<sub>3</sub> loading on different WZrO<sub>2</sub> (●) and WZrOH (□) catalysts.

### Promotion effect of platinum

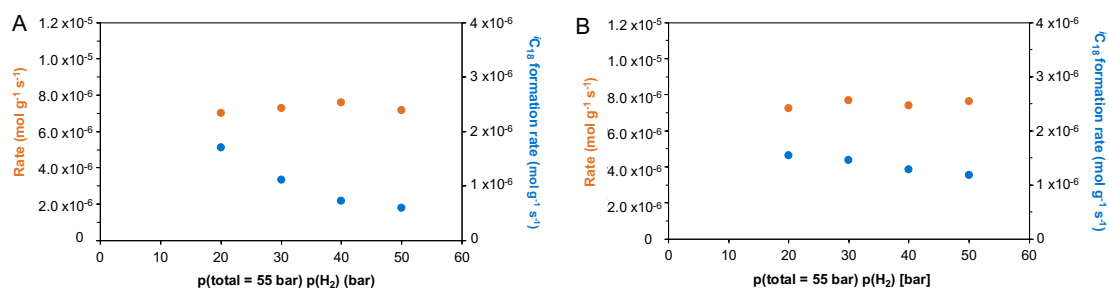


**Figure S4.9.** Rate of the octadecanol dehydration (●) and the *iso*-octadecane formation (●) over the 1Pt14.9WZrOH(4.5) (A) and 0.5Pt14.9WZrOH(4.5) (B) catalyst at different H<sub>2</sub> pressures and constant total pressure.

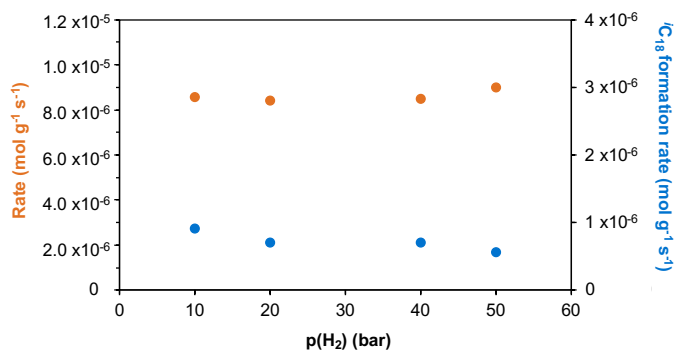


**Figure S4.10.** Rate of the octadecanol dehydration (●) and the *iso*-octadecane formation (●) as function of the  $\text{H}_2$  pressure over the 1Pt14.9WZrOH(4.5) catalyst.

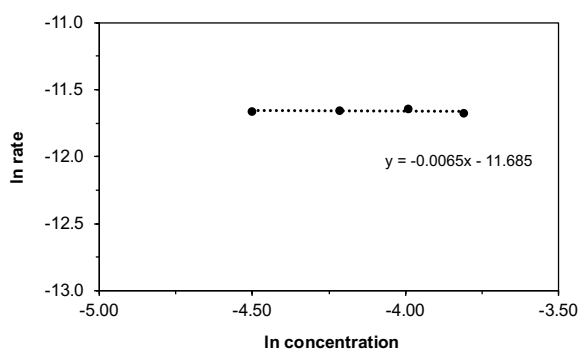


**Figure S4.11.** Rate dependency on the octadecanol concentration over the 0.5Pt16.2WZrOH(5.4) catalyst. Reaction conditions: catalyst (0.1 g), decalin (100 mL), 180°C,  $p(\text{H}_2)$  = 40 bar, 700 rpm.

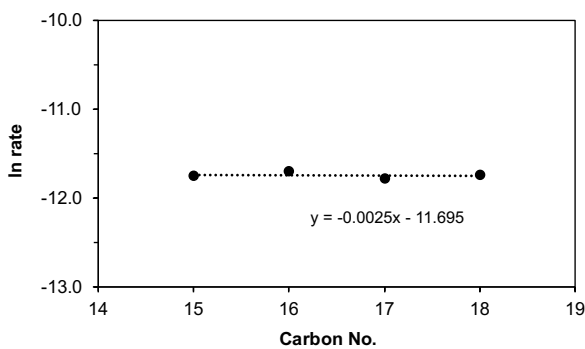


**Figure S4.12.** Rate dependency on the carbon chain length over the 1Pt14.9WZrOH(4.5) catalyst. Reaction conditions: catalyst (0.1 g), decalin (100 mL), 180°C,  $p(\text{H}_2)$  = 40 bar, 700 rpm.

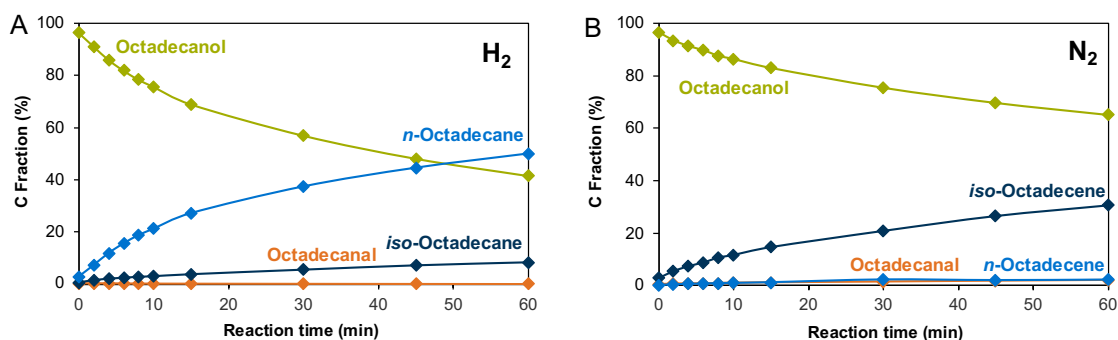


**Figure S4.13.** Product distribution of the octadecanol dehydration over the 0.5Pt20.6WZrOH(8.6) catalyst in  $H_2$  (A) and  $N_2$  (B) atmosphere. Reaction conditions: catalyst (0.1 g), octadecanol (0.5 g), decalin (100 mL),  $180^\circ C$ ,  $p(H_2/N_2) = 40$  bar, 700 rpm.

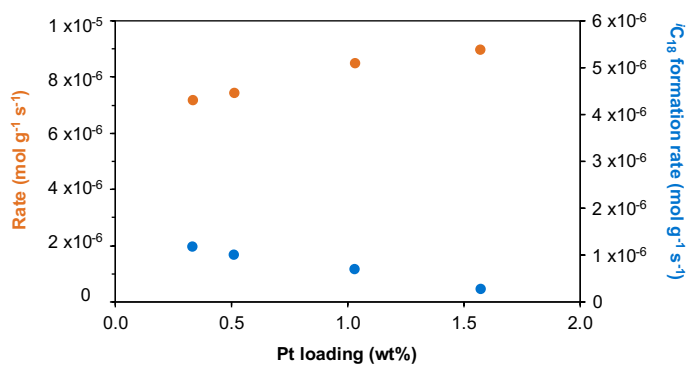


**Figure S4.14.** Rate of the octadecanol dehydration (●) and the *iso*-octadecane formation (●) as function of the Pt loading over Pt14.9WZrOH(4.5) catalysts.

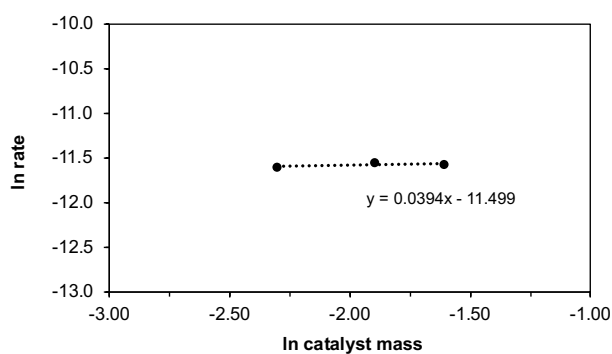
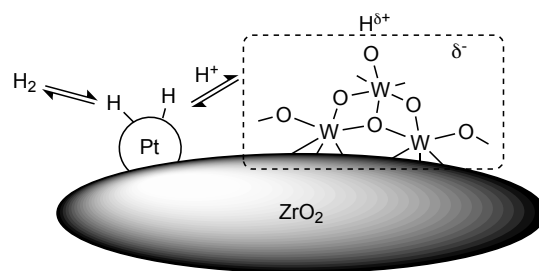


**Figure S4.15.** Rate dependency on the catalyst mass over the 0.5Pt16.2WZrOH(5.4) catalyst. Reaction conditions: octadecanol (0.5 g), decalin (100 mL),  $180^\circ C$ ,  $p(H_2) = 40$  bar, 700 rpm.



**Scheme S4.1.** The platinum-facilitated adsorption of hydrogen enables a partial reduction of the tungstates already at intermediate temperatures (Scheme adapted from Barton et al.<sup>1</sup>).

**Note S4.1.** The promotion effect of platinum addition on a crystalline  $\text{ZrO}_2$  support was also tested and showed a similar rate enhancement as the amorphous  $\text{ZrOH}$  support, e.g., ~51% increase from  $4.5 \times 10^{-6} \text{ mol g}^{-1} \text{ s}^{-1}$  to  $9.1 \times 10^{-6} \text{ mol g}^{-1} \text{ s}^{-1}$  with  $0.5\text{Pt}17.4\text{WZrO}_2(7.1)$  at  $200^\circ\text{C}$  reaction temperature.

### 4.8.2 Aqueous phase

As the microalgae are cultivated in an aqueous environment, the tungstated zirconia catalyzed octadecanol dehydration was also tested in water. However, no conversion could be observed. It is hypothesized that the apolar substrate is not in contact with the polar catalyst surface, which is blocked by the surrounding water. Thus, a more apolar character of the tungstate catalyst was implemented by choosing activated carbon as the support.

Interestingly, the dehydration of octadecanol with activated carbon supported tungstate catalysts (WC) shows high activity in both organic and aqueous phase with a similar product distribution (Figure S4.16 A and B).

The reaction order in octadecanol was determined to be zero in water and one in decalin. This can be interpreted as that the apolar substrate is stronger bonded to the carbon support in water due to its higher driving force towards the catalyst surface than in an apolar surrounding. Thus, the high octadecanol surface coverage of the catalyst in aqueous phase is causing a substrate independent reaction whereas the lower surface coverage in the organic solvent is leading to a first order rate dependency. As a consequence, even though the initial rate in decalin is higher than in water, the conversion is similar for both solvents, especially with increasing reaction time which can be seen in Figure S4.16 C.

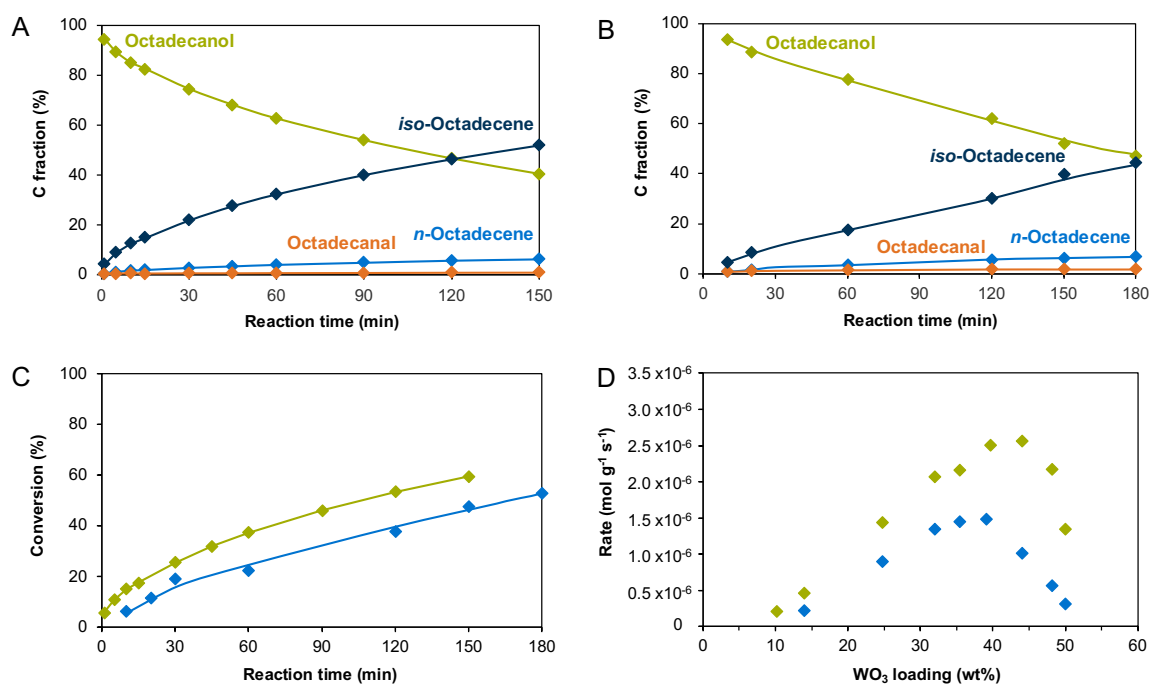


**Figure S4.16.** Product distribution of the octadecanol dehydration over the 25WC(1.4) catalyst in organic (A) and in aqueous (B) phase. Conversion (C) and rate as function of the WO<sub>3</sub> loading (D) of the octadecanol dehydration over the 25WC(1.4) catalyst in organic (◆) and aqueous (◈) phase. Reaction conditions: catalyst (0.20 g), octadecanol (0.45 g), solvent (100 mL), 240°C,  $p(\text{H}_2) = 40$  bar, 700 rpm.

Significantly, in Figure S4.16 D the rate dependency of the octadecanol dehydration on the tungsten loading in aqueous (◈) and organic (◆) phase shows once more a volcano-shaped relationship with a maximum above monolayer coverage. In water the highest rate was measured on the 39WC(2.3) catalyst with  $1.5 \times 10^{-6} \text{ mol g}^{-1} \text{ s}^{-1}$ , while the fastest conversion in decalin was obtained over the 44WC(2.6) catalyst with  $2.6 \times 10^{-6} \text{ mol g}^{-1} \text{ s}^{-1}$ . This implies that also for the activated carbon supported catalysts a more active species exists next to the isolated and polymeric mono-oxo  $\text{W}=\text{O}$ , and the  $m\text{-WO}_3$  nanoparticles.

#### 4.8.3 References of the supporting information

- (1) Barton, D. G.; Soled, S. L.; Meitzner, G. D.; Fuentes, G. A.; Iglesia, E. Structural and Catalytic Characterization of Solid Acids Based on Zirconia Modified by Tungsten Oxide. *Journal of Catalysis* **1999**, *181* (1), 57.

## 4.9 Extension of the carbon supported tungstate catalysts

### 4.9.1 Characterization

The synthesized activated carbon supported tungstate catalysts (xWC(y)) are summarized in Table E4.1. The W surface density is expectedly also increasing with the loading. However, the W surface density is considerably lower than on the zirconia supported tungstates, even at high tungsten loadings as the specific surface areas are significantly higher on the carbon support. In accordance with the zirconia supported tungstates, also for the carbon supported catalysts the BET surface area goes through a maximum which is located around 35 wt%  $\text{WO}_3$  (Figure E4.1). Together with the observations from the Raman data (Figure E4.2), it is, therefore, implied that the monolayer coverage is reached after a tungsten surface density of  $1.9 \text{ W nm}^{-2}$  for the carbon supported tungstate catalysts.

**Table E4.1.** Physiochemical properties of the studied WC catalysts.

	BET surface area ( $\text{m}^2 \text{ g}^{-1}$ )	W surface density ( $\text{W nm}^{-2}$ )
25 wt% $\text{WO}_3/\text{C}$	447	1.4
30 wt% $\text{WO}_3/\text{C}$	467	1.6
35 wt% $\text{WO}_3/\text{C}$	481	1.9
39 wt% $\text{WO}_3/\text{C}$	450	2.3
41 wt% $\text{WO}_3/\text{C}$	440	2.4
44 wt% $\text{WO}_3/\text{C}$	443	2.6
48 wt% $\text{WO}_3/\text{C}$	426	2.9
50 wt% $\text{WO}_3/\text{C}$	390	3.3

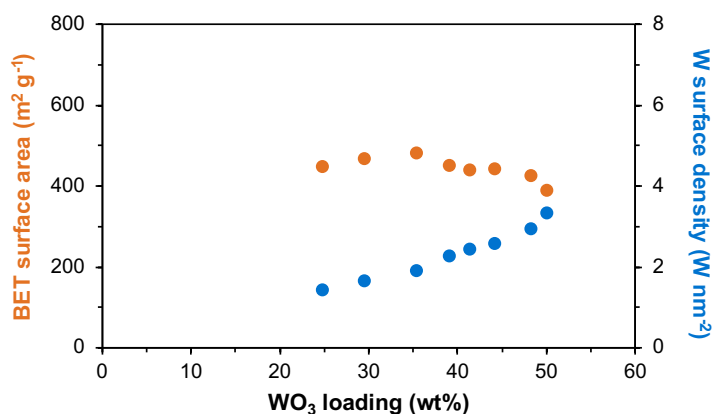


**Figure E4.1.** BET surface area (●) and W surface density (●) as function of the  $\text{WO}_3$  loading of different WC catalysts.

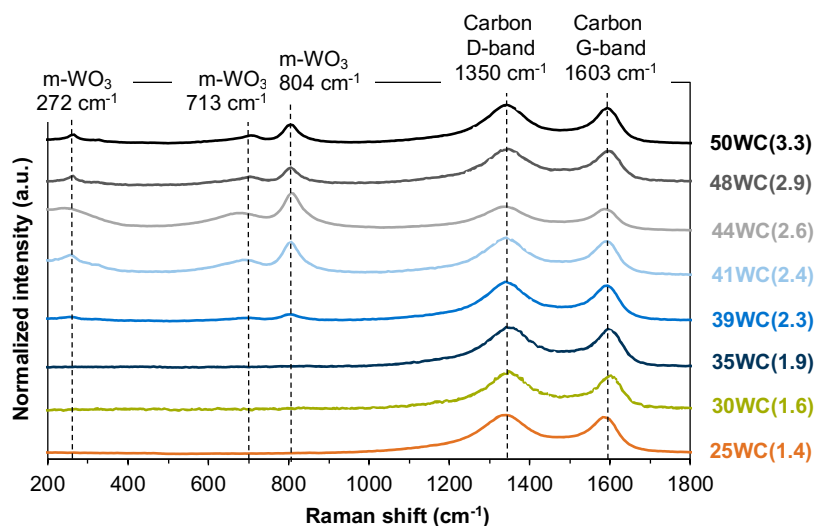


**Figure E4.2.** Raman shift of the WC catalysts with different  $\text{WO}_3$  loadings.

#### 4.9.2 Octadecanol dehydration on $\text{WO}_3/\text{C}$ catalysts

The high selectivity of octadecanol dehydration on  $\text{WO}_3/\text{C}$  catalysts towards *iso*-octadecene is not only comparable in aqueous as well as in organic phase (Figure S4.16 A and B), but is also similar to the selectivity on zirconia supported catalysts (Table E4.2). While *n*-octadecene and octadecanal were again only detected to a minor extent as side products.

**Table E4.2.** Comparison of the selectivity (S) towards *iso*-octadecene over the studied catalysts in water and decalin at similar conversion (X) (however, at different reaction times and conditions).

	Solvent	X (%)	$S_{\text{iso-octadecene}}$ (%)
25WC(1.4)	Water	53	84
25WC(1.4)	Decalin	53	87
17.4WZrO <sub>2</sub> (7.1)	Decalin	57	82
16.2WZrOH(5.4)	Decalin	63	89

The activation energy was slightly higher in aqueous compared to organic phase (e.g., 39WC(2.3) in water: 100 kJ mol<sup>-1</sup> vs. in decalin: 75 kJ mol<sup>-1</sup>, Figure E4.3).

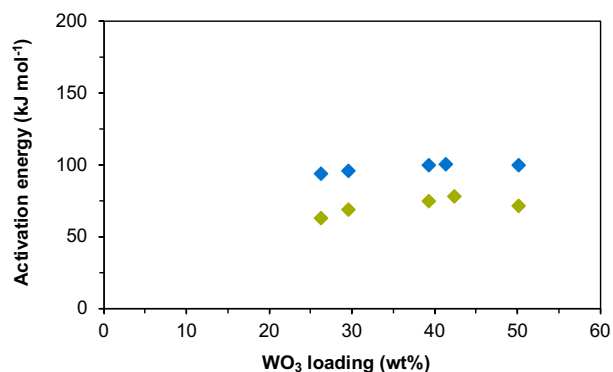


**Figure E4.3.** Activation energy of the octadecanol dehydration as function of the WO<sub>3</sub> loading in organic (◆) and aqueous phase (◆) on different WC catalysts.

The determination of the reaction order is depicted in Figure E4.4 in water (A, 0. order) and in decalin (B, 1. order).

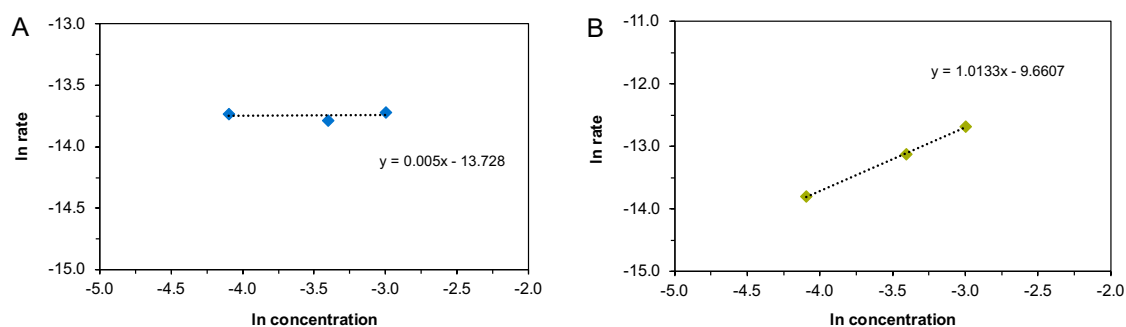
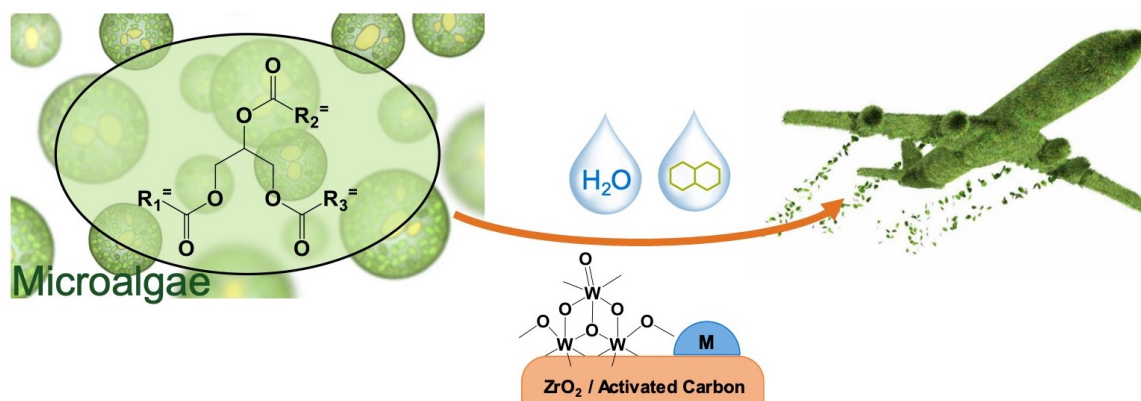


**Figure E4.4.** Rate dependency on the octadecanol concentration over the 50WC(3.3) catalyst in aqueous (A) and organic phase (B). Reaction conditions: catalyst (0.2 g), solvent (100 mL), 240°C,  $p(\text{H}_2) = 40$  bar, 700 rpm.

# Chapter 5

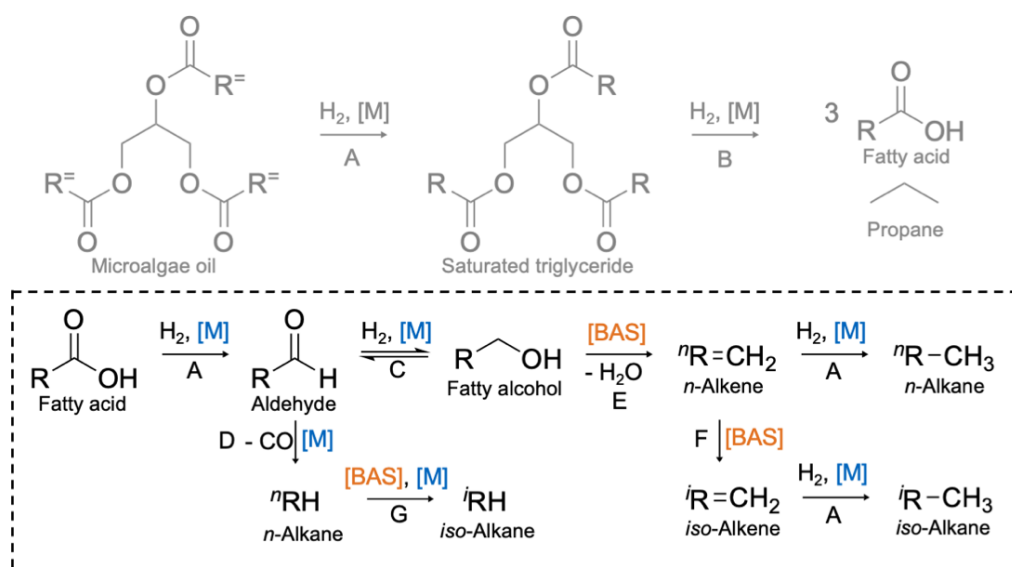
## Fatty acid hydrodeoxygenation on metal supported tungstate catalysts (M/WO<sub>3</sub>/ZrO<sub>2</sub> or M/WO<sub>3</sub>/C) in organic and aqueous phase



## 5.1 Introduction

In Chapter 4, the fatty alcohol dehydration step of the microalgae conversion to hydrocarbon fuel was investigated.<sup>1</sup> The conversion of this highly abundant and rapidly growing biomass resource is being considered as a promising alternative to petroleum-based fuels.<sup>2-6</sup> In this chapter, the hydrodeoxygenation of the fatty acid is studied.

Scheme 5.1 shows the complete mechanism of the microalgae oil conversion to hydrocarbon fuel with a bifunctional catalyst. After hydrogenation of the unsaturated bonds in the microalgae oil, the triglyceride undergoes hydrogenolysis, yielding fatty acids and propane. The fatty acid, which is further hydrogenated by the metal sites of the catalyst to aldehyde, then proceeds either *via* a dehydration or *via* a decarbonylation pathway. Following the former carbon preserving route, the fatty alcohol, which is in equilibrium with the aldehyde, is dehydrated by Brønsted acid sites (BAS) to *n*-alkenes. These can then be further hydroisomerized in the presence hydrogen by the metal and BAS sites to branched alkanes. The decarbonylation route results in the formation alkanes with one carbon atom less, which can also be further hydroisomerized.<sup>3,7,8</sup>



**Scheme 5.1.** Reaction mechanism of the microalgae oil hydrodeoxygenation to hydrocarbon fuel with a bifunctional catalyst and highlighted the fatty acid hydrodeoxygenation. A = hydrogenation, B = hydrogenolysis, C = (de-)hydrogenation, D = decarbonylation, E = dehydration, F = isomerization, G = isomerization and hydrogenation (adapted from Chapter 4).<sup>1</sup>

The previously studied catalysts, i.e., zirconia or carbon supported tungstates, were doped with different metals (Pt, Rh, Ru) and were evaluated in the conversion of stearic acid as fatty acid model compound under varying reaction conditions in order to maximize the yield of carbon preserving *iso*-octadecane (as oppose to *iso*-heptadecane) which could be utilized as kerosene in the aviation sector.<sup>9,10</sup>

## 5.2 Results and discussion

### 5.2.1 Zirconia supported tungstates

Figure 5.1 A shows that stearic acid was successfully and completely hydrodeoxygenated with the 0.5 wt% Pt/14.9 wt% WO<sub>3</sub>/ZrO<sub>2</sub> catalyst in an organic solvent (decalin) at 260°C and a hydrogen pressure of 40 bar within one hour. The stearic acid conversion followed mainly the dehydration pathway and resulted in the formation of *n*-octadecane (64%) and to a lower extent *iso*-octadecane (21%). Additionally, *n*- and *iso*-heptadecane were detected, which were formed via the decarbonylation route.

Figure 5.1 B depicts the stearic acid conversion at the same reaction conditions as in Figure 5.1 A, also with a 0.5 wt% Pt/14.9 wt% WO<sub>3</sub>/ZrO<sub>2</sub> catalyst, however, with a pre-calcined zirconia support in analogy to the procedure in Chapter 4.<sup>1</sup> In accordance to the previous chapter, the initial reaction rate of the pre-calcined zirconia (ZrO<sub>2</sub>) supported catalyst (Table 5.1: 2.0 x 10<sup>-6</sup> mol g<sup>-1</sup> s<sup>-1</sup>) was significantly lower compared to the amorphous zirconium hydroxide (Zr(OH)<sub>4</sub>) supported catalyst (Table 5.1: 7.7 x 10<sup>-6</sup> mol g<sup>-1</sup> s<sup>-1</sup>). Expectably, also the product distribution differs due to the lower Brønsted acidity in the pre-calcined catalyst. The selectivity towards *n*-octadecane increased to 87% while *iso*-octadecane decreased from 21 to 6%. The selectivity towards *n*-heptadecane remained the same while *iso*-heptadecane decreased from 10 to 2%. Therefore, the lower BAS concentration correlates with a lower isomerization activity.

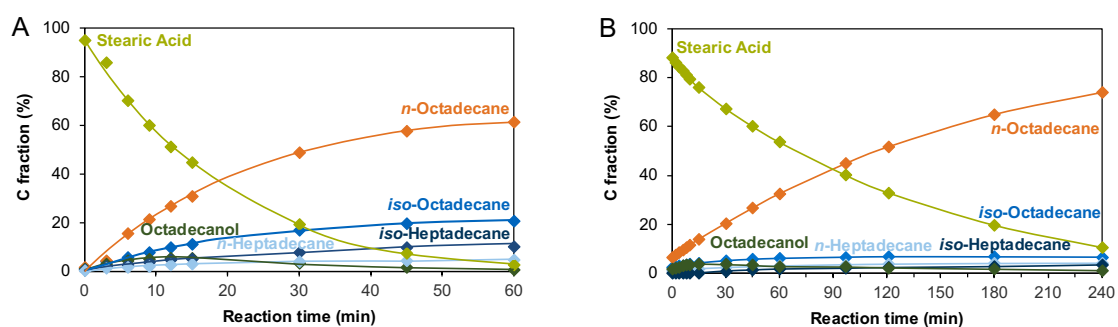


**Figure 5.1.** Product distribution of the stearic acid hydrodeoxygenation with 0.5 wt% Pt/14.9 wt% WO<sub>3</sub>/ZrO<sub>2</sub> catalysts on an amorphous zirconium hydroxide (Zr(OH)<sub>4</sub>) support (A) and on a pre-calcined zirconia (ZrO<sub>2</sub>) support (B). Reaction conditions: catalyst (0.2 g), stearic acid (0.5 g), decalin (100 mL), 260°C,  $p(\text{H}_2) = 40$  bar, 700 rpm.

**Table 5.1.** Comparison of the initial rate and the selectivities (S) with 0.5 wt% Pt/14.9 wt% WO<sub>3</sub>/ZrO<sub>2</sub> catalysts on a zirconium hydroxide (Zr(OH)<sub>4</sub>) support and on a zirconia (ZrO<sub>2</sub>) support. Reaction conditions: catalyst (0.2 g), stearic acid (0.5 g), decalin (100 mL), 260°C, *p*(H<sub>2</sub>) = 40 bar, 700 rpm.

Zirconia support	Initial rate (mol g <sup>-1</sup> s <sup>-1</sup> )	S <sub><i>n</i>-octadecane</sub> (%)	S <sub><i>iso</i>-octadecane</sub> (%)	S <sub><i>n</i>-heptadecane</sub> (%)	S <sub><i>iso</i>-heptadecane</sub> (%)
Zr(OH) <sub>4</sub>	7.7 x10 <sup>-6</sup>	64	21	5	10
ZrO <sub>2</sub>	2.0 x10 <sup>-6</sup>	87	6	5	2

The influence of the reduction time in hydrogen during the catalyst synthesis was investigated in terms of reaction rate and selectivity towards *iso*-octadecane. The results are summarized in Figure 5.2 and Table 5.2.

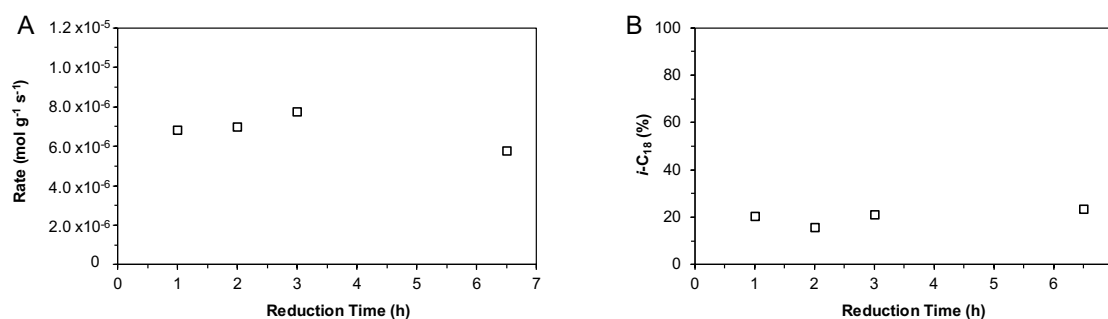


**Figure 5.2.** Dependency of the rate (A) and the carbon fraction of *iso*-octadecane (B) on the reduction time in hydrogen during the catalyst synthesis with 0.5 wt% Pt/14.9 wt% WO<sub>3</sub>/ZrO<sub>2</sub> catalysts. Reaction conditions: catalyst (0.2 g), stearic acid (0.5 g), decalin (100 mL), 260°C, *p*(H<sub>2</sub>) = 40 bar, 700 rpm.

**Table 5.2.** Comparison of the initial rate and the selectivities (S) with 0.5 wt% Pt/14.9 wt% WO<sub>3</sub>/ZrO<sub>2</sub> catalysts with varying reduction times. Reaction conditions: catalyst (0.2 g), stearic acid (0.5 g), decalin (100 mL), 260°C, *p*(H<sub>2</sub>) = 40 bar, 700 rpm.

Reduction time	Initial rate (mol g <sup>-1</sup> s <sup>-1</sup> )	S <sub><i>n</i>-octadecane</sub> (%)	S <sub><i>iso</i>-octadecane</sub> (%)	S <sub><i>n</i>-heptadecane</sub> (%)	S <sub><i>iso</i>-heptadecane</sub> (%)
1 h	6.8 x10 <sup>-6</sup>	66	20	5	9
2 h	7.0 x10 <sup>-6</sup>	73	16	4	7
3 h	7.7 x10 <sup>-6</sup>	64	21	5	10
6.5 h	5.8 x10 <sup>-6</sup>	62	23	2	12

A slight increase of the hydrodeoxygenation rate can be observed in Figure 5.2 A with increasing reduction time until 3 h. Prolonging the reduction time further led to a decrease of the rate, presumably due to sintering. The *iso*-octadecane selectivity (Figure 5.2 B) remained mainly around 20% for all tested reduction times. Thus, a reduction time of 3 h was subsequently used for the synthesis.

Further, as in Chapter 4,<sup>1</sup> the reaction was studied at different WO<sub>3</sub> loadings with a constant Pt loading at 0.5 wt% (Figure 5.3 and Table 5.3). In analogy to the previous findings, also the hydrodeoxygenation rate showed a volcano-shaped dependency on the WO<sub>3</sub> loading with the maximum at 16.4 wt%. Since the dehydration pathway is predominant in the hydrodeoxygenation reaction, this could result, in accordance with what was reported previously,<sup>1</sup> from the fact that the BAS concentration is maximized at this WO<sub>3</sub> loading. This in turn also leads to the highest *iso*-octadecane selectivity (Figure 5.3 B) which is highest with the 0.5 wt% Pt/16.4 wt% WO<sub>3</sub>/ZrO<sub>2</sub> catalyst at 37%.

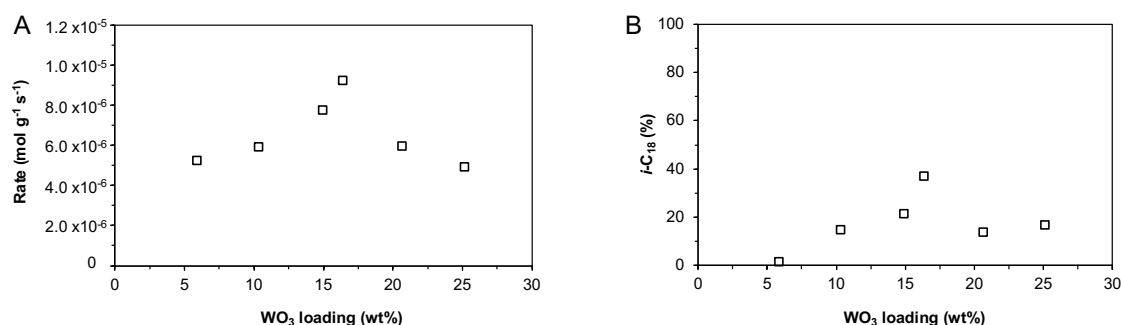


**Figure 5.3.** Dependency of the rate (A) and the carbon fraction of *iso*-octadecane (B) on the WO<sub>3</sub> loading with 0.5 wt% Pt promoted WO<sub>3</sub>/ZrO<sub>2</sub> catalysts. Reaction conditions: catalyst (0.2 g), stearic acid (0.5 g), decalin (100 mL), 260°C,  $p(\text{H}_2) = 40$  bar, 700 rpm.

**Table 5.3.** Comparison of the initial rate and the selectivities (S) with 0.5 wt% Pt promoted WO<sub>3</sub>/ZrO<sub>2</sub> catalysts with varying WO<sub>3</sub> loadings. Reaction conditions: catalyst (0.2 g), stearic acid (0.5 g), decalin (100 mL), 260°C,  $p(\text{H}_2) = 40$  bar, 700 rpm.

WO <sub>3</sub> loading	Initial rate (mol g <sup>-1</sup> s <sup>-1</sup> )	S <sub><i>n</i>-octadecane</sub> (%)	S <sub><i>iso</i>-octadecane</sub> (%)	S <sub><i>n</i>-heptadecane</sub> (%)	S <sub><i>iso</i>-heptadecane</sub> (%)
5.9 wt%	5.2 x 10 <sup>-6</sup>	91	1	5	0
10.3 wt%	5.9 x 10 <sup>-6</sup>	77	15	2	6
14.9 wt%	7.7 x 10 <sup>-6</sup>	64	21	5	10
16.4 wt%	9.2 x 10 <sup>-6</sup>	40	37	6	17
20.6 wt%	6.0 x 10 <sup>-6</sup>	75	14	4	6
25.1 wt%	4.9 x 10 <sup>-6</sup>	71	17	4	8

Figure 5.4 A shows the influence of the Pt loading on the stearic acid hydrodeoxygenation rate at constant WO<sub>3</sub> loading at 14.9 wt%. Increasing the loading from 0.3 to 1.0 wt% significantly increased the reaction rate from 3.8 x 10<sup>-6</sup> mol g<sup>-1</sup> s<sup>-1</sup> to 9.1 x 10<sup>-6</sup> mol g<sup>-1</sup> s<sup>-1</sup>. Increasing the Pt content is, as expected, beneficial for the first reaction step, the hydrogenation of the stearic acid. However, as shown in Chapter 4,<sup>1</sup> platinum has also a promoting effect on the dehydration rate by increasing the BAS concentration as result from a reduction of the tungsten already at mild temperatures in presence of hydrogen. For the present hydrodeoxygenation reaction it is, therefore,

presumed that platinum also enhances the second, rate determining dehydration step in addition to the first hydrogenation step. A further increase of the platinum loading did not lead to higher rates; in contrast, a small decrease was observed. The decrease at 1.6 wt% Pt (Table 5.4) could be due to sintering of the platinum. The selectivity towards *iso*-octadecane (Figure 5.4 B) continuously decreases upon higher platinum loadings as the unsaturated *n*-octadecenes are faster hydrogenated than isomerized at high Pt loadings.

Interestingly, the selectivity towards decarbonylation products (*n*- and *iso*-heptadecane, Table 5.4) decreases with increasing Pt loading. This could be due to the enhancement of the competitive dehydration reaction and at the same time the further shifting the aldehyde-alcohol equilibrium towards octadecanol. The *iso*-heptadecane selectivity decreased in line with *iso*-octadecane selectivity.

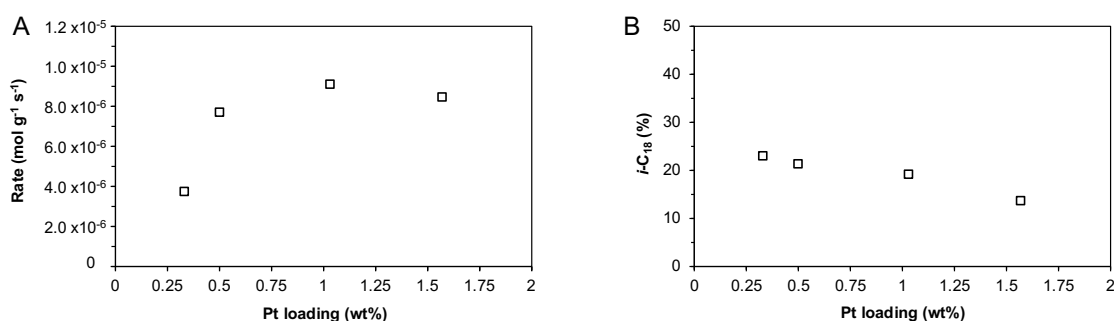


**Figure 5.4.** Dependency of the rate (A) and the carbon fraction of *iso*-octadecane (B) on the Pt loading with Pt promoted 14.9 wt% WO<sub>3</sub>/ZrO<sub>2</sub> catalysts. Reaction conditions: catalyst (0.2 g), stearic acid (0.5 g), decalin (100 mL), 260°C,  $p(\text{H}_2) = 40$  bar, 700 rpm.

**Table 5.4.** Comparison of the initial rate and the selectivities (S) with Pt promoted 14.9 wt% WO<sub>3</sub>/ZrO<sub>2</sub> catalysts with varying Pt loadings. Reaction conditions: catalyst (0.2 g), stearic acid (0.5 g), decalin (100 mL), 260°C,  $p(\text{H}_2) = 40$  bar, 700 rpm.

Pt loading	Initial rate (mol g <sup>-1</sup> s <sup>-1</sup> )	S <sub><i>n</i>-octadecane</sub> (%)	S <sub><i>iso</i>-octadecane</sub> (%)	S <sub><i>n</i>-heptadecane</sub> (%)	S <sub><i>iso</i>-heptadecane</sub> (%)
0.3 wt%	3.8 × 10 <sup>-6</sup>	60	23	5	12
0.5 wt%	7.7 × 10 <sup>-6</sup>	64	21	5	10
1.0 wt%	9.1 × 10 <sup>-6</sup>	68	19	4	8
1.6 wt%	8.5 × 10 <sup>-6</sup>	77	14	4	6

Lastly, the influence of different metals (platinum, rhodium, and ruthenium) was investigated (Figure 5.5 and Table 5.5). Figure 5.5 A and B demonstrate that the stearic acid hydrodeoxygenation reaction was also successful with 0.5 wt% Rh and 0.5 wt% Ru promoted WO<sub>3</sub>/ZrO<sub>2</sub> catalysts. The highest rates were observed for Pt (7.7 × 10<sup>-6</sup> mol g<sup>-1</sup> s<sup>-1</sup>) closely followed by Rh (7.4 × 10<sup>-6</sup> mol g<sup>-1</sup> s<sup>-1</sup>). Ru had by far the lowest hydrodeoxygenation rate (2.8 × 10<sup>-7</sup> mol g<sup>-1</sup> s<sup>-1</sup>) (Figure 5.5, Table 5.5). Figure 5.5 D displays that the selectivity towards *iso*-octadecane, in contrast, almost linearly

increases from Pt (21%) to Rh (30%) and finally is the highest for Ru (37%). A higher hydrodeoxygenation rate, thus, leads in turn to a lower selectivity towards isomerization. Further, the rhodium catalyst shows a higher selectivity towards the decarbonylation route (in total 24% *n*- and *iso*-heptadecane as opposed to Pt with 15%, Table 5.5). Whereas it is maximized for the ruthenium catalyst (34%, Table 5.5). Consequently, the highest overall hydrodeoxygenation rate with the Pt catalysts, results from Pt having the strongest enhancement effect on the dehydration route due to the increase of the BAS concentration.

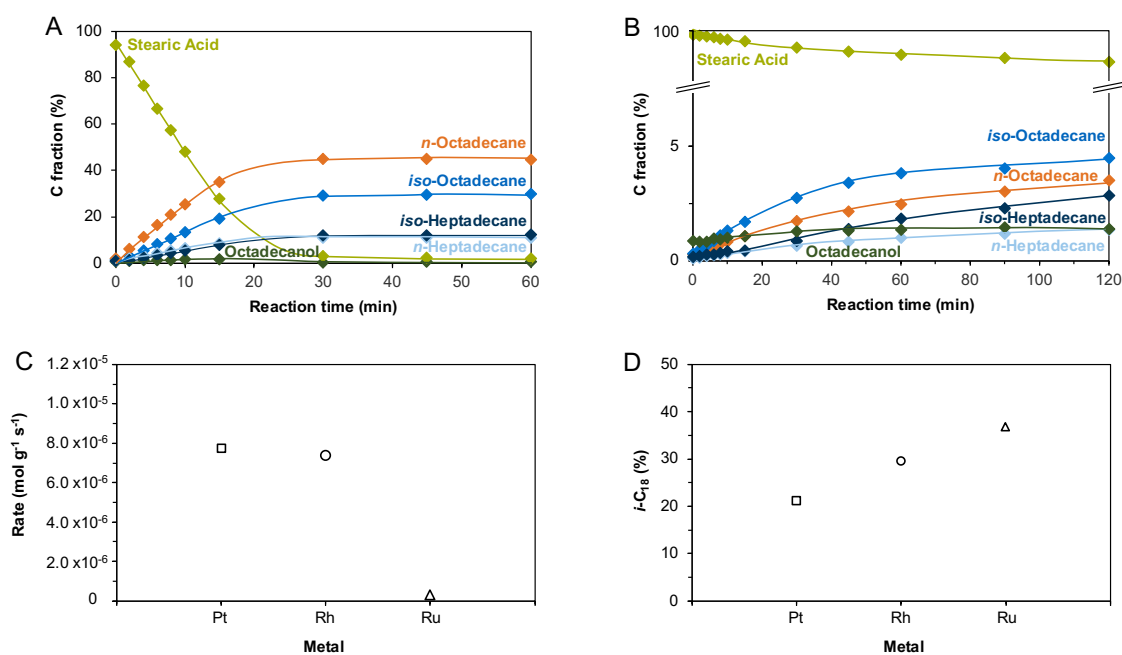


**Figure 5.5.** Product distribution of the stearic acid hydrodeoxygenation with 0.5 wt% Rh/16.1 wt% WO<sub>3</sub>/ZrO<sub>2</sub> (A) and 0.5 wt% Ru/16.1 wt% WO<sub>3</sub>/ZrO<sub>2</sub> (B). Dependency of the rate (C) and the carbon fraction of *iso*-octadecane (D) on different 0.5 wt% metal promoted WO<sub>3</sub>/ZrO<sub>2</sub> catalysts. Reaction conditions: catalyst (0.2 g), stearic acid (0.5 g), decalin (100 mL), 260°C,  $p(\text{H}_2) = 40$  bar, 700 rpm.

**Table 5.5.** Comparison of the initial rate and the selectivities (S) with different 0.5 wt% metal promoted WO<sub>3</sub>/ZrO<sub>2</sub> catalysts. Reaction conditions: catalyst (0.2 g), stearic acid (0.5 g), decalin (100 mL), 260°C,  $p(\text{H}_2) = 40$  bar, 700 rpm.

Metal	Initial rate (mol g <sup>-1</sup> s <sup>-1</sup> )	S <sub><i>n</i>-octadecane</sub> (%)	S <sub><i>iso</i>-octadecane</sub> (%)	S <sub><i>n</i>-heptadecane</sub> (%)	S <sub><i>iso</i>-heptadecane</sub> (%)
Pt	7.7 × 10 <sup>-6</sup>	64	21	5	10
Rh	7.4 × 10 <sup>-6</sup>	46	30	11	13
Ru	2.8 × 10 <sup>-7</sup>	29	37	11	23

This hypothesis was further investigated through kinetic measurements with the Pt and Rh catalyst. The reaction order for both catalysts was determined to be zero (Figure 5.6

A and B). The activation energy, on the other hand, was found to be over 30 kJ mol<sup>-1</sup> lower for the Pt catalyst (Pt: 74.9 kJ mol<sup>-1</sup> vs. Rh: 105.6 kJ mol<sup>-1</sup>, Figure 5.6 C and D). This supports the assumption that the Pt catalyst follows predominantly the dehydration route, which is enhanced by Pt increasing the BAS concentration, therefore, lowering the activation energy for this pathway as supposed to Rh and Ru which have a less pronounced preference towards one of the two pathways.

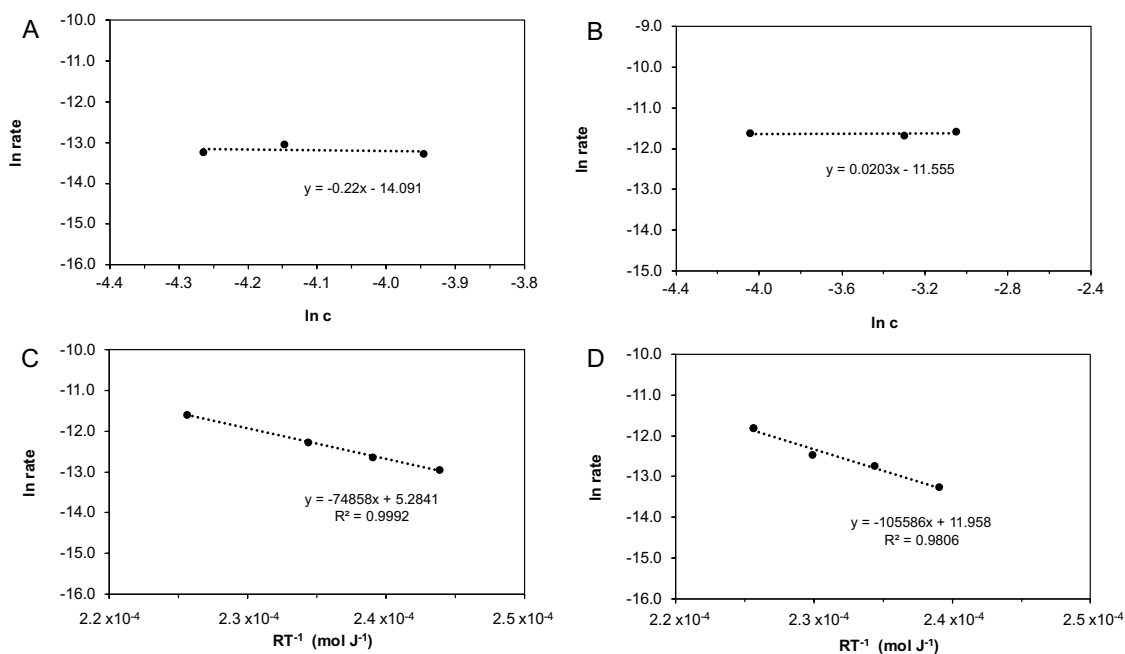


**Figure 5.6.** Rate dependency on the stearic acid concentration with 0.5 wt% Pt/16.4 wt% WO<sub>3</sub>/ZrO<sub>2</sub> (A) and 1 wt% Rh/14.6 wt% WO<sub>3</sub>/ZrO<sub>2</sub> (B) catalysts. Reaction conditions: catalyst (0.2 g), decalin (100 mL), 240°C,  $p(\text{H}_2) = 40$  (A) and 60 bar (B), 700 rpm. *Arrhenius*-plot of the stearic acid hydrodeoxygenation with 0.5 wt% Pt/ 16.4 wt% WO<sub>3</sub>/ZrO<sub>2</sub> (C) and 0.5 wt% Rh/14.6 wt% WO<sub>3</sub>/ZrO<sub>2</sub> (D). Reaction conditions: catalyst (0.2 g), stearic acid (0.5 g), decalin (100 mL),  $p(\text{H}_2) = 40$  bar, 700 rpm.

## 5.2.2 Carbon supported tungstates

In addition to zirconia, also the carbon supported tungstate catalysts from Chapter 4<sup>1</sup> were doped with metals in order to investigate their activity for the hydrodeoxygenation reaction of stearic acid. Due to the apolar character of the carbon catalysts, the reaction was tested both in an organic solvent and in water.

Figure 5.7 shows that stearic acid was not only successfully converted with the 0.5 wt% Pt/40 wt% WO<sub>3</sub>/C catalyst in the organic solvent (decalin, B) but with almost one order of magnitude faster in water (A) (decalin:  $1.2 \times 10^{-7} \text{ mol g}^{-1} \text{ s}^{-1}$ , H<sub>2</sub>O:  $1.1 \times 10^{-6} \text{ mol g}^{-1} \text{ s}^{-1}$ , Table 5.6). The product distribution in Figure 5.7 reveals that octadecanol and only the linear unbranched alkanes, *n*-heptadecane and *n*-octadecane, were detected. In decalin, the reaction followed predominantly the dehydration pathway (*S*<sub>*n*-C17</sub>: 15%, *S*<sub>*n*-C18</sub>: 63%, Table 5.6) while this trend was less pronounced in water, where the selectivity towards *n*-heptadecane was found to be 33% and towards *n*-octadecane 51%.

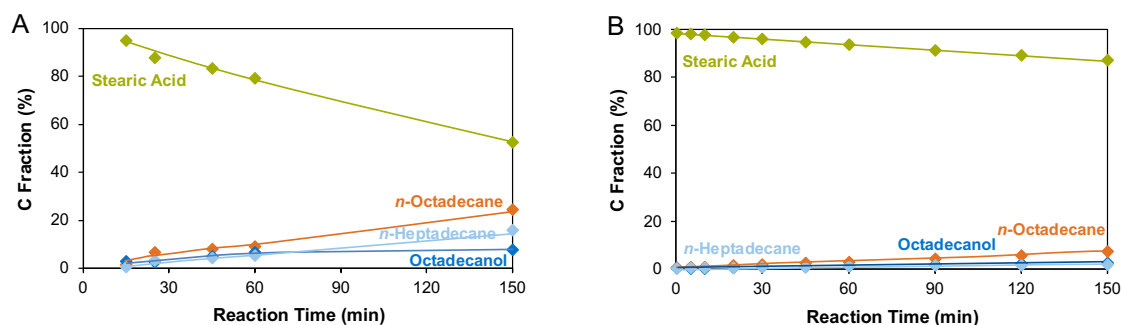


**Figure 5.7.** Product distribution of the stearic acid hydrodeoxygenation with a 0.5 wt% Pt/40 wt% WO<sub>3</sub>/C catalyst in water (A) and in decalin (B). Reaction conditions: catalyst (0.2 g), stearic acid (0.5 g), solvent (100 mL), 260°C,  $p(\text{H}_2) = 60 \text{ bar}$ , 700 rpm.

Increasing the Pt loading to 1 wt% resulted in a 55% higher reaction rate in water, thus, leading to 100% conversion already after 2.5h, and more than doubled the rate in decalin (H<sub>2</sub>O:  $1.7 \times 10^{-6} \text{ mol g}^{-1} \text{ s}^{-1}$ , decalin:  $2.6 \times 10^{-7} \text{ mol g}^{-1} \text{ s}^{-1}$ , Figure 5.8 B, Table 5.6). The product distribution remained mostly the same as for the 0.5 wt% Pt catalyst for both solvents (Figure 5.9 A and B), only in decalin the selectivity towards octadecanol increased from 21% to 41% while it decreased *n*-octadecane to 47%.

Chapter 5: Fatty acid hydrodeoxygenation on metal supported tungstate catalysts (M/WO<sub>3</sub>/ZrO<sub>2</sub> or M/WO<sub>3</sub>/C) in organic and aqueous phase

**Table 5.6.** Comparison of the initial rate, conversion after 2.5h and selectivities (S) with different metal promoted 40 wt% WO<sub>3</sub>/C catalysts in water and in decalin. Reaction conditions: catalyst (0.2 g), stearic acid (0.5 g), solvent (100 mL), 260°C,  $p(\text{H}_2) = 60$  bar, 700 rpm.

Metal	Solvent	Initial rate (mol g <sup>-1</sup> s <sup>-1</sup> )	X (%)	S <sub>n-heptadecane</sub> (%)	S <sub>n-octadecane</sub> (%)	S <sub>n-octadecanol</sub> (%)
0.5 wt% Pt	Water	1.1 x10 <sup>-6</sup>	48	33	51	16
	Decalin	1.2 x10 <sup>-7</sup>	13	15	63	22
1 wt% Pt	Water	1.7 x10 <sup>-6</sup>	100	32	51	17
	Decalin	2.6 x10 <sup>-7</sup>	26	11	47	41
0.5 wt% Ru	Water	1.1 x10 <sup>-7</sup>	14	23	28	49
	Decalin	0.7 x10 <sup>-7</sup>	8	53	24	23
1 wt% Rh	Water	5.9 x10 <sup>-7</sup>	63	80	10	10
	Decalin	9.0 x10 <sup>-7</sup>	69	33	43	24

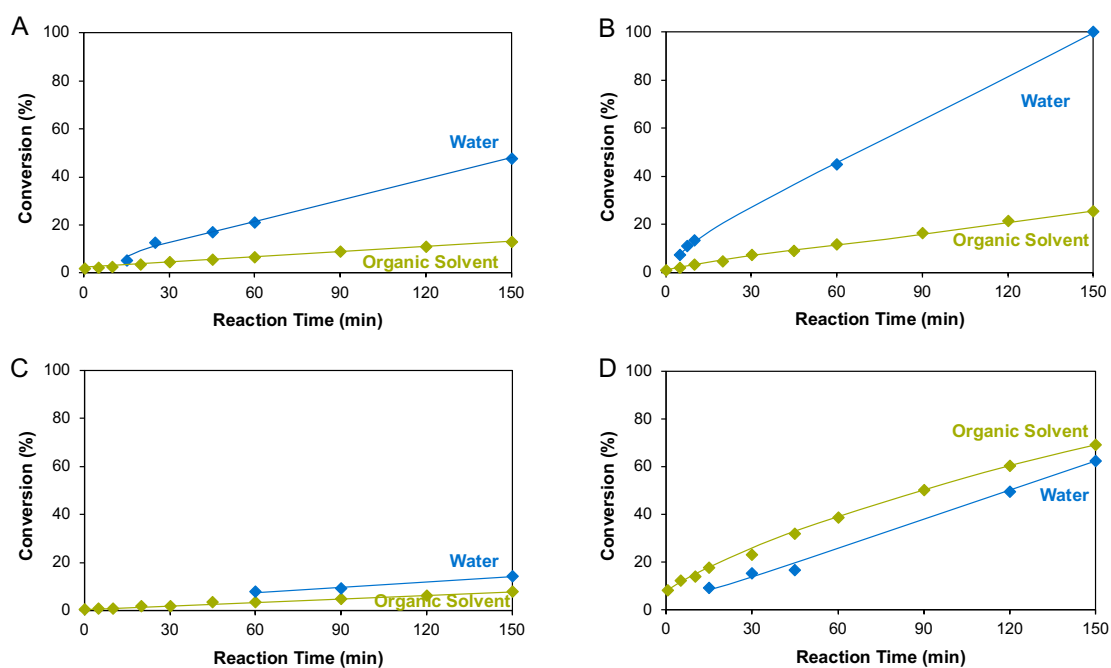


**Figure 5.8.** Conversion of the stearic acid hydrodeoxygenation with 0.5 wt% Pt (A), 1 wt% Pt (B), 0.5 wt% Ru (C), and 1 wt% Rh (D) promoted 40 wt% WO<sub>3</sub>/C catalysts in water (blue) and in decalin (green). Reaction conditions: catalyst (0.2 g), stearic acid (0.5 g), solvent (100 mL), 260°C,  $p(\text{H}_2) = 60$  bar, 700 rpm.

Figure 5.9 C shows that the hydrodeoxygenation rate in water is increased at a constant Pt content of 1 wt% with increasing tungsten oxide loading. This is presumably caused by higher BAS concentrations, which in turn enhance the dehydration of octadecanol to *n*-octadecane. This is consistent with the selectivity distribution in Table 5.7 which demonstrates the predominance of the dehydration pathway.

Based on the results in Chapter 4,<sup>1</sup> it is expected that the maximum of the rate enhancement in water is reached after a 40 wt% loading of WO<sub>3</sub>. The activation energy of the stearic acid hydrodeoxygenation with the 1 wt% Pt/40 wt% WO<sub>3</sub>/C catalyst was determined to be 132.5 kJ mol<sup>-1</sup>. The higher activation energy compared to the platinum promoted tungstated zirconia catalyst (74.9 kJ mol<sup>-1</sup>) falls in line with the lower reaction rate with the carbon-based catalyst despite the higher hydrogen pressure (60 bar for the carbon vs. 40 bar for the zirconia catalyzed reactions). The rate difference, however, is not very pronounced (1 wt% Pt/40 wt% WO<sub>3</sub>/C in H<sub>2</sub>O: 1.7 × 10<sup>-6</sup> mol g<sup>-1</sup> s<sup>-1</sup> vs. 0.5 wt% Pt/16.4 wt% WO<sub>3</sub>/ZrO<sub>2</sub> in decalin: 7.7 × 10<sup>-6</sup> mol g<sup>-1</sup> s<sup>-1</sup>), which in turns demonstrates that the platinum promoted tungstated carbon catalyst is remarkably well suited for the conversion of microalgae in aqueous environments to hydrocarbon fuels.

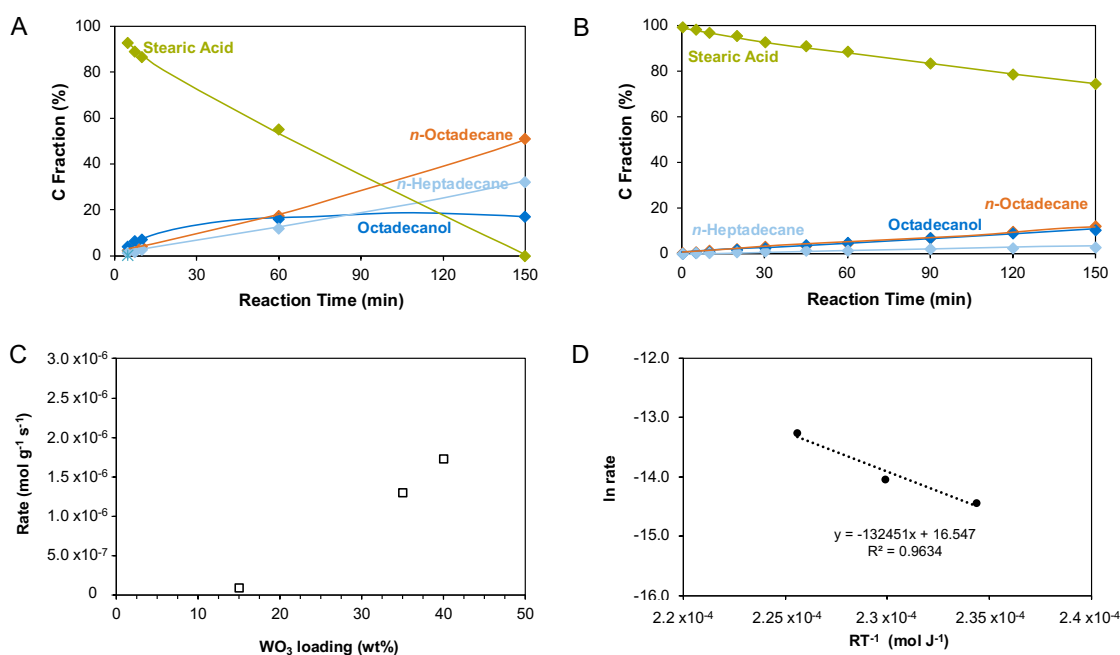


**Figure 5.9.** Product distribution of the stearic acid hydrodeoxygenation with 1 wt% Pt/40 wt% WO<sub>3</sub>/C catalyst in water (A) and in decalin (B). Rate dependency on the WO<sub>3</sub> loading with 1 wt% Pt promoted WO<sub>3</sub>/C catalysts in water (C). Arrhenius-plot of the stearic acid hydrodeoxygenation with 1 wt% Pt/40 wt% WO<sub>3</sub>/C catalyst in water (D). Reaction conditions: catalyst (0.2 g), stearic acid (0.5 g), solvent (100 mL),  $p(\text{H}_2) = 60$  bar, 700 rpm.

**Table 5.7.** Comparison of the initial rate, conversion after 2.5h and selectivities (S) with 1 wt% Pt promoted WO<sub>3</sub>/C catalysts with different WO<sub>3</sub> loadings in water. Reaction conditions: catalyst (0.2 g), stearic acid (0.5 g), water (100 mL), 260°C,  $p(\text{H}_2) = 60$  bar, 700 rpm.

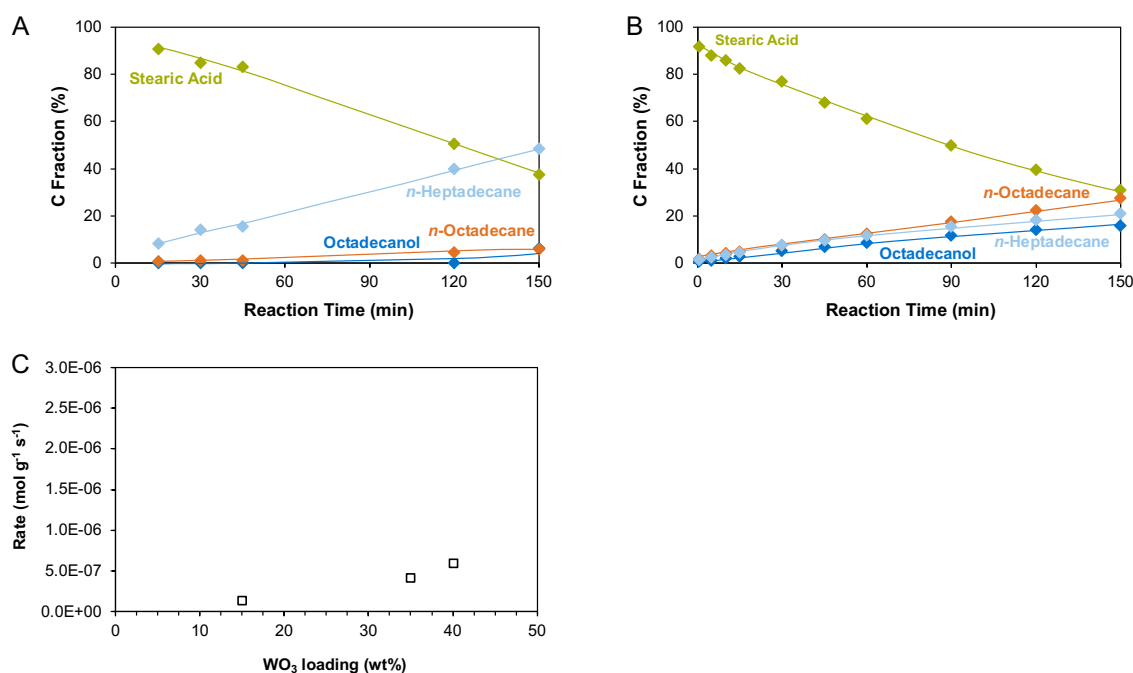
WO <sub>3</sub> loading	Initial rate (mol g <sup>-1</sup> s <sup>-1</sup> )	X (%)	S <sub><i>n</i>-heptadecane (%)</sub>	S <sub><i>n</i>-octadecane (%)</sub>	S <sub><i>n</i>-octadecanol (%)</sub>
15 wt%	9.2 x10 <sup>-8</sup>	20	34	26	40
35 wt%	1.3 x10 <sup>-6</sup>	88	32	52	16
40 wt%	1.7 x10 <sup>-6</sup>	100	32	51	17

Figure 5.8 C displays the significantly lower activity of a 0.5 wt% ruthenium doped catalyst. The reaction rate in water decreased by one order of magnitude and in decalin by 42% compared to 0.5 wt% Pt. Thus, also the superior activity in water diminished (H<sub>2</sub>O: 1.1 x10<sup>-7</sup> mol g<sup>-1</sup> s<sup>-1</sup>, decalin: 1.2 x10<sup>-7</sup> mol g<sup>-1</sup> s<sup>-1</sup>, Table 5.6). The selectivity in decalin changed towards a predominance of the decarbonylation pathway while there seems to be no preference between the two reaction routes in water.

The hydrodeoxygenation of stearic acid with a 1 wt% rhodium promoted tungstated carbon catalyst, on the other hand, showed a higher activity in decalin than in water (Figure 5.8 D, Table 5.6). Compared to the 1 wt% Pt catalyst, the reaction rate in water decreased by 66% but increased by almost one order of magnitude in decalin. Rhodium appears to promote the hydrodeoxygenation most in organic solvents (9.0 x10<sup>-7</sup> mol g<sup>-1</sup> s<sup>-1</sup>).

Interestingly, in water also the selectivity towards *n*-octadecane significantly decreased to 8% while *n*-heptadecane increased to 81%, showing that the stearic acid conversion almost exclusively follows the decarbonylation route (Figure 5.10 A, Table 5.6). While the faster conversion in decalin had a 43% selectivity towards *n*-octadecane and 33% towards *n*-heptadecane (Figure 5.10 B, Table 5.6). Hence, also for the carbon supported catalysts it seems to be beneficial for the catalytic activity to follow the dehydration route.

By increasing the tungsten oxide loading at a constant Rh loading of 1 wt% in water, an increase of the reaction rate was again observed. However, the enhancement effect was expectably less pronounced for the reaction mainly following the decarbonylation route (Figure 5.10 C, Table 5.8).



**Figure 5.10.** Product distribution of the stearic acid hydrodeoxygenation with 1 wt% Rh/40 wt% WO<sub>3</sub>/C catalyst in water (A) and in decalin (B). Rate dependency on the WO<sub>3</sub> loading with 1 wt% Rh promoted WO<sub>3</sub>/C catalysts in water (C). Reaction conditions: catalyst (0.2 g), stearic acid (0.5 g), solvent (100 mL),  $p(\text{H}_2) = 60$  bar, 700 rpm.

**Table 5.8.** Comparison of the initial rate, conversion after 2.5h and selectivities (S) with 1 wt% Rh promoted WO<sub>3</sub>/C catalysts with different WO<sub>3</sub> loadings in water. Reaction conditions: catalyst (0.2 g), stearic acid (0.5 g), water (100 mL), 260°C,  $p(\text{H}_2) = 60$  bar, 700 rpm.

WO <sub>3</sub> loading	Initial rate (mol g <sup>-1</sup> s <sup>-1</sup> )	X (%)	S <sub>n-heptadecane</sub> (%)	S <sub>n-octadecane</sub> (%)	S <sub>n-octadecanol</sub> (%)
15 wt%	1.3 x 10 <sup>-7</sup>	15	93	7	0
35 wt%	4.1 x 10 <sup>-7</sup>	39	81	8	11
40 wt%	5.9 x 10 <sup>-7</sup>	63	80	10	10

### 5.3 Conclusion

It has been demonstrated that stearic acid was successfully converted with metal promoted tungstated zirconia catalysts in an organic solvent and with metal promoted tungstated carbon catalysts additionally also in water. The hydrodeoxygenation reaction proceeded either *via* decarbonylation resulting in *n*- and *iso*-heptadecane or *via* dehydration forming *n*- and *iso*-octadecane.

The tungstated zirconia catalyst had a volcano-shaped rate dependency on the tungsten oxide loading with the highest rate and selectivity towards *iso*-octadecane on the 0.5 wt% Pt/16.4 wt% WO<sub>3</sub>/ZrO<sub>2</sub> catalyst due to the maximum BAS concentration.<sup>1</sup> As the hydrodeoxygenation follows predominantly the dehydration route for the Pt promoted catalysts, enhancing this step, in turn results in an overall increased activity and, at the same time, the high BAS concentration leads to an increase in isomerization. An optimum of the platinum concentration was found between 0.5 and 1 wt% with a trade-off between the increase in rate by higher Pt loading but the decrease in selectivity towards branched products due to faster hydrogenation of the olefins. Comparing platinum with other metals, rhodium, and ruthenium, showed that the hydrodeoxygenation rate increased in the order Ru << Rh < Pt, while the order of the selectivity towards *iso*-octadecane was inverted. Catalysts which proceed preferably *via* the decarbonylation pathway had lower hydrodeoxygenation rates while proceeding *via* dehydration resulted in higher rates. Therefore, Pt, following predominately the dehydration route, had the highest enhancement on the hydrodeoxygenation rate which was also confirmed by a lower activation energy.

For the carbon supported catalysts, 1 wt% Pt/40 wt% WO<sub>3</sub>/C catalyst showed the highest activity in water and completely converted stearic acid already after 2.5 h and is, thus, remarkably well suited for the conversion of microalgae in aqueous environments to hydrocarbon fuels. Rhodium was the most active catalyst in decalin. In general, also for the tungstated carbon catalysts there is a correlation between following the dehydration pathway and the highest rate enhancement.

## 5.4 Experimental

### 5.4.1 Chemicals

All chemicals were purchased commercially and were not further purified. The following chemicals were used: Nitrogen 5.0, hydrogen 5.0 and synthetic air (20.5 vol% oxygen, 79.5 vol% nitrogen) were obtained from *Westfalen*. Zr(OH)<sub>4</sub>·xH<sub>2</sub>O (XZO880/01) was supplied by *MEL Chemicals*. (NH<sub>4</sub>)<sub>6</sub>H<sub>2</sub>W<sub>12</sub>O<sub>40</sub>·xH<sub>2</sub>O (99.99% trace metals basis), Pt(NH<sub>3</sub>)<sub>4</sub>(NO<sub>3</sub>)<sub>2</sub> (99.995% trace metals basis), RuCl<sub>3</sub>·xH<sub>2</sub>O (ReagentPlus), RhCl<sub>3</sub>·xH<sub>2</sub>O (crystalline, ≥ 99.9 % trace metals basis), stearic acid (Grade I, ≥ 98.5 % (capillary GC)), *N,O*-bis(trimethylsilyl)trifluoroacetamide with trimethylchlorosilane (for GC derivatization, 99% (excluding TMCS)), stearyl stearate (≥ 98.0% (GC)), *n*-octadecane (99%), *n*-heptadecane (99 %) and diethyl ether (contains BHT, puriss. p.a., ACS reagent, reag. ISO, reag. Ph. Eur., ≥ 99.8 %) were acquired from *Sigma-Aldrich*. Decahydronaphthalene (mixture of *cis*- and *trans*-isomers, ≥ 99.0 %, for synthesis) and *n*-dodecane (≥ 99.0 %, for synthesis) were purchased from *Merck*. Activated carbon (2 mm & down) was provided by *Alfa Aesar*. Sodium chloride (99.5 % for analytical purposes) and sodium sulfate (99 %) were obtained from *Grüssing*.

### 5.4.2 Catalyst preparation

**M/WO<sub>3</sub>/ZrO<sub>2</sub>:** Firstly, the ammonium tungstate precursor solution was added dropwise onto the Zr(OH)<sub>4</sub>·xH<sub>2</sub>O support by incipient wetness impregnation, dried over night at 110 °C, and was then calcined in synthetic air (flow rate: 100 mL min<sup>-1</sup>) at 800 °C for 3 h (heating rate: 10 °C min<sup>-1</sup> until 700 °C, afterwards 5 °C min<sup>-1</sup>). The metals were subsequently incorporated onto the tungstated zirconia catalysts again by incipient wetness impregnation with the tetraammineplatinum nitrate/ ruthenium trichloride/ rhodium trichloride precursor solutions. The catalyst was thermally treated in nitrogen (flow rate: 100 mL min<sup>-1</sup>) at 400 °C for 3 h (heating rate: 3 °C min<sup>-1</sup>) and finally reduced in hydrogen (flow rate: 100 mL min<sup>-1</sup>) at 400°C for 3 h (heating rate: 3 °C min<sup>-1</sup>).

**M/WO<sub>3</sub>/C:** The carbon supported catalysts were also synthesized by incipient wetness impregnation of the activated carbon with the ammonium tungstate solution, dried over night at 110°C, followed by a thermal treatment in N<sub>2</sub> (flow rate: 100 mL min<sup>-1</sup>) at 400°C for 5 h (heating rate: 2°C min<sup>-1</sup>). The metals were likewise added to the tungstated carbon catalysts by incipient wetness impregnation with the tetraammineplatinum nitrate/ ruthenium trichloride/ rhodium trichloride precursor solutions. The thermal treatment in nitrogen (flow rate: 100 mL min<sup>-1</sup>) was conducted at 450 °C for 3 h (heating rate: 2 °C min<sup>-1</sup>), followed by the reduction in hydrogen (flow rate: 100 mL min<sup>-1</sup>) at 500°C for 4 h (heating rate: 2 °C min<sup>-1</sup>).

### 5.4.3 Analysis Methods

**Elemental analysis:** The tungsten and platinum content was analyzed photometrically by UV-VIS spectroscopy using a *Shimadzu UV-160* UV-VIS-NIR spectrometer. Tungsten samples were prepared by an alkaline pulping and platinum samples were prepared by acidic pulping. Ruthenium and rhodium samples were dissolved in acid before they were analyzed in an 280FS atomic adsorption system.

### 5.4.4 Catalytic measurements

The reactions were carried out in an autoclave (300 mL) from *Parr Instruments Co.* (type: *PST FS*, material: HASTELLOY C) with a temperature and stirring controlling device (*Parr Instruments Co. 4848 Reactor Controller*). A gas chromatography (GC) system (*Agilent Technologies 7890B GC*, *HP-5* capillary column (30 m, 0.32 mm inner diameter, 0.25 µm film), equipped with a flame ionization detector (FID) and a mass spectrometer (MS) (*Agilent Technologies 5977 MS*) was used to analyze the liquid samples. The data was evaluated with *MassHunter Workstation Software, Qualitative Analysis, Version B.06.00, Agilent Technologies (2012)*.

Reactant and catalyst were dissolved in 100 mL solvent (bidistilled water or decalin). The reactor was twice purged with H<sub>2</sub> or N<sub>2</sub>, after which the pressure was set to 6 bar and heated to the desired temperature with a heating rate of 10 °C per minute without stirring. The total pressure was adjusted 10 °C below the reaction temperature. The experiment was started as soon as the target temperature was reached by setting the stirring rate to 700 rpm. For reactions in the organic solvent in situ sampling was applied, while the aqueous phase products were extracted with 3 × 20 mL diethyl ether after each reaction. In order to improve the phase separation during the extraction, a small amount of sodium chloride was added to the reaction mixture. Afterwards, the organic phase was dried over sodium sulfate. *n*-Dodecane was used as an internal standard to monitor the carbon-balance.

## 5.5 References

- (1) Milaković, L.; Liu, Y.; Baráth, E.; Lercher, J. A. Dehydration of fatty alcohols on zirconia supported tungstate catalysts. *Catalysis Science & Technology* **2022**, *12* (20), 6084.
- (2) Guschina, I. A.; Harwood, J. L. In *Algae for Biofuels and Energy*; Borowitzka, M. A.; Moheimani, N. R., Eds.; Springer Netherlands: Dordrecht, **2013**, 17.
- (3) Peng, B.; Yao, Y.; Zhao, C.; Lercher, J. A. Towards Quantitative Conversion of Microalgae Oil to Diesel-Range Alkanes with Bifunctional Catalysts. *Angewandte Chemie International Edition* **2012**, *51* (9), 2072.
- (4) Peng, B.; Yuan, X.; Zhao, C.; Lercher, J. A. Stabilizing Catalytic Pathways via Redundancy: Selective Reduction of Microalgae Oil to Alkanes. *Journal of the American Chemical Society* **2012**, *134* (22), 9400.
- (5) Zhao, C.; Brück, T.; Lercher, J. Catalytic deoxygenation of microalgae oil to green hydrocarbons. *Green Chemistry* **2013**, *15*.
- (6) Mata, T.; Martins, A.; Caetano, N. Microalgae for biodiesel production and other applications: A review. *Renewable and Sustainable Energy Reviews* **2010**.
- (7) Foraita, S.; Liu, Y.; Haller, G. L.; Baráth, E.; Zhao, C.; Lercher, J. A. Controlling Hydrodeoxygenation of Stearic Acid to n-Heptadecane and n-Octadecane by Adjusting the Chemical Properties of Ni/SiO<sub>2</sub>-ZrO<sub>2</sub> Catalyst. *ChemCatChem* **2017**, *9* (1), 195.
- (8) Wang, W.; Liu, C.-J.; Wu, W. Bifunctional catalysts for the hydroisomerization of n-alkanes: the effects of metal-acid balance and textural structure. *Catalysis Science & Technology* **2019**, *9* (16), 4162.
- (9) Jiménez-Díaz, L.; Caballero, A.; Pérez-Hernández, N.; Segura, A. Microbial alkane production for jet fuel industry: motivation, state of the art and perspectives. *Microb Biotechnol* **2017**, *10* (1), 103.
- (10) Lim, J. H. K.; Gan, Y. Y.; Ong, H. C.; Lau, B. F.; Chen, W.-H.; Chong, C. T.; Ling, T. C.; Klemeš, J. J. Utilization of microalgae for bio-jet fuel production in the aviation sector: Challenges and perspective. *Renewable and Sustainable Energy Reviews* **2021**, *149*, 111396.



# Chapter 6

## Conclusions

This thesis offers valuable insights into the conversion of biomass resources to hydrocarbon fuels. It provides a comprehensive understanding of the hydronium-ion-catalyzed dehydration of substituted cyclohexanols from a mechanistic perspective. Additionally, it takes an application-driven approach to optimize the catalysts applied for the conversion of microalgae into fuels.

Investigating the hydronium-ion-catalyzed dehydration of substituted cyclohexanols in aqueous phase showed that the dehydration rate resulting from hydronium ions confined in the micropores of MFI and BEA zeolites were significantly higher than the rates without confinement. An increased stabilization of the transition state for tertiary alcohols shifted the tendency from a concerted (E2 mechanism, for the primary alcohols) to a stepwise dehydration (E1 mechanism). It was revealed that the primary, secondary, and tertiary alcohols all follow one compensation correlation between activation enthalpy and entropy, independent of the reaction mechanism and the environment. For a given transition enthalpy, increasing the reaction space, i.e., the reaction entropy, will result in an increase of the dehydration rate. The compensation correlations all intersect in a common point which represents the highest reaction rate. The dependence between the enthalpies and entropies is primarily determined by the position of the OH group. These experimentally derived dependencies, therefore, allow to predict the trends of the catalytic reactivities for alcohols independent of their specific substitution and the zeolite.

Further, the impact of the concentration of hydrated hydronium ions in MFI zeolites with varying Si/Al ratios on the aqueous phase dehydration of secondary alcohols which follow different mechanisms (4-methylcyclohexanol for E1 mechanism and *cis*-2-methylcyclohexanol for E2 mechanism) was studied. The increase of the turnover frequencies (TOF) within the obtained volcano-plots was attributed to the rise in the local ionic strength. The decrease resulted from the additional work needed to overcome the strong repulsive forces when the void space between neighboring hydronium ions dropped below a critical distance, necessitating ion pair reorganization. The maximum TOFs were consistently found at intermediate Si/Al ratios regardless of substitution or the different dehydration mechanisms. The reaction pathway, however, has great influence on the activation entropy and enthalpy as well as how they were

affected by the ionic strength. The formation of carbenium ions (E1) led to enthalpic stabilization at high ionic strength, while the associated complex formation (E2) was primarily supported by entropy. Despite the increased steric bulkiness, *cis*-2-McyOH showed notably higher dehydration rates than 4-McyOH due to the E2 pathway and, thus, the selective conversion to the energetically more favored Saytzeff-product.

Moreover, bifunctional metal supported tungstate catalysts (M/WO<sub>3</sub>/ZrO<sub>2</sub> or M/WO<sub>3</sub>/C; M = Pt, Rh, Ru) were synthesized, characterized, and optimized for the conversion of microalgae into hydrocarbon fuel in both organic and aqueous solvents. These catalysts were able to successfully catalyze the hydrodeoxygenation reaction of stearic acid, which was used as a model compound for the microalgae, into linear and branched long-chain hydrocarbons (hepta- and octadecane), applicable for (jet) fuels. In organic solvents, the metals promoting the tungstated zirconia catalysts, which follow predominantly the decarbonylation pathway (rhodium and ruthenium), had lower hydrodeoxygenation rates than those proceeding primarily *via* dehydration (platinum). Enhancing the dehydration step, thus, results in an overall increase in activity, and the thereby accompanying high BAS concentration also leads to an increase in isomerization. Varying the platinum concentration represents a trade-off between an increased rate due to higher Pt loading and a decrease in selectivity towards branched products due to faster olefin hydrogenation. A similar correlation between the reaction pathway and the rate enhancement was found for the metal promoted tungstated carbon catalysts. Platinum, predominantly following the dehydration pathway, resulted in the highest activity in water.

The crucial subsequent dehydration step of octadecanol was further thoroughly investigated. The studied supported tungstate catalysts (WO<sub>3</sub>/ZrO<sub>2</sub> or WO<sub>3</sub>/C) showed a volcano-shaped dehydration rate dependency on the tungsten loading. For the tungstate zirconia catalyst, the presence of a most active species, i.e., Zr-stabilized WO<sub>3</sub> clusters, was concluded to exist above monolayer coverage. XRD measurements revealed that the occurrence of these clusters correlated with the tetragonal zirconia phase. Maximizing this polymorph resulted in the highest BAS concentrations and, in turn, the highest octadecanol dehydration rates. Incorporating platinum onto the tungstated zirconia catalysts enhanced the dehydration rate due to a Pt facilitated hydrogen reduction of the tungstates already at moderate temperatures. The zirconia supported catalysts, however, were not active in aqueous phase due to the inaccessibility of the apolar substrate to the catalytic surface, which was covered by the surrounding water. Whereas the apolar carbon supported catalysts were successful in the dehydration of octadecanol in both the organic and aqueous phase.

Overall, these results could pave the way for the development of more efficient and sustainable processes for converting microalgae into renewable fuels, thus contributing to the global transition to cleaner energy sources.



---

# List of publications

## Journal contributions

Milaković, L.; Liu, Y.; Baráth, E.; Lercher, J. A. Dehydration of fatty alcohols on zirconia supported tungstate catalysts. *Catalysis Science & Technology* **2022**, 12 (20), 6084.

Milaković, L.; Hintermeier, P. H.; Liu, Y.; Baráth, E.; Lercher, J. A. Influence of Intracrystalline Ionic Strength in MFI Zeolites on Aqueous Phase Dehydration of Methylcyclohexanols. *Angewandte Chemie International Edition* **2021**, 60 (47), 24806.

Pfriem, N.; Hintermeier, P. H.; Eckstein, S.; Kim, S.; Liu, Q.; Shi, H.; Milaković, L.; Liu, Y.; Haller, G. L.; Baráth, E. et al. Role of the ionic environment in enhancing the activity of reacting molecules in zeolite pores. *Science* **2021**, 372 (6545), 952.

Milaković, L.; Hintermeier, P. H.; Liu, Q.; Shi, H.; Liu, Y.; Baráth, E.; Lercher, J. A. Towards understanding and predicting the hydronium ion catalyzed dehydration of cyclic-primary, secondary and tertiary alcohols. *Journal of Catalysis* **2020**, 390, 237.

## Conference contributions

ICC 2020 – the 17th International Congress on Catalysis, San Diego, USA

Presentation: *Aqueous phase Hydrodeoxygenation of Microalgae Oil to Transportation Fuels* (cancelled due to the Covid19 pandemic)

52. Jahrestreffen Deutscher Katalytiker 2019, Weimar

Poster & Short presentation: *Microalgae conversion to transportation fuels over tungsten-based catalysts*

DGMK Conference 2018 – Challenges for Petrochemicals and Fuels, Berlin

Presentation: *Conversion of microalgae oil to biokerosene over WO<sub>3</sub>/ZrO<sub>2</sub> supported metal catalysts*

Merck CURIOS2018 – Future Insight Conference, Darmstadt

Poster: *Conversion of microalgae oil to biokerosene over WO<sub>3</sub>/ZrO<sub>2</sub> supported metal catalysts*

51. Jahrestreffen Deutscher Katalytiker 2018, Weimar

Poster: *Conversion of stearic acid over WO<sub>3</sub>/ZrO<sub>2</sub> supported Cu catalyst*

# Statutory Declaration

I declare that I have authored this thesis independently, that I have not used other than the declared resources, and that I have explicitly marked all material which has been quoted either literally or by content from the used sources.

Chapters 2, 3 and 4 are reprinted with permission under the terms of the publishers. Edits have been made to the numbering and layout in order to improve the readability. At the end of the respective chapters, collaborators are acknowledged and their specific contribution is addressed.

Lara Milaković